



Using a surface energy budget framework to characterize grass-biophysical response to changes in climate in support of on-farm decision making in Ireland

Kazeem Abiodun Ishola

Thesis submitted to Maynooth University in fulfilment of the requirements for the Degree of Doctor of Philosophy

Irish Climate Analysis and Research Units (ICARUS),
Department of Geography, Maynooth University,
Maynooth, Co. Kildare, Ireland

Head of Department: Professor Gerry Kearns

Research Supervisors: Rowan Fealy, Prof. Gerald Mills, Reamonn Fealy



CONTENTS

Declaration.....	vi
Dedication and Acknowledgments.....	vii
List of Figures.....	ix
List of Tables.....	xv
List of Abbreviations and Acronyms.....	xvii
List of Symbols.....	xxi
Abstract.....	xxiv
Publications.....	xxv
1. Introduction.....	1
1.1 Overview.....	1
1.2 Plant physiological response to environment.....	5
1.3 Climate change context.....	8
1.4 Knowledge gaps.....	11
1.5 Research questions.....	14
1.6 Thesis structure.....	15
2. Literature review.....	18
2.1 Introduction.....	18
2.2 Theoretical framework of surface-air energy exchanges.....	20
2.2.1 Penman-Monteith (PM) equation.....	24
2.2.2 Surface and aerodynamic resistances.....	27
2.2.3 Monin-Obukhov Similarity Theory (MOST)	31
2.3 Micrometeorological measurements.....	36
2.4 Evolution of Land Surface Model based approaches.....	39
2.5 Role of land surface processes in extreme drought events.....	48
2.6 Estimating crop-water use at farm-scale.....	55
2.7 Implications of research on surface-air exchanges for Ireland.....	60
2.8 Key issues.....	62
3. Land surface modelling of surface radiation and energy fluxes using routine weather data: Parameterization and sensitivity to soil moisture regimes.....	65
Preface.....	65

Abstract.....	66
3.1 Introduction.....	67
3.2 Study area.....	69
3.2.1 Background climate.....	69
3.2.2 Site descriptions.....	71
3.3 Data.....	73
3.3.1 Flux measurements.....	74
3.3.2 Meteorological data.....	77
3.3.3 Soil water data.....	79
3.4 Methods.....	80
3.4.1 Model set-up.....	80
3.4.2 Surface resistance.....	84
3.4.3 Simulating fluxes at the test sites.....	87
3.5 Results.....	89
3.5.1 Evaluation of radiation and estimated fluxes.....	89
3.5.1.1 Net radiation.....	89
3.5.1.2 Sensible heat fluxes.....	90
3.5.1.3 Latent heat fluxes.....	92
3.5.2 Analysis of model sensitivity.....	95
3.5.2.1 Sensitivity of Q_E to soil and environmental factors.....	95
3.5.2.2 Estimation of surface fluxes using adjusted coefficients.....	98
3.6 Discussion.....	99
3.6.1 Physical control of surface resistance and surface fluxes.....	99
3.6.2 Uncertainties in surface heat flux simulations.....	104
3.7 Conclusion.....	107
4. A model framework to investigate the role of anomalous land surface processes in the amplification of summer drought across Ireland during 2018.....	109
Preface.....	109
Abstract.....	110
4.1 Introduction.....	111
4.2 Materials and Methods.....	115
4.2.1 In-situ meteorological data.....	115

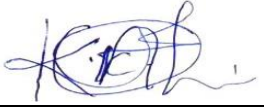
4.2.2	Gridded data.....	117
4.2.3	Satellite-derived products.....	119
4.2.4	Model description.....	121
4.2.5	Data analysis.....	123
4.3	Results.....	124
4.3.1	Evolution of 2018 summer drought across Ireland.....	124
4.3.2	Perturbations of land-atmosphere energy exchanges.....	128
4.3.3	Relationship between soil moisture and surface flux densities.....	133
4.4	Discussion.....	138
4.4.1	Changes in land surface processes during severe drought.....	138
4.4.2	Role of soil moisture in land-atmosphere exchanges during 2018 summer.....	141
4.5	Conclusion.....	143
5.	Mapping high-resolution farm-scale water use of pasture lands using Sentinel-2 data: Application for grass yield prediction.....	146
	Preface.....	146
	Abstract.....	147
5.1	Introduction.....	148
5.2	Materials and Methods.....	151
5.2.1	Sample research farms.....	151
5.2.2	Meteorological forcing data.....	153
5.2.3	Grass yield data.....	154
5.2.4	Satellite derived data.....	155
5.2.5	Mapping high resolution daily evapotranspiration.....	160
5.2.6	Relationship between ecosystem water use and yield.....	161
5.3	Results.....	164
5.3.1	Analysis of NIRv from Sentinel-2.....	164
5.3.2	Analysis of ET changes.....	169
5.3.2.1	Johnstown Castle.....	169
5.3.2.2	Athenry	171
5.3.2.3	Moorepark.....	173
5.3.3	Characteristics of ecosystem water use efficiency across the farms.....	176

5.3.4	Analysis of WUE-Yield correlations.....	180
5.4	Discussion.....	183
5.5	Conclusion.....	186
6.	Conclusions.....	188
6.1	Summary.....	188
6.1.1	Understanding LSS sensitivity and performance over Irish landscapes.....	189
6.1.2	Evaluating regional SEB and exchange processes during drought.....	191
6.1.3	Relating high resolution farm-scale water use to grass yields.....	193
6.2	Research Limitations.....	195
6.3	Implications for Policy.....	198
6.4	Future work.....	203
	Bibliography.....	206
	Appendix A: Comparison of shortwave broadband albedo models.....	237
	Appendix B: Python script used for simulating surface fluxes.....	239
	Appendix C: R script used for mapping terrestrial evapotranspiration, gross primary productivity and water use efficiency at Sentinel-2 scale	248
	Supplementary Information.....	256
	Paper 1: Improving a land surface scheme for estimating sensible and latent heat fluxes above grasslands with contrasting soil moisture zones (Published).	
	Paper 2: A model framework to investigate the role of anomalous land surface processes in the amplification of summer drought across Ireland during 2018, in revision.	
	Paper 3: Mapping high-resolution water use efficiency of pasture lands using Sentinel-2 data: Application for grass yield prediction, in preparation for submission.	

Declaration

I certify that this dissertation has not be submitted for a degree in this or any other university.

The contents of the thesis are the original work of the author and all secondary materials and literature used have been adequately acknowledged and referenced.

Signed: 
Kazeem Abiodun Ishola

Dedication and Acknowledgments

For Chevonne, Cyrus and Lucy

My profound gratitude to Almighty God, the giver of life, wisdom and vigour, for successful completion of this PhD project.

I am greatly indebted to my supervisors, Dr Rowan Fealy (Department of Geography, Maynooth University), Dr Gerald Mills (School of Geography, University College Dublin) and Dr Reamonn Fealy (Spatial Analysis Units, Teagasc, Ashtown-Dublin) for giving me the opportunity to carry out this project, and for their endless patience, support, encouragement, constructive suggestions and guidance which are pivotal to achieving the overall goal of this project and my career development on to this stage. Also to Dr Stuart Green for the assistance and encouragement at various stages. I appreciate the contributions of Emeritus Prof. Bert Holtslag, Dr Bert Heusinkveld and Dr Arnold Moene during my short visit to the Meteorology and Air Quality group of Wageningen University and Research (WUR) in the Netherlands in 2019. My sincere gratitude to the leadership of Irish Climate Analysis and Research Units (ICARUS) and the Department of Geography, Maynooth University for giving me a platform to work and learn. I thank all my colleagues both at ICARUS and Teagasc Spatial Analysis Units.

This project is fully funded by Teagasc under Walsh Fellowship Programme. I am grateful for this funding without which it may be uncertain to efficiently carry out this project. I am especially thankful to Prof. Peter Thorne (Director, ICARUS) for facilitating financial assistance for my short visit to WUR in 2019, acquisition of electronic gadgets used throughout this

project, scientific programming training at National University of Ireland, Galway in 2019 and Conference of Irish Geographers registration in 2018.

Special thanks to my mother and siblings for their endless prayers and encouragement to reach this point.

I have also received help, support, prayers and encouragement from individuals in and outside academics, including Dr Ifeoluwa Balogun, Dr Emmanuel Asaniyan, Prof. Emmanuel Okogbue, Dr A. Akinbobola, Mr and Mrs Adegbulugbe, Mr Tade Oni, Dr Dunsin Arodudu, Dr Oluwafemi Adeyeri, Dr Tobi Morakinyo, Dr Stephen Ogungbenro, Dr Akintomide Akinsanola, Dr Ezekiel Gbode, Pastor Kola Olubakin, Pastor Femi Akinbami, Ms Mary Morrisson and family, Mr Lucas Anuforum and family, Mrs Helen Adeoti, Mr Bode Olatunji and family, Mrs Aye, the management of Department of Meteorology and Climate Science, Federal University of Technology, Akure, Nigeria, Miss Clara Onugha, Mr Bode Famotemi, Mr Dare Adelanke and Miss Adesua Ohikueme.

I thank the Irish Meteorological Service and FLUXNET site investigators for sharing and providing free access to the data used in this project. Also to the services that provide access to Copernicus Global Land Service (CGLS) products, ERA5-Land Global Reanalyses products, European Space Agency (ESA) Sentinel products, and Moderate resolution Imaging Spectroradiometer (MODIS) products.

List of Figures

Figure 1.1: Trends in the value of gross output by sector (Conefrey, 2018).....	2
Figure 1.2: Plant stomatal size and density: Leaves with smaller, denser stomatal pores [left] have higher maximum stomatal conductance (g_{max}) and are more sensitive to closure during drought (i.e. larger loss of stomatal conductance during dehydration of leaves, indicated by thicker red arrow lines) than the leaves with larger, less dense stomata [right] (Henry et al., 2019).....	5
Figure 1.3: Illustration of ‘grass’ surface biophysical interactions. r_a is the aerodynamic resistance to momentum transfer, r_{sw} and r_{sc} are surface ‘stomatal’ resistance to water vapour and CO ₂ transfer, respectively.....	7
Figure 1.4: The coupling and feedback loop between the surface and the atmosphere during severely hot drought. The signs +, - and 0 indicate positive, negative and no feedback, respectively (Teuling, 2018).....	9
Figure 1.5: (a) True color Sentinel-2 images of South East region of Ireland during 2018 mid-summer; (b) Temporal evolution of national grass growth 2016 – 2018 from Teagasc PastureBase Ireland (Dillon et al., 2018). The rectangle box highlights the period of severe weather impacts on grass yields.....	11
Figure 1.6: Overview of the thesis structure.....	17
Figure 2.1: Variation of surface energy balance (SEB) terms for (a) daytime over land and; (b) nighttime over land (Stull, 1988). Signs are positive upward and negative downward, and arrow size indicates relative magnitude.....	21
Figure 2.2: Response of surface resistance (r_s) to water vapour deficit (Δq) according to different schemes over Cabauw grassland, the Netherlands (van de Boer et al., 2014a).....	29
Figure 2.3: Temporal evolution of different layers of the atmospheric boundary layer (ABL) over land (Stull, 1988).....	32
Figure 2.4: Schematic illustration of measurement principle of an eddy covariance system. The air flow looks turbulent but vertical movement can be measured from the flux tower (Hu et al., 2014).....	37
Figure 2.5: A schematic illustration of temporal evolution of land surface model processes, showing time of emergence of different model components and increasing complexity through time (Fisher and Koven, 2020).....	40
Figure 2.6: Concept of a typical Land Surface Model (LSM) structure, showing the components of surface radiation, energy and water budget (Adapted from Kumar et al., 2006).....	42

Figure 2.7: An illustration of soil moisture-evapotranspiration coupling framework that defines the three evaporative regimes (Adapted from Seneviratne et al., 2010).....	51
Figure 3.1: Map of soil drainage classes for Ireland (Irish Soil Information System by Teagasc for EPA, Creamer et al., 2014), showing the locations of test sites.....	71
Figure 3.2: The hourly surface energy balance closure at Johnstown Castle and Dripsey sites.....	77
Figure 3.3: Temporal evolution of in situ meteorological forcing data for Johnstown Castle. [top-bottom] air temperature, vapour pressure deficit, wind speed, soil temperature, volumetric water content and rainfall.....	78
Figure 3.4: Temporal evolution of in situ meteorological forcing data for Dripsey flux sites. Meteorological data except soil water (VWC) are available from Cork-Airport. [top-bottom] air temperature, vapour pressure deficit, wind speed, soil temperature, volumetric water content for 2005, and rainfall.....	79
Figure 3.5: Schematic diagram of surface energy balance estimates. The dotted line denotes the iteration process using MOST, while the dashed lines show the input and output variables and parameterization workflow.....	81
Figure 3.6: Relationship between daytime hourly measured (Q_{Nm}) and estimated (Q_{Ne}) net radiation flux over both sites.....	89
Figure 3.7: Relationship between daytime hourly measured (Q_{Hm}) and estimated (Q_{He}) sensible heat flux applying the Scheme with different r_s models over Johnstown Castle. The line plot is the diurnal cycle of Q_H , averaged for July, 2013.....	91
Figure 3.8: Relationship between daytime hourly measured (Q_{Hm}) and estimated (Q_{He}) sensible heat flux applying the Scheme with different r_s models over Dripsey. The line plot is the diurnal cycle of Q_H , averaged for July, 2010.....	92
Figure 3.9: Relationship between daytime hourly measured (Q_{Em}) and estimated (Q_{Ee}) latent heat flux applying the Scheme with different r_s models over Johnstown Castle. The line plot is the diurnal cycle of Q_E , averaged for July, 2013.....	94
Figure 3.10: Relationship between daytime hourly measured (Q_{Em}) and estimated (Q_{Ee}) latent heat flux applying the Scheme with different r_s models over Dripsey. The line plot is the diurnal cycle of Q_E , averaged for July, 2010.....	94
Figure 3.11: Sensitivity of daytime r_s and Q_E to environmental factors, averaged for January and July over Johnstown Castle. h_s (g kg^{-1}), S_r (W m^{-2}), c_{soil} ($\text{m}^3 \text{m}^{-3}$) and f_r is dimensionless. The calculated biases for January ($\approx -14 \text{ W m}^{-2}$) are similar for all factors. The dashed and solid lines are r_s and Q_E , respectively.....	96

Figure 3.12: Sensitivity of daytime r_s and Q_E to environmental factors, averaged for January and July over Dripsey. h_s (g kg^{-1}), S_r (W m^{-2}), c_{soil} ($\text{m}^3 \text{m}^{-3}$) and f_r is dimensionless. The calculated biases for January ($\approx -9 \text{ W m}^{-2}$) are similar for all factors. The dashed and solid lines are r_s and Q_E , respectively.....97

Figure 3.13: Relationship between daytime hourly measured and estimated Q_H [left] and Q_E [right] fluxes for 2013, applying the Scheme with optimized ($c_{soil} = 4.3 \text{ m}^3 \text{m}^{-3}$) r_s over Johnstown Castle.....98

Figure 3.14: Relationship between parameterized and measured averaged daily Q_H and Q_E over the selected sites. The daily variations of Q_E and Q_H in the course of a year are shown in the middle (c-d) and bottom (e-f) panels, respectively. The shaded portions are the 5th and 95th percentiles of uncertainty bound as calculated by LOESS regression.....100

Figure 3.15: Averaged diurnal variations of the measured θ of the top layer of the soil from 2004 to 2005 at Dripsey and for the year 2013 at Johnstown Castle. The gaps indicate periods with missing values. The horizontal dashed line is the threshold of θ at field capacity [blue] and wilting point [red], and the grey box is the (upper and lower critical θ at $0.25 \text{ m}^3 \text{m}^{-3}$ and $0.15 \text{ m}^3 \text{m}^{-3}$, respectively) bound of transitional soil moisture regime for both sites (after Shuttleworth, 1993)..... 102

Figure 4.1: Map of the study area showing the locations of selected weather stations and the dominant land cover types from 2018 CORINE Land cover product. The boxes A, B and C comprise of the grouped stations on the basis of similar precipitation variations..... 117

Figure 4.2: Comparisons between hourly measured and ERA5-Land volumetric water content (θ) across three independent grassland sites. The measured θ values are obtained from eddy covariance flux sites from previous studies (see Chapter three)..... 118

Figure 4.3: Spatial characteristics of monthly precipitation anomaly (z-score) for 2018 summer, relative to 21-year climatology (1999-2019). Thin lines represent county outlines.....125

Figure 4.4: Monthly anomalies of ERA5-Land surface soil water content (θ) and satellite-derived GEOV2 leaf area index (LAI); for 2018 summer, relative to 21-year climatology (1999-2019). (a-b) the spatial characteristics of both parameters; (c) inter-annual variations of monthly anomalies of θ , LAI and gridded precipitation, averaged over the entire region (blue, red and green horizontal dotted lines show the lowest negative scores for precipitation, θ and LAI, respectively).....127

Figure 4.5: Temporal evolution of model-derived mid-day land surface temperature anomaly (ΔT_s), compared with MODIS Terra ΔT_s during 2018 summer, relative to 2010-2019 average across the stations. The lines are derived from smoothed fits of locally weighted polynomial regression (LOESS). The shaded portions are the 5th and 95th percentiles of uncertainty bound as calculated by LOESS. Panels A, B and C are for stations in zones A, B and C, respectively, as highlighted in Figure 4.1 and Table 4.1.....129

Figure 4.6: Temporal evolution of in situ accumulated precipitation (first row), ERA5-Land volumetric water content (second row), in situ vapour pressure deficit (third row) and satellite-derived leaf area index (fourth row); during 2018 summer compared with climatology (1999-2019). Panels A, B and C are for stations in the respective zones highlighted in Figure 4.1. The peach shades represent the observed periods of abnormal surface and atmospheric conditions.....130

Figure 4.7: Temporal evolution of model-derived mid-day anomalous net radiative flux (ΔQ_N) (first row), sensible heat (ΔQ_H) and latent heat (ΔQ_E) fluxes (second row) and soil heat flux (ΔQ_G) (third row), during 2018 summer, relative to analysis period (2010-2019). Panels A, B and C are for stations in the respective zones highlighted in Figure 4.1. Values are the daily (10-15 hour) average.....133

Figure 4.8: Relationships between soil moisture (θ), evaporative fraction (EF) [first row] and MODIS NIRv [second row], based on segmented regression analysis during 2018 summer across the zones. The thick red lines are measures of sensitivity (slope) on the dry segment while dashed blue lines are for wet segment. The dashed orange lines show the θ -EF and θ -NIRv breakpoints and the horizontal green lines at the bottom show the confidence interval of θ breakpoints. ^a significant at p -value < 0.05. Panels A, B and C are for stations in the respective zones highlighted in Figure 4.1.....134

Figure 4.9: Relationships between soil moisture (θ), latent heat flux (ΔQ_E) [first row] and sensible heat flux (ΔQ_H) [second row], based on segmented regression analysis during 2018 summer across the zones. The thick red lines are measures of sensitivity (slope) on the dry segment while dashed blue lines are for wet segment. The dashed orange lines show the θ - ΔQ_E and θ - ΔQ_H breakpoints and the horizontal green lines at the bottom show the confidence interval of θ breakpoints. ^a significant at p -value < 0.05. Panels A, B and C are for stations in zones A, B and C, respectively, as highlighted in Figure 4.1 and Table 4.1.....136

Figure 4.10. Contour maps of the approximate start day of 2018 agricultural drought, based on the estimated critical soil moisture threshold (θ_c) in Table 4.3 for (a) evaporative fraction and (EF), (b) near-infrared reflectance of vegetation (NIRv). DOY is the day of the year.....137

Figure 5.1: Location of the sample research pasture farms and collocated weather stations. (A) Johnstown Castle (B) Athenry and (C) Moorepark. The highlighted plots are the sample areas used for analysis of each farm. The map of Ireland shows the herd population by County in 2019 (Source: Irish Cattle Breeding Federation).....152

Figure 5.2: Relationships between near infrared reflectance of vegetation (NIRv) and leaf area index, LAI [top]; fraction of absorbed photosynthesis active radiation, FAPAR [bottom] for 2017 [green] and 2018 [red] image dates across the farms. Values are derived from the highlighted sample grass plots in Figure 1.....159

Figure 5.3: (a) Sentinel2-derived near infrared reflectance of vegetation (NIRv) maps and; (b) histogram of NIRv values of selected image dates during 2017 and 2018 for Johnstown Castle farm. The vertical dashed red lines indicate the median NIRv values165

Figure 5.4: (a) Sentinel2-derived near infrared reflectance of vegetation (NIRv) maps and; (b) histogram of NIRv values of selected image dates during 2017 and 2018 for Athenry farm. No analysis for July 2017 due to lack of clear-sky Sentinel-2 images. The vertical dashed red lines indicate the median NIRv values167

Figure 5.5: (a) Sentinel2-derived near infrared reflectance of vegetation (NIRv) maps and; (b) histogram of NIRv values of selected image dates during 2017 and 2018 for Moorepark farm. No analysis for June of both years and July 2017 due to lack of clear-sky Sentinel-2 images. The vertical dashed red lines indicate the median NIRv values 168

Figure 5.6: The daily evapotranspiration (ET) changes at Senitnel2-scale for three selected image dates during 2017 and 2018 for Johnstown Castle farm. (a) ET maps and; (b) the distribution and trend of ET for near infrared reflectance of vegetation (NIRv) pixel values less than 0.25 and for NIRv pixel values greater than or equal to 0.25..... 170

Figure 5.7: The daily evapotranspiration (ET) changes at Senitnel2-scale for three selected image dates during 2017 and 2018 for Athenry farm. (a) ET maps and; (b) the distribution and trend of ET for near infrared reflectance of vegetation (NIRv) pixel values less than 0.25 and for NIRv pixel values greater than or equal to 0.25. No available cloud-free image in July of 2017..... 172

Figure 5.8: The daily evapotranspiration (ET) changes at Senitnel2-scale for three selected image dates during 2017 and 2018 for Moorepark farm. (a) ET maps and; (b) the distribution and trend of ET for near infrared reflectance of vegetation (NIRv) pixel values less than 0.25 and for NIRv pixel values greater than or equal to 0.25. No available cloud-free image in June and July of 2017 and June of 2018.....175

Figure 5.9: Relationships between daily evapotranspiration (ET) and gross primary productivity (GPP) derived from MODIS light use efficiency scheme, GPP_{MODIS} [top]; GPP derived from near infrared reflectance of vegetation, GPP_{NIRv} [bottom] for 2017 [green] and 2018 [red] image dates across the farms. Values are derived from the highlighted sample grass plots in Figure 5.1.....176

Figure 5.10: The daily water-use efficiency (WUE) maps at Senitnel2-scale for three selected image dates during 2017 and 2018 for Johnstown Castle farm. WUE_{MODIS} maps are derived from GPP-based MODIS light use efficiency scheme, while WUE_{NIRv} maps are derived from NIRv-based approach..... 177

Figure 5.11: The daily water-use efficiency (WUE) maps at Senitnel2-scale for three selected image dates during 2017 and 2018 for Athenry farm. WUE_{MODIS} maps are derived from GPP-based MODIS light use efficiency scheme, while WUE_{NIRv} maps are derived from NIRv-based approach. No available cloud-free image in July of 2017.....179

Figure 5.12: The daily water-use efficiency (WUE) maps at Senitnel2-scale for three selected image dates during 2017 and 2018 for Moorepark farm. WUE_{MODIS} maps are derived from GPP-based MODIS light use efficiency scheme, while WUE_{NIRv} maps are derived from NIRv-based approach. No available cloud-free image in June and July of 2017 and June of 2018.....180

Figure 5.13: Temporal evolution of measured weekly grass yields of 2017 and 2018 across the farms [first row]. Relationships between water-use indicators (daily actual evapotranspiration, ET and water-use efficiency, WUE) at 10-m pixel and grass yields [rows 2-4]. WUE_{MODIS} maps are derived from GPP-based MODIS light use efficiency scheme, while WUE_{NIRv} maps are derived from NIRv-based approach. Scatterplots contain image dates within the period in respective grey box in first row. Values are for highlighted sample grass plots in Figure 5.1.....181

Figure A1: Comparison between Liang (2001) based shortwave broadband albedo (α_{Liang}), and Li et al. (2018) based shortwave broadband albedo (α_{Li}) using the weighting coefficients (w_B) in Table A1 for (a) Johnstown Castle, (b) Athenry and (c) Moorepark, farms over the analysis period.....237

List of Tables

Table 3.1: Descriptions of grassland eddy covariance flux and synoptic stations used in this study. Meteorological data from Cork Airport (51.84°N, 8.48°W) at an elevation of 155 m were used for Dripsey. Johnstown Castle has a co-located weather station. The soil moisture properties are field capacity (θ_{FC}), saturation level (θ_{ST}) and wilting point (θ_{WP}), in order.....	72
Table 3.2: Descriptions of meteorology and eddy-covariance parameters used as forcings and for validation respectively.....	75
Table 3.3: Surface input parameters and corresponding values used at the selected stations.....	83
Table 3.4: Performance assessment of daytime ($Q_{S\downarrow} > 10 \text{ W m}^{-2}$) Q_H based on different r_s , over both stations. The italicized values show the r_s method that give the best agreement between estimated and measured Q_H . <i>RMSE and Bias (W m^{-2})</i>	90
Table 3.5: Performance assessment of daytime ($Q_{S\downarrow} > 10 \text{ W m}^{-2}$) Q_E based on different r_s , over both stations. The italicized values show the r_s method that give the best agreement between estimated and measured Q_E . <i>RMSE and Bias (W m^{-2})</i>	93
Table 3.6: Range of estimated r_s (s m^{-1}) during mid-day time ($Q_{S\downarrow} > 10 \text{ W m}^{-2}$ and $Q_{S\downarrow} > 100 \text{ W m}^{-2}$) over the selected stations. BB97 is based on the scheme using the default parameter values (i.e. Beljaars and Bosveld, 1997) for BB97; BB97 (optimised) is based on the updated optimised values for Johnstown Castle, employed in this study.....	95
Table 3.7: Adapted empirical coefficients of optimized r_s for Q_E estimation under different surface conditions.....	99
Table 4.1: Characteristics of the selected grassland synoptic stations. The soil types and drainage categories are based on the data from Irish Soil Information System (Creamer et al., 2014). The clustered zones A, B and C comprise of stations with similar precipitation variations.....	116
Table 4.2: A summary description of ground, gridded and satellite-derived products used in this study.....	121
Table 4.3: Site-specific ERA5-based critical soil moisture content (θ_c , $\text{m}^3 \text{ m}^{-3}$) (0-7cm layer) and date of onset of 2018 agricultural drought, derived using segmented regression relationships between θ , evaporative fraction (EF), and MODIS NIRv. Stations with relatively stronger θ -EF and θ -NIRv couplings are highlighted in bold. R^2_{adj} is the adjusted R^2	137
Table 5.1: A summary characteristics of Sentinel-2 Multispectral Imager spectral bands. w_B is the weighting coefficient for estimating shortwave broadband albedo (Liang, 2001).....	156

Table 5.2: Temporal coverage and corresponding instrument type of Sentinel-2 (S2) cloud-free images used over the sample farms, Johnstown Castle (tiles T29UPT and T29UPU); Athenry (tiles T29UNV); Moorepark (tiles T29UNT). * are the periods used in the plotted maps.....157

Table A1: Weighting coefficient (w_B) by spectral band for estimating shortwave broadband albedo, based on Liang (2001) and Li et al. (2018).....236

List of Abbreviations and Acronyms

ABL	Atmospheric Boundary Layer
AEZ	Agro-Ecological Zones
AGMET	Agrometeorology
ALEXI	Atmosphere-Land Exchange Inverse model
AMERIFLUX	America Flux network
ANN	Artificial Neural Network
ASCAT	Advanced Scatterometer
ASTER	Advanced Spaceborne Thermal Emission and Reflection Radiometer
AVHRR	Advanced Very High Resolution Radiometer
AWS	Automatic Weather Station
BATS	Biosphere-Atmosphere Transfer Scheme
BoA	Bottom of Atmosphere
BPLUT	Biome Parameter Look-up Table
BR	Bowen Ratio
BRDF	Bidirectional Reflectance Distribution Function
C3S	Copernicus Climate Change Service
CGLS	Copernicus Global Land Service
CNR	Compact Net Radiometer
CORINE	Coordination of Information on the Environment
CRAN	Comprehensive R Archive Network
CSO	Central Statistics Office
DM	Dry Matter
DEM	Digital Elevation Model
DOY	Day Of Year
EC	Eddy Covariance
ECMWF	European Center for Medium Range Weather Forecasting
EF	Evaporative Fraction
EPA	Environmental Protection Agency
ERA5	ECMWF Re-Analyses 5th generation

ESA	European Space Agency
ESI	Evaporative Stress Index
ET	Evapotranspiration
EUROFLUX	European Flux network
EUROSTAT	European Statistics
FAO	Food and Agriculture Organization
FAPAR	Fraction of Absorbed Photosynthetically Active Radiation
FIFE	First International satellite land surface climatology project Field Experiment
FLUXNET	global Flux Network
GHG	Green House Gases
GMT	Greenwich Meridian Time
GPP	Gross Primary Productivity
IIP	Island of Ireland Precipitation network
IPCC	Intergovernmental Panel on Climate Change
IRGA	InfraRed Gas Analyzer
ISBA	Interactions between Soil, Biosphere and Atmosphere
Kc	Crop coefficient
LAI	Leaf Area Index
LOESS	LOcally weighted polynomial regrESSion
LP DAAC	Land Processes Distributed Active Archive Center
LSM	Land Surface Model
LSS	Land Surface Scheme
LUE	Light Use Efficiency
METRIC	Mapping EvapoTranspiration at high Resolution with Internalized Calibration
MJ	MegaJoules
MODIS	MODerate resolution Imaging Spectroradiometer
MOST	Monin-Obukhov Similarity Theory
MSI	MultiSpectral Imager
NASA	National Aeronautics and Space Administration

NDVI	Normalized Difference Vegetation Index
NEE	Net Ecosystem Exchange
NIR	Near InfraRed
NIRv	Near-InfraRed reflection of vegetation
NOAH-MP	NOAH MultiParameterization
NR	Net Radiometer
NWP	Numerical Weather Predictions
OSU	Oregon State University
PAR	Photosynthetically Active Radiation
PBI	PastureBase Ireland
PBL	Planetary Boundary Layer
PDSI	Palmer Drought Severity Index
PFT	Plant Functional Type
PILPS	Project for Intercomparison of Land surface Parameterization Scheme
PM	Penman-Monteith model
PROBA-V	ESA satellite Vegetation instrument
PROSAIL	PROSPECT+SAIL radiative transfer model
PROSPECT	PROpriétésSPECTrales, leaf optical properties spectra model
PT	Priestly-Taylor model
QC	Quality control
RCM	Regional Climate Model
RH	Relative Humidity
RMSE	Root Mean Square Error
RS	Remote Sensing
SAIL	Scattering by Arbitrarily Inclined Leaves, canopy optical properties spectra model
SEB	Surface Energy Balance
SEBAL	Surface Energy Balance Algorithm for Land
SEBS	Surface Energy Balance System
SNAP	SentiNel Application Platform
SPDI	Standardized Palmer Drought Index

SPEI	Standardized Precipitation Evapotranspiration Index
SPI	Standardized Precipitation Index
SPOT-VGT	Satellite Pour l'Observation de la Terre Vegetation
SiB	Simple Biosphere model
SSiB	Simplified Simple Biosphere model
SURFLEX	Surface Flux Exchanges
TIR	Thermal InfraRed
ToA	Top of Atmosphere
TSEB	Two Source Energy Balance
UK	United Kingdom
USA	United State of America
VI	Vegetation indices
VPD	Vapour Pressure Deficit
VWC	Volumetric Water Content
WMO	World Meteorological Organization
WUE	Water Use Efficiency

List of Symbols

A_g	Soil heat transfer coefficient
B	Spectral band
c_p	Specific heat capacity of air
c_{soil}	Soil moisture coefficient
e	Vapour pressure
F_M	Soil moisture stress function
F_S	Solar radiation stress function
$F_{\Delta q}$	Air moisture deficit function
F_T	Near-surface temperature function
f_r	An empirical site-specific constant
g	Acceleration due to gravity
h_s	Moisture deficit coefficient
k	von Kàrmàn constant
L	Obukhov length
N	Cloud amount
P	Mean sea level pressure
Q_E	Latent heat flux
Q_G	Soil heat flux
Q_H	Sensible heat flux
Q_N	Net radiation
$Q_{L\downarrow}$	Incoming longwave radiation
$Q_{L\uparrow}$	Outgoing longwave radiation
$Q_{S\downarrow}$	Global solar radiation
$Q_{S\downarrow 24}$	Daily global solar radiation
$Q_{S\uparrow}$	Outgoing shortwave radiation
$Q_{\Delta S}$	Soil heat storage
R_d	Specific gas constant for dry air
R_v	Specific gas constant for water vapour
r_a	Aerodynamic resistance
r_s	Surface resistance

$r_{s,min}$	Minimum stomatal resistance
s	slope of saturated vapour pressure curves
S_r	Global radiation coefficient
T_a	Air temperature at 2 m
T_{min}	Daily minimum temperature
T_s	Surface temperature
T_{24}	24-hr moving average of 2-m temperature
u	Wind speed at 10 m
u_*	Friction velocity
w_B	Weighting coefficients of reflectance band
z_a	Observation height, 2 m.
z_{oH}	Surface roughness length for heat
z_{om}	Surface roughness length for momentum
α	Surface albedo
γ	Psychrometric constant
Γ_d	Dry adiabatic lapse rate
Δq_a	Specific humidity deficit at 2 m
Δq_s	Specific humidity deficit at the surface
ε	Surface emissivity
ε_a	Atmospheric emissivity
θ	Volumetric soil moisture in the root zone
θ_C	Critical soil moisture
θ_{FC}	Field capacity
θ_{ST}	Saturation point
θ_{WP}	Wilting point
θ_*	Temperature scale
ρ	Density of dry air
ρ_B	Surface reflectance band
ρ_w	Density of water
σ	Stefan Boltzmann's constant
ψ_H	Dimensionless stability term for heat

ψ_M

Dimensionless stability term for momentum

Abstract

This thesis, for the first time in Ireland, uses a framework that combines a land surface scheme (LSS) based on a surface energy budget theory, available environmental observations, land surface and atmospheric analyses, to understand essential mechanistic factors that determine grass growth response across the Irish landscape. A soil moisture model parameter (c_{soil}) is identified as the key factor that distinguishes soil types and their ability to retain water for plant growth, plant response to exchange processes, and drives the response of LSS in drying soils. A Modification of this parameter indicates that the LSS can be transferred to other locations. In the context of understanding the links between land surface dynamic processes and the persistence of 2018 summer drought regionally, drying soils and high atmospheric anomalies result in a reduced evapotranspiration (ET) process. This is the situation over grasslands in the east and south east of the country where a wet ‘evaporative’ regime quickly shifts into a ‘transitional’ regime in which vegetation functioning and ET are controlled by soil water availability. Particularly, a threshold value of soil moisture content that suggests the onset of 2018 agricultural drought has been found across the regions. The importance of water use efficiency for monitoring grass growth at field level and for distinguishing zones of optimum productivity is further discussed in the thesis. Overall, the findings demonstrate the potential consequences of climate change on Irish grasslands and the need for policies that are tailored to reinforcing observation networks to complement theories and model outputs akin to on-farm adaptation and optimization of water availability and productivity.

Publications

Aspects of the research contained in this thesis have been published, submitted or are in draft form in preparation for submission. Details of the outputs are provided below:

- 1) **K. A. Ishola**, R. Fealy, G. Mills, R. M. Fealy, S. Green, A. Jimenez-Casteneda, O. E. Adeyeri, 2018. Developing regional calibration coefficients for estimation of hourly global solar radiation in Ireland, *International Journal of Sustainable Energy*, 38(3), 297 – 311, DOI:10.1080/14786451.2018.1499645
- 2) **K. A. Ishola**, G. Mills, R. M., Fealy, Ó. Ní Choncubhair, R. Fealy, 2020. Improving a land surface scheme for estimating sensible and latent heat fluxes above grasslands with contrasting soil moisture zones. *Agric. Fores Meteor.* 294, 108151, <https://doi.org/10.1016/j.agrformet.2020.108151>
- 3) **K. A. Ishola**, G. Mills, R. M., Fealy, R. Fealy. A model framework to investigate the role of anomalous land surface processes in the amplification of summer drought across Ireland during 2018, revision submitted to *International Journal of Climatology* (Paper format provided in supplementary)
- 4) **K. A. Ishola**, R. M., Fealy, G. Mills, S., Green, R. Fealy. Mapping high-resolution water use efficiency of pasture lands using Sentinel-2 data: Application for grass yield prediction, in preparation for submission to *International Journal of Applied Earth Observation and Geoinformation*.
- 5) **Ishola, Kazeem Abiodun**, Fealy, Rowan, and Mills, Gerald, 2021. SURFLEX. Zenodo. <http://doi.org/10.5281/zenodo.4679843>.
The Zenodo repository contains the python codes for estimating SURface FLux EXchanges (SURFLEX) using limited routine weather data, published as a software tool.

1. Introduction

1.1 Overview

The agricultural sector is one of the most important economic sectors in the world due to its critical role in ensuring adequate food supply and its contribution to income and employment, accounting for 4 % of global gross domestic product (GDP) in 2018 (World Bank, 2021). In developing countries, agriculture can account for up to 25 % of a nation's GDP. In Ireland, the agricultural or agri-food sector plays a key role in the economy, accounting for more than 7 % of national gross value-added profit, 8 % of national employment and 10 % of overall merchandise exports from Ireland in 2017 (Conefrey, 2018; Teagasc, 2021).

Data from the Irish Central Statistics Office (CSO) demonstrate that, much of the increase in agricultural outputs and incomes in the last three decades has been driven by pasture-based commodities, particularly dairy and meat products, as shown in Figure 1.1 (Conefrey, 2018). These achievements are partly assisted by the development and implementation of policies and programmes (e.g. Food Harvest 2020, Grass10, Food wise 2025, etc.) devised by the relevant agri stakeholders, which are geared towards increasing the growth rate of the agri-food industry through optimal utilization of the natural grass resource base and delivery of high quality organic agricultural produce.

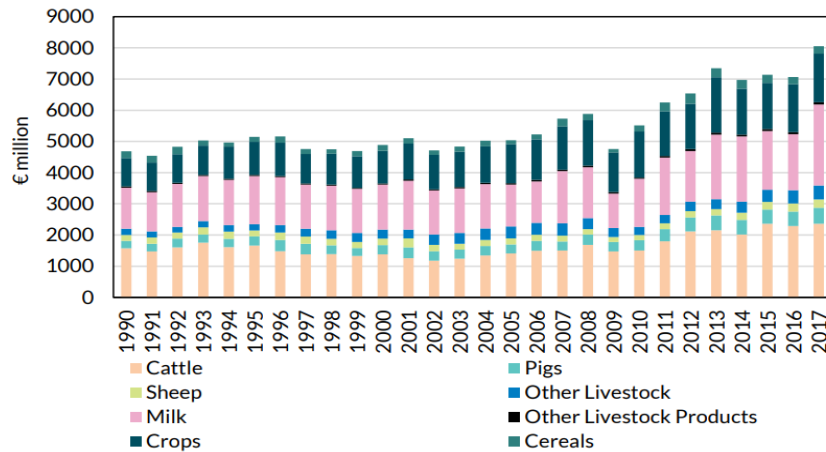


Figure 1.1. Trends in the value of gross output by sector (Conefrey, 2018)

The Irish agricultural landscape is primarily grass-dominated with approximately 90 % of the agricultural land area devoted to grass, representing about 52 % of the total land area (Jaksic et al., 2006). This abundant natural resource is largely linked to the temperate maritime climate (mild, wet winters and warm, moist summers) and fertile soils that are suited to grass growth. This has enabled the development of an efficient pasture-based production system and provides an important comparative advantage over its other international counterparts.

The regional distribution of pasture-based farming indicates that dairy farming dominates in the South and South-West in areas that are typically associated with limestone rich, well drained soils and long grass growth season (median of 330 days) (Keane and Collins, 2004; Green, 2019). The midlands and South East are dominated with mixed grazing on fertile well/moderately drained soils, beef production dominates around the border with Northern Ireland and in the North West, and sheep on the coastal uplands, in areas associated with poorly drained soils and a short grass growth season (Creamer et al., 2014; Green, 2019).

The most important factor that influences regional/local management of biological processes and the growth and performance of plants is the weather. The weather conditions required

for optimum grass growth are rarely met throughout a growing season. It has been reported that non-limiting soil water and soil temperatures above 5 °C are required for grass growth to occur (Hopkins, 2000). The soil water conditions, which are determined by soil type, precipitation and evapotranspiration, affects nutrient uptake, grass growth response and length of grazing season (Schulte et al., 2005).

Reflecting the regional variations in productivity, associated with soils and weather, efforts have been made to map and monitor agro-environmental conditions for optimal productivity (e.g. Hurtado-Uria et al., 2013a, 2013b). In many cases, meteorological data (e.g. solar radiation, precipitation and air temperature) from proximate weather stations are directly related to productivity. One limitation of this approach is that it does not take into account the variability in environmental factors (e.g. soil conditions) which also impact the plant growth in a region. For example, soil types vary in their water and heat holding capacity. Heavier soils (e.g. high clay content) can retain water longer relative to other soil types, reducing the impacts of high water deficits on plants grown over them. However, this soil type can become water logged and problematic for plant growth during prolonged periods of precipitation; these soils can also become untrafficable. Heavier soils warm up slowly, but retain heat longer into autumn, extending the grass growth and yields to later in the year (Fitzgerald et al., 2005, 2009).

Grass is grown over different soil characteristics across Ireland (e.g. Creamer et al., 2014), but a framework that integrates meteorology and environmental factors to provide explicit information about grass physiological response and growth at detailed spatial scales does not currently exist. A prognostic approach, incorporating the surface energy balance (SEB) framework, could potentially enhance an understanding of the processes, from point to

regional scales (e.g. Su, 2002), and consequently assist farmers to better understand, monitor and potentially predict growth response leading to more informed decision making.

The SEB is described by the net radiation (Q_N) at the surface, the surface sensible heat flux (Q_H) to the atmosphere by convection/advection, latent heat flux (Q_E) to the atmosphere by evaporation/transpiration, and soil heat flux (Q_G) to the subsurface by conduction (Arya, 2001). The partitioning of available energy ($Q_N - Q_G$) at the surface (e.g. vegetation) into Q_H and Q_E is very much dependent on the transpiration capacity of plants which is controlled by land surface state (e.g. soil conditions, vegetation structure, etc.) and prevailing atmospheric conditions. The SEB processes governing the local weather that determine grass growth can also be influenced by seasonal alterations in the mean climate, due to the alterations of plant's physiological response and processes, and with consequences for on farm productivity and income. An example of such impact is the 2018 fodder crisis (a growing season characterised by poor grass growth and lack of feed such as silage) (Dillon et al., 2018), which demonstrates the vulnerability of the Irish agricultural sector, particularly pastoral farming, to seasonal variations in weather. The use of diagnostic based approaches or simple correlations between meteorological variables and grass yields are lacking in that they provide an insufficient knowledge about the underlying mechanisms influencing the microclimate that govern grass growth.

In addition, as the climate changes, meteorological data alone can not be used to robustly investigate impacts on grass growth. The 2018 event provides an opportunity to explore how these gaps can be filled, by providing information relating to relevant parameters and how changes in these parameters influence grass water use and productivity at detailed spatial scales, which is the primary goal of this thesis. These can best be addressed by understanding

the physiological responses of plants, in terms of stomatal resistance, that scale up to influence ecosystem surface biophysical processes (CO₂, heat and water) in a changing climate.

1.2 Plant physiological response to environment

Plants growth depends on environmental factors, including light, atmospheric moisture, air temperature and soil water (e.g. Jarvis, 1976). In leaves, water is conducted from the root and transported upward through the xylem, or vascular tissue, to the stomatal pore where it is released in vapor form to the atmosphere through the stomata. At the same time, the opened stomata allow the uptake of CO₂ required for photosynthesis. Therefore, the rates of photosynthetic carbon uptake and water loss through transpiration from the canopy surface depend on the aperture size and density of stomatal pores (Figure 1.2), which are in turn regulated by environmental parameters and leaf morphology (Boisvenue and Running, 2013). The ability of a stomatal pore to allow transfer of water vapour from the canopy to the atmosphere is called the surface 'stomatal' conductance (g_s) and the inverse is referred to as surface 'stomatal' resistance (r_s , expressed in s m⁻¹).

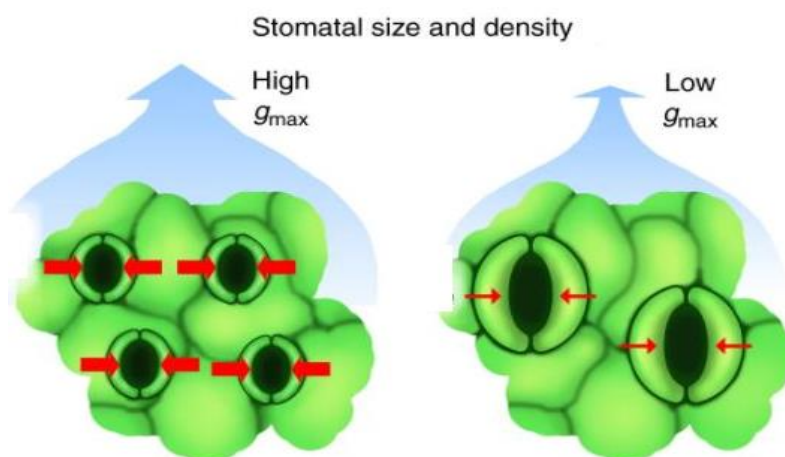


Figure 1.2. Plant stomatal size and density: Leaves with smaller, denser stomatal pores [left] have higher maximum stomatal conductance (g_{max}) and are more sensitive to closure during drought (i.e. larger loss of stomatal conductance during dehydration of leaves, indicated by thicker red arrow lines) than the leaves with larger, less dense stomata [right] (Henry et al., 2019).

Figure 1.3 shows a schematic illustration of surface biophysical interactions. At the canopy scale, plants regulate their stomatal aperture in response to environmental conditions, thus limiting or increasing the transport of water transpired via latent heat flux (Q_E) exchange. In wet conditions, stomata can either be in an opened or a closed state depending on the prevailing environmental conditions. During the day, stomata respond to increasing photosynthetically active radiation (PAR), soil water availability and atmospheric evaporative demand that is linked to rising air temperature, leading to low resistance and more transpiration and CO₂ uptake (Driesen et al., 2020). When the stomata openings are reduced, usually under conditions of water stress, the resistance is increased. As a consequence, little CO₂ is taken up due to reduced photosynthesis, and transpiration is lowered. During these periods, the available net radiation at the surface is largely transferred to the atmosphere in the form of sensible heat fluxes (Q_H) (Figure 1.3). Therefore, a plant's stomatal response is primarily driven by atmospheric conditions under wet regimes and by soil water availability during dry conditions (Seneviratne et al., 2010).

At night, stomata are mostly closed, leading to large resistance and almost null transpiration. Increasing temperature, which has been shown to have a positive effect on productivity (e.g. Toledo et al. 2011), also increases the vapour pressure deficit, thereby increasing transpiration rates through stomata opening, assuming no plant water stress and where PAR is not limited.

A plant's response is also determined by water use efficiency (WUE), which is a measure of tradeoffs between the plant's photosynthetic carbon assimilation and water loss through transpiration, and foliage light-use efficiency, of which both are recognized to vary across ecosystem types and leaf morphology in response to environmental conditions (Boisvenue and Running, 2013).

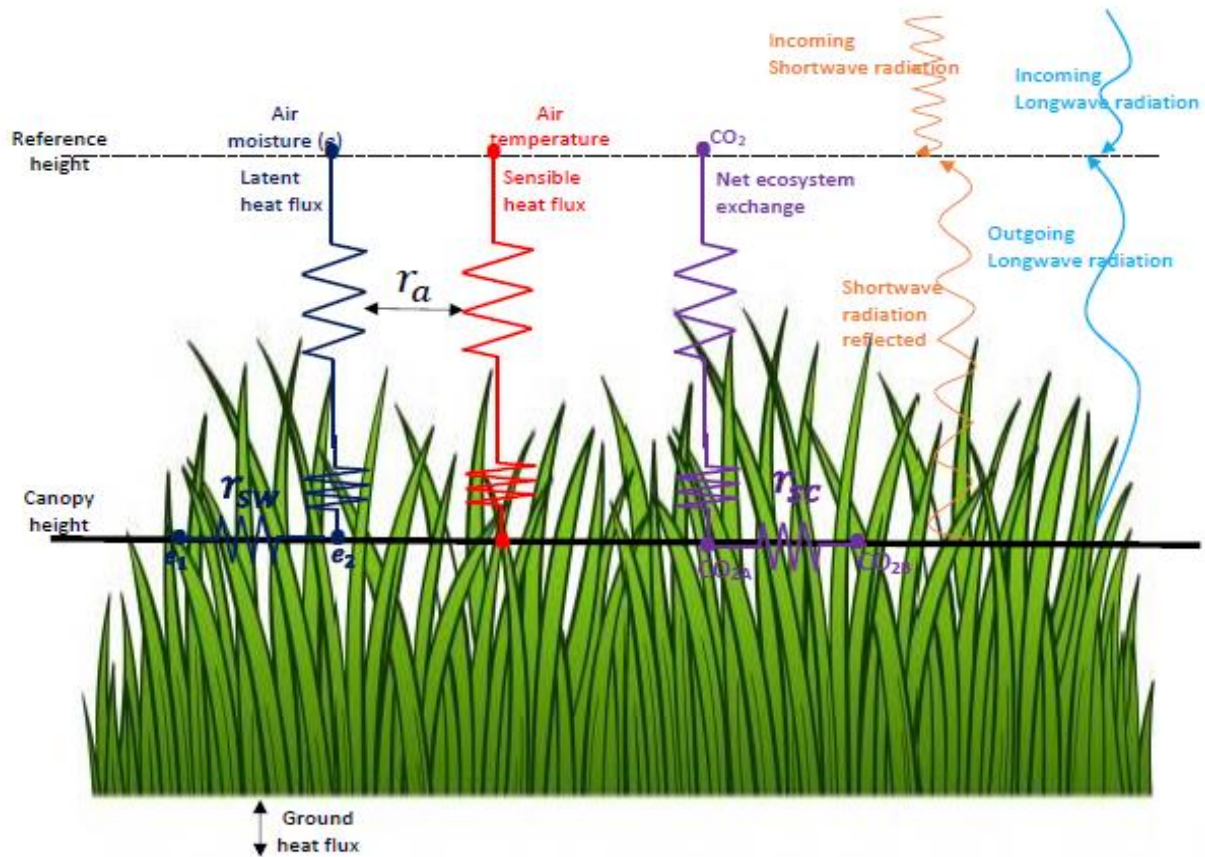


Figure 1.3. Illustration of ‘grass’ surface biophysical interactions. r_a is the aerodynamic resistance to momentum transfer, r_{sw} and r_{sc} are surface ‘stomatal’ resistance to water vapour and CO_2 transfer, respectively.

The proportion of visible light intercepted and used by a plant canopy for photosynthesis, depends on leaf morphology, which is primarily characterized by leaf area index (LAI), or the amount of leaf coverage per unit land area (Tardieu, 2013). Light use increases with LAI. At higher LAI ($> 5 \text{ m}^2 \text{ m}^{-2}$, no canopy gap), nearly all the available visible light at the surface is intercepted (Tardieu, 2013), ultimately leading to more productivity.

In contrast to light, a plant’s response to WUE may be nonlinear, and serves to allow proportional effects in favorable conditions through stomatal opening (Lu and Zhuang, 2010; Zhao et al., 2020). For a given photosynthesis, WUE decreases as the transpiration rises due to the increase in atmospheric evaporative demand and soil water availability (Tardieu, 2013). Moreover, these responses are different between plant types/species and under different intensities of drying (Lu and Zhuang, 2010; Zhao et al., 2020).

Generally, the positive effects of enhanced physiological responses (e.g. WUE), associated with increased CO₂ and warmer temperature, on productivity appear to largely dominate in some parts of Europe, including Ireland. However, occasional declines in productivity can also occur during periods of water stress in summer (e.g. Dillon et al., 2018), implying that the negative effects of water stress on these plant physiological traits can potentially outweigh the positive effects of CO₂ enhancement and warmer temperatures. Therefore, the key is the identification of the driving mechanisms that are responsive to environmental changes at site scale, for drought vulnerability and adaptation assessments.

1.3 Climate change context

Climate change, as the term is widely taken to connote anthropogenically induced changes in the climate system (IPCC, 2014), affects agricultural production due to the large dependence of farming activities on weather and ultimately climatic conditions. Conversely, agricultural activities also serve as a major source of GHG thereby contributing to climate change. Such changes in climate may influence agriculture in a positive way (e.g. CO₂ fertilization, warmer temperatures lengthening of growing seasons, more rainfall) or in a negative way (more drought, faster growth resulting in shorter life cycles, salinization, temperature above optimal or lethal levels) (e.g. Porter et al., 2014). In the context of negative effects, such as increased frequency or severity of drought episodes, plants respond by closing their stomata to conserve available water and/or avoid water loss through transpiration to prevent desiccation. Increasing surface stomatal resistance to moisture loss will ultimately lead to land-air feedback processes and further exacerbate the surface drying (Seneviratne et al., 2010). An illustration of such feedback processes between the surface and atmosphere during extreme weather event is shown in Figure 1.4.

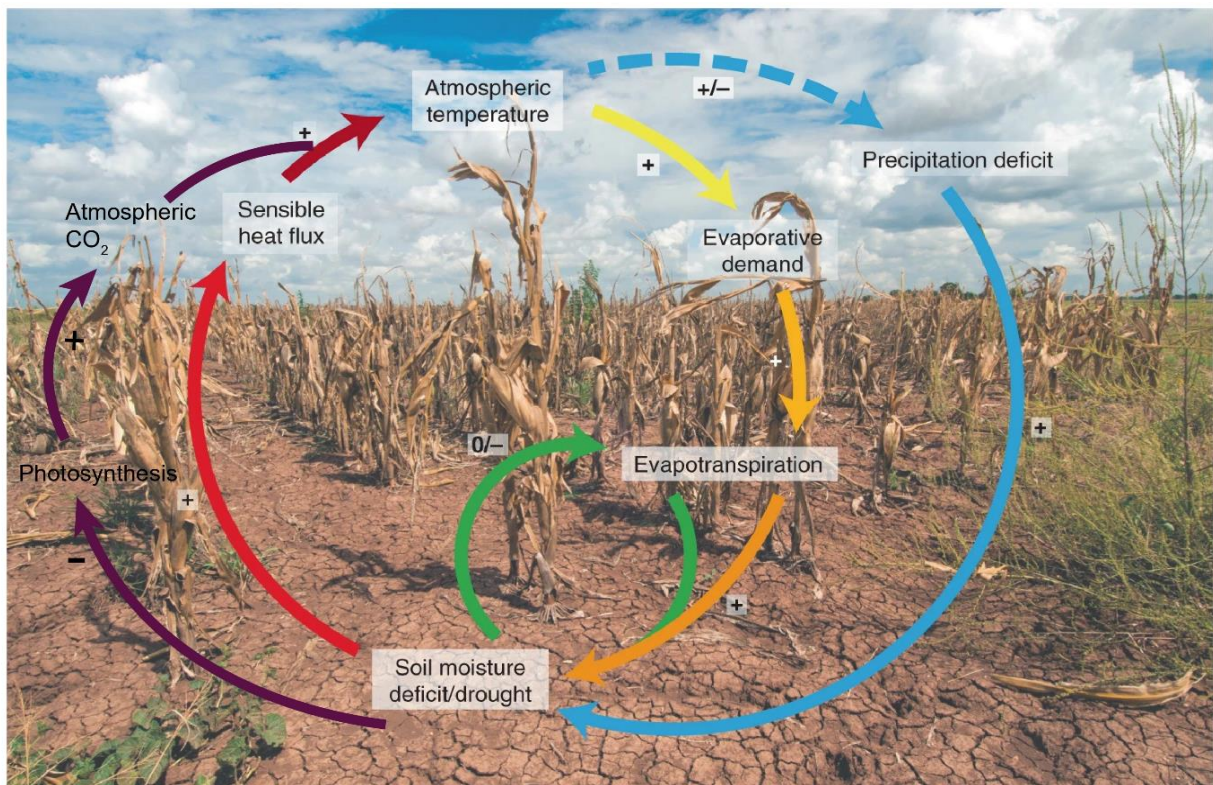


Figure 1.4. The coupling and feedback loop between the surface and the atmosphere during severely hot drought. The signs +, - and 0 indicate positive, negative and no feedback, respectively (Teuling, 2018).

Reflecting the ecosystem scale, It should be noted that plants growth and yield do not only respond to changes in surface climate but also to elevated CO₂ concentration, management practices, pests and diseases (Gentine et al., 2019), and this response differs across regions and plant types (e.g. Hatfield et al., 2011). For instance, a gradual increase in temperature and elevated CO₂ may lead to positive impact on production, through provision of favourable conditions for plant developmental rate, extension of length of growing season and rise in yields, in the higher latitudes (Deccache et al., 2011). However, under seasonally ‘summer’ dry regimes, soil moisture deficits are likely to increase due to the integrated effects of higher transpiration and atmospheric evaporative demand (linked to higher temperature) that facilitates soil drying and rising surface temperature, thereby reducing yield in rain-fed agriculture (Hatfield et al., 2011).

Climate change that negatively impact agriculture is not only driven by elevated CO₂ but also substantially by elevated methane (CH₄) production (Shindell, 2016). Methane from animal agriculture, particularly pasture-based production (e.g. cattle), is primarily formed during manure management and enteric fermentation (Liu et al., 2021). The latter produces the majority of CH₄ from ruminants by exhaling and belching, and this occurs during a chemical reaction between hydrogen (H₂) and CO₂ produced by bacteria, protozoa and anaerobic fungi in methanogenic microorganisms, in the rumen (Liu et al., 2021). Methane production leads to minimal crop fertilization but enhances surface ozone (formed through oxidization and in the presence of NO_x) which damages the vegetation by reducing photosynthesis and other physiological factors (Porter et al., 2014). During the last two decades, global emissions of CH₄ have been increased due to global rise in dairy and beef animals (e.g. Canadell et al., 2021). Such a rise in CH₄ emissions has augmented warming-induced climate extreme events and agricultural losses at a global scale (e.g. Shindell, 2016).

The impacts of extreme events such as heatwaves (periods of extreme high temperature) and droughts (periods of extreme water shortage) on agriculture are likely to become frequent in the future (Samaniego et al., 2018). Projected changes in climate suggest that, while some regions are likely to suffer from droughts events, other regions may become prone to rainstorms and increased flooding (IPCC, 2014). Evidence of these extreme changes is already manifesting across different regions. For instance, record breaking high temperatures were recorded across Europe during the 2018 summer (e.g., Magnusson et al., 2018). These warmer temperatures and rainfall deficits were found to be associated with negative yield anomalies, particularly in the Northern and Eastern Europe during the growing season (Beillouin et al., 2020). In Ireland, the event was evident on grass yield in summer (Figure 1.5a-

b), particularly the south eastern agricultural area (Figure 1.5a), with grass yields reduced by 5-10 % (1 ton ha^{-1}) of normal in 2018 (Falzoi et al., 2019).



(a)



(b)

Figure 1.5. (a) True color Sentinel-2 images of South East region of Ireland during 2018 mid-summer; (b) Temporal evolution of national grass growth 2016 – 2018 from Teagasc PastureBase Ireland (Dillon et al., 2018). The rectangle box highlights the period of severe weather impacts on grass yields.

1.4 Knowledge gaps

Traditional approaches to monitoring regional agro-environmental conditions in Ireland typically employ meteorological data from a proximate weather station as input to estimate crop growth and productivity. The studies using these approaches are few, site-specific and

lack the ability to explain the plant's physiological traits (e.g. stomatal resistance) that influence the mechanisms (moisture, heat and CO₂) driving the local meteorological conditions that govern plant growth. An alternative method, proposed here, employs the surface energy balance (SEB) concept as a framework for integrating relevant data, including airborne/satellite observations, meteorological observations, and geo-databases on land-cover, soil type and topography, to generate surface biophysical indices relevant to agriculture at a detailed spatial scale. One important advantage of this approach is its prognostic ability; which may lead to an improved understanding of the linkages between the land surface and atmosphere and potentially enable improved seasonal forecasting of grass growth. Again, no previous attempt to integrate traditional meteorological data with remote sensing approaches exists for Ireland using this overarching framework.

In addition, there are relatively few sites where all the required surface energy budget components, including net radiation (Q_N), sensible heat (Q_H), latent heat (Q_E) and soil heat (Q_G) fluxes, necessary for evaluating the response of agriculture to changes in climate in both the short and long term are available; where they exist, data are often incomplete and/or of limited duration. At the same time, there is often an extensive observation network available that has gathered key meteorological data (sunshine, wind, rainfall, etc.) over decades. Past and recent studies have also developed physically-based schemes that follow SEB concept to simulate the land-atmosphere exchanges based on routine meteorological observations (e.g. de Rooy and Holtslag, 1999). However, no study has applied these schemes to Ireland.

Regional climate projections for Ireland indicate that mean annual temperature will rise by 1 – 1.6 °C, with the largest increases in the east of the country (e.g. Nolan, 2015; Fealy et al., 2018). Mean annual, spring and summer rainfall are likely to significantly decrease, with heavy

rainfall in winter and autumn by mid-century, though the large spread between model ensemble members reflect uncertainty, particularly in mean rainfall for winter and autumn in Ireland (Nolan, 2015; Fealy et al., 2018). These projected changes in climate imply that the occurrence, frequency and intensity of drought events could increase during the growing season, which are already manifesting based on the record-breaking maximum temperature and rainfall deficits recorded in 2018 summer (Falzoi et al., 2019), followed by the 2020 spring dry spells, reported across the region (Met Eireann, 2020). Though, the reported drought episodes in Ireland in recent decades are less frequent and unrepresentative of prolonged drought climatology, relative to the periods prior to 1980s, based on historical evidence during the years 1850-2015 (Noone et al., 2017).

Meteorological droughts are well understood and sufficiently documented in Ireland (e.g., Noone et al., 2017). These studies are very recent but few have examined the physical processes that may trigger meteorological drought to persist into agricultural drought and associated land-atmosphere feedbacks. During periods of restricted water availability, the evolution of agricultural drought depends on site-specific changes in land surface processes, which can be described within the framework of a land surface scheme (e.g. Lansu et al., 2020). To date, studies have focused on meteorological drought, whereas the discussion on agricultural drought and the role of land-atmosphere interactions is missing in Ireland. Critically, the proposed methodology should enable a better understanding of such extreme events and the land-atmosphere interaction, in contrast to more traditional methods that employ standard meteorological variables. This is imperative since agricultural production across Ireland may switch from one that is rain-fed to one that requires irrigation and altered

management practices, to offset the associated impacts of extreme drought events on productivity.

1.5 Research questions

Grass growth is an important agricultural product, providing a low cost feed source for livestock farmers where profit margins are low, and contributes a relatively large percentage to the economy of Ireland. To optimize grass growth and yields, the existing knowledge and data gaps identified in Section 1.4 point towards several concerns relating to Ireland's future agri-environmental conditions, and the need to develop policy options which are spatially tailored to the constraints imposed by climate and the environment. To partly address these concerns, the following three research questions are to be answered in this research:

For the first step, this research builds on utilising a physically-based land surface scheme (LSS) (de Rooy and Holtslag, 1999) for Ireland in the context of understanding the surface-air exchanges of heat and moisture.

- Can a LSS be developed to simulate the terms of the surface energy budget in response to soil, vegetation and atmospheric variations across Ireland?
- Can a validated LSS be used to explore (and predict) the emergence and development of agricultural drought and its regional characteristics?
- Can the LSS be used to examine carbon uptake and water exchanges during dry and wet regimes, and be used to evaluate water use efficiency and grass yield at a farm scale?

This research seek to address these questions by integrating multi-source, near-real time information that will enhance our understanding of land surface physical processes that drive

the agro-environmental conditions of Ireland. This will consequently aid the development of a prototype information system that could provide benchmark information for farmers on their environmental and agronomic attributes in relation to the quantity of farm production and performance. This will enable them to engage more fully with their own localised agro-environmental conditions and help to optimize management decisions, technology and practice adoption in a changing climate.

1.6 Thesis structure

Each of the three research questions are addressed consecutively in Chapters 3-5. Figure 1.6 shows an overview of the chapters as they relate to research questions and associated publications.

Chapter 2 of this thesis provides a review of the theoretical basis of land-atmosphere energy budget framework, observations and modelling of surface flux densities, and applications for drought monitoring and yield predictions at different scales.

Chapter 3 provides an overview of the setup of the land surface scheme (de Rooy and Holtslag, 1999) used and its evaluation for selected grassland sites. The aim is to evaluate the performance of the scheme in replicating measured surface energy fluxes over grassland sites, and the sensitivity of the scheme to different soil conditions. Chapter 3 was published as follows:

Ishola, K. A., Mills, G., Fealy, R. M., Ní Choncubhair, Ó. and Fealy, R. (2020) Improving a land surface scheme for estimating sensible and latent heat fluxes above grasslands with contrasting soil moisture zones. *Agricultural and Forest Meteorology*, 294, 108151, <https://doi.org/10.1016/j.agrformet.2020.108151>

In Chapter 4, the utility of the scheme, in combination with satellite-derived products, ERA5-Land global reanalyses climate data and in-situ observations, to explain regional meteorological-agricultural drought propagation through changes in land surface processes is explored. The aim is to provide a framework to investigate the role of land-atmosphere interactions in exacerbating agricultural drought and understand the degree of vulnerability of Irish grasslands to climate change.

Ishola, K.A., Mills, G., Fealy, R.M. and Fealy, R. A model framework to investigate the role of anomalous land surface processes in the amplification of summer drought across Ireland during 2018, *International Journal of Climatology* (revision submitted; see supplementary information)

Chapter 5 assesses the relationships between ET, ecosystem WUE (a water-carbon coupling metric) and grass yields. The primary objectives are to map farm-scale water use metrics at high resolution using Sentinel-2 (10 m pixel size) data, and; relate the derived indices with yields.

Ishola, K.A., Mills, G. , Fealy, R.M., Green, S. and Fealy, R. Mapping high-resolution water use efficiency of pasture lands using Sentinel-2 data: Application for grass yield prediction, in preparation for submission to *International Journal of Applied Earth Observation and Geoinformation* (in draft)

The key findings of this thesis, policy implications and suggestions for future research are summarized in Chapter 6.

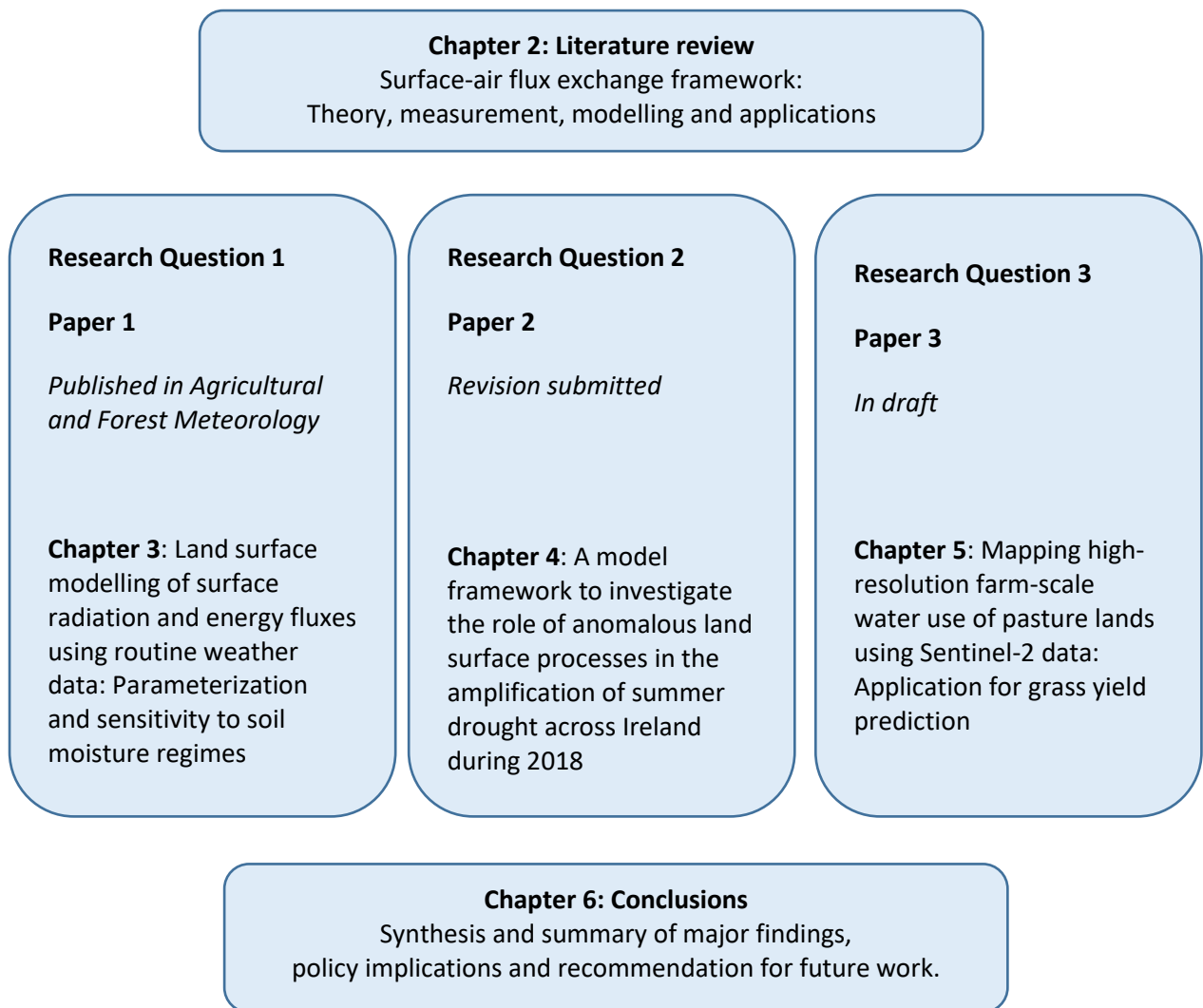


Figure 1.6. Overview of the thesis structure.

2. Literature review

2.1 Introduction

Understanding the response of agriculture to contemporary changes in climate is crucial to understanding likely future changes in vegetation growth and yield at global and regional scales. This response depends on the knowledge of complex dynamic processes that link the soil, vegetation and atmosphere, which can be described by combining theory, observations and models. Measurements of surface fluxes of heat and moisture can provide this understanding but are limited due to paucity of data. Often, meteorological data have been employed instead in 'conventional' approaches, such as statistical analysis/predictive models, in which different meteorological variables have been directly related to variation in yield among years (Brereton 1992; Holden and Brereton, 2002, 2003a, 2003b, 2004; Holden et al., 2003; Black et al., 2006; Hurtado-Uria et al., 2013a, 2013b).

For example, Phelan et al. (2015) used a stepwise multiple regression analysis to examine the association between grazing season length and bioclimatic variables for pasture farms across Europe. The study found significant positive association between mean grazing season length and mean temperature of coldest quarter and negative association with precipitation of the wettest month. Using a similar approach, Hurtado-Uria et al. (2013a) evaluated the relationship between grass growth and meteorological data over the period 1982 to 2010 for the south of Ireland. The study found that temperature had a large influence on grass growth in all seasons; evapotranspiration (ET) also played an important role for their period of analysis. However, in contrast to strong foliage response to spring temperature (Hurtado-Uria et al., 2013a), net ecosystem productivity was not significantly correlated with spring

temperature (Peichl et al., 2011), suggesting differences in response of grass growth and biophysical processes to temperature (Wingler and Hennessy, 2016).

In the context of both the seasonal and regional distribution, pasture-based production systems in relation to regional climate variations in Ireland indicate that the farming systems in the South East usually experience lower primary productivity (grass yield) in summer periods as a result of insufficient precipitation, higher evapotranspiration, and consequently soil moisture deficits, associated with the free draining soils (Fitzgerald et al., 2005). A later turn out date, when animals are put out to pasture, is experienced in the north of the country during spring, as the lower temperature during the spring delays the start of grass growth. The usually mild year round temperatures and ample summer precipitation experienced in the south west characterize this region as the most productive for grass growth (Fitzgerald et al., 2005). However, climate change is likely to alter this distribution of regional productivity. For example, the North East is expected to become more productive, particularly on well-drained soils, due to the projected earlier turn out associated with higher temperature in Spring (Fitzgerald et al., 2009). Locations in the midlands to the northern regions on poorly-drained soils in Ireland were also projected to increase in primary productivity by 2080, however, Fitzgerald et al. (2009) noted that farms on poorly-drained soils pose more challenge to farmers than those on well-drained soils in the future.

The inability to explain the role of biophysical processes in vegetation response to climate imposes a major limitation on more traditional approaches. Simulating the surface energy balance terms and relevant diagnostic parameters using available meteorological, soil and vegetation data serve as an alternative approach to improve our understanding of how agricultural systems respond to climate and how this response varies spatially. The

subsequent sections here provide a review in this context and outlines the theoretical framework that is widely utilized in land surface modeling of these terms.

2.2 Theoretical framework of surface-air energy exchanges

Land-atmosphere interactions are understood through the exchanges of heat, mass and moisture between the surface and the overlying atmosphere. For an ideal flat and homogenous surface, energy exchange is described by the net radiation (Q_N) at the surface, the surface sensible (Q_H) and latent (Q_E) heat fluxes to the atmosphere, and soil heat flux to the subsurface (Q_G) (Figure 2.1) (Arya, 2001). Q_N is usually dominated by solar radiation towards the surface during day light hours, and in the absence of solar radiation at night, Q_N is weaker and directed away from the surface. Consequently, the surface warms up during the day and cools at night, especially under stable and clear sky conditions (Arya, 2001).

Q_H is described as a direct energy flux at and above the surface due to vertical temperature gradients (Arya, 2001). In the immediate vicinity of the surface, Q_H exchange is primarily caused by conduction while at distances beyond few millimetres away from the interface, the heat transfer is governed by convection or advection of air. The surface is warmer than the overlying air during the day hours thus directing the heat flux away from the surface and vice versa for night hours (Figure 2.1).

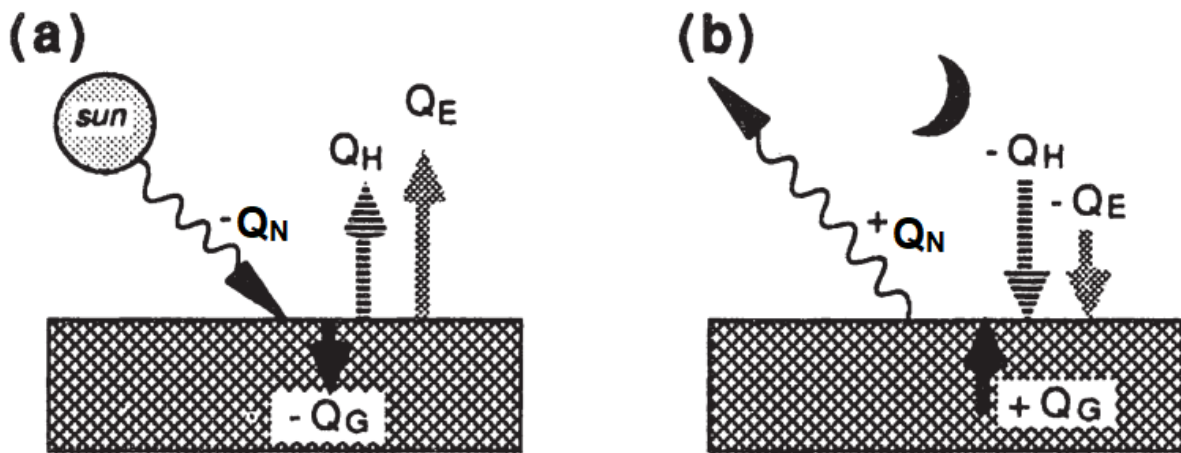


Figure 2.1. Variation of surface energy balance (SEB) terms for (a) daytime over land and; (b) nighttime over land (Stull, 1988). Signs are positive upward and negative downward, and arrow size indicates relative magnitude.

The Q_E flux is the flux of energy released as a result of evaporation/transpiration or condensation at the surface. In the situation where the air above the surface (e.g. water, moist soil, or vegetation) is drier (e.g. lower specific humidity usually in the daytime), the available energy is preferentially channelled into evaporation from the surface. At night, condensation can occur over relatively colder surfaces. The heat transfer through the ground medium (e.g. soil) occurs by conduction.

The balance of surface energy fluxes, assuming no heat is stored or released within the canopy surface, is:

$$Q_N = Q_H + Q_E + Q_G \quad (Wm^{-2}) \quad (2.1)$$

The net radiation (Q_N) is defined based on the balance of surface radiative fluxes, including surface shortwave radiation downward ($Q_{S\downarrow}$) and upward ($Q_{S\uparrow}$), and surface longwave radiation downward ($Q_{L\downarrow}$) and upward ($Q_{L\uparrow}$).

$$Q_N = Q_{S\downarrow} - Q_{S\uparrow} + Q_{L\downarrow} - Q_{L\uparrow} \quad (Wm^{-2}) \quad (2.2)$$

The magnitude of $Q_{S\downarrow}$ depends on the Sun's altitude, clarity of the atmosphere and the latitude. This parameter is available by means of observations or model estimation (Holtslag and van Ulden, 1983; Allen et al., 1998). The $Q_{S\uparrow}$ is a fraction of $Q_{S\downarrow}$ reflected back to the atmosphere and is a function of the surface albedo ($\alpha = \frac{Q_{S\uparrow}}{Q_{S\downarrow}}$). A parameterization of surface albedo based on solar elevation has been investigated (Beljaars and Bosveld, 1997; de Rooy and Holtslag, 1999), but for the purpose of simplicity, the recommended value for short grass ($\alpha = 0.23$; Oke, 1978) is often adopted (e.g. van de Boer et al., 2014a).

The longwave terms in (Equation 2.2) depend on the air (T_a) and surface (T_s) temperature and their respective emissivities. A simple approximation of the incoming longwave radiation in relation to T_a at a reference height (1 – 2 m) has been reported (Swinbank, 1963). However, this simple empirical relation does not account for the influence of cloud cover (N), thus, Holtslag and van Ulden (1983) proposed an optimized model:

$$Q_{L\downarrow} = \varepsilon_a \sigma T_a^4 + c_1 \left(\frac{N}{8}\right), \quad (2.2a)$$

$$\varepsilon_a = 1.2 \left(\frac{e_a}{T_a}\right)^{0.143}, \quad (2.2b)$$

where c_1 is an empirical constant (60 W m⁻²). A number of approximations have been proposed for atmospheric emissivity (ε_a), relating it to T_a and N (Idso, 1981; Holtslag and de Bruin, 1988), and actual vapour pressure (e_a , mbar) and T_a (Brutsaert, 1982). The latter (Equation 2.2b) is often preferred for estimation of ε_a (de Rooy and Holtslag, 1999; van de Boer et al., 2014a).

The estimation of $Q_{L\uparrow}$ depends primarily on the surface emissivity (ε) and T_s ,

$$Q_{L\uparrow} = \varepsilon\sigma T_s^4 + (1 - \varepsilon) Q_{L\downarrow} \quad (2.2c)$$

The literature indicates that, ε ranges from 0.9 – 0.95 for long to short grass (Oke, 1978) and 0.94 is used in this research (de Rooy and Holtslag, 1999). T_s is critical for estimating $Q_{L\uparrow}$ and all of the non-radiative terms, and is discussed in more detail in Section 2.2.3.

A number of approaches for estimating soil heat flux (Q_G) have been developed and evaluated with measured values in the past (Nickerson and Smiley, 1975; Deardorff, 1978; Schayes, 1982; de Rooy and Holtslag, 1999; van de Boer, 2014a). van Ulden and Holtslag (1985) proposed a simple approximation of Q_G (Equation 2.3) for short grass using the 24-hour moving average of T_a . This is on the basis that the average T_a resembles the root zone soil temperature.

$$Q_G = -A_G(T_{24} - T_s), \quad (2.3)$$

where T_{24} is the 24-h mean of 2-m temperature (K), T_s is the estimated surface temperature (K), A_G is an empirical constant for soil heat transfer ($\text{W m}^{-2} \text{K}^{-1}$), which is site-specific (de Rooy and Holtslag, 1999). This approximation has been recognized to be consistent for short grass under different weather conditions (e.g. de Rooy and Holtslag, 1999; van de Boer et al., 2014a).

The surface radiation and energy flows, particularly the surface turbulent fluxes, Q_H and Q_E , at the interface between the earth's surface and atmosphere, play a key role in energy and water cycle. Hence, knowledge of these exchanges are critical for climate and hydrological modelling, improving weather forecasting models, and for many agricultural applications,

such as monitoring plant water-uptake, crop growth and performance, irrigation management practices, etc. (Jacob et al., 2002; Kustas et al., 2004; Dodds et al., 2005; Consoli et al., 2006). An expanded discussion of these components and application to Ireland is provided in Keane and Collins (2004).

Q_E , which is often used as a measure of evapotranspiration (ET) (evaporation from soils + transpiration from vegetation), provides a link between water, carbon and energy exchanges (Xu et al., 2014), thereby influencing the formation and growth of clouds, rainfall patterns, and variability in extreme weather phenomena, such as the heatwaves and droughts, with associated impacts on terrestrial ecosystems and climate (Bateni and Entekhabi, 2012; Wang and Dickinson, 2012). ET represents the largest surface moisture flux exchange with the atmosphere, accounting for more than half of total precipitation regionally and nearly equal to precipitation in semi-arid regions (Engman and Gurney, 1991). Therefore, a consistent and reliable estimation of Q_E flux is central to an in-depth understanding of land-atmosphere interactions, agro-meteorology, water resources management and climate studies (Rigden and Salvucci, 2015). However, obtaining reliable measurements of surface fluxes and ET is non-trivial. Due to spatial heterogeneity in ecosystems, soils and weather conditions, the interactions between scales of physical processes result in the need for complex techniques of surface flux measurements and estimations (Bastiaanssen et al., 1998a).

2.2.1 Penman-Monteith (PM) Equation

The Penman-Monteith (PM) equation is a linearized version of the SEB (Equation 2.1) that is commonly used to estimate the Q_E flux or ET (e.g. Allen et al., 1998). The original equation to estimate evaporation from an open water surface, combining energy balance with mass transfer, was derived by Penman (1948). This was further developed by Monteith (1965) who

introduced surface resistance factors for ecosystem surfaces, linking the equation to the leaf or canopy, depending on the values of resistance employed. The combined equation discriminates between surface resistance (r_s) to water vapour through stomata opening, and aerodynamic resistance (r_a) to heat upward from the canopy surface, which can be derived from Monin-Obukhov Similarity Theory (MOST) universal function (Monin and Obukhov, 1954) (see Section 2.2.3). The resistances are discussed further in Section 2.2.2. The PM equation provides essential physical expressions of the Q_E flux as follows:

$$Q_E = \frac{r_a s(Q_N - Q_G) + \rho c_p (e_s - e_a)}{(s + \gamma)r_a + \gamma r_s}, \quad (2.4)$$

where s and γ are the slope of saturation vapour curve and psychrometric constant and e_a and e_s are the actual and saturated vapour pressures, respectively. The difference between e_a and e_s is referred to as the vapour pressure deficit (VPD).

Under well-watered conditions, Equation (2.4) is controlled by the available energy ($Q_N - Q_G$), so that the equation can be simplified as follows (Priestly and Taylor, 1972):

$$Q_E = \alpha_{PT} \frac{s}{s + \gamma} (Q_N - Q_G), \quad (2.5)$$

where α_{PT} is the Priestly-Taylor (PT) coefficient, which ranges between 1.2 and 1.3 (Agam et al., 2010).

However, Equation 2.5 is dependent only on available energy, which will not be valid for water-limiting conditions when the influence of r_s and VPD more strongly influence Q_E (e.g. Equation 2.4) (e.g. Akumaga and Alderman, 2019). The PM equation is widely accepted as a standard equation (adopted by the United Nations Food and Agriculture Organisation, UN FAO) for estimating Q_E or ET. The method is now commonly referred to as FAO-56 PM (Allen

et al., 1998) and has been found to work well in several locations, provided the required input data are available (e.g. Xing et al., 2008).

The PM approach to estimating ET requires input data of solar radiation, air temperature, relative humidity, and wind speed. One major limitation is that these required data may not be readily available, particularly in data-scarce regions, resulting in the use of simpler approaches (e.g. Priestley-Taylor, Thornthwaite, Makkink, etc.) that require more limited data inputs (e.g. Lang et al., 2017). Akumaga and Alderman (2019) confirmed that crop ET estimates based on PT could be significantly different from FAO-56 PM ET estimates in the arid/semi-arid and rainfed conditions during winter over Oklahoma. The FAO-56 PM demonstrates superiority over other methods of Q_E flux under semi-arid climatic conditions (e.g. López-Urrea et al., 2006). However, Sentelhas et al. (2010) noted that FAO-56 PM may be less accurate over Southern Ontario, relative to other methods (e.g. Thornthwaite) if either the net radiation (Q_N) or air temperature component is missing.

To overcome problems of missing or unmeasured input variables, Allen et al. (1998) suggested procedures for calculating missing input climatic variables (e.g. net radiation, wind speed and vapour pressure deficit). Such procedures require evaluation over different locations and climates as shown in Sentelhas et al. (2010) for Canada, Popova et al. (2006) for Bulgaria et al. (2008) for Tunisia and in Stöckle et al. (2004) for five different locations in the USA, Syria, the Philippines, Spain and the Netherlands.

Whether the Q_E flux is derived diagnostically as a residual of SEB terms (Equation 2.1) or based on the prognostic Penman-Monteith (PM) model (Equation 2.4) (Penman, 1948; Monteith, 1981; Allen et al., 1998), the analytic context of both methods is usually based on

the Monin-Obukhov Similarity Theory (MOST) (Monin and Obukhov, 1954). The MOST theory is discussed in Section 2.2.3.

2.2.2 Surface and aerodynamic resistances

The surface ‘stomatal’ resistance (r_s) (inverse of stomatal conductance) plays a key role in the parameterization of vegetation evapotranspiration or latent heat flux (Q_E), thus regulating surface energy budget over land (e.g. Buckley and Mott, 2013; Buckley et al., 2017). It represents the resistance to water transport through the stomata to the canopy surface (e.g. Figure 1.4), and is a function of environmental factors. The behaviour of the system is therefore crucial for water and carbon cycles, agricultural response, performance and productivity in a changing climate (Buckley and Mott, 2013; Buckley et al., 2017).

Quantifying r_s requires inputs which are non-trivial to measure or estimate, but not many are intractable. In most cases, r_s estimates are obtained by inverting the PM equation of Q_E (Equation 2.4) for model parameterization or evaluation (e.g. van de Boer et al., 2014a). Because of the importance of r_s to biological systems, models that predict r_s for a given environmental condition vary depending on the goal or problem to be addressed (e.g. Jarvis, 1976; Ball et al., 1987; Collatz et al., 1991). These models range from empirical to mechanistic, but the former is widely used in many applications, due to its simplicity and modular structure that allows coupling with Earth system models (Buckley and Mott, 2013; Li et al., 2013; Lansu et al., 2020; Ma et al., 2021). One of the first and most commonly used empirical r_s models is the Jarvis-type (Jarvis, 1976) approach, which is parameterized principally as a function of external environmental forces, including air temperature (T_a), air moisture deficit (Δq), solar radiation ($Q_{s\downarrow}$) and soil moisture content (θ).

$$r_s = r_{s,min} LAI^{-1} F(T_a, \Delta q, Q_{s\downarrow}, \theta), \quad (2.6)$$

where $r_{s,min}$ is the minimum stomatal resistance for optimum condition, defined as the extent to which potential evaporation (at $r_s = 0 \text{ s m}^{-1}$) can be reached and is vegetation dependent (van de Boer et al., 2014a). LAI is the leaf area index. F is the dimensionless response function (scaling factor ranging from 0 – 1) for the respective environmental factor.

The Jarvis r_s scheme may be sensitive to changes in Δq , depending on the degree of dryness and temperature (e.g. Lansu et al., 2020). When r_s is high due to high Δq and low soil moisture content, it may limit the transpiration and carbon fixation abilities of plants. Again, this also varies among plant species, and acts in tune with other environmental drivers (e.g. Lansu et al., 2020).

Δq is largely driven by T_a under warm temperature and thus, indicate a strong linear relationship between both variables. Such links between Δq and T_a have justified tuning/modifying the Jarvis-type parameterization (e.g. Beljaars and Bosveld, 1997, van de Boer et al., 2014a), though modifying the Jarvis-type approach does not necessarily produce a unique set of response functions (van Heerwaarden and Teuling, 2014). To this end, different expressions of the dependence of r_s on Δq response function ($F_{\Delta q}$) exist, including those used in the Interactions between Soil, Biosphere and Atmosphere (ISBA-Ags) scheme (Calvet et al., 1998), the National Centers for Environmental Prediction (NCEP) Noah scheme (Chen et al., 1996), the European Center for Medium-Range Weather Forecasts (ECMWF) HTESSEL scheme (Balsamo et al., 2009), optimized Jarvis formulation by de Rooy and Holtslag (1999) (dRH99) and Beljaars and Bosveld (1997) (BB97), etc. In many of these expressions, the dependence of r_s on other environmental factors (e.g. soil moisture) are either excluded or assumed negligible. van de Boer et al. (2014a) compared different approaches for calculating the $F_{\Delta q}$ term over grassland at Cabauw, the Netherlands (Figure 2.2). The study found

significant and large differences between dRH99 and the selected schemes, when the atmosphere is saturated ($\Delta q = 0$) or dry ($\Delta q > 10 \text{ g kg}^{-1}$).

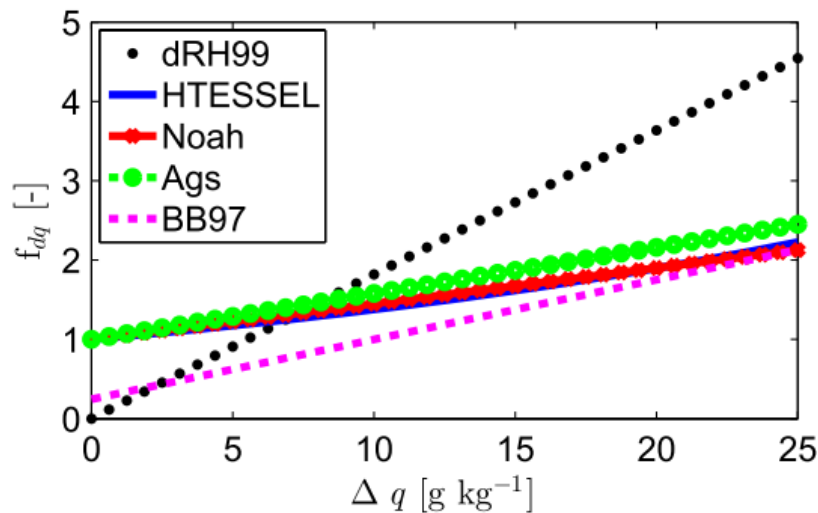


Figure 2.2. Response of surface resistance (r_s) to water vapour deficit (Δq) according to different schemes over Cabauw grassland, the Netherlands (van de Boer et al., 2014a).

Although, the HTESSSEL, Aqs, and Noah schemes appear consistent, van de Boer et al. (2014a) found large differences between the measured and estimated r_s using only Δq in all the schemes. In other studies (e.g. Allen et al., 1998), r_s values were estimated, assuming a hypothetical grass reference surface and non-limiting water. In this case, the dependence on response functions is excluded. However, water availability acts to regulate r_s under limiting soil moisture (Russell, 1980; Sherratt and Wheater, 1984) and consequently plays a prominent role in modulating surface heat and moisture fluxes (Sherratt and Wheater, 1984; Betts and Ball, 1995; 1998; Senevirante et al., 2010). Therefore, only a ‘complete’ expression that includes all the response functions can potentially explain stomatal behaviour, consistent with observations, under increasing water stress (e.g. Lansu et al., 2020). van de Boer et al. (2014a) suggested BB97 as a logical approach to integrate all the response functions with a considerably small offset between measured and estimated r_s .

Moreover, the main disadvantages of the Jarvis-type empirical approach are that it requires multiple environmental variables, many of which might not be routinely available (e.g. soil moisture), and provides little insight about the physiological mechanisms (e.g. photosynthesis) of stomatal control (e.g. Buckley and Mott, 2013; Buckley, 2017). Hence, the introduction of a 'Ball-Berry' scheme (Equation 2.7) (Ball et al., 1987), which expresses r_s as a function of net photosynthesis (A), CO₂ concentration at canopy surface (C_s), relative humidity at canopy surface (h_s) and residual of r_s when A is zero ($r_{s,min}$).

$$r_s = \left(r_{s,min}^{-1} + m \frac{Ah_s}{C_s} \right)^{-1}, \quad (2.7)$$

The parameter m is an empirical constant that varies among foliage.

In contrast to the Jarvis scheme in which r_s response is derived from the nexus between the biotic system (e.g. $r_{s,min}$ and LAI) and meteorological parameters, the Ball-Berry scheme postulates that the coupling is between meteorological variables, biotic system and plant's dynamic response, through changes in photosynthesis, intercellular CO₂ concentrations and respiration (Niyogi et al., 1998). In a comparison of a number of physiological-based schemes, Kim and Verma (1991), Jacobs (1994) and Niyogi and Raman (1997) indicated that the Jarvis scheme showed some differences between measured and estimated r_s , and an unstable response to atmospheric changes, relative to the selected physiological-based schemes. Other studies have also affirmed that physiological 'photosynthesis'-based schemes can replicate measured stomatal behaviour more closely (Collatz et al., 1991; Jacobs, 1994). The physiological photosynthesis-based scheme, though perceived to be simple, may require a cumbersome parameterization process due to the requirement of a separate biochemical model for photosynthesis (A) (Buckley and Mott, 2013; Ma et al., 2021). In spite of the acknowledged shortcomings, empirical based approaches (e.g. Jarvis, Ball-Berry) are widely

recognized to be suitable for prediction of stomatal behaviour in situations where the required parameters can be confidently estimated (Buckley, 2017). To date, the empirical schemes continue to inform predictions of energy, water and carbon exchanges across modelling community (e.g. Lansu et al., 2020; Ma et al., 2021).

Apart from r_s , the aerodynamic resistance (r_a) also partly determines the partitioning of available energy ($Q_N - Q_G$) into turbulent fluxes. It represents the resistance to sensible heat and water vapour transfer from the canopy or ground surface to the overlying atmosphere (e.g. Figure 1.3), and can be approximated using MOST (see Section 2.2.3) (e.g. van de Boer et al., 2014a):

$$r_a = \frac{1}{ku_*} \left[\ln \left(\frac{z_a}{z_{oH}} \right) - \psi_H \left(\frac{z_a}{L} \right) + \psi_H \left(\frac{z_{oH}}{L} \right) \right], \quad (2.8)$$

where k is the von Kármán constant. u_* is the friction velocity. z_a , and z_{oH} are the reference height and roughness length for heat, respectively, L is the Obukhov length and ψ_H is the MOST universal function for heat. All parameters are explained in detail in the next section.

2.2.3 The Monin-Obukhov Similarity Theory (MOST)

The Monin-Obukhov Similarity Theory (MOST) was developed by Monin and Obukhov (Monin and Obukhov, 1954) for the surface layer of the atmospheric boundary layer (ABL), otherwise known as the constant-flux layer (Figure 2.3). This layer extends upto 100 m (~10 % of ABL) from the surface during daytime when most of the surface exchange processes occur. During daytime, the incident radiation heats the surface quickly, leading to rising eddies and development of an unstable surface layer associated with higher wind speeds, surface mixing and increased turbulent fluxes (Liang et al., 2012) (Figure 2.3).

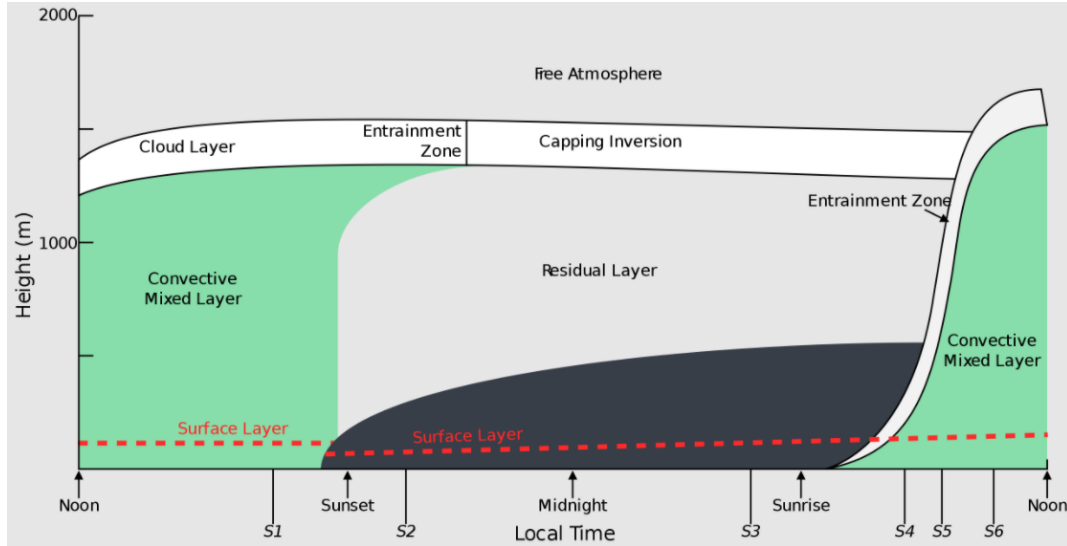


Figure 2.3. Temporal evolution of different layers of the atmospheric boundary layer (ABL) over land (Stull, 1988).

The MOST theory relates the turbulent fluxes of heat and momentum to non-dimensional vertical gradients of temperature and winds, respectively through its universal stability functions in the surface layer (e.g. Paulson, 1970; Businger et al., 1971; Dyer, 1974). When MOST is applied to estimate heat and momentum, it is often called flux-profile method:

$$Q_H = -\rho C_p u_* \theta_* , \quad (2.9)$$

where ρ is the air density, C_p specific heat capacity at constant pressure, u_* and θ_* are the scaling quantities, friction velocity and potential temperature, respectively. For a stationary and horizontally uniform surface, the scaling parameters are given as:

$$\Delta\theta = \theta_a - \theta_s = \frac{\theta_*}{k} \left[\ln\left(\frac{z_a}{z_{oH}}\right) - \psi_H(\zeta_a) + \psi_H(\zeta_o) \right], \quad (2.10)$$

$$\psi_H = 2 \ln \left[\frac{1+x^2}{2} \right] \quad \text{for } \zeta < 0, \quad (2.10a)$$

$$u = \frac{u_*}{k} \left[\ln\left(\frac{z_a}{z_{om}}\right) - \psi_m(\zeta_a) + \psi_m(\zeta_o) \right] \quad (2.11)$$

$$\psi_m = 2 \ln \left[\frac{1+x}{2} \right] + \ln \left[\frac{1+x^2}{2} \right] - 2 \tan^{-1}(x) + \frac{\pi}{2} \quad \text{for } \zeta < 0, \quad (2.11a)$$

$$\psi_m = \psi_H = -5\zeta \quad \text{for } \zeta > 0, \quad (2.11b)$$

$$\psi_m = \psi_H = 0 \quad \text{for } \zeta = 0, \quad (2.11c)$$

$$x = (1 - 16\zeta)^{0.25}, \quad (2.11d)$$

where k is the von Kármán constant. z_a, z_{oH}, z_{om} are the reference height, roughness lengths for heat and momentum, respectively. Both z_{oH} and z_{om} lengths are taken such that the downward-extrapolated profiles of Equation 2.10 produce effective temperature at the radiation level and the profiles of Equation 2.11 result in zero value for wind speed. de Rooy and Holtslag (1999) noted that for homogenous surfaces the local z_{oH} and z_{om} depend only on the local surface cover thus, z_{oH} can be defined as 10% of z_{om} . The potential temperature θ_a is derived, by adjusting the air temperature adiabatically for the height above the ground, as; $\theta_a = T_a + \frac{gz_a}{c_p}$ (de Rooy and Holtslag, 1999). ψ_H and ψ_m are the MOST universal functions for heat and momentum, respectively, which are derived from the stability parameter $\zeta = \frac{z}{L}$ using Businger-Dyer representations of similarity functions (Businger 1966, Dyer, 1967; Paulson, 1970). The subscripts 'a' and 'o' denote the vertical reference and canopy heights, respectively.

The scaling parameters in (2.12) and (2.13) are related with Q_H and L by;

$$\theta_* = - \frac{Q_H}{u_* \rho c_p} \quad (2.12)$$

$$L = \frac{u_*^2 T_a}{k \theta_* g} \quad (2.13)$$

L is the Obukhov length, which was originally derived for dry air (Monin and Obukhov, 1954). It is a dimensional height above the surface where the turbulence generated by buoyancy (heat production) equals the mechanically (shear) generated turbulence, describing a layer where stratification influence is negligible (Foken, 2006). Below this layer, shear production dominates over buoyancy. It is a parameter that helps to characterize the dynamic and thermodynamic processes within the atmospheric boundary layer and, in turn, the conditions of stability and instability of the surface layer. L is zero for neutral stratification and positive (negative) for stable (unstable) stratifications. Foken (2006) noted that the L must be defined based on virtual potential temperature for the parameter to be independent of height and be physically appropriate for moist condition.

Estimation of the scaling parameters requires the determination of the vertical gradients of wind and temperature from measurement at different levels, which are not available at typical meteorological stations where instruments are typically obtained at a single level (2 m above the earth's surface). Hence, MOST is often coupled with the radiative energy terms (described in Section 2.2) to solve these problems iteratively (Mohan and Siddiqui, 1998; de Rooy and Holtslag, 1999; Niu et al., 2011). After convergence, the resulting Q_H is then used to estimate surface temperature T_s :

$$T_s - T_a = \frac{Q_H r_a}{\rho c_p} + z_a \Gamma_d \quad (2.14)$$

where r_a is the aerodynamic resistance (Section 2.2.2) and Γ_d is the dry adiabatic lapse rate.

Despite the reported accuracy (approximately 10 – 20 %) of MOST for an ideal state (Foken, 2006), the assumptions of steady and horizontally uniform flow limit its application over heterogeneous surfaces, such as forests, grassland, crops, etc. The choice of the k value for

MOST application has also been debated (Foken, 2006). For instance, the derived $k = 0.35$ from experiments with the eddy covariance (EC) method undertaken in Kansas in 1968, and applied in the Businger universal functions (Businger et al., 1971), has been criticized (Wieringa, 1980). Wieringa (1980) argued that this value may be unrealistic due to flux tower problems associated with flow distortion and irregular performance of the phase-shift sonic anemometers. In response, Högström (1988) modified Businger's universal functions and derived a value for $k = 0.40$. For more than five decades, this value has been widely accepted as the standard value (Foken, 2006).

Another issue associated with MOST is in the roughness sublayer, found approximately 2 – 3 times the canopy height above the vegetated surfaces (Raupach et al., 1980; Garratt, 1980). In an urban setting or tall vegetation (canopy height > 10 cm), the constant-flux layer is often shallow, while the roughness sublayer may extend up to tens of meters in thickness. As a result, application of MOST may not be appropriate under this condition. Depending on the thickness of the roughness sublayer, the flux-profile method, using MOST universal functions, must be modified before it is applied (Foken, 2006). Since its development, MOST provides the theoretical basis for various micro-meteorological measurements (e.g. Scintillometry), experimental and estimation techniques.

An important caveat with the use of MOST is the uncertainty associated with the use of general or universal functions. All universal functions are derived for dry conditions, their applications for moist conditions and complex terrain can result in discrepancies (Foken, 2006). Nonetheless, the method is widely used and accepted in land surface parameterization schemes (e.g. Niu et al., 2011) due to its simplicity and reliability.

2.3 Micrometeorological measurements

Turbulent flux measurements (e.g. Q_E) can be directly obtained from in-situ measurements, using methods such as eddy covariance (EC), Bowen ratio (BR), scintillometry, lysimetry, water balance, surface renewal and sap flow. The most commonly used techniques for on-site surface flux measurements are the EC and BR methods. In particular, EC is widely recognized to be the most reliable to directly measure turbulent fluxes and widely accepted and applied in many studies evaluating model outputs, and/or ABL experiments (e.g. Campioli et al., 2016; Ní Choncubhair et al., 2017; Kiely et al., 2018; Gerling et al., 2019; Martens et al., 2020). A number of field experiments have been conducted across the continents, such as the EUROFLUX, AMERIFLUX, etc. and contribute to the global networks in FLUXNET (Baldocchi et al., 2001).

The EC system derives surface turbulent fluxes of heat, moisture, CO₂ and momentum through statistical covariance (correlation) and fast response sensors at typically high frequencies of 5-20 Hz (Garratt and Hicks, 1990; Högström and Bergstrom, 1996); 10 Hz is commonly used. In principle, the technique samples the upward and downward turbulent air parcels transporting scalars between the canopy surface and ABL (Figure 2.4). These scalars are measured using a 3D sonic anemometer for vertical wind velocity, and an open, enclosed or closed -path infrared gas analyzer for measuring H₂O density and CO₂ concentration (Burba and Anderson, 2010). Measurements of Q_E made with an open path must however be corrected for possible effects of temperature and humidity on air density (Webb et al., 1980; Leuning et al., 2007).

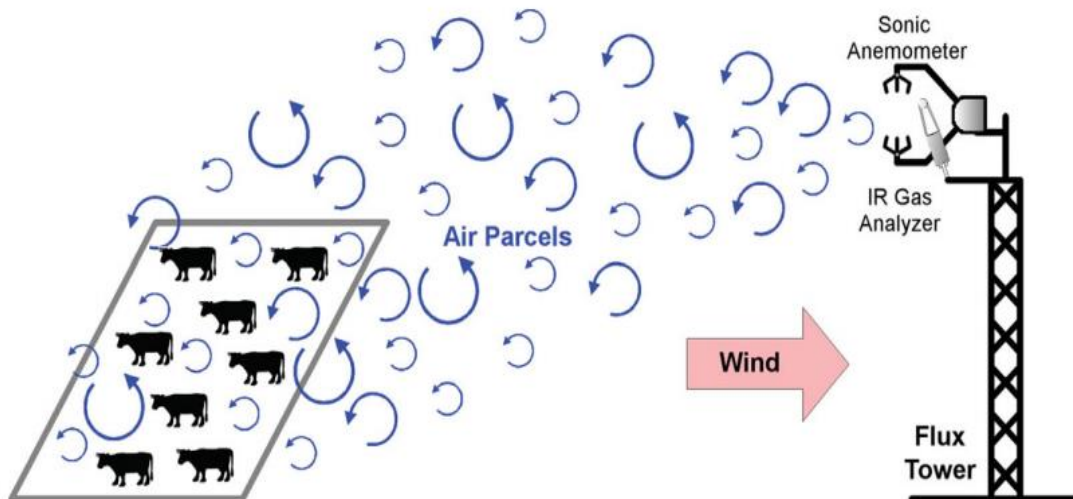


Figure 2.4. Schematic illustration of measurement principle of an eddy covariance system. The air flow looks turbulent but vertical movement can be measured from the flux tower (Hu et al., 2014).

One major setback of the EC system is that turbulent fluxes, particularly Q_E are often underestimated, leading to the non-closure of the energy balance equation. The surface energy imbalance has been reported within the range of 10-30 % across different biomes and weather conditions (e.g. Twine et al., 2000; Wilson et al., 2002), even after correction (de Bruin et al., 2005). Reasons for non-closure problems and other limitations of EC system have been well documented (Foken, 2008; Allen et al., 2011). Therefore, caution should be applied when interpreting flux measurements from EC or when these measurements are used to evaluate model outputs.

While the EC measurement offers certain advantages, the cost of instrumentation, maintenance and measurement are quite expensive, the instruments are susceptible to weather conditions, leading to sparse data, e.g. FLUXNET (Baldocchi et al., 2001), and the measurements cannot be used for spatially explicit information about surface flux densities due to surface heterogeneity and uneven distribution of sites.

Satellite remote sensing products provide useful information required to develop and apply alternative techniques for quantifying surface fluxes at regional/continental scale (e.g. Anderson et al., 2011). However, direct measurement of fluxes using remote sensors is not possible because the vertical profile of turbulent fluxes do not have a spectral signature that can be detected in and retrieved from either nadir or limb remote sounding techniques. As a result, models that incorporate earth observation data have been developed for flux estimations at regional scales (e.g. Bastiaanssen et al., 1998a; Su, 2002).

To summarise, there exist a variety of methods for estimating fluxes which can be categorized into: 1) empirical triangle method, 2) diagnostic SEB approaches, 3) prognostic land surface models, 4) machine learning and 5) data assimilation approaches (Bastiaanssen et al., 1998a, 1998b; Su, 2002; Allen et al., 2007; Oleson et al., 2010; Tang et al., 2010; Anderson et al., 2011; Niu et al., 2011; Chirouze et al., 2014; Zheng et al., 2015; Minacapilli et al., 2016; Zhu et al., 2017; Holmes et al., 2018). Of these approaches, the second and third are more physically based. In contrast, the last two approaches are partly driven by observations, and so the upscaled fluxes, based on machine learning approaches in particular, are often used to evaluate other approaches (Bonan et al., 2011; Draper et al., 2018; Zhang et al., 2020). It should be noted that, observation-driven global and regional surface flux estimates remain a subject of active debate, regarding which machine learning algorithm and/or predictor variables is/are the most appropriate, and the uncertainties associated with global atmospheric forcing data and surface energy balance closure problem with EC systems (Wang et al., 2017; Jung et al., 2019). Generally, all the methods can be applied to a wide range of surface and atmospheric conditions, but in some cases may require a large number of inputs

to derive the fluxes. For the purpose of this research, only the studies that have used a prognostic land surface modeling approach are reviewed in the next section.

2.4 Evolution of Land Surface Model based approaches

The development and implementation of the theory described in Section 2.2, as physically-based parameterization schemes to simulate the surface-air exchanges, spans nearly five decades, from the 1970s to present, with the emergence of different land surface model (LSM) components and increasing complexity through time (Figure 2.5) (Fisher and Koven, 2020). Initial studies on the role of soil moisture led to the evolution of first generation LSM which is based on a simple water balance model commonly referred to as 'bucket model' for evaporation and runoff estimations (Manabe, 1969). This model is recognized as the simplest to apply due to the various assumptions and omissions, including the assumption of spatially uniform soil properties, non-inclusion of plant water-uptake in the root zone, surface resistance, omission of transpiration component, etc. (Pitman, 2003; Zhao and Li, 2015). Although, this approach is still being applied today (e.g. Gentine et al., 2012; Williams et al., 2020), the simplification of the bucket model is a significant limitation associated with the first generation of LSMs, and has been shown to be inadequate for representing surface hydrology from diurnal to interannual scales, based on the Project for Intercomparison of Land surface Parameterization Schemes (PILPS) (Henderson-Sellers et al., 1995; Pitman, 2003).

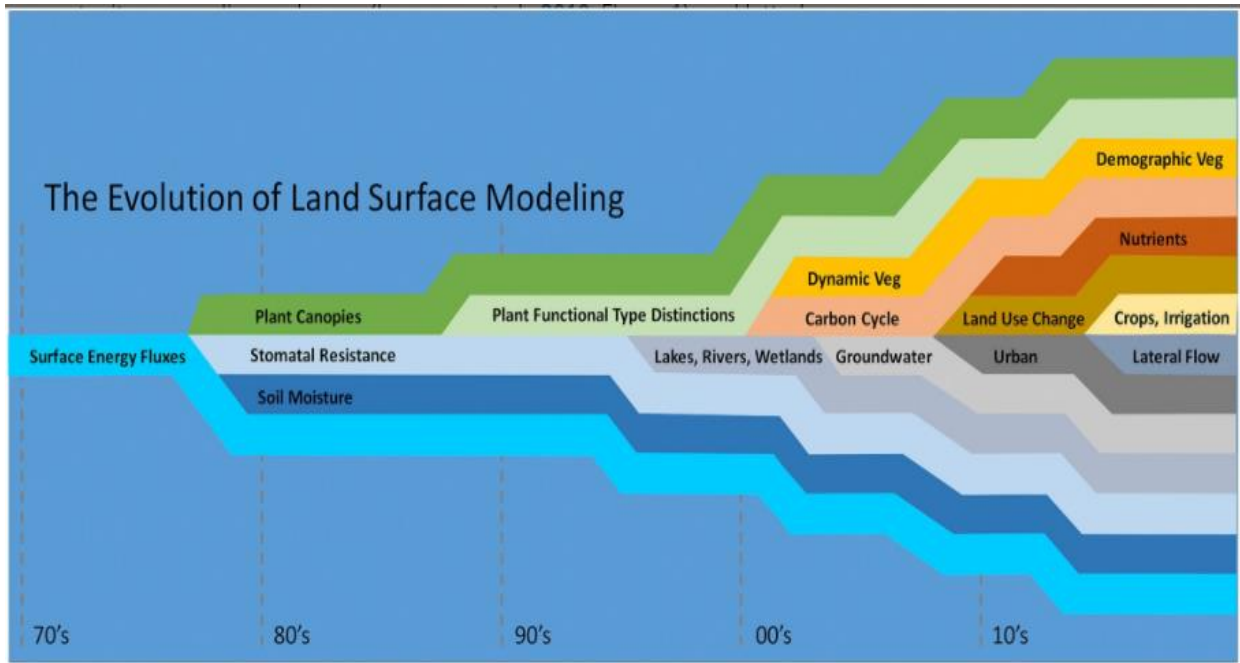


Figure 2.5. A schematic illustration of temporal evolution of land surface model processes, showing time of emergence of different model components and increasing complexity through time (Fisher and Koven, 2020).

Motivated by these limitations, Deardorff (1978) shifted the attention from the role of soil moisture to the contribution of vegetation to Q_E flux. In the model structure, soil is represented in two layers to facilitate estimation of soil heat conduction, a force-restore model (Bhumralkar, 1975) is coupled to simulate surface temperature and vegetation is explicitly represented as a layer above the surface. This contribution led to the development of the second generation of LSMs, and form the basis upon which several successors of this model, including the Simple Biosphere (SiB) model (Sellers et al., 1986) and the associated simplified version (SSiB) (Xue et al., 1991), the land surface model Interactions between Soil, Biosphere, and Atmosphere (ISBA) (Noilhan and Planton, 1989), Biosphere-Atmosphere Transfer Scheme (BATS) (Dickinson et al., 1993) and Noah LSM (Ek et al., 2003) were developed. For instance, in the SiB model, soil is represented by three layers and vegetation by two layers, corresponding to the ground cover and canopy layer. In addition, Noah LSM separates the vertical structure of soil into four depths, corresponding to 10 cm, 40 cm,

100 cm, and 200 cm in the subsurface, and with a single layer, separately above the surface for vegetation and snow. In contrast to the first generation LSMs, the representation of stomatal conductance, as a product of different environmental stress functions (e.g. Equation 2.6) (Jarvis, 1976) to control transpiration process, is central to the efficacy of the second generation models (Viterbo, 2002). The second generation LSMs are more physically based, improve the representation of land-atmosphere interactions at daily time scale (Beljaars et al., 1996; Viterbo et al., 1999), and outperform the first generation models based on PILPS assessments (Henderson-Sellers et al., 1995; Pitman, 2003).

However, emerging developments in the land surface modelling communities suggest that carbon flux exchange, which is not explicitly represented in the second generation LSMs, plays a critical role in land-atmosphere interactions, especially in a changing climate (e.g. Cox et al., 2000). This motivated the improvement of plant physiology by introducing semi-empirical vegetation conductance models (Collatz et al., 1991). This is a biochemical model that combines leaf photosynthesis and transpiration processes through stomatal conductance. As such, it is based on the principle that the biophysical control on transpiration acts to optimize carbon fluxes through photosynthesis, and conserving plant water by stomata closure. This explicit representation of biological control, as a proxy for the role of carbon, on land-atmosphere interactions gave rise to the third generation LSMs (Collatz et al., 1991; Sellers et al., 1992, 1997). An illustration of emergence times of the various components of LSMs and increasing complexity through time is provided in Figure 2.5.

The structure of a typical state-of-the-art LSM has three submodel components which can be categorized as hydrology (energy and water budgets), carbon cycle and dynamic vegetation modules (Figure 2.6) (e.g. Krinner et al., 2005). A submodel can be run independently or in a

combined configuration, depending on the problem to be addressed. For an application in hydrology (Figure 2.6), the LSM component of the energy or water budget is often termed a land surface scheme (LSS), as it describes only the components related to surface-atmosphere exchanges of heat, moisture, momentum at sub-daily time scales, and in many cases parameterization of photosynthesis is often excluded in the scheme (e.g. Ek et al., 2003; Balsamo et al., 2009).

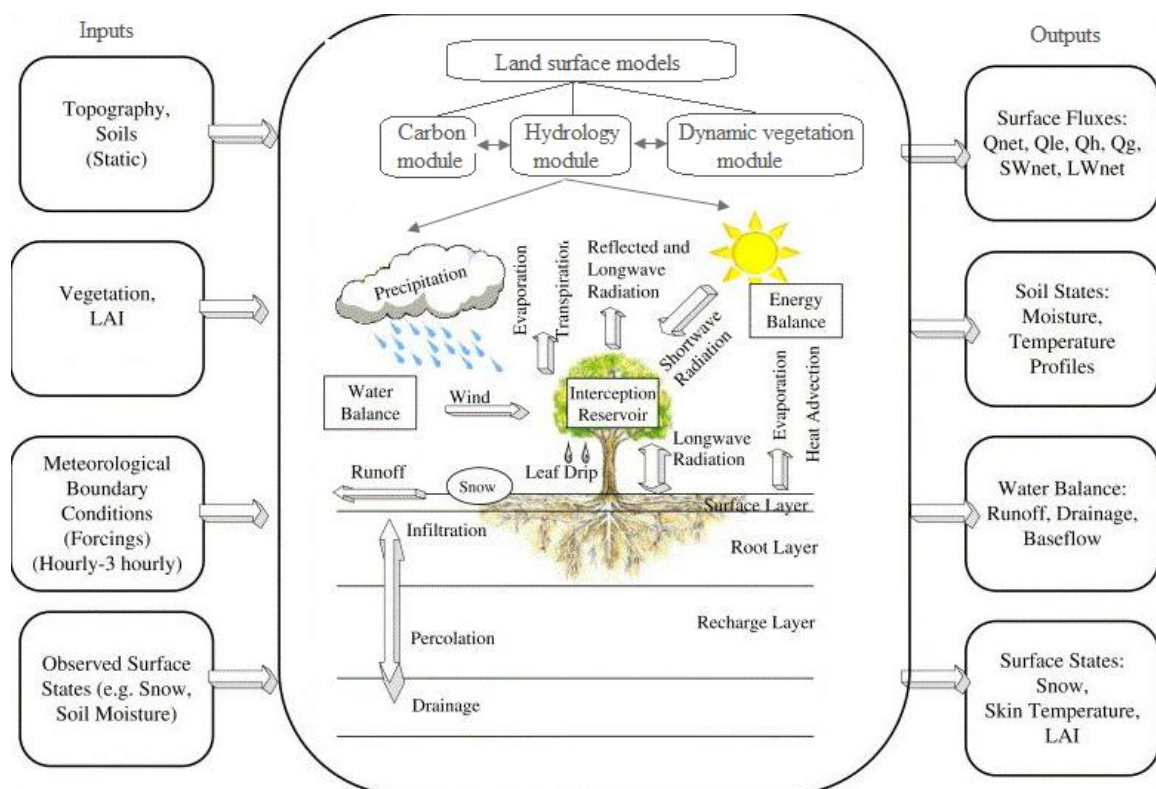


Figure 2.6. Concept of a typical Land Surface Model (LSM) structure, showing the components of surface radiation, energy and water budgets (Adapted from Kumar et al., 2006)

While many LSS have been introduced in the recent past in a bid to improve global and regional climate simulations, a key component is still germane to the sensitivity and performance of a LSS in simulating surface fluxes, consequently Earth system models (Knist et al., 2017). This component is the representation of soil and vegetation properties (e.g. soil temperature, soil moisture, soil hydraulic conductivity, soil type, Leaf Area Index (LAI), surface albedo, rooting depth, canopy height, etc.), which is critical for model initialization and

operation (e.g. Knist et al., 2017). Use of models comes with caveats if the required atmospheric forcing are not sufficiently available or not appropriately used (Bauer et al., 2015; Knist et al., 2017). Therefore, the choice of a scheme often depends on the availability of the required meteorological parameters.

To this end, a number of studies have related surface fluxes of heat, moisture and momentum with available weather parameters that are either routinely measured or available from model outputs in order to develop a land surface scheme for estimating surface fluxes (e.g. Chen et al., 1996; de Rooy and Holtslag, 1999; Lu et al., 2014). In many cases, either the sensible heat flux or latent heat flux or the complete SEB terms were evaluated. For example, de Bruin and Holtslag (1982) evaluated the difference between using a LSS that is based on the PM equation, which requires a high number of input parameters, and a modified Priestly-Taylor-based (PT) scheme, which requires only net radiation, air temperature and a specification of moisture conditions at the surface, to determine surface turbulent fluxes during unstable conditions over Cabauw, the Netherlands. Their study demonstrated that both schemes produced similar results during unstable ($0 \geq \textit{stability parameter} \geq -0.3$) environmental conditions. They suggest that, while the simplified scheme may be applicable practically, the method requires evaluation for different environmental conditions. These findings are also supported by Holtslag and van Ulden (1983) who used a simple empirical LSS scheme based on flux-profile relations (see Section 2.2.3), limited weather data on wind speed, air temperature and total cloud cover, and a simple modified PT approach for deriving estimates of daytime (neutral and unstable weather conditions) surface fluxes and boundary layer parameters. The usefulness of these methods for nighttime ($Q_N < 0$) applications was demonstrated by van Ulden and Holtslag (1983, 1985) and Holtslag and de Bruin (1988). Smith

(1990) proposed a simple, alternative, approach to parameterise surface flux densities during nighttime (stable weather conditions). Mohan and Siddiqui (1997) compared and tested different estimation schemes of turbulent parameters during both stable and unstable regimes. Berkowicz and Prahm (1982a) also applied a flux-profile method to simulate surface fluxes of momentum and heat across different experimental sites.

Berkowicz and Prahm (1982b) estimated sensible heat fluxes using the resistance method and PM equation. The resistance method is based on the analogy of Ohm's law in which the potential difference of a quantity (e.g. temperature) is dependent on the properties of the medium of the flux considered, and can only be applied where the flux is regarded as constant throughout the medium. Berkowicz and Prahm (1982b) found satisfactory agreement between model results of surface resistance and sensible heat flux when compared with experimental data from two wet, dense canopy grassland sites and one less-dense canopy grassland site, across Europe. The study also demonstrated that surface resistance correlates well with vapour pressure deficit, suggesting the importance of this approach for estimating the Q_E flux. Jacovides et al. (1991) compared profile and resistance methods for estimating ET and sensible heat fluxes above a grassland site in the UK. Under near-neutral or slightly unstable environmental conditions, the profile method appeared to reproduce measured sensible heat fluxes and the friction velocity. The study also demonstrated the accuracy of PM for estimating ET and its insensitivity to changes in atmospheric stability. In a similar study, Galinski and Thomson (1995) evaluated three schemes, derived by Holtslag and van Ulden (1983), Berkowicz and Prahm (1982b) and Smith (1990), respectively, using measured sensible heat flux above agricultural fields in the UK. They demonstrated that the Berkowicz and Prahm scheme had the smallest errors and highest correlation, while both the Smith

(1990) and Holtslag and van Ulden (1983) schemes displayed the largest *RMSE* and mean bias, respectively during daytime. All the schemes tended to underestimate the daytime sensible heat flux.

Chen et al. (1996) evaluated four land surface schemes, distinguished by the number of input parameters and the representation of soil/vegetation canopy, using First International satellite land surface climatology project Field Experiment (FIFE) observations. They showed that the soil water bucket model by Manabe (1969) resulted in an overestimation of evaporation during wet periods, leading to an unrealistically large underestimation of the sensible heat flux. Similarly, the two-layer simple water balance model by Schaake et al. (1996) resulted in evaporation estimates that matched well with the observations during wet conditions but underestimated evaporation during dry periods. Both the Oregon State University (OSU) and SSiB models, with more explicit representation of soil and vegetation (Pan and Mahrt, 1987; Xue et al., 1991), performed similarly and were able to reproduce the observed evaporation, sensible heat flux, soil moisture and surface skin temperature at seasonal and diurnal scales. Chen et al. (1996) further suggested that the treatment of surface resistance scheme is crucial to reducing relatively wet and dry biases in evaporation.

Beljaars and Bosveld (1997) evaluated daytime ($Q_{S\downarrow} > 5 \text{ W m}^{-2}$) Q_E flux estimates derived using the PM model, and modified PT (de Bruin and Holtslag, 1982), based on their sensitivity to model coefficients of Jarvis type surface resistance (r_s) (Jarvis, 1976; Stewart, 1988) at Cabauw. In their analysis, they derived optimal model coefficients based on the best fit of r_s to observations. Using the optimal coefficients, the study found the more complex PM to have the lowest error, relative to other approaches used, and consequently recommended a new version of the Jarvis-Stewart (Jarvis, 1976; Stewart, 1988) surface resistance approach, based

on the derived optimal coefficients for applications under similar conditions. De Rooy and Holtslag (1999) proposed and evaluated a new LSS, based on profile relationships and observations from the grassland site, at Cabauw. They also analysed the sensitivity of their scheme to different approximations of r_s , including the optimized Jarvis approach (Beljaars and Bosveld, 1997). In a more recent study, van de Boer et al. (2014a) applied the modified versions of Jarvis r_s , and de Rooy and Holtslag scheme in a manner that separates the dependency of flux densities on air from surface temperatures, at two sites with different land cover types. Lu et al. (2014) proposed and evaluated a parameterization scheme for estimating surface flux densities using continuous surface and air temperatures and net radiation measurements, and without calculating surface and aerodynamic resistances.

These studies employed routine weather observations, in combination with EC measurements, to parameterize and develop a LSS to estimate SEB terms; the schemes are largely distinguished by the type and number of input parameters. At the same time, the estimation of surface turbulent fluxes is largely based on the PM model, coupled with MOST and empirical r_s scheme (e.g. Jarvis and Ball-Berry) (Collatz et al., 1991; Shrestha et al., 2018). Many of the working LSS in Earth system models, including the Noah land surface model with multiparameterization options (NOAH-MP) (Niu et al., 2011), Simplified Simple Biosphere model (SSiB) (Xue et al., 1991), etc. build on these approaches, but fundamentally vary in complexity, and input surface and atmospheric parameters, and these differences are still recognized to be quite large (Chen et al., 1997; Li et al., 2016). Overall, there appears to be an agreement among the previous and recent studies that the improvement of LSS should focus more on those model parameters relating to r_s , vegetation and soil, that stand to influence

the sensitivity and performance of the schemes above different plant functional types (PFTs) (Prentice et al., 2014; Li et al., 2016; Qiu et al., 2018)

The LSS and observational-driven examination of surface exchange processes have also improved the understanding of surface-air coupling processes and impacts across spatial and temporal scale (Seneviratne et al., 2010; Dirmeyer, 2011; Knist et al., 2017). The coupling strength measures the degree to which atmosphere responds to anomalies in the land surface state (e.g. soil moisture) in a consistent manner, and therefore influences ABL evolution, convection and cloud development, consequently affecting the precipitation patterns, and the frequency and intensity of climate extreme events (e.g. heatwaves and droughts) (e.g. Seneviratne et al., 2010; Teuling, 2018). While quantifying the coupling strength depends on the variables involved and feedback processes to be addressed, the link between soil moisture and Q_E/ET or evaporative fraction (EF) is often conceptually used to understand soil moisture-climate signals (e.g. Seneviratne et al., 2010; Miralles et al., 2012).

Evidence from model simulations have identified geographical 'hot-spots' of strong land-atmosphere coupling on the global scale for boreal summer, based on the multimodel experiments of the Global Land-Atmosphere Coupling Experiment (GLACE) (Koster et al., 2006). At continental scale, Knist et al. (2017) compared summertime (June-August) land-atmosphere coupling strength using an ensemble of regional climate models (RCMs) from the subset of ERA-Interim-driven European domain Coordinated Regional Climate Downscaling Experiment (EURO-CORDEX) across Europe. The study found strong (weak) coupling in southern (northern) Europe, and a transition zone ranging from strong to weak coupling, covering a large part of central Europe, though they noted that the coupling strength in the transition zone is overestimated in many of the RCMs employed. In the context of climate

change, a transition zone or even a weak coupling zone is likely to shift in response to perturbations in land surface processes associated with projected changes in large-scale precipitation pattern (e.g. Dirmeyer et al., 2021). Such regional shifts of land-atmosphere coupling regimes can induce and intensify climate extremes such as compound 'hot drought' events, which can be potentially explored using LSS owing to their explicit representation of both land surface and atmospheric processes in an integrated manner.

2.5 Role of land surface processes in extreme drought events

Drought monitoring and prediction is a fundamental issue for water resource and agricultural management, particularly in regions where agricultural activities are dominantly rain-fed. At a continental scale, drought conditions typically result from extended periods of atmospheric warming, associated with anticyclonic blocking of rain-inducing mechanisms, leading to a high atmospheric demand for ET, and consequently soil moisture deficits and suppression of low cloud formation, all of which can act to further exacerbate the initial drought conditions (Seneviratne et al., 2010; Samaniego et al., 2018; Teuling, 2018). Hence, drought evolution and propagation through hydrological regimes are typically a consequence of complex interactions among land, atmosphere and management practices, which may require LSS to explain and understand their complexity and dynamics (van Loon et al., 2016; Quintana-Seguí et al., 2020).

Different types of drought are recognized based on their development, frequency, intensity and impacts (e.g. van Loon et al., 2015). They are namely: 1) meteorological drought (1-3 months), defined on the basis of rainfall anomalies, 2) hydrological drought (6-24 months), defined on the basis of extremely low levels of groundwater, lakes, reservoirs and unusually low streamflow in rivers, 3) agricultural drought (1-6 months), defined on the basis of high

soil moisture deficits, affecting plant growth and productivity, and 4) socioeconomic drought, when the demand for water exceeds the supply (van Loon et al., 2015; Falzoi et al., 2019; Moore, 2020). Of these drought types, the first is well studied and documented across Europe, including Ireland (e.g. Noone et al., 2017; Falzoi et al., 2019; Murphy et al., 2020; Moore et al., 2020; Vicente-Serrano et al., 2020). Typically, these studies have employed standard drought indices, such as the widely used Palmer Drought Severity Index (PDSI) and the standardized version (SPDI) (Palmer, 1965; Ma et al., 2014), the standardized precipitation index (SPI) (McKee et al., 1993), the standardized precipitation evapotranspiration index (SPEI) (Vicente-Serrano et al., 2010; Begueria et al., 2014), etc. for characterizing drought severity. For example, Todd et al. (2013) analyzed drought characteristics using reconstructed precipitation and temperature series, and the self-calibrated PDSI for three sites in Southeast England from 1697 to 2011. The study identified multiple drought-rich periods which were caused by prolonged rainfall deficits and intensified by high temperatures. Other studies have also identified multiple drought-rich years using SPEI (Potop et al., 2014) and multiple drought indices (Brázdil et al., 2015) for the Czech Republic, SPI for Serbia (Gocic and Trajkovic, 2014), and both SPI and SPEI for Spain (Domínguez-Castro et al., 2019). Many of these studies have linked the identified years of prolonged drought to sequences of dry spring and summer seasons. Brázdil et al. (2015) noted that much of the drought episodes before 1880 can be attributed to precipitation deficits, whereas the droughts of recent decades (beginning from the 21st century) are more strongly related to high temperatures aggregated by the effect of climate-driven anthropogenic forcing (rise in atmospheric CO₂ concentration). This is further supported by a more recent study by Vicente-Serrano et al. (2020) who, using reconstructed rainfall series and SPI, concluded that the long-term trend of meteorological droughts can not be confirmed using precipitation records alone in Western Europe.

In Ireland, Wilby et al. (2015a, 2015b) investigated persistent meteorological droughts using the Island of Ireland precipitation (IIP) network 1850–2010. Noone et al. (2017) also used the IIP data and SPI to study, detect and document historical drought episodes and related socio-economic impacts. Murphy et al. (2020) evaluated historical meteorological droughts using reconstructed precipitation records 1748–2000 and SPI at 12-month time scale applied to the UK and Ireland. More recently, Meresa et al. (2021) examined changes in hydrometeorological drought using multiple drought indicators, which were derived from a conceptual hydrological model outputs and climate model outputs from CMIP6. They demonstrated for selected catchments that the meteorological and hydrological drought propagation lags by 3–5 months in the baseline period and such lag times are likely to increase with climate change. The phenomenon of flash drought events occurring within a few days or weeks has also been studied (Hunt *et al.*, 2014; Otkin *et al.*, 2018). The findings from these studies highlight the vulnerability of various parts of Europe to an increasing number of drought episodes, and the importance of understanding the associated drivers and propagation in a changing climate (Samaniego et al., 2018).

Moreover, the occurrence of a prolonged meteorological drought coupled with high atmospheric water demand can result in high soil moisture deficits, with severe implications for ecosystem functioning and agricultural productivity (e.g. Fink et al., 2004; Conti et al., 2005; García-Herrera et al., 2010; Dole et al., 2011; Alexander, 2011; Zscheischler et al., 2018; Miralles et al., 2019; Schuldt et al., 2020). The integrated effects of decreasing soil moisture and increasing evaporative demand and vegetation stress are often explained based on changes in land-air exchange processes (Figure 2.7) (Seneviratne et al., 2010). Under limiting soil water conditions and increasing atmospheric demand, plants are likely to respond by closing their stomata to conserve the available water and prevent desiccation, leading to an

increase in r_s and decrease in ET. As a consequence, the available energy is largely channelled into Q_H which in turn results in a positive feedback on air temperature (Seneviratne et al., 2010; Miralles et al., 2019). The land surface state, in particular soil moisture, plays a critical role when ET is constrained by water stress.

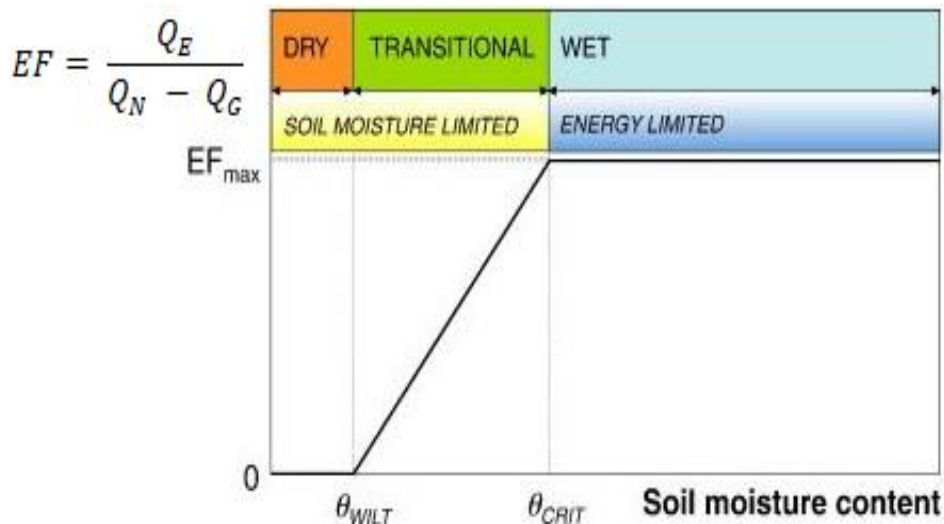


Figure 2.7. An illustration of soil moisture-evapotranspiration coupling framework that defines the three evaporative regimes (Adapted from Seneviratne et al., 2010).

In a wet, energy-limited regime, soil moisture content is sufficiently available, thus Q_E is primarily limited by the available energy and the state of the ABL. In a transitional and dry, water-limited regime, the moisture supply from land to entirely compensate for atmospheric demand for ET is largely restricted, leading to a land-atmosphere coupling where Q_E is constrained by soil moisture content (Seneviratne et al., 2010).

Previous studies using EC measurements and/or LSM outputs have demonstrated the role of these land surface processes in the amplification of drought and heatwaves. For example, Black et al. (2004) investigated the factors contributing to the summer 2003 European heatwave using modelled data and observations of the surface energy budget from a University of Reading (grass) field site. They demonstrated that the anomalously clear skies

and increased net radiative fluxes experienced during June 2003 led to an excess water loss from the European land area in the following month of July. Black et al. (2004) found that when radiative forcing was weaker in July in central Europe, Q_E fluxes were anomalously negative due to a lack of soil moisture, leading to higher surface temperatures and Q_H fluxes. Zaitchik et al. (2006) subsequently highlighted the role that early vegetation growth, resulting from higher air temperature experienced during the spring, coupled with rainfall deficits, led to an early season soil moisture deficit during 2003 and likely exacerbated the temperature extremes recorded during 2003 European heatwave. Fischer et al. (2007a, 2007b) also explored the role of land surface processes during 2003 using a regional climate model. In particular, they investigated the contribution of soil moisture anomalies and interactions with the overlying air through turbulent exchanges. Black et al. (2004), Zaitchik et al. (2006) and Fischer et al. (2007a, 2007b) all concluded that soil moisture deficits largely controlled the partitioning of Q_N between Q_E and Q_H fluxes during 2003 mid-summer across Europe. Other studies have also shown a close connection between soil moisture, decreasing ET and summer temperature extremes (e.g. Hirschi et al., 2011; Quesada et al., 2012; Miralles et al., 2014; Philip et al., 2018).

While enhanced surface sensible heat fluxes are typically most evident in regions that exhibit a strong coupling between soil moisture and ET (e.g. Southern Europe) (Knist et al., 2017), regions can switch between energy-limited and moisture-limited regimes over the course of a year or depending on land cover (Seneviratne et al., 2010). Such shifts in evaporative regime have been examined by determining a critical soil moisture threshold (θ_{crit}), derived from the relationship between soil moisture and evaporative fraction (Figure 2.7) (Seneviratne et al., 2010; Denissen et al., 2021). Other studies have also derived this critical threshold based on observations and model outputs using different theoretical frameworks (Akbar et al., 2018;

Haghighi et al., 2018; Feldman et al., 2019; Denissen et al., 2020). In the context of climate change projections, humid regions may experience seasonal shift from wet to transitional regimes under critical mean soil drying, a feature that has manifested during the 2018 record-breaking high temperatures and extreme drought condition experienced across many parts of Europe (Buras et al., 2019; Dirmeyer et al., 2021). For example, Buitink et al. (2020) found that the estimated critical soil moisture content increased linearly with soil depth, reflecting decreasing available plant water access from the root zone as the 2018 drought progressed over two experimental sites in the Netherlands. Using field data and ERA5-Land reanalyses data, Dirmeyer et al. (2021) also found consistent and strong evidence of a seasonal shift in evaporative regime across most parts of Europe, but noted that ERA5-Land data underestimated the impact of very dry soils on the atmosphere, particularly over Britain. The findings from Dirmeyer et al. (2021) suggest that degree of changes in land surface processes may vary locally depending on the soil characteristics. This was previously concluded by Jaksic et al. (2006) who showed that the impact of soil moisture variability on net ecosystem functioning is small and similar between dry and wet years, whereas the soil moisture regimes were different for both years, over a grass field site in the south of Ireland.

Vegetation also plays a critical role in regulating the link between soil moisture and the atmosphere (Lansu et al., 2020). The role of vegetation is related through its response to incident radiation, changes in surface albedo, and changes in surface roughness that determines surface friction and turbulence, which may vary spatially and seasonally depending on the background climate and land cover (Duveiller et al., 2018). For example, grassland typically has a higher surface albedo than the forest, suggesting a decrease in ET and ultimately leading to cooling or warming depending on which of these processes dominates (Li et al., 2015, 2021). However, due to local effects, the changes in land surface

processes may vary for different biomes during summer climate extremes. Teuling et al. (2010) using FLUXNET observations found a systematic difference in the partitioning of net radiative flux anomalies into sensible and latent heat fluxes between grass and forests during the 2003 European climate extremes. The ET fluxes were lower over forest than grassland, leading to a positive climate forcing, whereas the reverse is expected based on the deeper root structure associated with forest biomes. Using a conceptual ABL model, Stap et al. (2014), van Heerwaarden and Teuling (2014) and Lansu et al. (2020) demonstrated that the findings of Teuling et al. (2010) could be replicated by showing that the surface resistance of forests increased in response to stomata closure and high vapour pressure deficits (VPD), during conditions of anomalously high incident radiation, relative to grasslands. It should be noted that vegetation-atmosphere signals have been recognized to be species dependent (Gu et al., 2006; Aires et al., 2008a, 2008b; McGloin et al., 2019). Recently, Li et al. (2021) showed that vegetation green-up of temperate and boreal evergreen forests may amplify warming and droughts through a significant increase in Q_H anomalies. In contrast, cooling feedbacks dominated for grasslands, temperate needleleaf and deciduous forests in response to high ET flux anomalies during years of high vegetation canopy coverage in North America (Li et al., 2021).

As soil drying may span several days to weeks, whereas VPD changes can occur rapidly over short time scales (sub-daily), drought-like water stress driven by VPD may occur even under conditions of sufficient soil water (Gu et al., 2006). Sulman et al. (2016) disentangled the contributions of VPD and soil water to exchange processes during drought and non-drought years using multiyear records of EC measurements over forest land cover. They found that the magnitudes of observed photosynthesis and transpiration to both VPD and soil water anomalies are similar. Lansu et al. (2020) also found from their model simulations that the

effect of VPD feedback can be more than 50% of apparent soil moisture depletion, and therefore argued that previous studies may have erroneously attributed the effects of aridity on air temperature to dry soils. Although, Ireland has been shown to be vulnerable to summer climate extremes and associated impacts (Dillon et al., 2018; Falzoi et al., 2019; Murphy et al. 2020), related studies which have sought to understand the role of land surface processes are lacking. Such gaps need to be explored to understand how they can be better managed and due to the fact that the occurrence of such extremes are projected to increase in both frequency and intensity as a consequence of anthropogenic induced changes in the climate system (Samaniego et al., 2018).

2.6 Estimating crop-water use at farm-scale.

In addition to acting as the primary mechanism for transferring water from the soil to the atmosphere, plant water use is also a critical ecosystem indicator that can assist farmers to understand crop water dynamics and performance within their local environment. Actual ET dynamics are influenced by many factors, including vegetation type, soils, atmosphere, and management activities, indicating complex processes that may be quite expensive to monitor explicitly at ground level (e.g. Singh et al., 2020). Remotely sensed observations provide an opportunity to develop alternative and potentially more cost-effective approaches for estimating actual ET at both local and global scales (e.g. Mu et al., 2007; Anderson et al., 2011; Singh et al., 2020). Many of these approaches are based on either diagnostic SEB methods or the PM equation (see Section 2.2.1). The former relies on land surface temperature (T_s) derived from radiometric thermal infrared (TIR) spectral signatures provided at regional and global scales (e.g. Landsat) to estimate ET, derived as a residual of the SEB terms (Bastiaanssen

et al., 1998a, 1998b; Su, 2002). Although the PM equation is more physically based, the method is reliant on a large number of input parameters. In contrast, Allen et al. (1998) simplified the PM approach to allow for a more limited number of input parameters which has been widely applied as the standard (FAO-56 PM) for many agricultural applications (e.g. Vanino et al., 2018).

Previous studies using these approaches are either based on cross-comparisons of models, quantifying water use of different biomes, assessing the scale effects of using fine (e.g. Landsat) and coarse resolution (e.g. MODIS) satellite observations or combining the satellite observations to derive ET at a high spatial and temporal resolutions (Gebremichael et al., 2010; Anderson et al., 2012; Senay et al., 2017; Yang et al., 2018; Singh et al., 2020). Moran et al. (1996) estimated evaporation rates by combining the PM equation with measurements of surface temperature and reflectance of semiarid grasslands. Zhang et al. (2010) assessed global terrestrial ET using satellite-derived normalized difference vegetation index (NDVI) in combination with the PM and PT approaches. Vanino et al. (2018) explored the potential of Sentinel-2A and FAO-56 PM to estimate potential ET and irrigation water requirement of a tomato field in central Italy. He et al. (2019) used a blended Landsat-MODIS vegetation index in a modified MOD16 algorithm framework (Mu et al., 2007) to evaluate field-scale ET over C₃/C₄ crops in the continental USA. Singh et al. (2020) also explored the potential of integrating Landsat and Sentinel-2 data to map field-scale ET using SEB model over an irrigation district, California. More recently, García-Gutiérrez et al. (2021) evaluated actual ET in drip irrigated vineyards based on different modelling approaches and Sentinel-2 data in central Chile. Ma et al. (2021) coupled water vapour and carbon uptake to propose an ET modelling framework, based on the PM equation and Sentinel-2 data. They verified this

framework over three experimental sites covered with maize and/or wheat crops, and further discussed the scale effects on model performance at field scale. In central Ireland, Spiliotopoulos et al. (2017) estimated ET and evaporative fraction (EF) from a mixed land cover site using the Mapping Evapotranspiration at High Resolution with Internalized Calibration (METRIC) model (Allen et al., 2007) and Landsat data.

The consistency of model applications across different biomes (e.g. Norman et al., 2003; Su et al., 2005, 2007; McCabe and Wood, 2006) has also motivated several studies relating ET to crop productivity (Bastiaanssen and Ali, 2003; Mishra et al., 2013; Tadesse et al., 2015; Anderson et al., 2016a, 2016b; Mladenova et al., 2017; Yang et al., 2018). Crop yield can be predicted from actual ET which is a measure of the amount of water used by the crop. This relationship is represented in a mathematical model called the crop water production function, reflecting the conversion rule between the crop yield and water factor (Abteu and Melesse, 2012). It can be used to determine crop water demand and increase the efficiency of crop water use for optimum yield production. Applying both the surface energy balance algorithm for land (SEBAL) and a two-source surface energy balance system (TSEB), Abteu and Melese (2012) found positive (negative) correlations between Q_E (BR) and crop yields over wheat and soybean fields. Gobbo et al. (2019) used the SEBAL model to derive ET and maize yield maps with a relative error less than 0.3 % across different irrigation management zones in Italy. Correlations between Evaporative Stress Index (ESI), a remote sensing drought indicator based on the Atmosphere-Land EXchange Inverse (ALEXI) model, the associated flux Disaggregation approach (DisALEXI) (Anderson et al., 2007), and crop yields have also been investigated across different regions including the USA (e.g., Otkin et al., 2016; Mladenova et al., 2017; Yang et al., 2018), Brazil (Anderson et al., 2016a), and the Czech Republic (Anderson

et al., 2016b). In many cases, the ESI has demonstrated the capability to provide better relationship with crop yields than the traditional correlations between vegetation indices and precipitation index (e.g., SPI). The results from previous studies, using remote sensing-based ESI, suggest that the index can be used for early warning predictions of drought onset and flash drought events (Otkin et al., 2018), and most importantly demonstrating the capacity to explain the regional variability in crop yields both in water- and energy- limited crop growing regions (Yang et al., 2018).

However, achieving optimal crop yield depends on the water use efficiency (WUE), defined as the photosynthetic carbon assimilation per unit of water used by the crop (e.g. Hatfield and Dold, 2019; Gentine et al., 2019). The indicator is often estimated as the ratio of vegetation gross primary productivity (GPP) and ET at ecosystem level. GPP represents the rate of carbon assimilation by terrestrial plants through photosynthesis, and the photosynthetic carbon fixation capacities of different crops vary in response to changes in environmental factors (e.g. Monteith, 1972; Wang et al., 2020). Thus, GPP plays a major role in many ecosystem functions. The key parameter for estimating GPP, and consequently WUE, is the light-use efficiency (LUE), which characterises the ability of plants to convert the absorbed visible light/radiation into organic dry matter through photosynthesis (e.g. Wang et al., 2020). The efficiency of light use in the PAR domain differs between plant species. For example, C₄ plants, which are adapted to warm/hot seasonal conditions under wet or dry environments, are thought to be higher in light use due to more efficient photosynthesis rate of leaves compared to C₃ plants, which are more adapted to cool/cold seasons under wet or dry environments (Tardieu, 2013). To date, several existing models that are process-based and/or based on LUE theory are used to derive GPP; however, they vary greatly in terms of the estimated values

(Dechant et al., 2020; Jiang et al., 2020; Wang et al., 2020; Ma et al., 2021). Of these models, the LUE theory is recognized to provide deeper understanding of the key processes of vegetation carbon sequestration (e.g. Wang et al., 2020), and by extension the WUE of crops. WUE is recognized as a key parameter for predicting yields in many crop prediction models. To date, such models can either be regression-based or mechanistic models (e.g. CropSyst, AquaCrop) (Stockle et al., 1994; Steduto et al., 2009). For example, in the AquaCrop model, yield is linearly related with normalized WUE, scaled by harvest index and the basal crop coefficients, water stress and temperature stress (Steduto et al., 2009). González-Dugo and Mateos (2008) used spectral vegetation indices to benchmark the WUE of irrigated cotton and sugarbeet crops and found both linear and non-linear relationships between ET and yield. Campos et al. (2018) proposed a remote sensing approach using the AquaCrop framework to examine the relationship between WUE and yield of maize and soyabean in Nebraska. They demonstrated the ability of a constant normalized WUE to replicate measured yield across crop phenological stages, but noted that the assumption of a constant, though conservative for maize and soyabean, needs further testing for all C₃/C₄ plants. Khan et al. (2019) combined ET derived from METRIC and CropSyst model to estimate biomass production and yield at high resolution in four dryland agricultural sites.

In the context of climate extremes, Kørup et al. (2017) evaluated the WUE tolerance of C₃ and C₄ perennial grass species under drought stress and drought-treated conditions. They found a positive relationship between dry matter (DM) and WUE under well-watered conditions, but DM decreased for all species and cultivars under drought stress. However, grass growth increased in drought-treated plots for a period after drought stress, concomitant with higher WUE. These findings are not consistent with models, in which the WUE increases

monotonously when the process is assumed to be regulated by surface resistance, with a slight reduction in photosynthesis during periods of water stress (Flexas and Medrano, 2002; Liu et al., 2016). Lu and Zhuang (2010) and Zhao et al. (2020) investigated WUE responses to dryness progression of different ecosystems, including grassland using a modelling approach. They demonstrated that the WUE of plants show a biphasic trend with drought intensity: WUE first increased progressively as drought moves from developmental to moderate drought stage, and then decreased as the drought intensity increased beyond a moderate level. Reichstein et al. (2002) and Yu et al. (2008) suggested that the decline in WUE during extreme drought events is likely associated with reduction in carbon assimilation capacities due to impairment of electron transport and carboxylation capacity. The responses of C₃ and C₄ plant's WUE are also different due to a completely different patterns of stomatal response to environmental conditions and photosynthesis, and the competition between carbon and oxygen in C₄ versus C₃ (e.g. Hatfield and Dold, 2019).

Hence, the assumption that under elevated CO₂, crop yields increase with increasing WUE, depends on the type and species of plant, and the ambient meteorological conditions (Gentine et al., 2019; Hatfield and Dold, 2019). Therefore, WUE serves as a potentially useful tool for better understanding changes in water availability and a plant's physiological response to both weather and climate.

2.7 Implications of research on surface-air exchanges for Ireland

To date, research in Ireland akin to modeling surface energy exchanges to understand how agriculture would respond to changes in climate is lacking. Previous related studies are few and are largely based on experimental measurements of terrestrial ecosystem exchanges (e.g. CO₂) using EC system, of which the observations are either incomplete or limited duration

over grasslands (e.g. Peichl et al., 2012; Ní Choncubhair et al., 2017) and peatlands (Sottocornola and Kiely, 2010a, 2010b; McVeigh et al., 2014; Kiely et al., 2018). Of these studies, the enhancement and reduction of net ecosystem exchange (NEE) and its components were reported to depend on the seasons, plant species, environmental and management controls. According to Jaksic et al. (2006), measured NEE over a managed grassland site in the south west of Ireland was similar for the same months in different wet and dry years. This was attributed to the fact that the soil moisture content was well above wilting point at the site, though the measured soil moisture values were different between the two years. Jaksic et al. (2006) concluded that the NEE for humid grassland was not sensitive to variability of climate (e.g. precipitation) for their period of analysis.

This conclusion was further supported by Peichl et al. (2012) who demonstrated, over managed grassland in the southeast of Ireland, that the observed reduction of net CO₂ uptake (NEE) and increased BR, associated with increased (decreased) Q_H (Q_E) fluxes, were more pronounced 2-3 weeks following harvest compared to grazing practices with continued net carbon uptake. Thus, the exchanges of carbon, water and energy were primarily controlled by the choice of grassland management practices, with no observed effect of environmental factors in the region. While Kiely et al. (2018) supported the control of management practices (e.g. silage cutting) on carbon exchanges above humid managed grassland, the study also highlighted that climate, particularly temperature, was a strong control of CO₂ fluxes in winter. Ní Choncubhair et al. (2017) also demonstrated that the observed increase in net CO₂ uptake of a C₄ grass species, *Micanthus*, was significantly driven by above-ground growth and leaf expansion, and may potentially further enhance carbon sink as it reaches maturity, relative to a C₃ grass species, *Reed Canary*, in the south east of Ireland.

Although the findings from these studies are important, as they partly reveal the role of soil conditions in exchange processes, the analyses were primarily limited to the south of Ireland, and focused more on CO₂ fluxes based on observations that are few in terms of spatial and temporal coverage. At the same time, Irish grasslands are primarily rainfed, suggesting that water availability plays a critical role in grassland both in terms of the turn-out timing and duration of grazing season, and timing of harvesting herbage (e.g. silage, hay) (Jaksic et al., 2006). Hence, water availability can potentially drive grass physiological response, scaling up to influence the surface exchanges of carbon, heat and moisture, and consequently on grass performance and yield, and length of grazing season. Apart from these, Irish grasslands have been shown to be vulnerable to climate change in recent past (e.g. Dillon et al., 2018), due to the rising frequency and severity of climate extreme events (e.g. droughts) which is partly driven by perturbations in surface exchange processes regionally (Seneviratne et al., 2010; Teuling, 2018; Dirmeyer et al., 2021). Therefore, the proposed framework here would enable a multi source data integration approach that is capable of providing explicit information akin to carbon, heat and moisture fluxes, to better understand the grassland response to climate change over both the short and long -term across the country. This knowledge is important for pasture-based farmers to make the best informed decisions in relation to their management activities.

2.8 Key issues

Several issues in relation to surface flux measurements, land surface modelling and exchange processes are identified, some of which are detailed as follows. The land surface characteristics (e.g. land cover, soils and topography) are spatially non-uniform. These surface heterogeneities exert a significant influence on meteorological forcing data, including

downward shortwave radiation, near-surface temperature, wind speed, cloud amount, precipitation and atmospheric moisture. For instance, the amount of downward shortwave radiation depends on the topographic characteristics (e.g. elevation, slope and aspect) of the site. Soil and vegetation characteristics control the distribution of soil moisture and land surface energy budget, particularly evaporation (Viterbo, 2002). Evaporation is regulated by soil water; a systematic bias in soil water would therefore propagate into evaporation estimates, implying a hot, dry or wet bias, depending on the season. The conflicting roles of evaporation suggest the contributing role of the land surface state in earth system model approaches (Viterbo, 2002).

Generally, the spatially non-uniform patterns of land surface and dynamic nature of meteorological forcing are quite complex to represent in a land surface modelling framework (Duan et al., 2006; Fisher and Koven, 2020). As such, the approach of model formulation, quality of meteorological forcing data and selection of appropriate empirical constants or model parameter remain key issues confronting the ability of a land surface model to accurately quantify the land surface processes at different scales (Zhao and Li, 2015; Fisher and Koven, 2020).

Eddy covariance measurements of surface energy fluxes are widely used to calibrate and evaluate model simulations (Beljaars and Bosveld, 1997; van de Boer et al., 2014a). However, the EC approach often underestimates surface turbulent fluxes by 10-30 %, relative to the measured available energy, resulting to issues associated with energy balance closure (Wilson et al., 2002; Foken, 2008; Franssen et al., 2010; Stoy et al., 2013). Even under ideal flat, homogenous and short vegetation conditions, this closure problem is also present (e.g. Twine et al., 2000). The closure problem may arise from the failure to measure heat storage terms

as part of measurement programmes (e.g. Heusinkveld et al., 2004); large-scale turbulent circulations over heterogeneous landscapes that are not captured by EC methods (Mauder et al., 2007; Stoy et al., 2013); the assumption of no advection, and; inaccurate Q_N measurements (e.g. Foken, 2008). While several studies (e.g., Aubinet et al., 2000; Twine et al., 2000) have made concerted efforts to address this problem, the surface energy imbalance remains a key issue of how flux measurements should be interpreted, and how model-derived surface energy fluxes should be evaluated with measured when the EC approach is used (Twine et al., 2000).

3. Land surface modelling of surface radiation and energy fluxes using routine weather data: Parameterization and Sensitivity to soil moisture regimes

Preface

Published as:

Ishola, K.A., Mills, G., Fealy, R.M., Ní Choncubhair, Ó. and Fealy, R., 2020. Improving a land surface scheme for estimating sensible and latent heat fluxes above grasslands with contrasting soil moisture zones. *Agricultural and Forest Meteorology*, 294, 108151, 1-18. <https://doi.org/10.1016/j.agrformet.2020.108151>

This chapter is an extended version of the above paper (see supplementary for full article), and serves as a prelude to the subsequent chapters, designed to lay the foundation upon which the subsequent papers were built. Here, the prognostic ‘land surface modeling’ framework described in Chapter 2 was employed to link radiation models with surface ‘stomatal’ resistance (r_s) schemes, MOST theory and Penman-Monteith equation- hereafter referred to as a land surface scheme (LSS). **The initial and broad objective is to evaluate the potential of a LSS, adapted for use in a different climate from which it was developed, for estimating surface flux densities and diagnostic parameters under wet and dry regimes.**

This paper recognized the paucity of data and therefore anticipated that a research interest in surface climate or surface flux simulation using this LSS may require the following two components (see also Figure 2.6): (1) routine weather observations with soil moisture, ideally from WMO standard ground stations but may also incorporate satellite/reanalysis data; (2) some metadata of soils and vegetation. However, no such applicable scheme has been evaluated over Ireland, thus, the question remained as to how a LSS might perform across Irish landscapes with different soil characteristics, using limited available observations. To this end, a model performance evaluation at two test sites is provided in this Chapter.

Abstract

Knowledge of soil-vegetation-atmosphere energy exchange processes is essential for examining the response of agriculture to changes in climate in both the short and long term. However, there are relatively few sites where all the flux measurements necessary for evaluating these responses are available; where they exist, data are often incomplete and/or of limited duration. At the same time, there is often an extensive observation network available that has gathered key meteorological data (sunshine, wind, rainfall, etc.) over decades. Simulating the terms of the surface energy balance (SEB) using available meteorological, soil and vegetation data can improve our understanding of how agricultural systems respond to climate and how this response will vary spatially. Here, we employ a physically-based 'LSS' scheme to simulate the SEB fluxes over a mid-latitude, maritime temperate environment using routine weather observations. The latent heat flux is a critical SEB term as it incorporates the response of the plant to environmental conditions including available energy and soil water. This response is represented in modelling schemes through surface resistance (r_s), which is usually expressed as a function of near-surface water vapour alone. In this study, we simulate the SEB over two grassland sites, where eddy flux observations are available, representing imperfectly- and poorly- drained soils. We employ three different formulations of r_s , representing varying degrees of sophistication, to estimate the surface fluxes. Due to differences in soil moisture characteristics between the sites, we ultimately focused our attention on an r_s formulation that accounted for soil water retention capacity, based on the Jarvis conductance model; the results at both hourly and daily intervals are in good agreement, with *RMSE* values of $\approx 40 \text{ W m}^{-2}$ for sensible and latent heat fluxes at both sites. The findings show the potential value of using routine weather observations to generate the SEB where flux observations are not available and the importance of soil

properties in estimating surface fluxes. These findings could contribute to the assessment of past and future climate change on grassland ecosystems.

3.1 Introduction

Information on the exchange of heat and moisture at the Earth's surface is needed to evaluate the performance of climate models in simulating land-atmosphere interactions (e.g. Knist et al., 2017) and for applications in a number of areas, such as agricultural productivity, soil moisture and hydrology, boundary-layer development, etc. (de Bruin et al., 1993; van den Hurk et al., 2000; Chen and Dudhia, 2001; Jung et al., 2010; Lathuilliere et al., 2012; van de Boer et al., 2013; van de Boer et al., 2014b). Typically, these exchanges are expressed in terms of the surface energy balance (SEB) (Section 2.2) which stipulates that net radiation (Q_N) is expended as sensible heat flux by conduction with the soil (Q_G) and as sensible (Q_H) and latent (Q_E) heat fluxes by turbulence with the overlying atmosphere. However, measurements of these flux densities are not routine practice, partly due to the complexity of turbulence measurement and the relative cost of instrumentation (Haymann et al., 2019). To overcome this challenge, past and recent studies have developed physically-based schemes to simulate these exchanges based on routine meteorological observations (de Bruin and Holtslag, 1982; Holtslag and van Ulden, 1983; Holtslag and de Bruin, 1988; Viterbo and Beljaars, 1995; Chen et al., 1996; Beljaars and Bosveld, 1997; Mohan and Siddiqui, 1998; de Rooy and Holtslag, 1999; van de Boer et al., 2014a; Lu et al., 2014). Although the choice of scheme is dependent on the availability of input meteorological parameters, the analytic context is usually based on the Monin-Obukhov Similarity Theory (MOST) (Section 2.2.1), which uses vertical profiles of air temperature, humidity and wind to simulate the fluxes of

heat, vapour and momentum, respectively, within the atmospheric surface layer. However, issues remain with these schemes. For example, Chen et al. (1997) found large discrepancies between schemes that have been partly attributed to the dependence on empirical constants derived from site specific data.

de Rooy and Holtslag (1999) proposed and evaluated a scheme for estimating SEB fluxes using a minimal number of input parameters derived from single-level routine weather observations. The methodology was developed based on observations made over short grass in Cabauw, the Netherlands, and has not been evaluated elsewhere. More recently, van de Boer et al. (2014a) proposed a modified version of this scheme which was evaluated at two locations over different land cover types. This modified scheme accounts for the dependency of each flux on air, rather than surface, temperature as in de Rooy and Holtslag (1999). In addition, it employs a modified formulation for surface resistance (r_s) a key parameter in the estimation of Q_E as it accounts for soil moisture content and the transfer of soil water to the atmosphere by evapotranspiration.

There are different methods of parameterizing r_s (Kim and Verma, 1991; Jacobs, 1994) but one of the most widely used is that of Jarvis (Jarvis, 1976), which incorporates environmental controls, including atmospheric (radiation, temperature, vapour pressure deficit, CO₂ concentration), vegetation (Leaf Area Index) and soil (soil water) factors (e.g. Stewart, 1988; Beljaars and Bosveld, 1997; Niyogi and Raman, 1997; de Rooy and Holtslag, 1999; van de Boer et al., 2014a). Where it is assumed that there is no moisture stress, the dependence of r_s on soil water content has either been excluded (van de Boer et al., 2014a) or assumed to be negligible (de Rooy and Holtslag, 1999). However, under conditions of increasing soil moisture stress, water availability acts to regulate r_s (Russell, 1980; Sherratt and Wheeler, 1984) and

consequently plays a prominent role in modulating heat and moisture fluxes (Sherratt and Wheeler, 1984; Betts and Ball, 1995; 1998; Senevirante et al., 2010). Increased r_s due to limited water availability affects evapotranspiration and is a major factor controlling the productivity of terrestrial ecosystems (Ciais et al., 2005; De Boeck et al., 2011; Reichstein et al., 2007; Teuling et al., 2006; Zhang et al., 2012). The parameterisation of r_s has also been identified as playing a significant role in contributing to model uncertainties in estimating Q_E and gross primary production (GPP) in land surface models (Li et al., 2016).

In this chapter, the influence of available soil moisture on the simulation of energy fluxes using the de Rooy and Holtslag (1999) scheme is examined. Two grassland sites in Ireland that have the same precipitation regime but are distinguished by their soil characteristics and are defined as imperfectly- and poorly- drained soils are identified. The primary objectives are to; (1) examine whether the de Rooy and Holtslag (1999) scheme is transferrable to Irish sites; (2) evaluate if meteorological data from one location can be employed to estimate the measured surface fluxes at a nearby location, and; (3) evaluate the response of surface fluxes to three different parameterizations of surface resistance (r_s).

The study seeks to extend the value of flux estimates to places where such observations are not available and contribute to the improvement and applicability of land surface schemes over grassland ecosystems.

3.2. Study area

3.2.1 Background Climate

The climate of Ireland is dominated by westerly airflow off the North Atlantic and consequently exhibits a maritime temperate climate (Peel et al., 2007). Based on the long

term averages over the period from 1981 to 2010, Ireland typically experiences cool summers with daily maximum ranging from 18 to 20 °C and mild winters (8 °C); minimum temperatures fall below 0 °C on approximately 40 (10) days per year at inland (coastal) areas. Annual average rainfall is just over 1200 mm, which is distributed nearly evenly throughout the year. The highest rainfall is typically recorded in upland regions on the west coast. Rainfall amounts decline moving eastwards, associated with airflow interactions with topography. However, topographic variations across the island are relatively small – the average elevation is 118 m a.s.l. and the highest peak is just over 1000 m a.s.l. A summary description of the climatology of the region is reported in Walsh (2012).

The climate in Ireland provides conditions suitable for the year-round grass growth, particularly along coastal margins in the south of the country which records a median grass growing season length of 330 days (Keane and Collins, 2004). Consequently, grassland land-cover is the most important crop and accounts for more than 90% of the land under agricultural production (McEniry et al., 2013) and 56% of the total land area (EUROSTAT, 2015). Due to the year-round precipitation, excessive soil moisture is generally more problematic for grass production than water deficits (McDonnell et al., 2018), particularly on poorly drained soils. However, soil moisture deficits are periodically experienced during the summer months, typically in the east and south east of the country (Dwyer and Walsh, 2012), associated with the location of well drained soils (Figure 3.1). In terms of soil characteristics, the General Soil Map of Ireland classifies the south-east as mostly free-draining sandy soils, with limestone-rich soils in the south and midlands, and acid and peat soils on mountains, hills and the western seaboard (Gardiner and Radford, 1980). More detailed soil properties

combining previous and existing soil survey information for Ireland is available from Creamer et al. (2014).

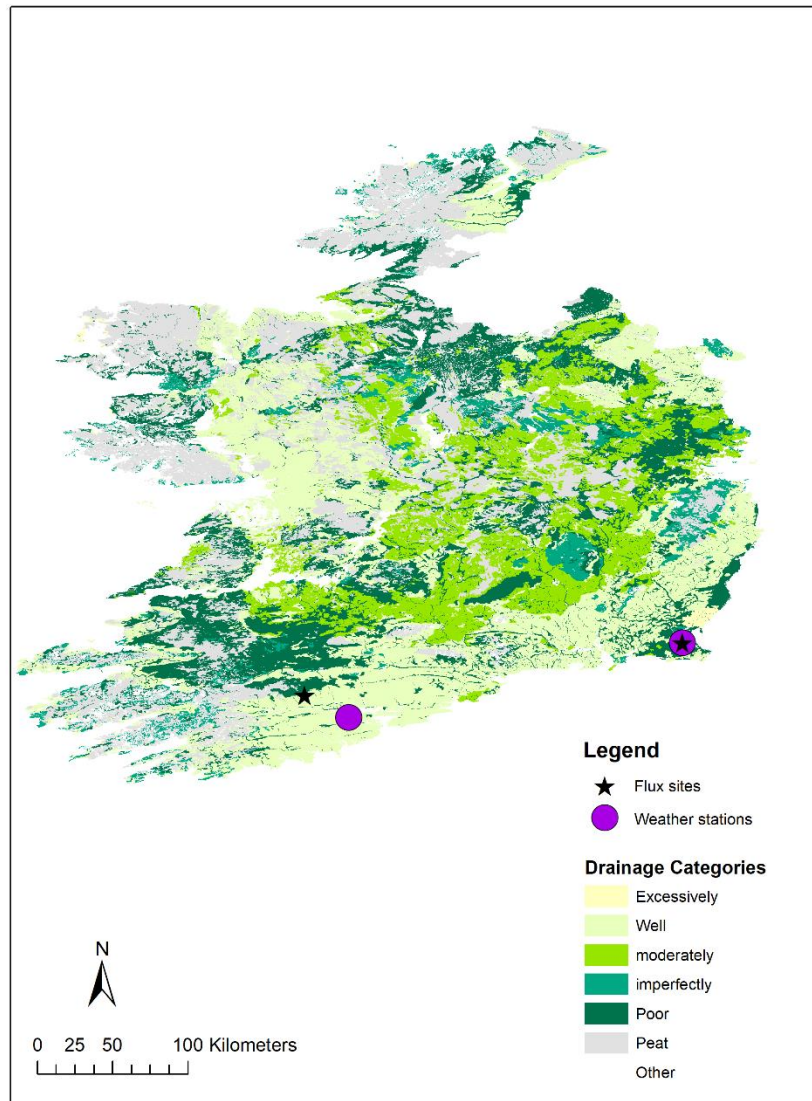


Figure 3.1. Map of Soil drainage classes for Ireland (Irish Soil Information System by Teagasc for EPA, Creamer et al., 2014), showing the locations of test sites.

3.2.2 Site descriptions

Two sites are employed in this study representing imperfectly drained (Johnstown Castle, Co. Wexford) and poorly drained (Dripsey, Co. Cork) soil characteristics; Table 3.1 provides

summary information on each site and Figure 3.1 shows the site locations. Both sites have available eddy covariance (EC) flux tower measurements.

Station	Lat/Long (°)	Elevation (m)	Soil description	Moisture properties (θ_{FC} , θ_{ST} , θ_{WP})	Drainage class	Time period
Johnstown Castle	52.29°N, 6.49°W	58	A combination of gley, brown earths and free draining fine siliceous loam soils.	32% 59% 17%	Imperfect	2013
Dripsey	51.98°N, 8.75°W	186	Gley water-logged soils.	32% 45% 12%	Poor	2010

Table 3.1. Descriptions of grassland eddy covariance flux and synoptic stations used in this study. Meteorological data from Cork Airport (51.84°N, 8.48°W) at an elevation of 155 m were used for Dripsey. Johnstown Castle has a co-located weather station. The soil moisture properties are field capacity (θ_{FC}), saturation level (θ_{ST}) and wilting point (θ_{WP}), in order.

Details on the vegetation and soil characteristics associated with the flux tower footprints are as follows:

- i) Johnstown Castle: Two main types of soil (Gleys and Brown Earths), have been reported within the flux site footprint (Peichl et al., 2012). The soil within the flux footprint (< 150 m) is moderately to imperfectly drained Gley (FAO classification: Gleyic Cambisol). The soils transition to moderately or well drained Brown Earths (Cambisol) at the outer

edge of the flux footprint. The soil class in this area therefore varies from moderately to imperfectly drained, and the land cover is grass.

- ii) Dripsey: The EC footprint is over grass cover on a soil type that impedes water movement and can become waterlogged (Kiely et al., 2018) and is classed as a poorly drained Gley soil.

More detailed descriptions on the soil properties, climatology and EC footprints at Dripsey and Johnstown Castle are reported in Kiely et al. (2018) and Peichl et al. (2012), respectively.

Detailed information on vegetation height and leaf area index (LAI) are not available for the periods corresponding with flux measurements made at Dripsey, but Kiely et al. (2018) reported LAI values ranging from $\approx 2 \text{ m}^2 \text{ m}^{-2}$ in winter to $\approx 6 \text{ m}^2 \text{ m}^{-2}$ in summer. At Johnstown Castle, LAI is estimated from measurements of grass dry matter yield concurrent with the EC observations and an allometric relationship established with leaf area index meter readings. Modelled LAI values range between 0.1 (winter) and $6.8 \text{ m}^2 \text{ m}^{-2}$ (summer) for this site, with an average LAI of $2.2 \text{ m}^2 \text{ m}^{-2}$.

3.3 Data

The study employs available routine weather observations to parameterize surface fluxes of heat and moisture over the two grassland sites described above. In the following sections, the observed flux data available for each site is discussed followed by a description of the available meteorological and soil water data. A summary of the EC flux and meteorological parameters used as input to, and evaluation of, the scheme employed is presented in Table 3.2.

3.3.1 Flux measurements

Sensible and Latent Heat fluxes

Half-hourly EC flux measurements of Q_H and Q_E are available from the European Fluxes Database Cluster (<http://www.europe-fluxdata.eu/>) (Papale et al., 2006) for Dripsey (Kiely et al., 2018) for the year 2010. In order to avoid any potential bias, we only employed non gap-filled data (Level 2 data). Half-hourly EC flux measurements of Q_H and Q_E were also obtained for Johnstown Castle for the year 2013 (Unpublished results). The instrumentation at both sites consists of an open-path infra-red gas analyser (IRGA) for measuring H₂O density and CO₂ concentration, in combination with a 3D sonic anemometer. The EC data were logged at 10 Hz and averaged over 30-minutes intervals (see Table 3.2 for a list of instruments at each site).

Data processing procedures at both sites were similar and are documented elsewhere: Sottocornola and Kiely (2010a, 2010b) for Dripsey; and Ní Choncubhair et al. (2017) for Johnstown Castle. These procedures include spike removal (Vickers and Mahrt, 1997), the Webb-Pearman-Leuning correction (Webb et al., 1980; Moncrieff et al., 1997a), sonic anemometer tilt correction using the double rotation method (Kaimal and Finnigan, 1994) and spectral attenuation corrections after Moncrieff et al. (1997b). Some data filtering procedures, which differ from the above approaches, were applied to Dripsey and are described in Kiely et al. (2018). Here, poor quality data based on quality control flags (QC = 2) were removed and flux observations recorded when precipitation exceeded 1 mm over an hour window were removed as these are likely to generate errors in Q_E measurements using open-path sensors (e.g. Ma et al., 2015).

Variables	Usage		Instrumentation
	Forcing	Validation	
Q_N		x	NR-Lite (Johnstown Castle) and CNR1 (Dripsey) (Kipp & Zonen, Delft, The Netherlands)
$Q_{S\downarrow}$	x		
T_a	x		
u	x		
P	x		
RH	x		
Precipitation			
Sunshine hours			
Q_H, Q_E		x	IRGA gas analyzers, LI-7500 (LI-COR, Lincoln, NE) at 6 m for Dripsey and; 2.28 m (1 st Jan. – 26 th Feb.), 2.72 m (26 th Feb. – 23 rd Oct.), 2.85 m (23 rd Oct. – 31 st Dec.) for Johnstown Castle.
θ	x		CS616 (Johnstown Castle) and CS615 (Dripsey) (Campbell Scientific, Shepherd, UK)

Table 3.2. Descriptions of meteorology and eddy-covariance parameters used as forcings and for validation respectively.

A statistical examination of the processed data for all sites showed typical ranges of -100 – 400 W m⁻² for Q_H and Q_E ; individual observations outside of these ranges were excluded from further analysis (following Ma et al., 2015).

Following these pre-processing steps, a significant percent (original plus filtered) of flux data at each site was classed as missing: 24 % and 32 % of Q_H and Q_E , respectively at Johnstown Castle and 28 % and 31 % of Q_H and Q_E at Dripsey. While the proportion of data gaps from Johnstown Castle mainly arose from the quality control procedures, the higher proportion of missing data from Dripsey was due to a combination of both the number of missing values in

the original data and the quality control processes, outlined above. After the filtering processes, the proportion of nighttime data slightly exceeded the daytime data at both sites. At Johnstown Castle, approximately 51 % (2,941 hours) and 49 % (2,939 hours) of Q_E data remained for nighttime and daytime (08:00 – 18:00) hours, respectively. Similarly, 53 % (3,188 hours) and 47 % (2,851 hours) of data for Dripsey were available for analysis.

Net Radiation

Half-hourly measurements of Q_N from Dripsey for 2010 are available from the European Fluxes Database Cluster (Papale et al., 2006). For Johnstown Castle, Q_N measurements for 2013 are available from previously unpublished research. Hourly values of Q_N in the range -100 and 700 W m⁻² were selected for the subsequent analysis (following Shi and Liang, 2014).

The energy budget closure is an efficient approach to evaluate the consistency of scalar flux densities measured by EC systems (Twine et al., 2000). The approach relates available energy ($Q_N - Q_G$) to turbulent fluxes ($Q_H + Q_E$) in order to determine the magnitude of non-closure of measured fluxes by EC systems. EC measurements are known to underestimate the turbulent fluxes (Q_H and Q_E) and overestimate Q_N resulting in non-closure of the energy balance (Wilson et al., 2002; Foken, 2008; Franssen et al., 2010; Stoy et al., 2013). Other potential reasons for non-closure are discussed extensively in the literature and include; the failure to measure heat storage terms as part of measurement programmes (e.g. Heusinkveld et al., 2004); large-scale turbulent circulations over heterogeneous landscapes that are not captured by EC methods (Mauder et al., 2007; Stoy et al., 2013); the assumption of no advection and; inaccurate Q_N measurements (e.g. Foken, 2008). Over the sites available for the present study, the hourly energy budget closure (ignoring the Q_G and $Q_{\Delta S}$ terms) is approximately 69 % at Johnstown Castle and 60 % at Dripsey (Figure 3.2). These closure values

are comparable with previously reported values, which lie within 53 – 99 % (e.g. Wilson et al., 2002).

3.3.2 Meteorological data

On-site hourly meteorological observations for the same periods of EC measurements are available for Johnstown Castle but at Dripsey these data are only available at Cork Airport (155 m a.s.l), which is approximately 25 km from the site.

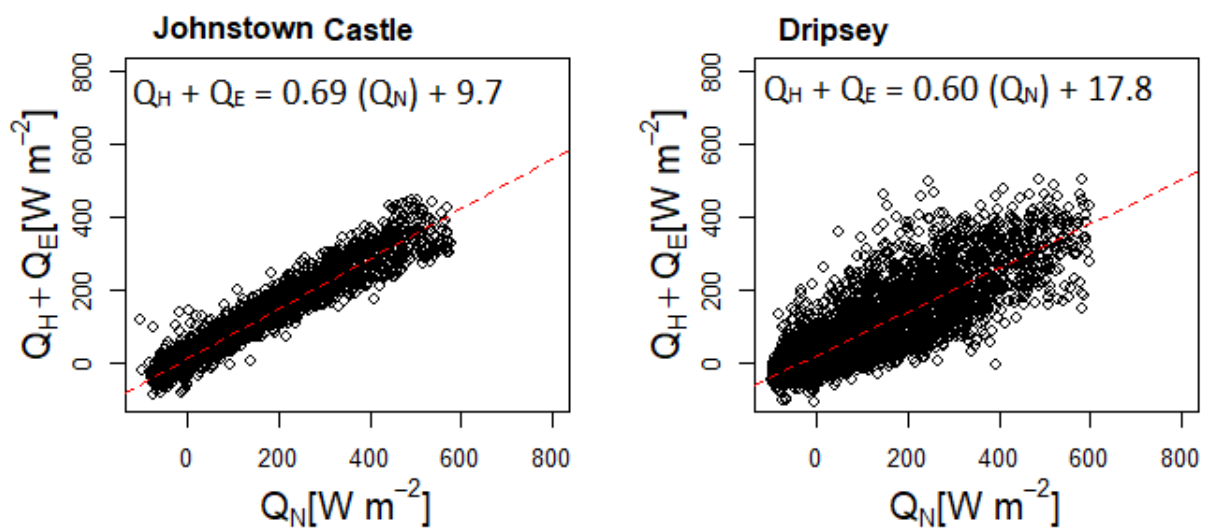


Figure 3.2. The hourly Surface energy balance closure at Johnstown Castle and Dripsey sites.

Both meteorological stations conform to World Meteorological Organisation (WMO) guidelines and report on global solar radiation ($Q_{s\downarrow}$, $W m^{-2}$) or sun duration (hours), air temperature ($^{\circ}C$), relative humidity (%), pressure (kPa), wind speed ($m s^{-1}$) and precipitation (mm). As cloud amount (oktas) was only available from Cork Airport, it was excluded from the subsequent analysis; this value was set ≈ 0 in the calculation of $Q_{L\downarrow}$. Global solar radiation was not available from Cork Airport, therefore hourly $Q_{s\downarrow}$ data was estimated for this site based on observations of sunshine duration following Allen et al. (1998). The hourly meteorological observations correspond with the periods for which the flux data are available at the two

sites. The meteorological conditions during the study periods at the selected sites are presented in Figures (3.3 – 3.4).

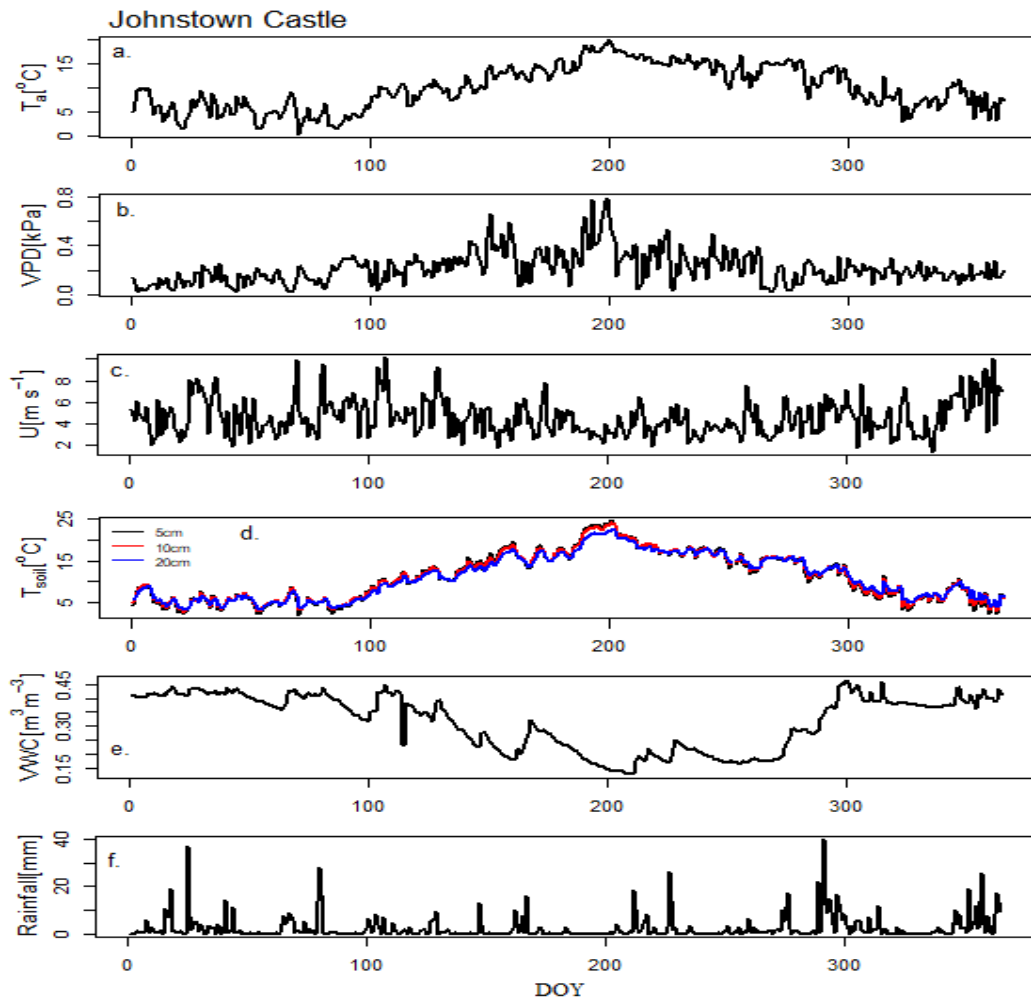


Figure 3.3. Temporal evolution of in situ meteorological forcing data for Johnstown Castle. [top-bottom] air temperature, vapour pressure deficit, wind speed, soil temperature, volumetric water content and rainfall.

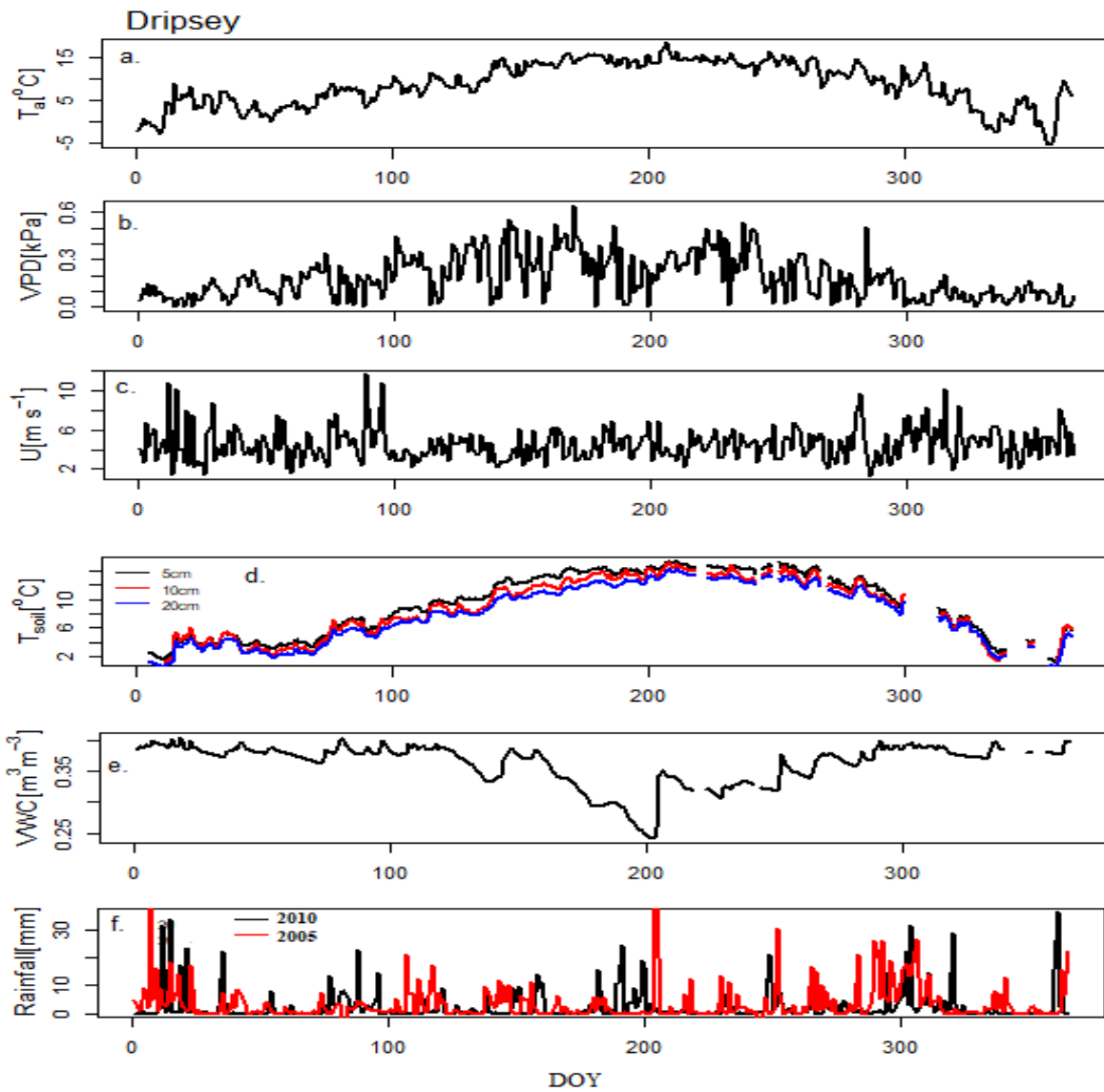


Figure 3.4. Temporal evolution of in situ meteorological forcing data for Dripsey flux sites. Meteorological data except soil water (VWC) are available from Cork-Airport. [top-bottom] air temperature, vapour pressure deficit, wind speed, soil temperature, volumetric water content for 2005, and rainfall.

3.3.3. Soil water data

Soil water content, measured as the volumetric water content (θ , $\text{m}^3 \text{m}^{-3}$) in the upper 20 cm of the soil, was measured at both sites at half-hourly intervals using CS615/CS616 time domain reflectometers (Table 3.2).

At Johnstown Castle, these measurements are contemporaneous with the available EC flux measurements. At Dripsey, measurements are only available for 2004 and 2005, which coincides with periods when flux measurements are either not available or gap-filled (European Fluxes Database Cluster Level 3 and 4 data). While the general meteorological conditions at Dripsey during 2004 and 2005 were wetter than those experienced in 2010 (1174 mm; 1183 mm and 974 mm, respectively), the cumulative precipitation during 2005 was very similar in profile to 2010, up to October, after which the soils would have been close to or at field capacity (Figure 3.4 e-f).

3.4 Methods

3.4.1 Model set up

The scheme to estimate the fluxes of heat, moisture and momentum from limited routine weather data was adapted from de Rooy and Holtslag (1999). The scheme was originally developed over a grassland ecosystem using extensive and well-documented datasets from Cabauw, the Netherlands, and covering a variety of weather conditions. The scheme computes the turbulent fluxes (Q_H and Q_E) through a set of sequential calculations (Figure 3.5). The required inputs are: air temperature T_a (K) at observation height z_a (2 m), relative humidity RH (%), wind speed u (m s^{-1}) at 10 m, mean sea level pressure P (kPa), global solar radiation $Q_{s\downarrow}$ (W m^{-2}) and cloud amount N (oktas).

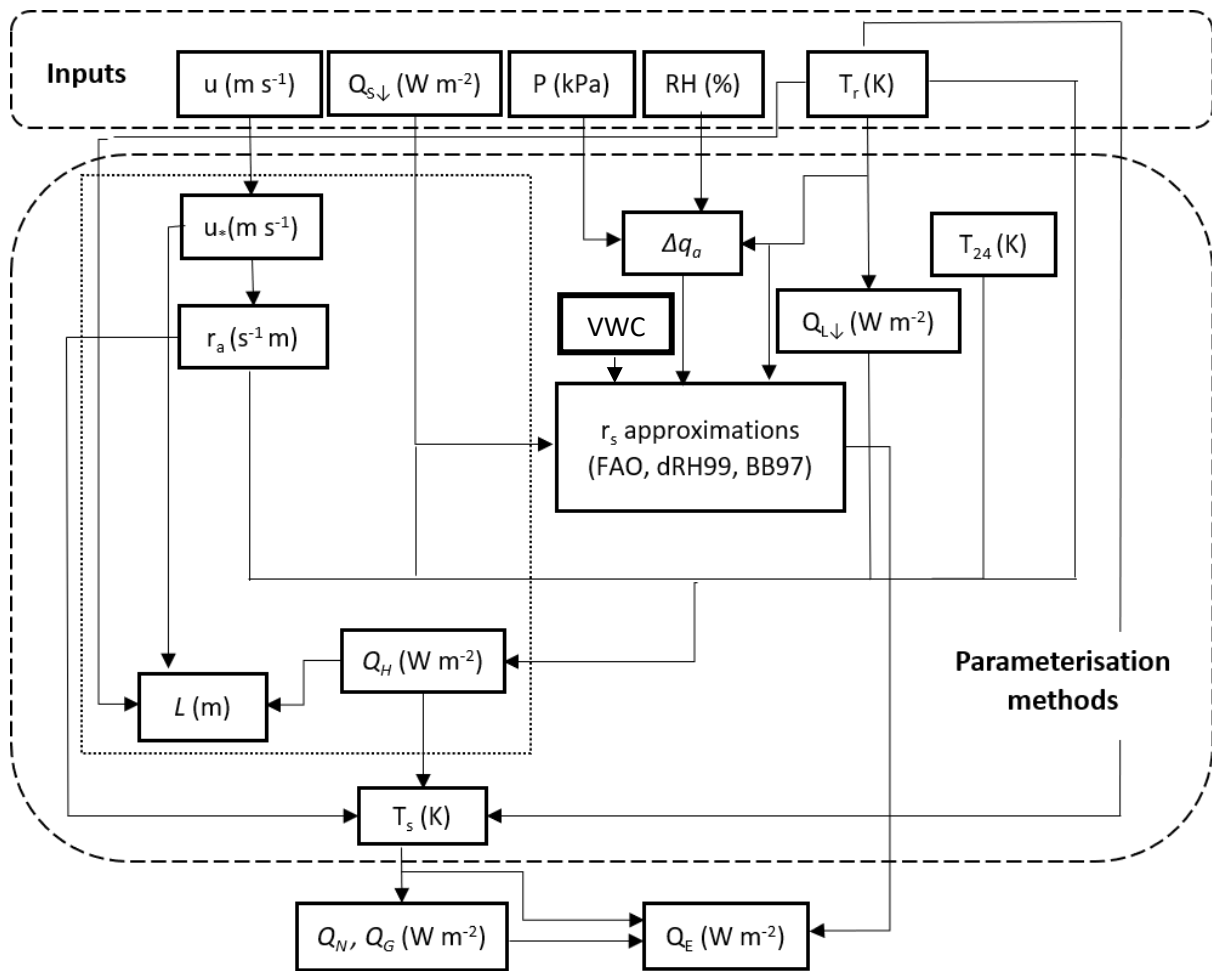


Figure 3.5. Schematic diagram of surface energy balance estimates. The dotted line denotes the iteration process using MOST, while the dashed lines show the input and output variables and parameterization workflow.

In the initial step, the variables that can be obtained directly from the inputs, such as the 24-h mean of 2-m temperature, T_{24} (K), vapour pressure, e (kPa), specific humidity deficit, Δq_a (g kg^{-1}), psychrometric constant, γ (kPa K^{-1}), and the slope of the saturated vapour pressure curve, s (kPa K^{-1}), are estimated. An iterative procedure then estimates the following parameters: friction velocity, u_* (m s^{-1}), aerodynamic resistance, r_a ($\text{s}^{-1} \text{m}$), Q_H (W m^{-2}), and subsequently temperature scale θ_* (K) and Obukhov length L (m), using flux profile relations (Paulson, 1970). The profile method adopts the MOST to describe the profile relationships of important scaling quantities, u_* , θ_* and L ; r_a is also expressed in terms of a flux-profile

relationship. In this study, the empirical stability correction functions used in the profile method are based on those derived for unstable surface layer by Paulson (1970) and Dyer (1974), which relate the fluxes of heat and momentum to their non-dimensional vertical gradients.

The friction velocity, u_* , aerodynamic resistance r_a and sensible heat, Q_H are calculated as follows:

$$u_* = \frac{uk}{\left[\ln\left(\frac{z_a}{z_{om}}\right) - \psi_m\left(\frac{z_a}{L}\right) + \psi_m\left(\frac{z_{om}}{L}\right) \right]}, \quad (3.1)$$

$$r_a = \frac{1}{ku_*} \left[\ln\left(\frac{z_a}{z_{oH}}\right) - \psi_H\left(\frac{z_a}{L}\right) + \psi_H\left(\frac{z_{oH}}{L}\right) \right], \quad (3.2)$$

and

$$Q_H = \frac{(X-Y)(A-B)+C}{X+Z(X-Y)}, \quad (3.3)$$

where

$$X = (s + \gamma) \left[s + \gamma \left(1 + \frac{r_s}{r_a} \right) \right], \quad (3.3a)$$

$$Y = s(s + \gamma), \quad (3.3b)$$

$$A = (1 - \alpha)Q_{s\downarrow} + Q_{L\downarrow} + 3\varepsilon\sigma T_a^4 + A_g T_{24}, \quad (3.3c)$$

$$B = (4\varepsilon\sigma T_a^3 + A_g)(T_a + z_a\Gamma_d), \quad (3.3d)$$

$$C = -(s + \gamma), \quad (3.3e)$$

$$Z = (4\varepsilon\sigma T_a^3 + A_g)(r_a / \rho c_p), \quad (3.3f)$$

where, ψ_H and ψ_m are the dimensionless stability correction terms for heat and momentum respectively (Beljaars and Holtslag, 1991). The specified dimensionless constants include the surface albedo, $\alpha = 0.23$, and surface emissivity, $\varepsilon = 0.94$. We employed the following empirical values: $A_g = 9.0 \text{ W m}^{-2} \text{ K}^{-1}$, Stefan Boltzmann's constant (σ) = $5.67 \times 10^{-8} \text{ W m}^{-2} \text{ K}^{-1}$, observation height $z_a = 2 \text{ m}$, dry adiabatic lapse rate $\Gamma_d = 0.01 \text{ K m}^{-1}$, air density $\rho = 1.225 \text{ kg m}^{-3}$, specific heat capacity of air $c_p = 1005 \text{ J kg}^{-1} \text{ K}^{-1}$, von Kármán constant $k = 0.41$, surface roughness length for heat $z_{oH} = 0.001 \text{ m}$ and momentum $z_{om} = 0.01 \text{ m}$ (Table 3.3). The incoming longwave radiation $Q_{L\downarrow}$ (W m^{-2}) is estimated using the formulations described in Section 2.2.

Surface parameter	Value
Emissivity, ε	0.94
Albedo, α	0.23
Soil heat transfer coefficient, A_g	$9 \text{ W m}^{-2} \text{ K}^{-1}$
Roughness length for heat, z_{oH}	0.001 m
Roughness length for momentum, z_{om}	0.01 m
Surface resistance, r_s	different formulations

Table 3.3. Surface input parameters and corresponding values used at the selected stations

Initially, the iterative procedure makes a first guess of u_* , r_a and subsequently Q_H , assuming neutral stability conditions ($1/L = 0$). Using this initial estimate of Q_H , the parameters θ_* and L are calculated (see Section 2.2.3). This procedure is repeated until the Q_H values from one iteration to the next change by $\leq 10^{-5} \text{ W m}^{-2}$, achieved through the stability correction terms and based on the level of agreement between the estimated and measured values. The estimated Q_H (W m^{-2}) is then used to sequentially derive surface temperature T_s (K), which in turn is used to estimate Q_G (W m^{-2}) and Q_N (W m^{-2}), as follows:

$$T_s = T_a + \frac{Q_H r_a}{\rho c_p} + z_a \Gamma_d, \quad (3.4)$$

$$Q_G = A_g (T_s - T_{24}), \quad (3.5)$$

$$Q_N = [(1 - \alpha)Q_{s\downarrow} + (\varepsilon_a - 1)(\varepsilon_a \sigma T_a^4)] - [4\varepsilon \sigma T_a^3 (T_s - T_a)], \quad (3.6)$$

where ε_a is the apparent atmospheric emissivity (see Section 2.2).

Finally, Q_E (W m^{-2}) is computed using the Penman-Monteith formulation (Monteith, 1981), as follows,

$$Q_E = \frac{r_a s(Q_N - Q_G) + \rho c_p (e_s - e_a)}{(s + \gamma)r_a + \gamma r_s} \quad (3.7)$$

The turbulent fluxes (Q_H and Q_E) both rely on surface resistance (r_s) which represents the role of environmental factors, such as plant growth and soil moisture availability in regulating the surface-air exchange of water vapour.

3.4.2 Surface resistance

There are several formulations in the literature for estimating appropriate values for r_s for different land-cover and environmental conditions. The simplest of these is the FAO value which is constant and based on a grass reference crop height of 0.12 m (Allen et al., 1998), that is

$$r_s = 70 \text{ s m}^{-1} \quad (3.8)$$

A more physically-based formulation was proposed by de Rooy and Holtslag (1999) based on a statistical relationship between r_s and the vapour density deficit (Δq_a) in the overlying air,

$$r_s = a + b \frac{e_s - e_a}{p} \frac{R_d}{R_v} = 10 \Delta q_a, \quad (3.9)$$

where, a (0 s m^{-1}) and b ($10 \text{ s kg m}^{-1} \text{ g}^{-1}$) are empirical constants and p is pressure such that $\frac{e_s - e_a}{p}$ is dimensionless. The remaining terms are constants, R_d is specific gas constant for dry air ($287 \text{ J kg}^{-1} \text{ K}^{-1}$) and R_v is specific gas constant for water vapour ($462 \text{ J kg}^{-1} \text{ K}^{-1}$).

Jarvis (1976) proposed a formulation for stomatal conductance, the inverse of surface resistance, that accounts for plant growth through the inclusion of environmental factors and a minimum surface resistance ($r_{s,min}$), specific to plant type and leaf area index (LAI),

$$r_s = \frac{r_{s,min}}{LAI} F_S F_{\Delta q} F_T F_M, \quad (3.10)$$

Where $r_{s,min}$ represents the optimum conditions for evapotranspiration as a function of solar radiation (F_S), water vapour ($F_{\Delta q}$), air temperature (F_T) and soil moisture (F_M) (Jarvis, 1976; Stewart, 1988). For short grass, the value of $r_{s,min}$ is 110 s m^{-1} . Although the LAI of short grass changes seasonally (van den Hurk et al., 2000), a fixed value of $2 \text{ m}^2 \text{ m}^{-2}$ is commonly used (e.g. Beljaars and Bosveld, 1997; de Rooy and Holtslag, 1999; van den Hurk et al., 2000; 2003; van de Boer et al., 2014a).

Beljaars and Bosveld (1997) modified the Jarvis-Stewart approximation by removing the air temperature term (F_T), due to its correlation with radiation, and included a scaling factor (f_r), to adjust r_s to a particular surface (van de Boer et al., 2014a), as follows,

$$r_s = f_r \frac{r_{s,min}}{LAI} F_S^{-1} F_{\Delta q}^{-1} F_M^{-1} \quad (\text{Beljaars and Bosveld, 1997}) \quad (3.11)$$

Based on observations over the Cabauw grassland site which has poorly drained soils, Beljaars and Bosveld (1997) derived an optimised value for f_r of 0.47. Values for $r_{s,min}$ and LAI are as stated above.

The response function F_S to $Q_{s\downarrow}$ is described (following Beljaars and Bosveld, 1997; van de Boer et al., 2014a) as:

$$F_S = \frac{Q_{s\downarrow}(S_{rm} - S_r)}{S_{rm}Q_{s\downarrow} + S_r(S_{rm} - 2Q_{s\downarrow})}, \quad (3.11a)$$

where the empirical coefficients S_{rm} and S_r are given as 1000 W m^{-2} and 230 W m^{-2} , respectively.

The response function $F_{\Delta q}$ to atmospheric moisture deficit is calculated as,

$$F_{\Delta q} = \frac{1}{(1 + h_s \Delta q)}, \quad (3.11b)$$

where Δq is the difference between the water vapour deficit at the reference height (2 m) and surface (Chen and Dudhia, 2001). Following Beljaars and Bosveld (1997) and van de Boer et al. (2014a) we adopt a fixed value of 3 g kg^{-1} for the vapour deficit at the surface. Different values of h_s have been adopted in the literature (e.g. Stewart and Gay; 1989; Chen et al., 1996; van den Hurk et al., 2000; Chen and Dudhia, 2001, Ronda et al., 2001), however, 0.16 kg g^{-1} is employed here as it has previously been used over grassland land cover (Beljaars and Bosveld, 1997; van de Boer et al., 2014a).

F_M is a soil moisture response function and is given as,

$$F_M = 1 \quad \text{for } \theta > \theta_{FC}, \quad (3.11c)$$

$$F_M = 1 + c_{soil}(\theta - \theta_{FC}) \quad \text{for } \theta < \theta_{FC}, \quad (3.11d)$$

where θ ($\text{m}^3 \text{ m}^{-3}$) is the volumetric soil moisture in the root zone and θ_{FC} ($\text{m}^3 \text{ m}^{-3}$) is the volumetric water content at field capacity specific to soil type (Table 1). We initially employ a value of $6.3 \text{ m}^3 \text{ m}^{-3}$ for c_{soil} (following Beljaars and Bosveld, 1997); this parameter alters the

relationship (i.e. slope) between conductance and soil moisture and consequently the sensitivity of F_M to changes in soil moisture.

3.4.3 Simulating fluxes at the test sites.

To address our three primary objectives, here we evaluate the de Rooy and Holtslag (1999) scheme against the measured fluxes at the Johnstown Castle and Dripsey grassland sites. In particular, we focus on the different formulations for surface resistance (r_s) and their ability to estimate surface fluxes at i) a site that exhibits similar soil moisture properties to the Cabauw site, over which the scheme was originally developed, and ii) a site with differing soil moisture properties.

In the following section we use abbreviations to represent the different formulations used to obtain r_s :

1. FAO to identify r_s obtained using Eq. 3.8
2. dRH99 to identify r_s obtained using Eq. 3.9 and,
3. BB97 to identify r_s obtained using Eq. 3.11

The analysis is carried out for daytime only ($Q_{s\downarrow} > 10 \text{ W m}^{-2}$) when the majority of evapotranspiration takes place. At Johnstown Castle, we employ data from the nearby meteorological station and θ from the EC flux site as input to the scheme. At Dripsey, we employ data from Cork Airport, which is 25 km distant and is the closest suitable meteorological station. Due to the absence of soil moisture measurements for the period of study, we employ soil moisture data from 2005 as a surrogate to test the BB97 formulation in estimating r_s and Q_E at this site. We justify this on the basis that the cumulative precipitation during 2005, when the volumetric water content measurements are available, and 2010,

when the flux measurements were obtained, display a similar profile during the period when soil moisture is likely to be most influential (Figure 3.4). Section 3.5 presents the results of the analysis.

Beljaars and Bosveld (1997) derived values for the f_r , S_r , h_s and c_{soil} coefficients employed in BB97 based on their model fit to the measured data at Cabauw. To assess the influence of these specified values on r_s and consequently Q_E at both sites, we undertook a local sensitivity analysis, employing a one-at-a-time technique. For each coefficient value altered, the remaining values are held at their original, specified values. We initially perturbed the values of f_r , S_r , h_s and c_{soil} at Johnstown Castle, where all the required measured input variables are available. For consistency and robustness of model evaluation, we conducted a similar sensitivity analysis for the Dripsey site, employing soil moisture data from 2005. Finally, we employ the optimised values derived from the sensitivity analysis to derive estimated Q_H and Q_E at Johnstown Castle, where the default values for BB97 failed to replicate the measured fluxes; results from the sensitivity analysis are presented in Section 3.5.2

The de Rooy and Holtslag (1999) scheme is used, with different approximations of r_s , to simulate hourly radiation and turbulent fluxes at each observation site. The estimated hourly Q_N , Q_H and Q_E and daily averaged Q_H and Q_E fluxes were compared with the observed fluxes at each site using a number of statistical measures including root mean square error (*RMSE*), bias, standard deviation (*sd*) and correlation coefficient (*r*), and results are presented below.

3.5 Results

3.5.1 Evaluation of radiation and estimated surface fluxes

3.5.1.1 Net radiation

Figure 3.6 shows the relationship between estimated and measured (daytime) hourly Q_N values for both sites. The estimated (measured) Q_N values are: between -90 and 600 W m^{-2} (-100 and 635 W m^{-2}) at Johnstown Castle and; between -66 and 553 W m^{-2} (-100 and 600 W m^{-2}) at Dripsey. At Johnstown Castle, the model tended to overestimate negative values of Q_N and underestimate large positive values. At Dripsey, the underestimation of Q_N is likely attributable to its reliance on Q_{Sl} which was derived based on hourly sun duration obtained from a distant meteorological site. Overall model performance at the two sites indicates: a $RMSE = 69.7 \text{ W m}^{-2}$ ($sd = 158$ and 153 W m^{-2} for the estimated and measured values, respectively) at Johnstown Castle and; a $RMSE = 91.6 \text{ W m}^{-2}$ ($sd = 144$ and 149 W m^{-2} for the estimated and measured values) at Dripsey.

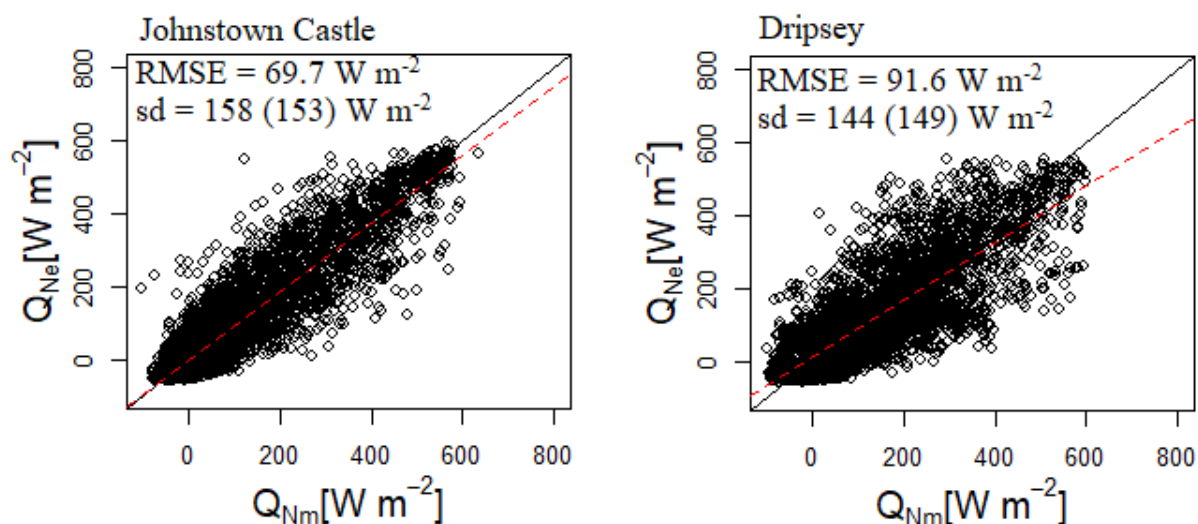


Figure 3.6. Relationship between daytime hourly measured (Q_{Nm}) and estimated (Q_{Ne}) net radiation flux over both sites.

These results are broadly comparable with other similar studies. For example, Holtslag and van Ulden (1983) derived a linear relationship between $Q_{S\downarrow}$, solar elevation and total cloud cover, in combination with other components of the surface radiation budget, to estimate Q_N under both clear and cloudy sky conditions at Cabauw and obtained a *RMSE* of 63 W m^{-2} for Q_N under all conditions.

3.5.1.2 Sensible heat fluxes

Table 3.4 shows the performance metrics for the estimated hourly Q_H for both sites using the three formulations for r_s outlined above. Of these, dRH99 was found to perform the best across all metrics and both sites, but particularly at Johnstown Castle, displaying the lowest *RMSE* and bias and highest r values. BB97 performs the poorest at Johnstown Castle, displaying the highest *RMSE* and bias compared to the other two methods. In contrast, at Dripsey, BB97 produces metrics that are very similar to dRH99.

r_s method	Dripsey			Johnstown Castle		
	<i>RMSE</i>	<i>Bias</i>	r	<i>RMSE</i>	<i>Bias</i>	r
dRH99	38.2	9.4	0.78	36.1	8.3	0.83
BB97	39.8	11.9	0.77	51.8	23.4	0.83
FAO	44.7	16.7	0.77	43.8	15.9	0.82

Table 3.4. Performance assessment of daytime ($Q_{S\downarrow} > 10 \text{ W m}^{-2}$) Q_H based on different r_s , over both stations. The italicized values show the r_s method that give the best agreement between estimated and measured Q_H , *RMSE and Bias* (W m^{-2})

Figures 3.7 and 3.8 display the scatterplots of measured and estimated hourly Q_H , using the three formulations of r_s , at Johnstown Castle and Dripsey, respectively; they also show the

daily cycle of Q_H , during daylight hours, averaged for the month of July for the respective year of observation. At Johnstown Castle, BB97 significantly overestimates Q_H (which is evident in the July graph) while both dRH99 and FAO match the measured values more closely (Figure 3.7). In general, large positive hourly values of Q_H are underestimated at Dripsey but daytime values during July are very close (Figure 3.8). Of the three r_s methods, dRH99, at both sites, and BB97, at Dripsey, produced results that are most comparable with Holtslag and van Ulden (1983) who employed a modified Priestly-Taylor approach to estimate Q_H and Q_E above a short-grass covered surface at Cabauw; they reported a $RMSE$ of 34 W m^{-2} between measured and estimated Q_H .

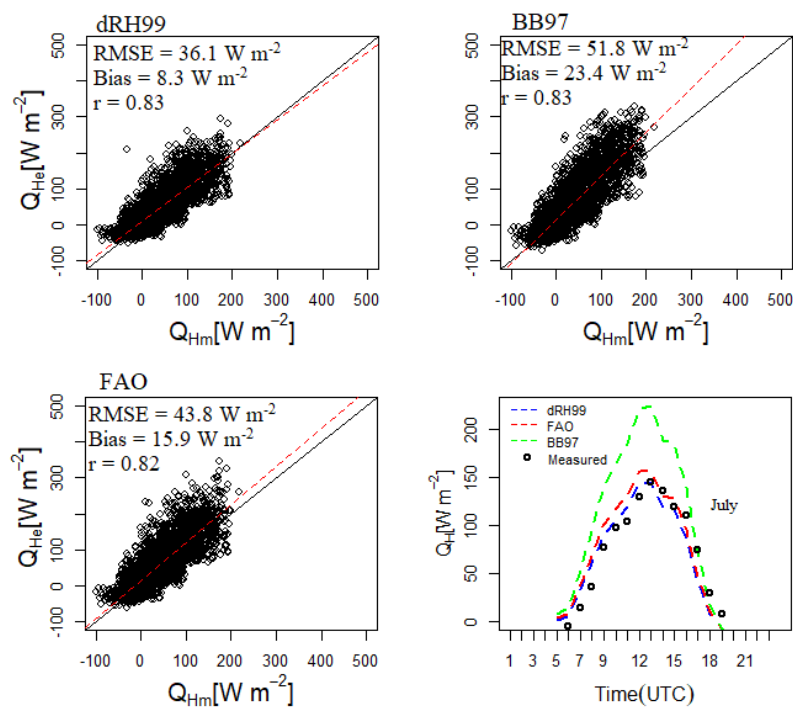


Figure 3.7. Relationship between daytime hourly measured (Q_{Hm}) and estimated (Q_{He}) sensible heat flux applying the Scheme with different r_s models over Johnstown Castle. The line plot is the diurnal cycle of Q_H , averaged for July, 2013.

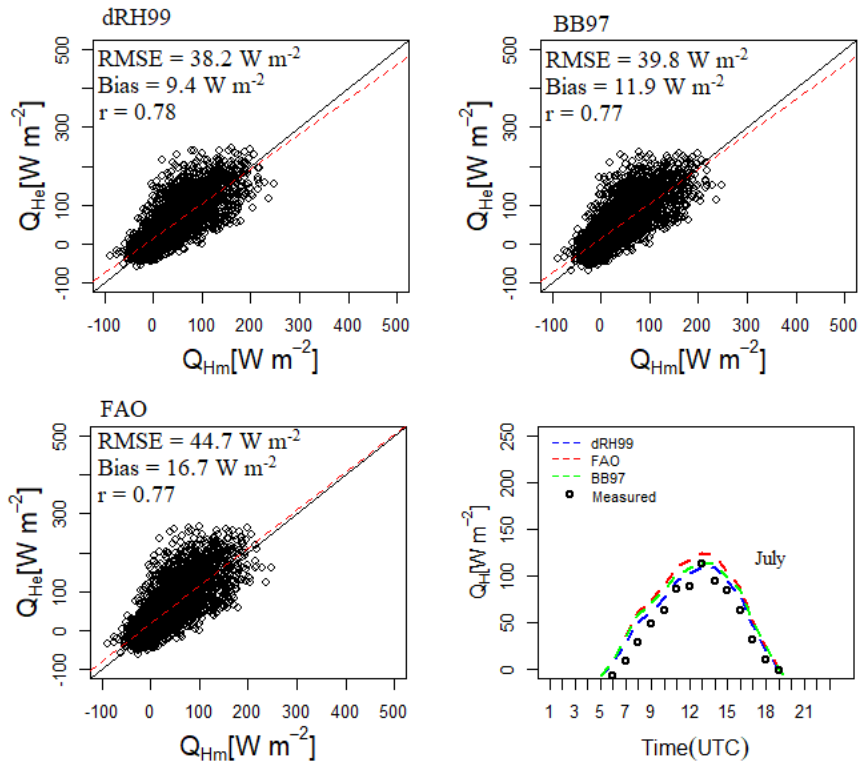


Figure 3.8. Relationship between daytime hourly measured (Q_{Hm}) and estimated (Q_{He}) sensible heat flux applying the Scheme with different r_s models over Dripsey. The line plot is the diurnal cycle of Q_H , averaged for July, 2010.

3.5.1.3 Latent heat fluxes

Table 3.5 shows the statistics for the estimated and measured Q_E values for both sites. Although the FAO method employs a constant r_s value, it produced the best fit at Johnstown Castle ($RMSE = 34.9 \text{ W m}^{-2}$, $bias = -6.7 \text{ W m}^{-2}$ and $r = 0.85$) (Table 3.5), followed by dRH99 ($RMSE = 43.1 \text{ W m}^{-2}$, $bias = 11.7 \text{ W m}^{-2}$ and $r = 0.84$). Employing the default Beljaars and Bosveld (1997) values, BB97 performed very poorly at this site ($RMSE = 56.1 \text{ W m}^{-2}$, $bias = -29.9 \text{ W m}^{-2}$ and $r = 0.62$). At Dripsey, FAO produced the best fit in terms of RMSE and r value ($RMSE = 38.9 \text{ W m}^{-2}$ and $r = 0.84$), but displayed the highest bias ($bias = -11.8 \text{ W m}^{-2}$) of the three methods. dRH99 performed the poorest at this site, with the highest RMSE and lowest r value ($RMSE = 48.7 \text{ W m}^{-2}$ and $r = 0.78$) relative to the other two methods. BB97 resulted

in the lowest bias value of all methods ($bias = -2.1 \text{ W m}^{-2}$), and an RMSE and r value comparable to FAO ($RMSE = 41.2 \text{ W m}^{-2}$ and $r = 0.83$).

r_s method	Dripsey			Johnstown Castle		
	RMSE	Bias	r	RMSE	Bias	r
dRH99	48.7	5.6	0.78	43.1	11.7	0.84
BB97	<i>41.2</i>	<i>-2.1</i>	<i>0.83</i>	56.1	-29.9	0.62
FAO	38.9	-11.8	0.84	<i>34.9</i>	<i>-6.7</i>	<i>0.85</i>

Table 3.5. Performance assessment of daytime ($Q_{Sd} > 10 \text{ W m}^{-2}$) Q_E based on different r_s , over both stations. The italicized values show the r_s method that give the best agreement between estimated and measured Q_E . RMSE and Bias (Wm^{-2})

Figures 3.9 and 3.10 show scatterplots of hourly measured and estimated Q_E , based on the different r_s formulations, for Johnstown Castle and Dripsey, respectively; they also show the daily cycle of Q_E for daylight hours, averaged for the month of July. While FAO produced the lowest RMSE and bias values at Johnstown Castle (Table 3.5), both FAO and dRH99 are shown to overestimate Q_E , evident during the mid-day hours in July, when radiation is most intense; BB97 significantly underestimates Q_E , evident during July (Figure 3.9). At Dripsey, all r_s methods underestimate Q_E , with the largest underestimates associated with FAO. Holtslag and van Ulden (1983), in their study over Cabauw, report a RMSE of 56 W m^{-2} between measured and estimated Q_E ; results for all r_s methods used here are consistent with this finding.

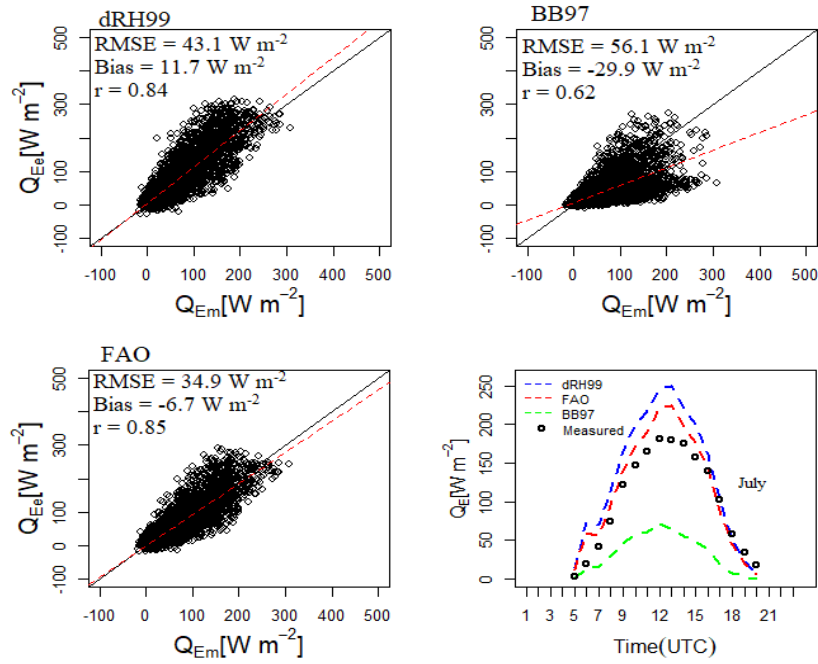


Figure 3.9. Relationship between daytime hourly measured (Q_{Em}) and estimated (Q_{Ee}) latent heat flux applying the Scheme with different r_s models over Johnstown Castle. The line plot is the diurnal cycle of Q_E , averaged for July, 2013.

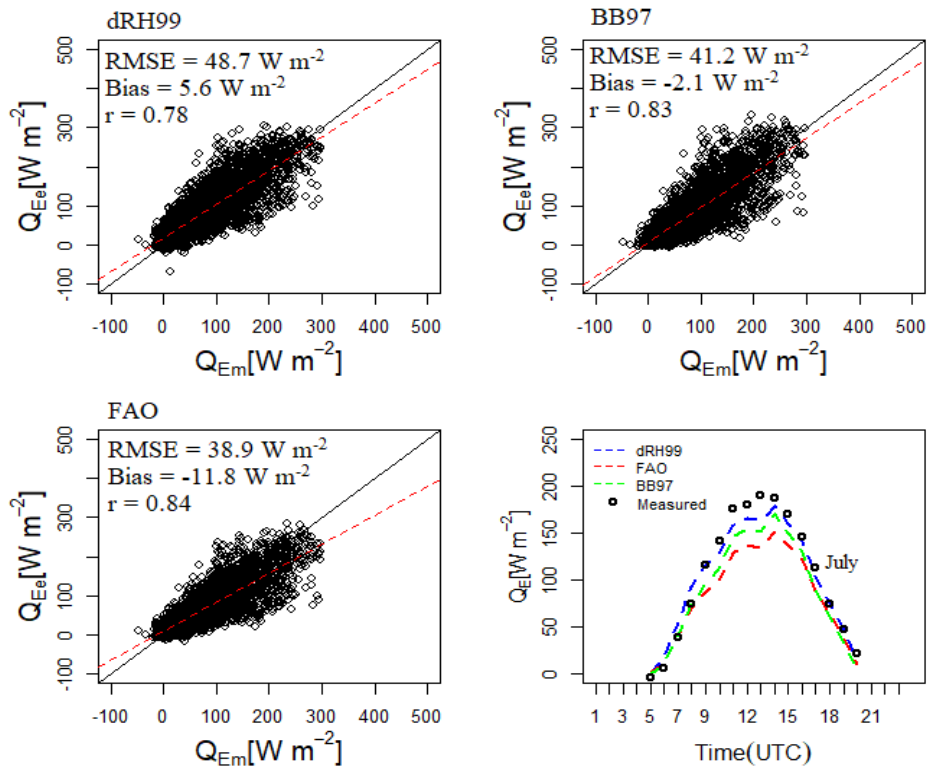


Figure 3.10. Relationship between daytime hourly measured (Q_{Em}) and estimated (Q_{Ee}) latent heat flux applying the Scheme with different r_s models over Dripsey. The line plot is the diurnal cycle of Q_E , averaged for July, 2010.

3.5.2 Analysis of model sensitivity

To explore the difference in performance between the r_s formulations, we examined the calculated r_s ranges during daytime hours for both dRH99 and BB97. From Table 3.6, the range in r_s values are larger for BB97 than for dRH99, at both sites. The large difference in estimated r_s values between dRH99 and BB97 result in a marked contrast in the estimated Q_E values at Johnstown Castle (Figure 3.9). In contrast, the difference in the range of r_s values at Dripsey between methods is smaller; smaller differences are also apparent in the estimated Q_E between these methods at this site. To further examine this, we focus our attention on BB97 to understand the role of the environmental response factors in regulating r_s and consequently Q_E at both sites.

r_s method	Johnstown Castle		Dripsey	
	$Q_{s\downarrow} > 10 \text{ W m}^{-2}$	$Q_{s\downarrow} > 100 \text{ W m}^{-2}$	$Q_{s\downarrow} > 10 \text{ W m}^{-2}$	$Q_{s\downarrow} > 100 \text{ W m}^{-2}$
dRH99	0 – 100	0 – 100	0 – 90	0 – 90
BB97	25 – 15800	25 - 2613	25 – 1300	25 – 175
BB97 (optimised)	25 - 2450	20 - 400	-	-

Table 3.6. Range of estimated r_s (s m^{-1}) during mid-day time ($Q_{s\downarrow} > 10 \text{ W m}^{-2}$ and $Q_{s\downarrow} > 100 \text{ W m}^{-2}$) over the selected stations. BB97 is based on the scheme using the default parameter values (i.e. Beljaars and Bosveld, 1997) for BB97; BB97 (optimised) is based on the updated optimised values for Johnstown Castle, employed in this study.

3.5.2.1 Sensitivity of Q_E to soil and environmental factors

A sensitivity analysis on BB97 was conducted by altering the values of f_r , S_r , h_s and c_{soil} , individually, and leaving the remaining coefficients unchanged.

At Johnstown Castle, the estimated Q_E was found to be largely insensitive, within the range of values tested, to alterations in either h_s , associated with the atmospheric moisture deficit function ($F_{\Delta q}$), or S_r , associated with the radiation function (F_S) (Figure 3.11, top) during

January or July. In contrast, during July, r_s and consequently Q_E was found to be very sensitive to changes in c_{soil} , associated with the soil moisture function (F_M) (Figure 3.11, bottom left).

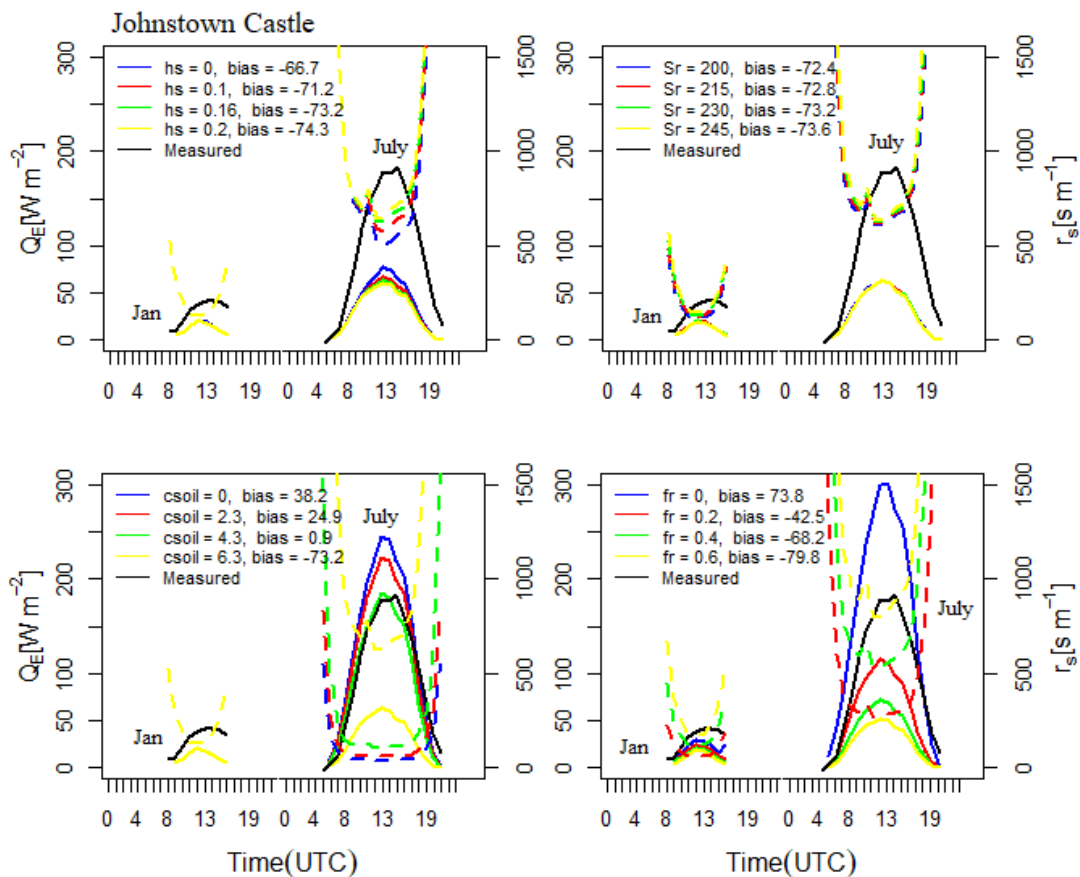


Figure 3.11. Sensitivity of daytime r_s and Q_E to environmental factors, averaged for January and July over Johnstown Castle. h_s (g kg⁻¹), S_r (W m⁻²), c_{soil} (m³ m⁻³) and f_r is dimensionless. The calculated biases for January (≈ -14 W m⁻²) are similar for all factors. The dashed and solid lines are r_s and Q_E , respectively.

When the default value (6.3 m³ m⁻³) for c_{soil} was employed, the average daytime value of r_s increased significantly (≈ 600 s m⁻¹), suppressing the estimated Q_E values (Figure 3.9). When $c_{soil} = 0$ m³ m⁻³, equivalent to setting $F_M = 1$, the estimated Q_E increases to near its potential, in response to low daytime r_s (< 50 s m⁻¹) values. Setting c_{soil} values within the range of 2.3 – 4.3 m³ m⁻³ resulted in Q_E estimates with the lowest bias, relative to measured values. A similar response was found for f_r ; estimated Q_E decreased from its potential ($f_r =$

0) with increasing f_r . A $c_{soil} = 4.3 \text{ m}^3 \text{ m}^{-3}$ was ultimately selected, based on the bias value (0.9 W m^{-2}) for the month of July.

At Dripsey, changes to h_s , S_r and c_{soil} had little or no impact on r_s and consequently Q_E (Figure 3.12, top and bottom left), during either January or July. Similar to the findings at Johnstown Castle, r_s was found to increase with increasing f_r so that the corresponding Q_E decreases, evident during the mid-day hours in both January and July.

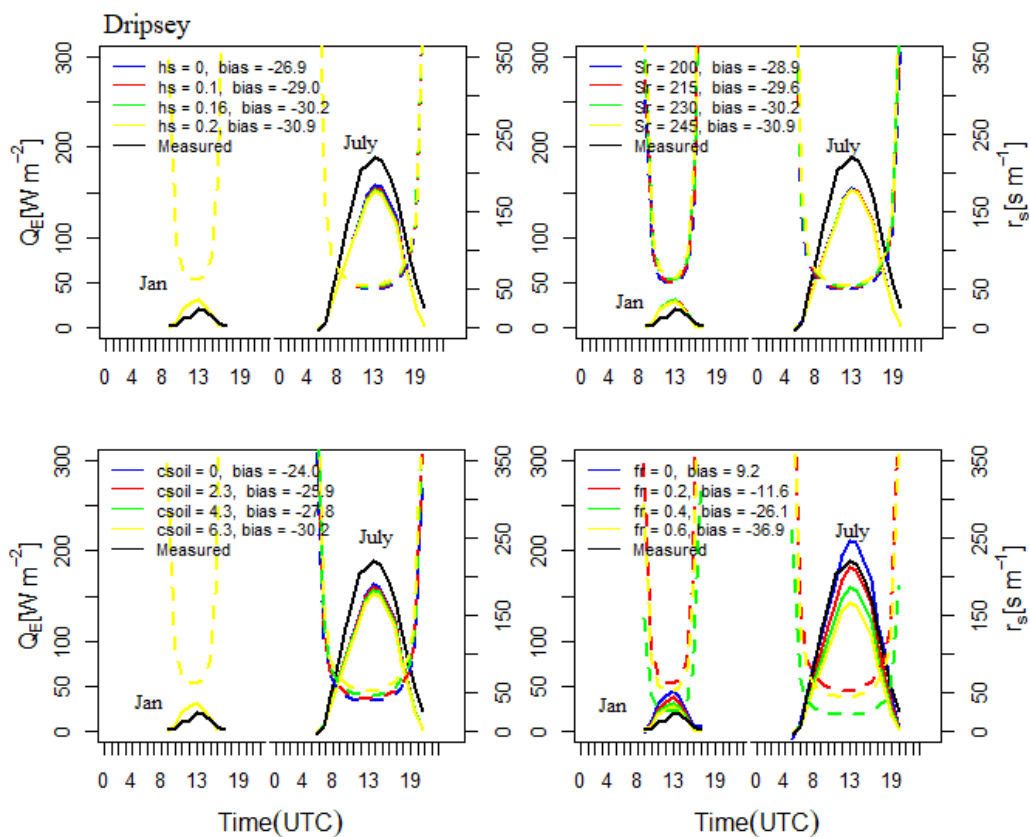


Figure 3.12. Sensitivity of daytime r_s and Q_E to environmental factors, averaged for January and July over Dripsey. h_s (g kg^{-1}), S_r (W m^{-2}), c_{soil} ($\text{m}^3 \text{ m}^{-3}$) and f_r is dimensionless. The calculated biases for January ($\approx -9 \text{ W m}^{-2}$) are similar for all factors. The dashed and solid lines are r_s and Q_E , respectively.

3.5.2.2 Estimation of surface fluxes using adjusted coefficients

Figure 3.13 (top) shows the hourly measured and estimated fluxes of Q_E and Q_H and averaged hourly day time values for July (Figure 3.13, bottom). The use of adjusted values (Table 3.7) at Johnstown Castle improves the RMSE and bias for Q_E ($RMSE = 37.8 \text{ W m}^{-2}$, $bias = -9.7 \text{ W m}^{-2}$) and Q_H ($RMSE = 41.7 \text{ W m}^{-2}$, $bias = 15.3 \text{ W m}^{-2}$) and the r value for Q_E ($r = 0.82$). The diurnal cycle (Figure 3.13, bottom) shows clearly that Q_E is significantly improved, matching more closely with the measured values during July. Overall, the magnitudes of daytime hourly estimated (measured) Q_H were within the range -60 and 320 W m^{-2} (-100 and 220 W m^{-2}), while that of Q_E were within -100 and 350 W m^{-2} (-20 and 310 W m^{-2}). At Dripsey, using the original BB97 values which proved to be optimum for this site, the surface fluxes were estimated within the range -68 and 235 W m^{-2} for Q_H and within -11 and 330 W m^{-2} for Q_E .

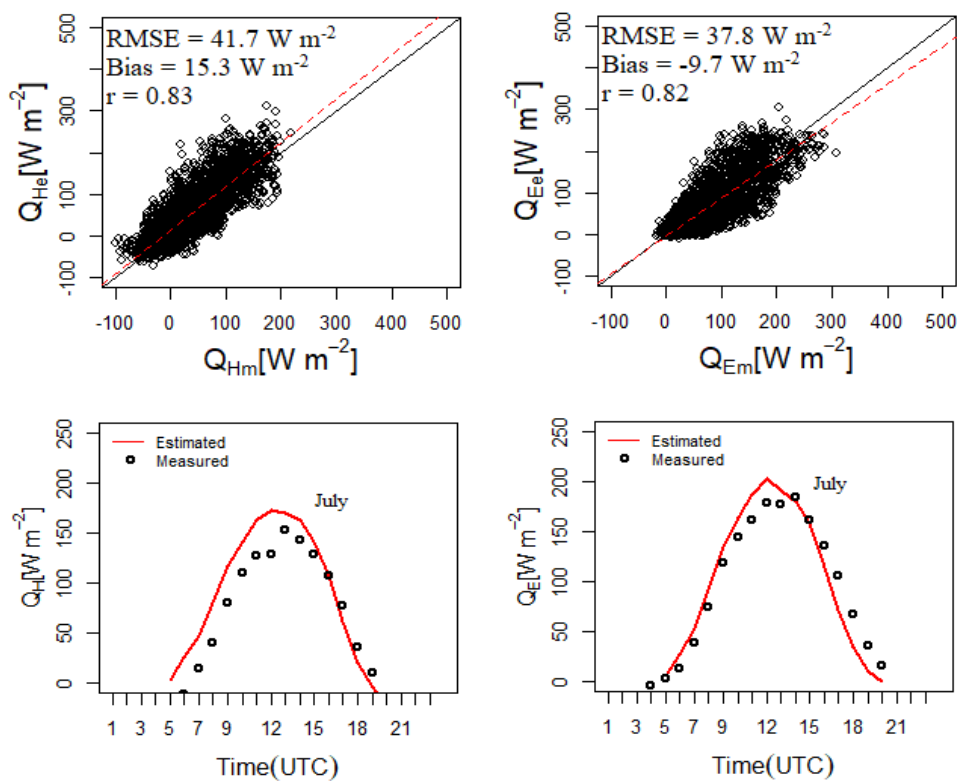


Figure 3.13. Relationship between daytime hourly measured and estimated Q_H [left] and Q_E [right] fluxes for 2013, applying the Scheme with optimized ($c_{soil} = 4.3 \text{ m}^3 \text{ m}^{-3}$) r_s over Johnstown Castle.

Soil Drainage Characteristics	Model Parameter	Range	Optimised value	Units
Imperfectly drained (Johnstown Castle)	f_r	0 – 0.6	0.47	-
	h_s	0 – 0.2	0.16	g kg ⁻¹
	c_{soil}	0 – 6.3	4.3	m ³ m ⁻³
	S_r	200 - 245	230	W m ⁻²
Poorly drained (Dripsey)	f_r	0 – 0.6	0.47	-
	h_s	0 – 0.2	0.16	g kg ⁻¹
	c_{soil}	0 – 6.3	6.3	m ³ m ⁻³
	S_r	200 - 245	230	W m ⁻²

Table 3.7. Adapted empirical coefficients of optimized r_s for Q_E estimation under different surface conditions

Averaged daily Q_H were estimated between -50 W m^{-2} and 170 W m^{-2} at both sites; daily Q_E values ranged between -15 W m^{-2} and 190 W m^{-2} at both sites (Figure 3.14, top). While both sites showed similar exchanges of Q_H , at both hourly and daily time scales Q_E was higher than Q_H . This indicates that the surface conditions at these sites were wet, in general, resulting in lower Δq_a and r_s and consequently, higher Q_E . The broader pattern shows the seasonal variation in the fluxes, which are low in winter and peak in summer (Figure 3.14, bottom).

3.6. Discussion

3.6.1 Physical control of surface resistance and surface fluxes

In this study, we evaluated the land surface parameterization scheme of de Rooy and Holtslag (1999) as a means of deriving surface energy fluxes using routine meteorological data. Although the scheme was developed using observations made over short grass grown on poorly drained soil, they suggested it could be adjusted for use elsewhere if the surface parameters, particularly surface resistance (r_s), are modified to local conditions by using

appropriate parameterization schemes. Beljaars and Bosveld (1997) indicate that r_s can vary owing to a range of environmental factors, including soil moisture, photosynthetically active radiation (PAR) and near-surface moisture deficit. Here, we focus on three different methods (namely FAO, dRH99 and BB97) of representing r_s , representing varying levels of sophistication, within the scheme.

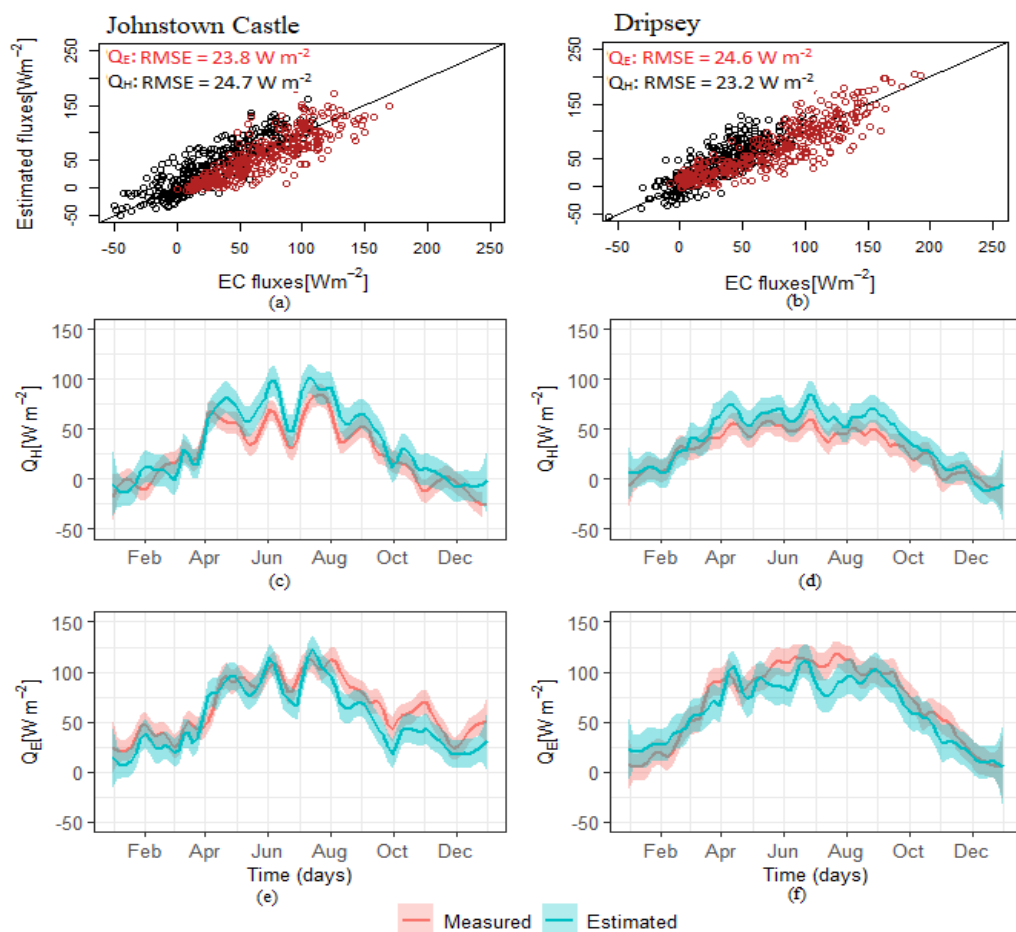


Figure 3.14. Relationship between parameterized and measured averaged daily Q_H and Q_E over the selected sites. The daily variations of Q_E and Q_H in the course of a year are shown in the middle (c-d) and bottom (e-f) panels, respectively. The shaded portions are the 5th and 95th percentiles of uncertainty bound as calculated by LOESS regression.

The FAO method requires no information on atmospheric and site conditions and assigns a fixed value for r_s . Estimates using this method performed relatively well in estimating Q_E but

poorly in estimating Q_H at both sites. The dRH99 method incorporates the near-surface moisture deficit but did not perform as well as FAO for Q_E , but did better than FAO for Q_H at both sites. The most sophisticated method (BB97), using the standard values for the environmental response factors (i.e. f_r , S_r , h_s and c_{soil}), provided a good fit to both Q_H and Q_E at Dripsey but performed poorest of all methods at Johnstown Castle.

These results may seem counterintuitive, as the FAO method with the least information performs well, relative to the other methods with regard to Q_E . In part this can be explained by the constrained nature of the energy budget, which allocates the energy available (that is, $Q_N - Q_G$) into Q_H and Q_E . As FAO underestimates Q_H , more energy is channelled into Q_E . Similarly the improved performance of dRH99 for Q_H results in a weaker result for Q_E . However, the intriguing result is for the most sophisticated method (BB97), which includes many of the physical controls on r_s , performs well at Dripsey using standard values but poorly at Johnstown Castle for both Q_H and Q_E . As both Johnstown Castle and Dripsey experience similar meteorological conditions (Figures 3.2-3.4), we hypothesised that this is due to the soil moisture characteristics (Table 1), which are not considered by dRH99.

Figure 3.15 shows the average daily values of soil moisture (θ) of Dripsey and Johnstown Castle for the years available. Seneviratne et al. (2010) classified evapotranspiration regimes into types. A wet regime is defined as energy-limited, and occurs when θ lies above a critical soil moisture level (θ_{CT}). When θ falls below θ_{CT} (typically between 0.5-0.8 of θ_{FC}) (Seneviratne et al. 2010; after Shuttleworth, 1993) the regime is classed as moisture-limited and 'transitional'. At Dripsey, daily θ varies between 0.25 to 0.4 $\text{m}^3 \text{m}^{-3}$ over the two year period and only drops below θ_{FC} for short periods; from the 6th June to the 8th August during 2004 (\approx 64 days) and from the 28th June to the 23rd July during 2005 (\approx 26 days).

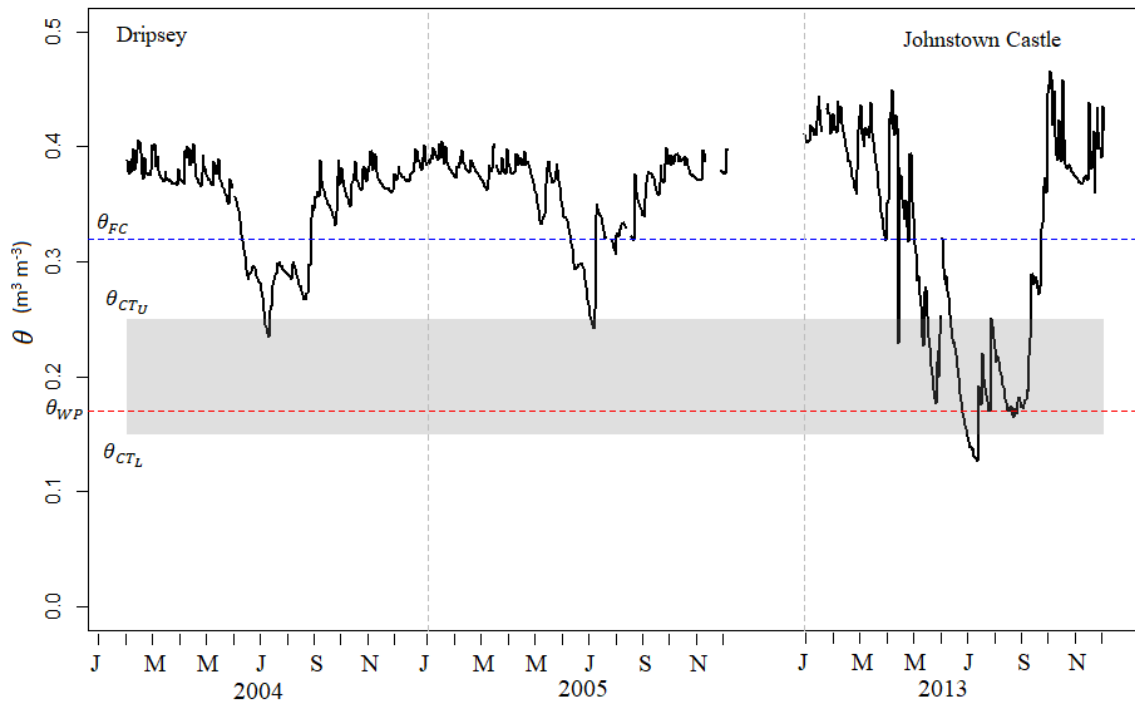


Figure 3.15. Averaged diurnal variations of the measured θ of the top layer of the soil from 2004 to 2005 at Dripsey and for the year 2013 at Johnstown Castle. The gaps indicate periods with missing values. The horizontal dashed line is the threshold of θ at field capacity [blue] and wilting point [red], and the grey box is the (upper and lower critical θ at $0.25 \text{ m}^3 \text{ m}^{-3}$ and $0.15 \text{ m}^3 \text{ m}^{-3}$, respectively) bound of transitional soil moisture regime for both sites (after Shuttleworth, 1993).

At Johnstown Castle, θ varies between 0.12 to $0.47 \text{ m}^3 \text{ m}^{-3}$ over the measurement period; however, θ falls below θ_{CT} for an extended period from the 23rd May to the 30th September during 2013 (≈ 131 days). Consistent with the soil drainage characteristics, the heavier soils at Dripsey maintain sufficient moisture throughout the year; this meets the definition of a wet regime where Q_E is constrained by the available energy. At Johnstown Castle, in the absence of precipitation, the soil moves from a wet to a transitional regime and Q_E becomes moisture-limited. This suggests that the impact of the different methods for obtaining r_s values will be most evident during transitional soil moisture regimes. BB97 is the only method that can incorporate these effects into the calculation of surface resistance (r_s).

The sensitivity analysis identified the c_{soil} coefficient, which acts to modify the plants ability to access soil moisture below field capacity (θ_{FC}) as a critical variable. A value of $c_{soil} \approx 6.3 \text{ m}^3 \text{ m}^{-3}$ was estimated by Beljaars and Bosveld (1997) based on observations at a poorly-drained site (Cabauw), similar to the Dripsey site, which fits the characteristics of an energy-limited evapotranspiration regime. However, we found that a value of $c_{soil} \approx 4.3 \text{ m}^3 \text{ m}^{-3}$ was better suited to the imperfectly-drained soils at Johnstown Castle, which often experiences a transitional regime. The adjusted c_{soil} value reduced the range of r_s values (Table 3.7) and improved results for both hourly and daily Q_H and Q_E estimates (Figure 3.13; Figure 3.14). These results indicate that r_s depends very strongly on soil moisture regimes, particularly during a transitional period where θ falls below θ_{CT} , so that the use of a constant value or a linear relation where air moisture response is the only driver of r_s may prove inferior. This supports the conclusion of Beljaars and Bosveld (1997), who established that all the environmental response parameters are important for stomatal control during dry periods, in order to obtain a good flux simulation.

The estimates of surface energy fluxes generated by the de Rooy and Holtslag (1999) scheme using the BB97 method that adjusts to soil moisture conditions, generates both hourly ($RMSE \approx 40 \text{ W m}^{-2}$) and daily ($RMSE \approx 24 \text{ W m}^{-2}$) statistics that are comparable with other similar studies. For instance, Holtslag and van Ulden (1983), using calculated $Q_{S\downarrow}$ as an input into their scheme, obtained half-hourly measures of $RMSE \approx 34 \text{ W m}^{-2}$ for Q_H during daytime over grassland at Cabauw, the Netherlands. The errors of estimated Q_E using different spatial evapotranspiration (ET) models including mapping ET at high resolution with internalized calibration (METRIC) (Allen et al., 2007), surface energy balance systems (SEBS) model (Su, 2002), two-source energy balance (TSEB) model (Norman et al., 1995), triangle model, and

surface energy balance algorithm for land (SEBAL) (Bastiaanssen et al., 1998a) are within the range $\approx 30 - 80 \text{ W m}^{-2}$ (Long and Singh, 2013), which also correspond to results in this study. Estimated daily ET fluxes using an upscaled evaporative fraction (EF) scheme have also been found to range between 5 and 40 W m^{-2} (Colaizzi et al., 2006; Sobrino et al., 2007; Tang et al., 2013).

3.6.2 Uncertainties in surface heat flux simulations

It is important to recognise several potential sources of error in this work and their likely effect on the findings.

Energy budget closure: The energy flux estimates generated here using the de Rooy and Holtslag scheme are evaluated by comparison with EC measurements made at two sites. It is important to acknowledge that there are likely to be errors in the measured fluxes that can be assessed as part of energy budget closure (see section 3.3.1). Here, the closure is measured as $Q_N - (Q_H + Q_E)$ and the results for both sites (Figure 3.2) are consistent with those reported in the previous studies (e.g Wilson et al., 2002). The major reason for the non-closure here is the absence of substrate heat flux (Q_G) observations but there are also likely to be errors associated with the measured terms (Heusinkveld et al., 2004). EC measurements are known to underestimate the turbulent sensible (Q_H) and latent (Q_E) heat fluxes mainly because they do not capture the effects of large-scale eddies that are linked to landscape heterogeneity (Foken, 2008). We do not attempt to evaluate the magnitude of the underestimates in this work but Foken (2008) indicates that these may be between 10-20 %. This should be borne in mind when evaluating the estimated turbulent fluxes using BB97, which employ adjusted parameters to improve the fit to observations.

Additionally, EC measurements have gaps which could be associated with system maintenance, power or equipment failures, micrometeorological conditions under which the assumptions of EC measurements are not met, etc. (Wutzler et al., 2018). Depending on the proportion of missing data, the quality of data for analysis can potentially impact the results of model evaluation, particularly if the gaps are large and skewed to a particular season or meteorological conditions. Several attempts to gap-fill missing data have been consolidated in recent decades, with a view of improving robustness and accurateness of the resulting data and model analysis, and obtaining temporally continuous data of surface fluxes (e.g. Falge et al., 2001; Wutzler et al., 2018). These methods are available as open-source tools (e.g. Wutzler et al., 2018). However, gap-filled data could as well bias model validation since they are rather based on data synthesis, and no general consensus as to which technique or tool is superior (Boudhina et al., 2018). Though the proportions of missing flux measurements used in this study are considerably high, the values are within the standard range between 25 and 35 % (Falge et al., 2001; Boudhina et al., 2018), and the non gap-filled data are fairly spread across the year of analysis.

Meteorological observations: The de Rooy and Holtslag (1999) scheme requires inputs on solar radiation, air temperature, humidity, etc. to estimate fluxes. Ideally, these meteorological observations are complete and available at the site of study. This was not the case for Dripsey, where the scheme used data obtained for a site 25 km distant (Cork Airport) where observations of solar radiation ($Q_{S\downarrow}$) and cloud cover were not available. The study estimated $Q_{S\downarrow}$ from sunshine hours using a modified Angstrom-model but could not account for the impact of clouds on $Q_{L\downarrow}$; as a result, estimated Q_N is likely to be lowered, especially at night. This error will affect all surface energy fluxes but, given the focus on daytime

evaporation, the impact is likely to be small. While the estimated Q_G values were not evaluated in this study, de Rooy and Holtslag (1999) also highlighted that, an overestimation of Q_G may result in negative bias in $Q_N - Q_G$ that is used to estimate Q_E .

Finally, the need to estimate radiation components (rather than using observations) will result in errors that will impact on the turbulent flux estimates produced by the different methods.

Model parameters: Apart from the uncertainties associated with meteorological forcings and EC measurements, a land surface scheme could also suffer from uncertainties in model parameter values. Model parameters are used to represent the physical property of the system, and can act or interact to influence the behaviour of the system (Arsenault et al., 2018). In essence, employing prescribed values for some selected parameters without calibration or optimization may potentially alter the solution of the remaining parameters, especially because the general application of prescribed values may be uncertain (Li et al., 2020a). In this study, we have focused on optimising a few selected parameters relating to Jarvis-type surface resistance model, while keeping the standard values of the remaining parameters (e.g. minimum stomatal resistance, surface emissivity, surface roughness, etc) in the scheme. Though the specified model parameter values have been established as appropriate for short grass, we should acknowledge that employing improper parameter values may pose a fundamental shortcoming to the model internal dynamics and its simulations.

3.7 Conclusion

This chapter evaluated an existing physically-based scheme for estimating surface energy fluxes over two independent sites with contrasting soil moisture characteristics. The radiative and non-radiative components were parameterized from limited routine weather observations for daytime conditions over grass-covered surfaces at Johnstown Castle and Cork Airport in Ireland. The parameterized fluxes were further evaluated against observed EC flux measurements at Johnstown Castle and Dripsey (25km from Cork Airport). Our main objectives are to test whether the original de Rooy and Holtslag (1999) scheme, which was derived at a grassland site in the Netherlands (Cabauw) can be transferred to other grassland sites and take into account different soil characteristics. The study focused in particular on the role of surface resistance (r_s) in regulating the daytime turbulent heat fluxes of Q_H and Q_E . Three methods of varying sophistication (FAO, dRH99 and BB97) were applied to the estimation scheme at the two test sites, which represent poorly (Dripsey) and imperfectly (Johnstown Castle) drained soils. While BB97 and dRH99 produced a good fit to observed Q_E values at Dripsey (a site that is similar to Cabauw), the fit at Johnstown Castle was poor. The differences in results were attributed to soil moisture characteristics and only BB97 accounts for this property. A critical variable in this method of deriving r_s is the soil moisture coefficient (c_{soil}), which accounts for the water available to plants for evapotranspiration; the value of c_{soil} used in BB97 ($6.3 \text{ m}^3 \text{ m}^{-3}$) was suited to the wet soil conditions at Dripsey but not at Johnstown Castle. This study finds that $c_{soil} \approx 4.3 \text{ m}^3 \text{ m}^{-3}$ resulted in Q_H and Q_E values that agree well with the measured values over imperfectly drained soil.

An additional finding from this work was that the use of off-site meteorology, similar to the site of interest, can be reliably employed to estimate the measured surface fluxes at a

location; we demonstrated this at Dripsey, where the nearest suitable meteorological station was located ≈ 25 km's away. Notwithstanding the uncertainties associated the estimation of $Q_{s\downarrow}$ from sun hours and the use of soil water from a similar precipitation year (i.e. 2005), the estimated fluxes agree well with the measured values at this site. In the absence of direct soil moisture measurements and based on the soil drainage characteristics at Dripsey, the use of $F_M = 1$ in combination with standard optimal coefficients of BB97 is likely to produce similar results to dRH99.

The surface energy imbalance is always characterized to be partly a consequence of an underestimation of turbulent heat fluxes by EC techniques. Given the measures of observed surface energy balance closure at the test sites which, while they do not account for Q_G , are consistent with previous studies, we can conclude that the uncertainty of the parameterization scheme associated with the systematic bias of EC measurements of turbulent heat fluxes is relatively smaller. Notwithstanding the problems of surface energy balance closure of EC measurements, the estimated fluxes improved significantly through the adjustment of a c_{soil} adjusted to account for the soil moisture conditions. Generally, the de Rooy and Holtslag (1999) scheme demonstrated good performance in replicating the measured fluxes over grass-covered surfaces exhibiting different soil moisture characteristics and using routine weather observations for daytime weather conditions at both sites. On the basis of the analysis conducted here, we therefore conclude that the land surface scheme is sensitive to soil types that exhibit different drainage characteristics; whether the optimised coefficient for c_{soil} in this study is more generally applicable, remains to be tested.

4. A Model Framework to Investigate the Role of Anomalous Land Surface Processes in the Amplification of Summer Drought across Ireland during 2018.

Preface

In revision as:

Ishola, K. A., Mills, G., Fealy, R. M., Fealy R., 2021. A model framework to investigate the role of anomalous land surface processes in the amplification of summer drought across Ireland during 2018, 1-27pp – revision submitted to *International Journal of Climatology*

Here the LSS is applied to a number of grass field sites, covering the entire Ireland domain, having (i) identified a key physical property (c_{soil}) that allows us to distinguish between soil types, their ability to retain water accessible to plants and plant response to exchanges; and (ii) developed and evaluated the model outputs against the available observations at two test sites, in the previous paper. The current manuscript to be submitted is provided under supplementary information (paper 2). The primary aim was to explore the ability of the scheme, in combination with global reanalyses and satellite-derived products, to improving our understanding of a specific extreme weather event such as the 2018 summer drought at regional scale. The broad pursuant question here is: **Can a validated LSS be used to explore (and predict) the emergence and development of agricultural drought and its regional characteristics?** This study will allow us to examine the potential consequences of climate change which predicts more intense dry periods in summer in the future.

The chapter/paper is an extended version partly based on the comments received on the preliminary results presented at International Symposium on Climate-Resilient Agri-Environmental Systems (ISCRAES), Dublin, Ireland.

Abstract

Here, we explore the utility of a physically-based land surface scheme with in-situ observational data, along with global gridded reanalyses and satellite-derived products to analyse the spatial and temporal evolution of the 2018 summer drought event in Ireland, over fourteen grassland sites. Applying segmented regression models, the study quantifies a critical soil moisture threshold, θ_c , a key determinant of the transition from wet to dry evaporative regimes. For our analysis period (2010-2019), we find that the impacts of the event on surface-air energy exchanges were dominated first by atmospheric anomalies and subsequently by soil moisture constraints as the accumulated rainfall deficit increased throughout the summer months. This was particularly evident in the East and South-East of the country. Due to its latitude and ample year round rainfall, Ireland is typically energy limited in the context of evaporation, however, during 2018 regions within the country displayed a strong linear coupling between soil moisture and both evapotranspiration and vegetation response, suggesting a shift into a transitional or water limited regime, beginning from the 22 June. The θ_c findings are important to understanding the soil moisture context under which land-atmosphere couplings are strongest in water-limited regimes across the country. Therefore, these findings should help improve the treatment of soil parameters in weather prediction models, required for sub-seasonal and seasonal forecasts, consequently enhancing early warning systems of summer climate extremes in the future.

4.1 Introduction

Droughts and heatwaves are extreme weather conditions which are commonly defined by periods of soil water shortage and high near-surface air temperature anomalies, respectively. These weather conditions may be mutually reinforcing as high temperatures increase the atmospheric demand for water vapour, which can only be met if there is sufficient available water in the soil profile. As soil water becomes limited, more of the energy available at the surface is expended as sensible, rather than latent heat, and the near surface air temperature increases (Seneviratne et al., 2010). When these ‘compound’ events evolve simultaneously, they can result in a wide range of impacts, including water scarcity, tree mortality and agricultural loss, wildfire occurrence and air pollution thus impacting ecosystems, decreases in agricultural productivity and impact human health and well-being (Fink et al., 2004; Conti et al., 2005; García-Herrera et al., 2010; Dole et al., 2011; Alexander, 2011; Zscheischler et al., 2018; Miralles et al., 2019; Schuldt et al., 2020).

At a continental scale, the weather conditions of the 2018 European summer (April to August) were exceptional with a higher near-surface temperature and lower rainfall receipts relative to the long-term (1981-2010) mean (Magnusson et al., 2018). These conditions were associated with the presence of a large anticyclonic system located over central and northern Europe, which blocked the normal passage of moisture bearing Atlantic storms over Western Europe (Buras et al., 2019; Kornhuber et al., 2019; Rösner et al., 2019; Dirmeyer et al., 2021). The resulting heatwave and drought were extreme, surpassing previous records (e.g. 2003 European heatwave), with several stations across Europe reporting record breaking daily maximum temperatures (Buras et al., 2019; Rösner et al., 2019; Dirmeyer et al., 2021). The impact of this event was especially evident in northern Europe; as an example, Sweden

experienced exceptionally severe wildfires (Albergel et al., 2019; Buras et al., 2019; Rösner et al., 2019; Dirmeyer et al., 2021).

Ireland, which is situated on the western maritime fringe of Europe, also experienced unusually warm and dry conditions during the Summer of 2018, though to a lesser extent than those experienced in the more continental regions of Europe. Here, the cumulative rainfall deficit increased from April onwards, although the arrival of Storm Hector in mid-June replenished water supplies in the north and west of the country (Met Éireann Report, 2018a). Thereafter, the influence of the European blocking anticyclone reasserted itself and between 25 June and 15 July most weather stations reported both heatwave and absolute drought conditions (Met Éireann Report, 2018b; Moore, 2020). The 2018 event impacted water resources with consequent impacts on grass growth productivity resulting in the increased cost of agricultural produce and consequently impacted farmers' incomes here (Dillon et al., 2018). These impacts were preconditioned by the cold ground temperature arising from the exceptional snow fall that was associated with cold airmass advecting around high pressure from Siberia towards the country dubbed the 'Beast from the East', from the end of February and lasted for about a week, causing a very late onset of grass growth season by about a month relative to an average year (Dillon et al., 2018).

The occurrence of both droughts and heatwaves, and their associated impacts, have become more frequent over the last three decades across Europe, but in Ireland the reported prolonged droughts are less frequent in recent decades than prior to 1980s (e.g. Noone et al., 2017). Such events are projected to be more widespread and intense due to climate change (Beniston, 2004; Pal et al., 2004; Meehl and Tebaldi, 2004; Samaniego et al., 2018). Previous studies on meteorological drought, in Ireland and across western Europe, are well-

documented (e.g. Noone et al., 2017; Falzoi et al., 2019; Murphy et al., 2020; Vicente-Serrano et al., 2020). However, the increasing number of episodes of surface dryness warrants investigation of agricultural drought, particularly the complexities associated with quantifying the integrated effects of decreasing soil moisture, increased evaporative demand and increased vegetation stress during extreme hot and dry conditions (e.g. Ciais et al., 2005).

Under conditions of increasing soil moisture deficit and atmospheric evaporative demand, vegetation responds by closing its stomata to minimise water loss to the atmosphere (e.g. transpiration) to prevent desiccation; absorbed radiation is subsequently dissipated in the form of sensible heat, the overall effect of which results in a positive feedback on air temperature (Seneviratne et al., 2010; Miralles et al., 2019). Such feedbacks are driven by the land surface and specifically soil moisture when evapotranspiration becomes constrained by the reduction in available water (e.g. transitional regime - Seneviratne et al., 2010). In contrast, when soil moisture (θ) is above some critical threshold, evapotranspiration (ET) becomes energy limited. While enhanced surface sensible heat fluxes are typically most evident in regions that exhibit a strong coupling between soil moisture and evaporation (e.g. Southern Europe) (Knist et al., 2017), regions can switch between energy limited and moisture limited regimes over the course of a year or depending on land cover (Seneviratne et al., 2010). For example, Ireland has a maritime temperate climate with ample year-round rainfall, yet frequently experiences seasonal soil moisture deficits; typically associated with those locations defined as having well-drained soil characteristics. During periods of prolonged rainfall deficits and increased summer temperature-assuming advection is insignificant, such regions are likely to experience agricultural drought with consequent impacts on plant productivity.

Typically, an energy limited and a moisture limited regimes are distinguished based on soil moisture-evaporative fraction framework. Evaporative fraction (EF) (defined as the ratio of latent heat flux and available energy at the land surface) is an important metric, reflecting the partitioning of available energy into surface turbulent fluxes, and providing the fundamental knowledge on the coupling and feedback processes at the interface between the land and atmosphere (Seneviratne et al., 2010). Within a θ -EF space, EF is often conceptualized as bilinearly segmented as a function of θ , separating the regimes at a critical soil moisture content (θ_c) (e.g. Figure 2.7) (Seneviratne et al., 2010; Buitink et al., 2020; Denissen et al., 2021). In essence, the θ_c is derived from the point at which θ and EF become linearly coupled under which ET becomes limited by drying soils. Buitink et al. (2020) used a similar framework but replaced EF with satellite-derived ecosystem indicators, near infrared reflectance of vegetation (NIRv) and vegetation optical depth (VOD), to allow for a more precise analysis of how vegetation productivity is related to soil moisture during 2018 drought event at two sites in the Netherlands. Other studies have also derived this critical threshold based on observations and model outputs using different theoretical frameworks (Akbar et al., 2018; Haghighi et al., 2018; Feldman et al., 2019; Denissen et al., 2020). Overall, determining θ_c is key to predicting timescale of plant response, ET decay and consequently the emergence and progression of agricultural drought.

Exploring the response of surface energy fluxes to soil moisture and atmospheric anomalies using eddy covariance measurements or land surface models can potentially provide a better understanding of a plant's physiological response to climate change (Graf et al., 2020; Lansu et al., 2020). Additionally, quantifying anomalous surface-atmosphere heat and moisture exchanges could be used as an indicator for the early warning or prediction of summer climate

extremes. However, flux observations are generally difficult to obtain and may not exist for specific regions of interest; similarly, the use of a numerical land surface model with its computational and data requirements maybe beyond the reach of many individual researchers. Consequently, this research evaluates the use of a simple land surface scheme, which employs readily available meteorological and surface data, to investigate the role of land-atmosphere exchange processes across Ireland during the 2018 summer drought. Using the land surface scheme, the study seeks to analyse (i) the evolution of the 2018 drought at sub seasonal-to-seasonal and regional scales; (ii) the anomalies in simulated land-atmosphere energy exchanges; and, (iii) the role of soil moisture in modulating land-atmosphere exchange processes.

We combine a physically-based land surface scheme with in-situ observational data, along with readily accessible global gridded reanalyses and satellite-derived data products to address these objectives. The physically-based scheme used here has previously been established as having the capability to reproduce measured surface fluxes with some degrees of reliability (de Rooy and Holtslag, 1999; Ishola et al., 2020, Chapter 3). The method outlined offers the potential for improving management strategies, particularly during anomalous warm and dry events, and for delineating areas with differential drought responses.

4.2 Materials and Methods

4.2.1 In-situ meteorological data

Hourly meteorological observations were obtained from fourteen automatic weather stations (AWS) across Ireland (Table 4.1 and Figure 4.1) from the Irish Meteorological Service, Met Éireann. These stations are sited over short grass cover, consistent with WMO guidelines and

report on global solar radiation ($Q_{s\downarrow}$, $W m^{-2}$) or sun duration (hours), air temperature ($^{\circ}C$), relative humidity (%), pressure (kPa), wind speed ($m s^{-1}$) and precipitation (mm). As cloud amount is only available at relatively few stations, we subsequently exclude the cloud input in the land surface scheme to ensure consistency in approach across all stations. For stations where sunshine hours are available, including Knock Airport, Casement (Aerodrome), Shannon Airport and Cork Airport (Figure 4.1), hourly $Q_{s\downarrow}$ data were estimated for these stations based on observations of sunshine duration following Allen et al. (1998). The hourly meteorological observations were obtained for the summer months of May to August. Due to the differences in the start of operations of a number of the AWS, we focus the main analysis on the most recent decade (2010-2019) to ensure consistent temporal coverage of meteorological data across all stations.

Station	Lat/Long ($^{\circ}N$, $^{\circ}W$)	Elevation (m)	Soil type	Drainage class	Region	Zone
Belmullet	54.228, 10.007	9	Peat	Poor	Northwest	
Claremorris	53.711, 8.991	69	Coarse loam	Well	Nortwest	
Finner	54.494, 8.243	33	Coarse loam	Poor	North	A
Knock Airport	53.906, 8.817	201	Fine loam	Imperfect	Northwest	
Malin Head	55.372, 7.339	20	Peat	Poor	North	_____
Casement	53.306, 6.439	91	Fine loam	Moderate	East	
Dublin Airport	53.428, 6.241	71	Fine loam	Moderate	East	
Dunsany	53.499, 6.699	83	Fine loam	Moderate	East	B
Johnstown Castle	52.292, 6.489	52	Fine loam	Imperfect	Southeast	
Oak Park	52.861, 6.915	62	Fine loam	Moderate	Southeast	_____
Cork Airport	51.847, 8.486	155	Fine loam	Well	South	
Moorepark	52.164, 8.264	46	Coarse loam	Well	South	C
Shannon Airport	52.689, 8.918	15	Loam	Well	Southwest	
Valentia	51.929, 10.239	24	Coarse loam	Well	Southwest	

Table 4.1. Characteristics of the selected grassland synoptic stations. The soil types and drainage categories are based on the data from Irish Soil Information System (Creamer et al., 2014). The grouped zones, A, B and C, comprise of stations with similar precipitation regimes.

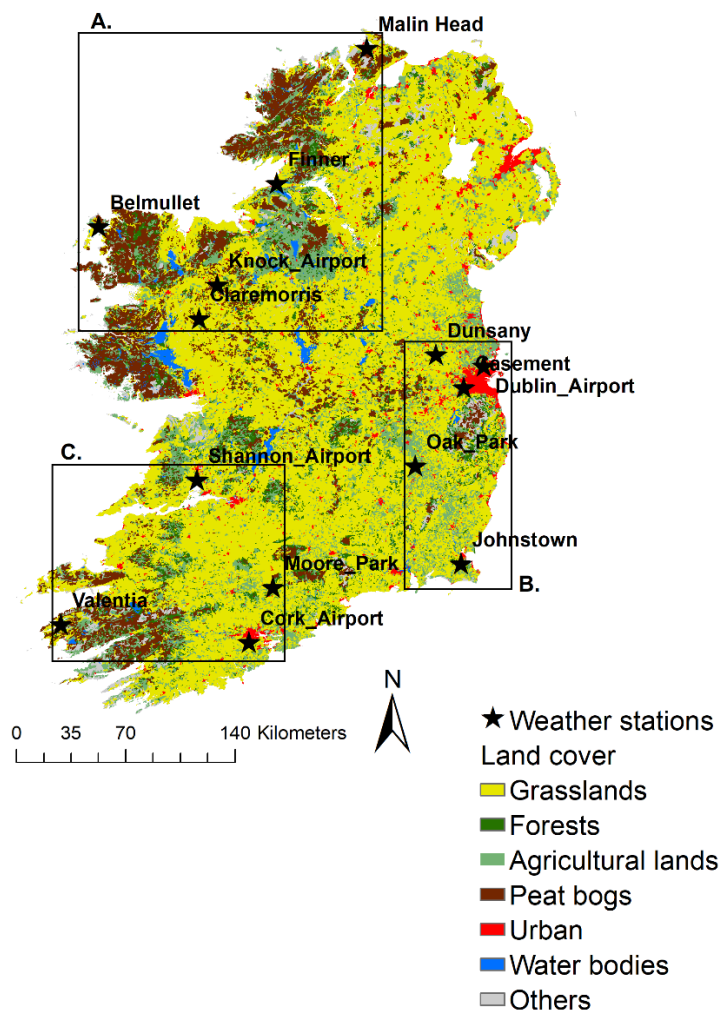


Figure 4.1. Map of the study area showing the locations of selected weather stations and the dominant land cover types from 2018 CORINE Land cover product. The boxes A, B and C comprise of the stations grouped on the basis of similar precipitation regimes.

4.2.2 Gridded data

Gridded daily total precipitation data for Ireland were also obtained from the Irish Meteorological Service, Met Éireann, for the period from 1999 to 2019. This period is consistent with the satellite derived Leaf Area Index (LAI) product outlined below. This data available at 1 km² grid resolution was generated by Met Éireann using interpolation techniques applied to in-situ rainfall data from over 500 rainfall stations across the Republic of Ireland (Walsh, 2012).

The land surface scheme employed requires soil moisture measurements, however, the measurement of this parameter is not routine practice in Ireland, as in many other countries, therefore we employed gridded reanalysis soil moisture data from the European Centre for Medium Range Weather Forecasting (ECMWF) ERA5-Land data, obtained from the C3S Copernicus Climate Data Store. ERA5-Land is the latest global reanalysis product from ECMWF, which employs improved historical observations and is run at a finer spatial resolution (atmosphere 0.25°; land 0.1°) relative to its predecessor, ERA-Interim (Hersbach and Dee, 2016). We obtained ERA5-Land hourly volumetric water content (θ) ($\text{m}^3 \text{m}^{-3}$) in the top soil layer (0-7 cm) for the land area of Ireland, for the period 1999 to 2019. The product has also been evaluated at the global scale (e.g. Li et al., 2020b). An independent evaluation of the θ product shows that ERA5-Land reasonably estimates available measured soil moisture obtained at three Irish grassland sites, representative of different soil texture characteristics (Figure 4.2).

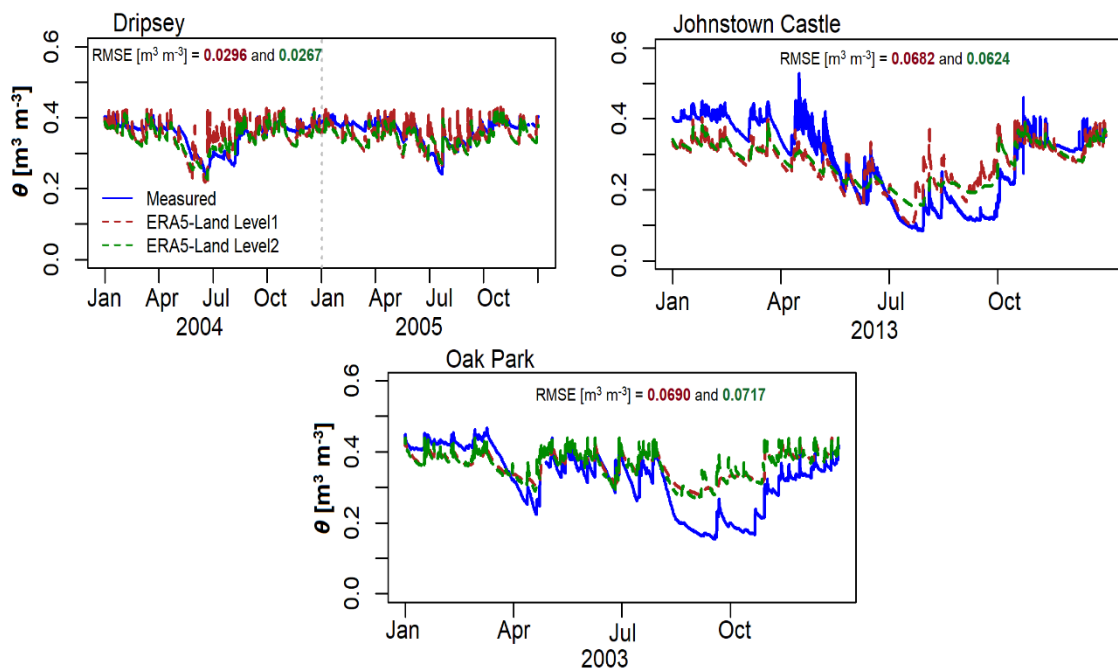


Figure 4.2. Comparisons between hourly measured and ERA5-Land volumetric water content (θ) across three independent grassland sites. The measured θ values are obtained from eddy covariance flux sites from previous studies (see Chapter three)

The offsets between measured and ERA5-Land θ values are largely represented in θ values below $0.25 \text{ m}^3 \text{ m}^{-3}$, and may be explained by the leaf area index monthly climatology used as input in ERA5-Land (Boussetta et al., 2013). It should also be noted that the ERA5-Land θ at the surface soil layer was evaluated with measured θ at the deeper soil layer (20 cm) across the sites. The surface θ derived from models or satellites are thought to decouple from θ in the deeper soil profile where plants may take up water depending on root density, and consequently may not explain the dynamics of processes in the root zone (Buitink et al., 2020). However, the choice of ERA5-Land surface θ to diagnose drought processes, as in many studies in recent past (e.g. Dirmeyer et al., 2021), is on the basis that soil moisture anomalies develop progressively down deeper soil layers in the course of a drought event, as plants increase water uptake from near the surface to the subsurface (Buitink et al., 2020). Thus, ERA5-Land subsurface θ values may further lead to larger offsets under $0.25 \text{ m}^3 \text{ m}^{-3}$, since the soil moisture contents at the deeper layers are always higher than at the upper soil layers.

4.2.3 Satellite-derived products

We obtained satellite-derived Leaf Area Index (LAI) from the Copernicus Global Land Service (CGLS) project, which are derived from SPOT-VGT and PROBA-V, prior to and from 2014, respectively. The LAI quantifies the greenness of plants and can be observed per unit horizontal surface area from space (Albergel et al., 2019). The CGLS LAI product, beginning in 1999, employed SPOT-VGT; the method by Baret et al. (2013) has been used to retrieve LAI from PROBA-V. Here, we use the CGLS LAI GEOV2 product which is at 1 km^2 spatial and 10-day temporal resolution (Albergel et al., 2019). The product development is outlined by Verger et al. (2014).

The land surface temperature (T_s) is a critical parameter that governs the land-atmosphere coupling, and can be used to evaluate model derived estimates of surface energy fluxes. We obtained T_s from the Moderate Resolution Imaging Spectroradiometer (MODIS) (MOD11A1, version 6) from the Land Processes Distributed Active Archive Center (LP DAAC) (Wan et al., 2015).

In addition, the near-infrared radiation reflected by vegetation (NIRv) is an important index for monitoring ecosystem functioning, and has previously been employed to link soil moisture induced vegetation stress with gross primary productivity (GPP) at various scales during drought events (Badgley et al., 2017; 2019; Baldocchi et al., 2020; Buitink et al., 2020). The NIRv index is derived from the product of the normalized difference vegetation index (NDVI) and near infra-red (NIR) reflectance ($NIRv = NDVI \times NIR$) (e.g. Badgley et al., 2017). We obtained daily MODIS (MCD43A4, version 6) red (620-670 nm) and NIR (841-876 nm) nadir-adjusted reflectance images from the same source (Schaaf and Wang, 2015).

The MODIS T_s and reflectance images are available at 1 km and 500 m resolutions, respectively and were obtained for the period of 2010 to 2019, corresponding with the period of AWS measurements outlined in Section 4.2.1. The T_s data obtained was derived from the Terra satellite which acquires data every 1 to 2 days, and passes from north to south over the equator in the morning, while reflectance data are derived from 16-day composites of MODIS Terra and Aqua satellite products. A summary description of data used is provided in Table 4.2.

Product	Variable	Resolution (Spatial, temporal)	Temporal coverage	Source
In situ	Global solar radiation/sunshine duration, 2-m temperature, relative humidity, m.s.l pressure, wind speed	Hourly	2010–2019	Met Éireann
Gridded	Precipitation	1 km ² , Daily	1999-2019	Met Éireann
	ERA5-Land surface volumetric water content (0-7cm)	0.1°, Hourly	1999-2019	Hersbach and Dee (2016)
Satellite	GEOV2 Leaf area index	1 km ² , 10-day	1999-2019	Verger et al. (2014)
	MOD11A1 land surface temperature	1 km, Daily	2010-2019	Wan et al. (2015)
	MCD43A4 nadir-adjusted red and near-infrared reflectances	500 m, Daily	2010-2019	Schaaf and Wang (2015)

Table 4.2. A summary description of in-situ, gridded and satellite-derived data products used in this study.

4.2.4 Model description

The land surface scheme (LSS) used in this study, fully described in Ishola et al. (2020) and Chapter 3, employs the widely utilised Monin-Obhukov Similarity Theory (MOST) (Section 2.2.3). MOST uses profile relationships of near-surface temperature, wind and humidity, to describe the vertical exchange of heat, moisture, and momentum, respectively with the atmosphere (Paulson, 1970). In addition, the scheme incorporates simplified parameterizations of radiation components and heat transport to the subsurface (following van Ulden and Holtslag, 1985) and the land surface energy budget is quantified using the Penman-Monteith model (Monteith, 1981). Here, we employ the land surface scheme with available in-situ meteorological data (Section 4.2.1) to simulate hourly surface energy fluxes

for mid-day hours (10-15 hr) from May to August, for the period 2010 to 2019. We focus on this portion of the day as the bulk of the land surface exchanges typically occur during this time interval.

During soil water limiting conditions, latent heat flux (Q_E) becomes constrained by the surface resistance (r_s). r_s , which is incorporated into the land surface scheme following the approach implemented by Beljaars and Bosveld (1997), van de Boer et al. (2014a) and see also Section 3.4.2, is based on the Jarvis approach (Jarvis 1976).

The r_s coefficients employed in the land surface scheme here were previously evaluated at a small number of sites in Ireland where in-situ soil moisture measurements were available (Chapter 3). However, as the present study employs gridded soil moisture derived from ERA5-Land reanalysis data, the land surface scheme may underestimate r_s and consequently, overestimate Q_E due to potential overestimation of soil water in extremely dry surface (Dirmeyer et al., 2021) (Figure 4.2). Due to the lack of measurements or information on field capacity nationally, we employ a default value for θ_{FC} of $0.3 \text{ m}^3 \text{ m}^{-3}$ which was a necessary assumption; in spite of this simplifying assumption, the focus of this study is on soil drying, and the general tendency of soil drying and its impact on evapotranspiration should be captured.

Furthermore, we calculated two biophysical metrics, land surface temperature (T_s) and evaporative fraction (EF), employing fluxes derived from the land surface scheme as follows,

$$T_s = T_a + \frac{Q_{Hra}}{\rho c_p} + z_a \Gamma_d, \quad (4.1)$$

$$EF = \frac{Q_E}{Q_N - Q_G}, \quad (4.2)$$

where T_a is the near-surface temperature, r_a is the aerodynamic resistance, z_a is the reference height, Γ_d is the dry adiabatic lapse rate, ρ is the air density and c_p is the specific heat capacity of air. These biophysical metrics are important for understanding the role of land-atmosphere feedbacks on extreme weather events such as heatwaves and drought.

4.2.5 Data analysis

We initially calculated anomalies (Z-score) of monthly precipitation, volumetric water content (θ) and LAI for the individual months of May to August, relative to the 1999 to 2019 period, to provide an initial overview of the evolution of the 2018 summer drought event. On the basis of definition of agricultural regions (see Chapter 1) and initial evaluation of precipitation, we subsequently grouped the individual AWS stations into broadly representative geographic regions (Figure 4.1). For example, the north west (Zone A) tends to be wetter and cooler, due to its proximity to Atlantic storm tracks, and has a large proportion of peat soils; the east coast (Zone B) is typically drier, receives more global solar radiation and has a high proportion of moderately and well drained soils. Similar to the north west region, the south west (Zone C) is also wet but experiences higher average temperatures; soils in this zone are mainly classified as imperfectly or poorly drained. Due to its favourable climate, this zone is dominated by grassland. The 'Golden Vale', a region known for its high quality dairy production systems, is located within this group. These zones provide the basis for presenting the results of the land surface scheme.

To analyse synoptic timescale variability during the 2018 event, cumulative precipitation and deviations of daily θ , vapour pressure deficit (VPD) and LAI are also calculated for each zone for the period May to August, relative to 2010 to 2019. We also applied segmented regression

to determine the relationship between daily soil moisture, sensible heat and latent heat fluxes, employing the evaporative fraction (EF) metric for the summer period in each zone. The goal is to identify if critical soil moisture thresholds occur and the period during which the soil moisture control of exchange processes become effective across the zones. We applied a similar approach to the NIRv data, as a way of comparing with the EF based approach, and which provides a means of linking soil moisture to vegetation productivity and ecosystem functioning.

For the segmented regression, we employed the approach of Muggeo (2003) to determine linear model-fits between soil moisture and anomalous surface fluxes, EF and NIRv to detect both the significant shift slope (sensitivity) and breakpoint between segments. The breakpoint value indicates the presence of a critical threshold of soil moisture at which the land-atmosphere shifts to 'hypersensitive' regimes, resulting in higher temperature and drier soils while the slope characterises the severity of dry/wet segments (Benson and Dirmeyer, 2020; Buitink et al., 2020). We used the CRAN R 'segmented' package to estimate these metrics (Muggeo, 2021).

4.3 Results

4.3.1 Evolution of 2018 summer drought across Ireland

Figure 4.3 shows the spatial characteristics of the 2018 summer standardized monthly total precipitation anomaly (Z-score), relative to 1999-2019 climatology across the region. Applying the McKee et al. (1993) drought categories, the 2018 meteorological drought progressively moved from mild/moderate drought conditions (0 - -1.49) in May to more widespread extreme drought conditions (< -2.0) in June, evident across the eastern, southern and south-

western part of the country, while the north-west continued with mild/moderate conditions (0 - -1.49) during these months. The rainfall deficits gradually improve in the subsequent months, with the July rainfall anomaly characterized as moderate drought conditions, with the exception of the midlands; August was characterized by mild drought conditions in the eastern and southern half of the country, with wet conditions (> 0) in the north and north-west. The mild drought conditions experienced in the north-west during June, relative to the rest of the country, were likely associated with the arrival of Storm Hector in mid-June, bringing rainfall across this region (Met Éireann, 2018a). The observed magnitude, extent and timing of the 2018 meteorological drought are in agreement with those reported by Falzoi et al. (2019).

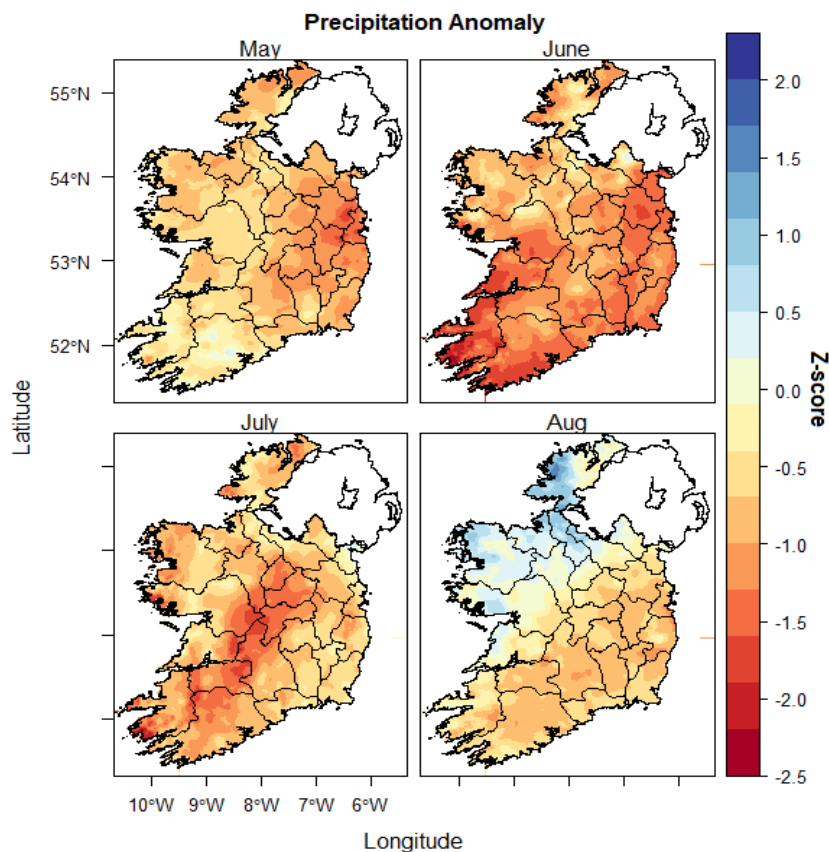


Figure 4.3. Spatial characteristics of monthly precipitation anomaly (z-score) for the Republic of Ireland during summer 2018, relative to 21-year climatology (1999-2019). Thin lines represent county outlines.

To assess the land surface response, the degree of surface dryness is initially characterized based on anomalies of soil moisture and LAI. Figure 4.4a shows the magnitude and spatial extent of ERA5-Land θ and GEOV2-LAI anomalies for the individual months of May to August, 2018. In contrast to the mild/moderate meteorological drought evident in May (Figure 4.3), the soil moisture conditions display normal conditions across the country – likely reflecting the fact that above average rainfall occurred at most stations in the preceding month of April (Met Eireann Report, 2018b). However, following the rainfall deficits which continued into June (Figure 4.3), soil moisture conditions deteriorate, particularly evident along the east coast (Figure 4.4a). By July, the surface conditions continue to deteriorate leading to high negative soil moisture anomalies (index < -2.0) being experienced across the country, with extreme negative anomalies (< -3.0) being experienced along the usually wet west coast.

While the negative soil moisture conditions began to improve or recover in the north and west during August, the east, south and southwest of the country continued to experience negative soil moisture anomalies. The impact on vegetation response, represented by anomalies in GEOV2 LAI, closely track the evolving soil moisture conditions (Figure 4.4b). These findings are consistent with those of Albergel et al. (2019), who found similar perturbations (index > -1.0 and -2.0) in surface soil moisture, derived from the Advanced Scatterometer (ASCAT), and GEOV2-LAI during the month of July in 2018 in the UK region. In addition, there is a strong spatial coherence between the gridded precipitation, ERA5-Land θ and satellite derived GEOV2-LAI in terms of the evolution of the meteorological and agricultural drought characteristics over the study period.

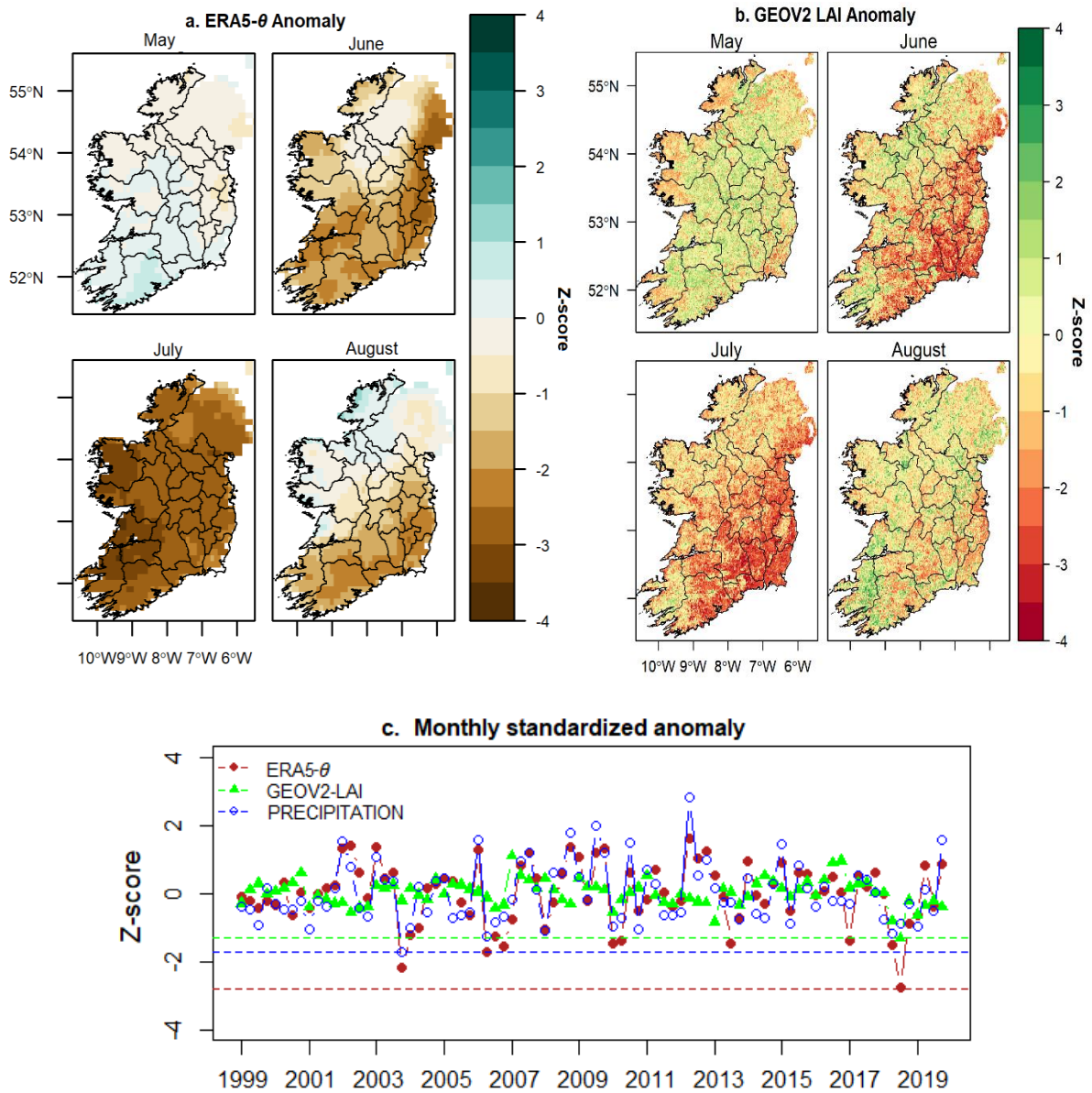


Figure 4.4. Monthly anomalies of ERA5-Land surface soil water content (θ) and satellite-derived GEOV2 leaf area index (LAI); for 2018 summer, relative to 21-year climatology (1999-2019). (a-b) the spatial characteristics of both parameters; (c) inter-annual variations of monthly anomalies of θ , LAI and gridded precipitation, averaged over the entire region (blue, red and green horizontal dotted lines show the lowest negative scores for precipitation, θ and LAI, respectively).

To place the conditions experienced during 2018 in context of previous summer drought events, Figure 4.4c displays the individual monthly (May, June, July and August) anomalies of rainfall, soil moisture (ERA5-Land θ) and LAI (GEOV2) for the period 1999 to 2019, averaged over the entire country. It is clear that larger rainfall deficits occurred during the 2003

European summer drought in Ireland, reported as one of the driest summers on record (e.g. Casty et al., 2005; Jaksic et al., 2006), yet no clear impact on vegetation productivity is observed during the 2003 drought event based on GEOV2-LAI. This suggests that the 2003 meteorological drought did not fully propagate into agricultural drought across the island, which may be related to the timing of the precipitation deficits, which occurred in August of that year. In contrast, summer 2018 shows both water and vegetation stress conditions, as revealed by the high negative anomalies in precipitation, θ and LAI (Figure 4.4c). In addition, the largest negative soil moisture and vegetation anomalies in the last 21 years occurred in July 2018, with a negative peak anomaly (≈ -2.8) for θ , concurrent with the peak negative anomaly (≈ -1.3) for LAI.

In the next section, we present the results of the land surface scheme, to explore if perturbations occurred in the surface energy budget which could have potentially contributed to aggravating the observed surface dryness across Ireland during the summer of 2018.

4.3.2 Perturbations of land-atmosphere energy exchanges

To evaluate the robustness of model-derived surface energy fluxes, we initially compared the mid-day temporal evolution of observed MODIS Terra (for pixels representing the individual weather stations (Figure 4.1) and the LSS derived surface temperature anomaly (ΔT_s) (Figure 4.5). Results show high positive ΔT_s for both the Terra and model estimates (peaking at +5-10 K and +8-15 K, respectively) between late June and early July across the selected stations. These results are consistent with previous findings (e.g. Zaitchik et al., 2006) and suggest the strong role of daytime anomalous surface feedbacks on atmospheric temperature during this period. While the temporal profiles of LSS-derived ΔT_s are largely consistent with the observed Terra ΔT_s across stations, the LSS estimates display a warm bias, which is likely

attributed to an offset in timing between the LSS estimated values and time of overpass of the satellite; the LSS-derived ΔT_s values are based on the average of mid-day values (from 10 to 15 hour), while Terra-derived ΔT_s values are based on satellite observations at the overpass (10.30 GMT). Consequently, the Terra-based ΔT_s are unlikely to capture the large magnitude in surface temperature which typically occurs in the afternoon, when insolation is at its peak.

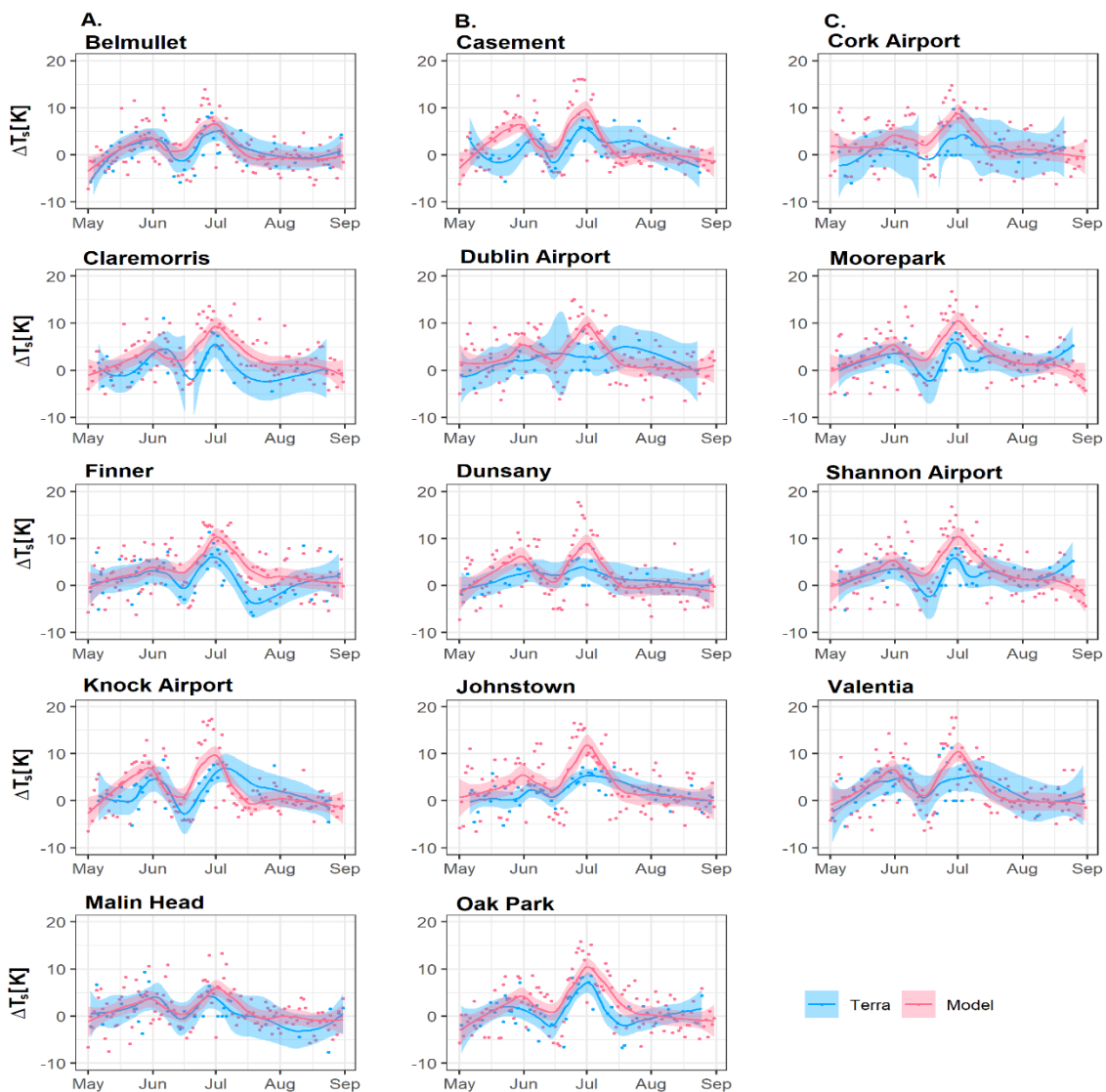


Figure 4.5. Temporal evolution of model-derived mid-day land surface temperature anomaly (ΔT_s), compared with MODIS Terra ΔT_s during 2018 summer, relative to 2010-2019 average across the stations. The lines are derived from smoothed fits of locally weighted polynomial regression (LOESS). The shaded portions are the 5th and 95th percentiles of uncertainty bound as calculated by LOESS. Panels A, B and C are for stations in zones A, B and C, respectively, as highlighted in Figure 4.1 and Table 4.1.

Figure 4.6 shows the temporal evolution of in-situ accumulated rainfall (Figure 4.6 a-c), ERA5-Land volumetric water content (Figure 4.6 d-f), in-situ vapour pressure deficit (Figure 4.6 g-i) and satellite-derived leaf area index (Figure 4.6 j-l) for the period May to August 2018, compared with the climatology (1999-2019), aggregated for the three zones (A, B, C) previously outlined (Figure 4.1).

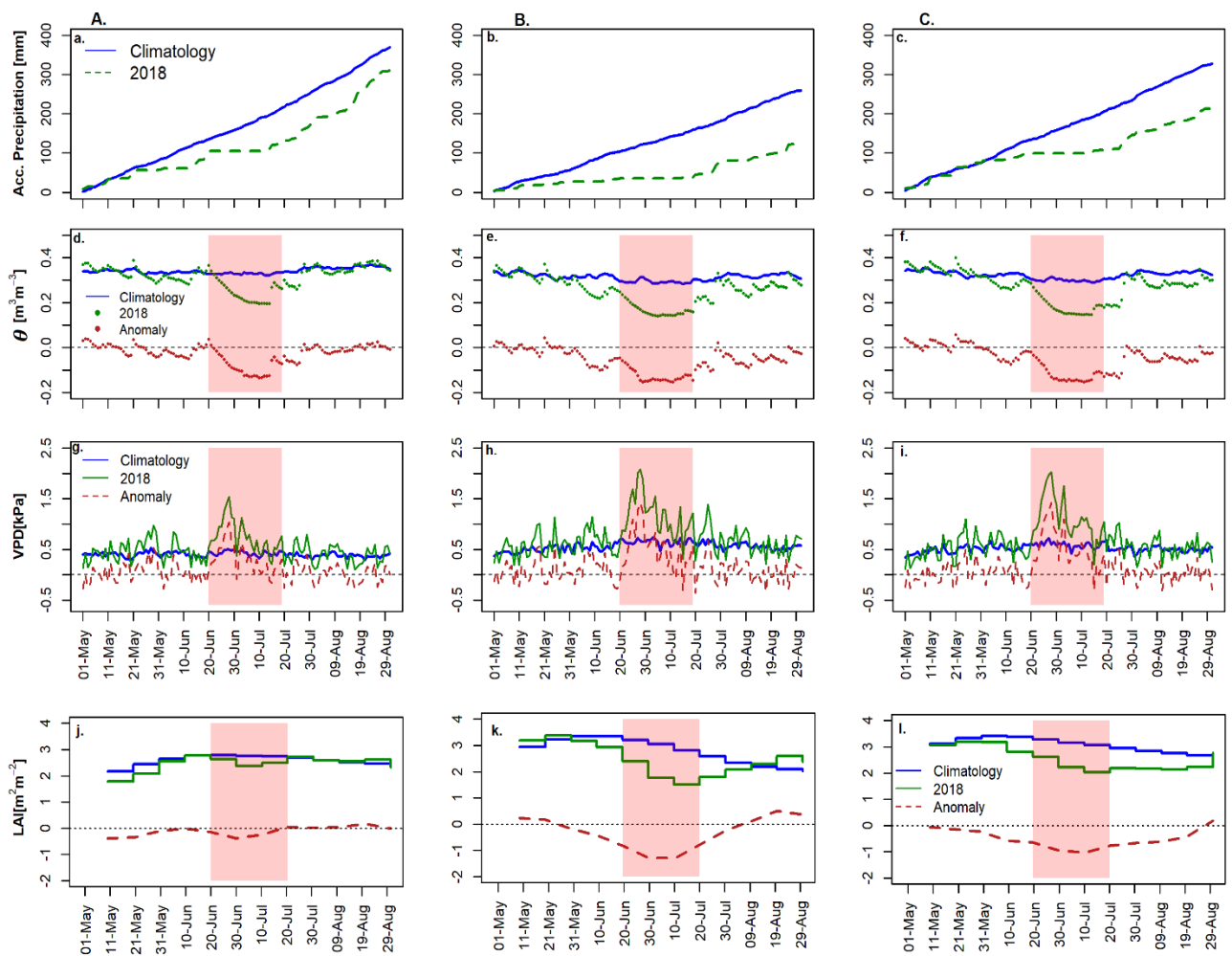


Figure 4.6. Temporal evolution of in situ accumulated precipitation (first row), ERA5-Land volumetric water content (second row), in situ vapour pressure deficit (third row) and satellite-derived leaf area index (fourth row); during 2018 summer compared with climatology (1999-2019). Panels A, B and C are for stations in the respective zones highlighted in Figure 4.1. The peach shades represent the observed periods of abnormal surface and atmospheric conditions

In each zone, the cumulative rainfall clearly shows a departure from climatology beginning from just prior to, or around, June 1 (Figure 4.6 a-c). In the northwest (zone A), the 2018 cumulative rainfall, while lower, remains closer to climatology, indicating smaller rainfall

deficits during June-August, relative to zones B (east coast) and C (southwest). This is consistent with the gridded precipitation data in Figure 4.3. The rainfall deficits also begin later in zone C.

In the northwest (zone A), decreasing volumetric soil moisture (θ) (Figure 4.6d) becomes evident from mid-June (approx. 2-3 weeks after the onset of meteorological drought), likely buffered by the normal or above normal rainfall receipts in April and the arrival of Storm Hector in the northwest in mid-June, and reach their lowest negative anomaly (relative to the climatology) of approximately $-0.13 \text{ m}^3 \text{ m}^{-3}$ (40 %) around 4 July. Concurrently, vapour pressure deficits (VPD) increased above normal effective from 21 June and peak on the 27-28 June with anomalous values (> 200 % relative change) of +1.0 kPa (Figure 4.6g), while LAI shows negligible change during this period (Figure 4.6j).

For the east of the country (zone B), the negative θ anomaly (relative change), which began earlier than in zone A (northwest), decreased by $-0.15 \text{ m}^3 \text{ m}^{-3}$ (50 %), corresponding with the highest positive VPD anomaly of +1.4 kPa (> 200 %) and lowest negative anomaly of LAI of $-1.5 \text{ m}^2 \text{ m}^{-2}$, from 28 June (Figure 4.6 e, h, k). The timing of changes in θ , VPD and LAI in the southwest (zone C) (Figure 4.6 f, i, l) largely follow those observed in the east (zone B), but slightly reduced in magnitude.

The highlighted periods of strong surface (e.g. soil moisture, LAI) and atmospheric (e.g. rainfall, VPD) anomalies largely correspond to the LSS simulated periods of higher positive anomalies (relative change) in both the net radiative and energy fluxes. ΔQ_N anomalies $\approx +200\text{-}250 \text{ W m}^{-2}$ (80-90 % relative increase) across the three zones (Figure 4.7a-c) indicate the strong and persistent influence of the anticyclonic system, suppressing low cloud formation over the land surface, between 22 June and 3 July across all the country. In spite of the

similarity in radiative forcing conditions, anomalies in the mid-day sensible (ΔQ_H) and latent (ΔQ_E) heat fluxes differ across each of the zones, reflecting differences in the partitioning of available energy. For instance, in the northwest (zone A), the net radiation surplus gives rise to an anomaly in ΔQ_E , of +100-120 W m⁻² (\approx 90 % relative increase), largely at the cost of ΔQ_H . This is consistent with higher ΔQ_N and VPD, with plants still able to access available, but declining, soil water, between the 22 – 30 June (Figure 4.7d). While the general responses are similar for zones B and C, with the land surface scheme simulating an enhanced positive ΔQ_E anomaly, of +60-90 W m⁻² (40-90 % relative increase) and +50-100 W m⁻² (30-70 % relative increase), respectively (Figure 4.7e-f). However, by the end of June, ΔQ_H exceeds ΔQ_E in zone B (east) and ΔQ_H is equivalent to ΔQ_E in zone C (southwest), providing mechanistic evidence of the land-atmosphere feedback resulting in enhanced VPD (Figure 4.6 h, i) relative to zone A (Figure 4.6g), starting from 27 June in zone B (Figure 4.7e) and 1 July in zone C (Figure 4.7f). Generally, these results indicate positive ΔQ_E anomalies, in excess of normal, enhanced by high positive anomalies of ΔQ_N prior to 27th June. The observed changes between late June and early July in the east (zone B) and southwest (zone C) highlight the potential differentiating role of soil moisture availability, and support the divergent landscape physiological responses (Figure 4.4b) to atmospheric anomalies relative to the northwest (zone A).

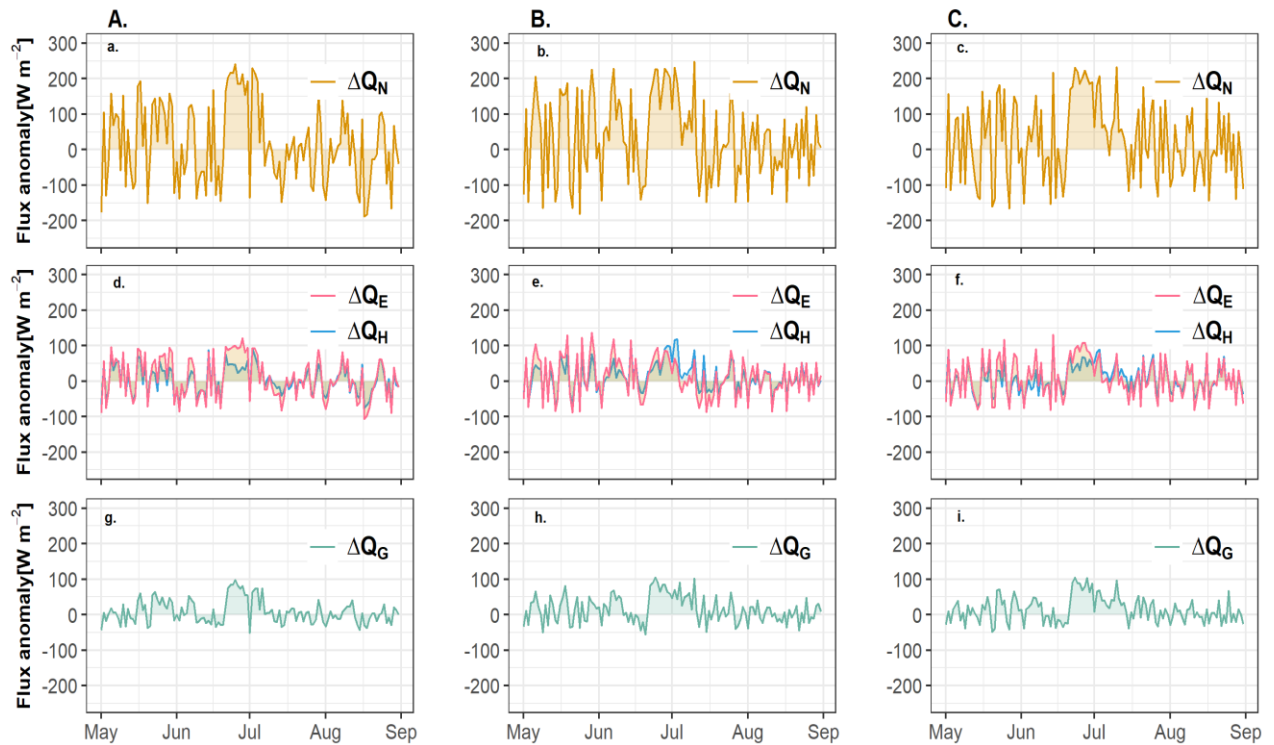


Figure 4.7. Temporal evolution of model-derived mid-day anomalous net radiative flux (ΔQ_N) (first row), sensible heat (ΔQ_H) and latent heat (ΔQ_E) fluxes (second row) and soil heat flux (ΔQ_G) (third row), during 2018 summer, relative to analysis period (2010-2019). Panels A, B and C are for stations in the respective zones highlighted in Figure 4.1. Values represent the day time (10:00-15:00) average.

4.3.3 Relationship between soil moisture and surface flux densities

To try to understand the role of soil moisture availability on the anomalous land-atmosphere heat and moisture exchanges during summer 2018, we explored the relationships between daily ERA5-Land soil moisture and anomalies of EF and NIRv (Figure 4.8), and separately for sensible and latent heat flux anomalies (Figure 4.9), based on the metrics (slope and breakpoints) derived from segmented regression models for each zone. The segmented regression results for individual stations and the contour map of the onset of agricultural drought based on estimated θ_c are provided in Table 4.3 and Figure 4.10, respectively. It should be noted that the results here are exploratory and based on a LSS specified θ_{FC} value ($0.3 \text{ m}^3 \text{ m}^{-3}$), as stated previously.

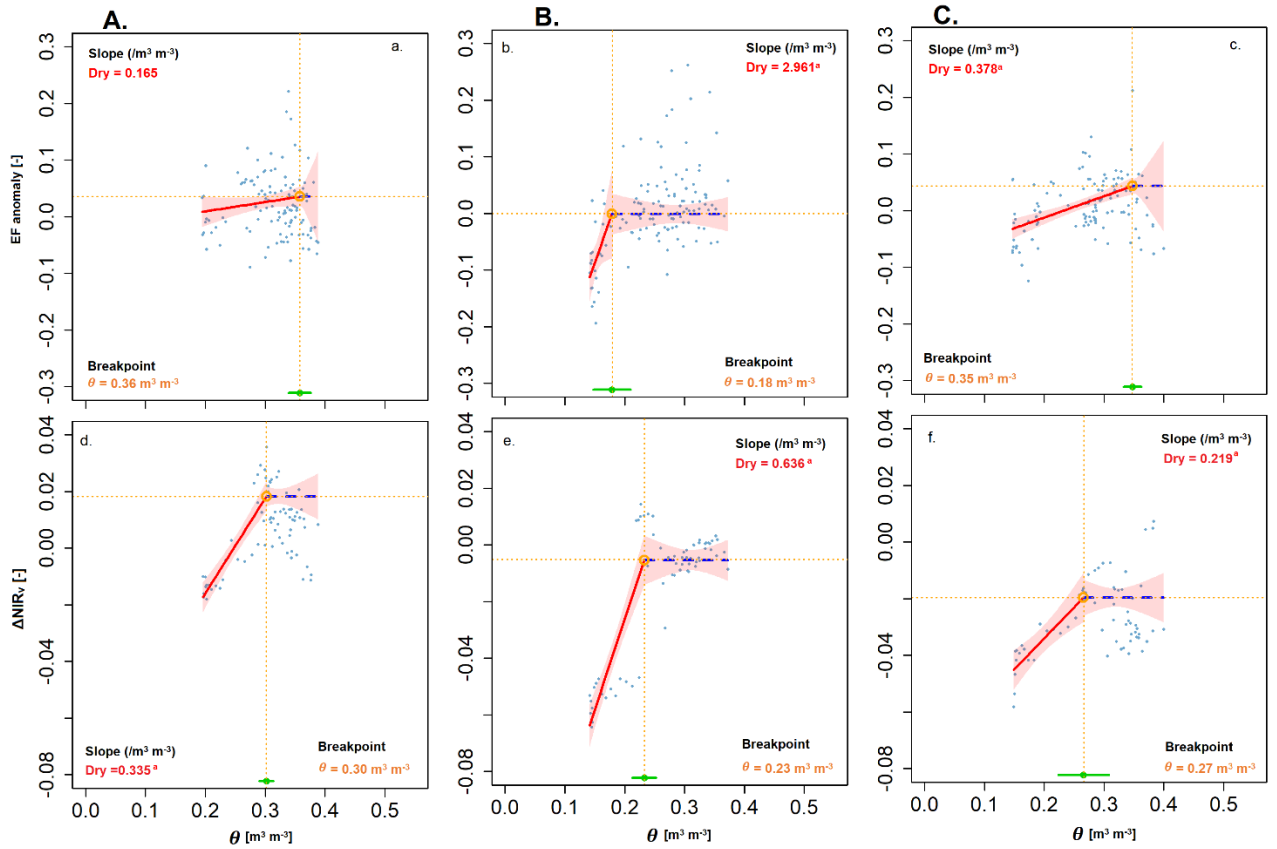


Figure 4.8. Relationships between soil moisture (θ), evaporative fraction (EF) [first row] and MODIS NIRv [second row], based on segmented regression analysis during 2018 summer across the zones. The thick red lines are measures of sensitivity (slope) on the dry segment while dashed blue lines are for wet segment. The dashed orange lines show the θ -EF and θ -NIRv breakpoints and the horizontal green lines at the bottom show the confidence interval of θ breakpoints. ^a significant at p -value < 0.05. Panels A, B and C are for stations in the respective zones highlighted in Figure 4.1.

While the models detect a breakpoint (critical θ threshold, $\theta_c \approx 0.36 \text{ m}^3 \text{ m}^{-3}$) separating wet and transitional regime in the northwest zone (zone A) (Figure 4.8a), the $\frac{\delta EF}{\delta \theta}$ sensitivity in the transitional segment (adjusted $R^2 = 0.05$) is insignificant and relatively low (close to 0). In contrast, the $\frac{\delta NIRv}{\delta \theta}$ approach identified a critical θ threshold (θ_c) $\approx 0.30 \text{ m}^3 \text{ m}^{-3}$ with a higher sensitivity indicated in the transitional segment (adjusted $R^2 = 0.60$) (Figure 4.8d). This indicates that the landscapes in zone A (northwest) largely sustain the conditions in which changes in EF is independent of soil moisture during the hydrological season. The direction of the slope in the wet segment is not considered realistic, which may be informed by the

optimization routines used to detect the critical points that separate the segmented fits. However, the θ -EF relationship is clearly captured in the east (zone B) (Figure 4.8 b, e) where the approach identified a critical threshold θ_c of $\approx 0.18 \text{ m}^3 \text{ m}^{-3}$, a value that is likely to lie close to the wilting point

The sensitivity ($\frac{\delta EF}{\delta \theta} \approx 0$) is negligible in the wet segment, but a significant and steep slope is observed in the transitional segment (adjusted $R^2 = 0.29$), indicating that EF is constrained and linearly coupled with the surface during the period when soil moisture content is below the critical point. Findings are consistent for the θ -NIRv approach ($\theta_c = 0.23 \text{ m}^3 \text{ m}^{-3}$ and adjusted $R^2 = 0.77$). The estimated θ_c values are identical to those derived using measured θ at deeper soil layer, from two sites in the Netherlands (Buitink et al., 2020). Hence, these findings suggest that drying soils increase the sensitivity of land-atmosphere coupling, in turn aggravating the surface drying, based on ERA5-Land θ (note that ERA5-Land underestimates very dry soils for a number of Irish sites). The results of this exploratory analysis in the southwest (zone C) identify a critical θ threshold (θ_c) $\approx 0.35 \text{ m}^3 \text{ m}^{-3}$, similar to zone A, but with a significantly higher $\frac{\delta EF}{\delta \theta}$ sensitivity in the transitional segment (adjusted $R^2 = 0.23$) (Figure 4.8c). Comparing with the θ -NIRv approach, the sensitivity is similar (adjusted $R^2 = 0.32$) but with a higher estimate ($0.35 \text{ m}^3 \text{ m}^{-3}$) of θ_c (Figure 4.8f).

Both the EF and NIRv approaches agree on the coupling for zones B (east) and C (southwest), however, the differences in estimated θ_c suggest causality in θ -EF framework that may not be inferred using statistical regression analysis. Independent assessments based on the relations of ERA5-Land θ with model-derived sensible heat (Q_H) and latent heat (Q_E) fluxes (Figure 4.9) show that Q_H is the major mechanistic factor driving the θ -EF signals, and likely

responsible for the increased atmospheric sensitivity that contributed to occurrence of the abnormally warm and dry days during summer 2018, as revealed in zones B and C.

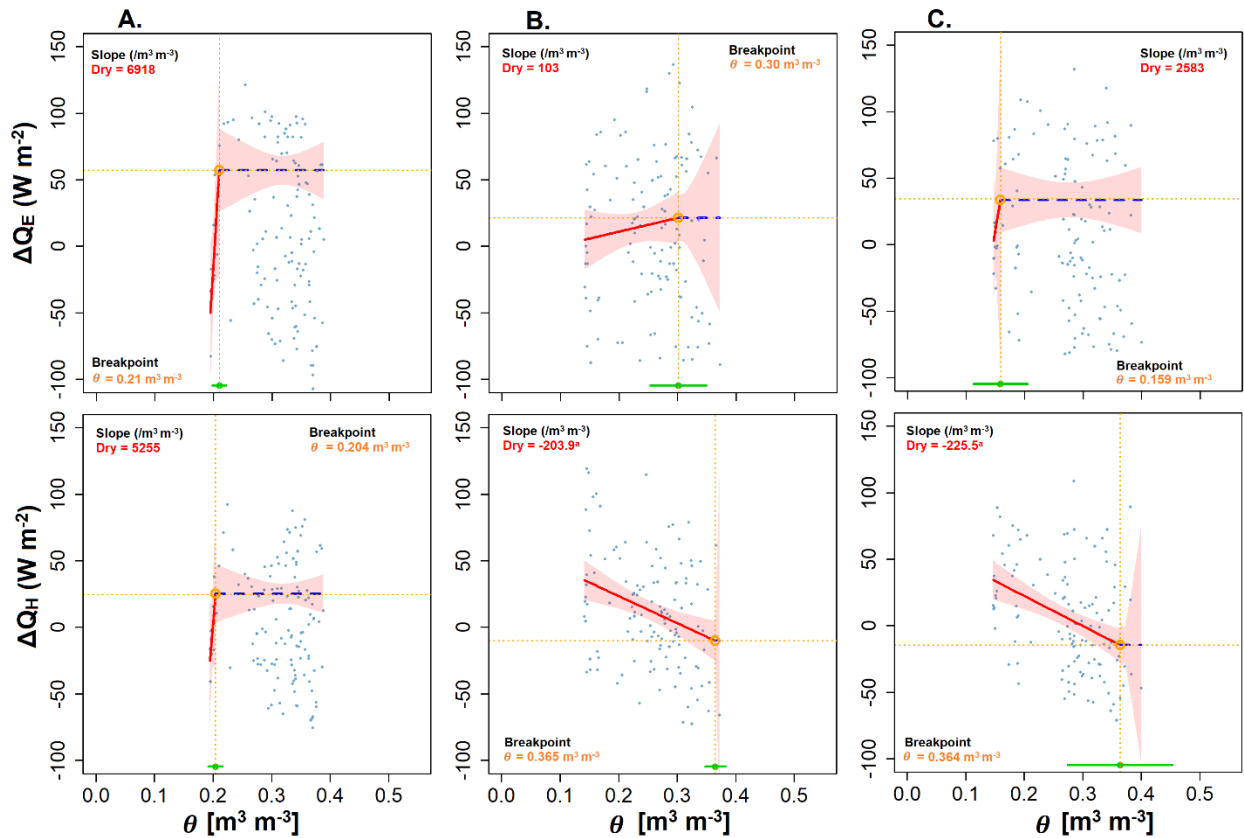


Figure 4.9. Relationships between soil moisture (θ), latent heat flux (ΔQ_E) [first row] and sensible heat flux (ΔQ_H) [second row], based on segmented regression analysis during 2018 summer across the zones. The thick red lines are measures of sensitivity (slope) on the dry segment while dashed blue lines are for wet segment. The dashed orange lines show the θ - ΔQ_E and θ - ΔQ_H breakpoints and the horizontal green lines at the bottom show the confidence interval of θ breakpoints. ^a significant at p -value < 0.05. Panels A, B and C are for stations in zones A, B and C, respectively, as highlighted in Figure 4.1 and Table 4.1.

Station	EF			NIRv		
	θ_c	R^2_{adj}	Start date	θ_c	R^2_{adj}	Start date
Belmullet	0.282	0.04	12 June	0.295	0.37	08 June
Claremorris	0.388	0.09	22 May	0.373	0.18	23 May
Finner	0.244	0.08	09 July	0.328	0.21	26 June
Knock Airport	0.375	0.14	20 June	0.249	0.04	29 June
Malin-Head	0.177	0.28	26 June	0.138	0.46	29 June
Casement	0.203	0.09	26 June	0.389	0.72	22 May
Dublin Airport	0.109	0.48	26 June	0.154	0.31	22 June
Dunsany	0.315	0.04	06 June	0.327	0.26	05 June
Johnstown Castle	0.146	0.44	26 June	0.138	0.59	27 June
Oak Park	0.296	0.10	19 June	0.269	0.56	22 June
Cork Airport	0.336	0.05	28 May	0.177	0.56	29 June
Moorepark	0.358	0.06	27 May	0.218	0.40	25 June
Shannon Airport	0.431	0.10	25 May	0.218	0.04	29 June
Valentia	0.178	0.42	24 June	0.226	-0.002	15 June

Table 4.3. Site-specific ERA5-based critical soil moisture content (θ_c , $\text{m}^3 \text{m}^{-3}$) (0-7cm layer) and date of onset of 2018 agricultural drought, derived using segmented regression relationships between θ , evaporative fraction (EF), and MODIS NIRv. Stations with relatively stronger θ -EF and θ -NIRv couplings are highlighted in bold. R^2_{adj} is the adjusted R^2 .

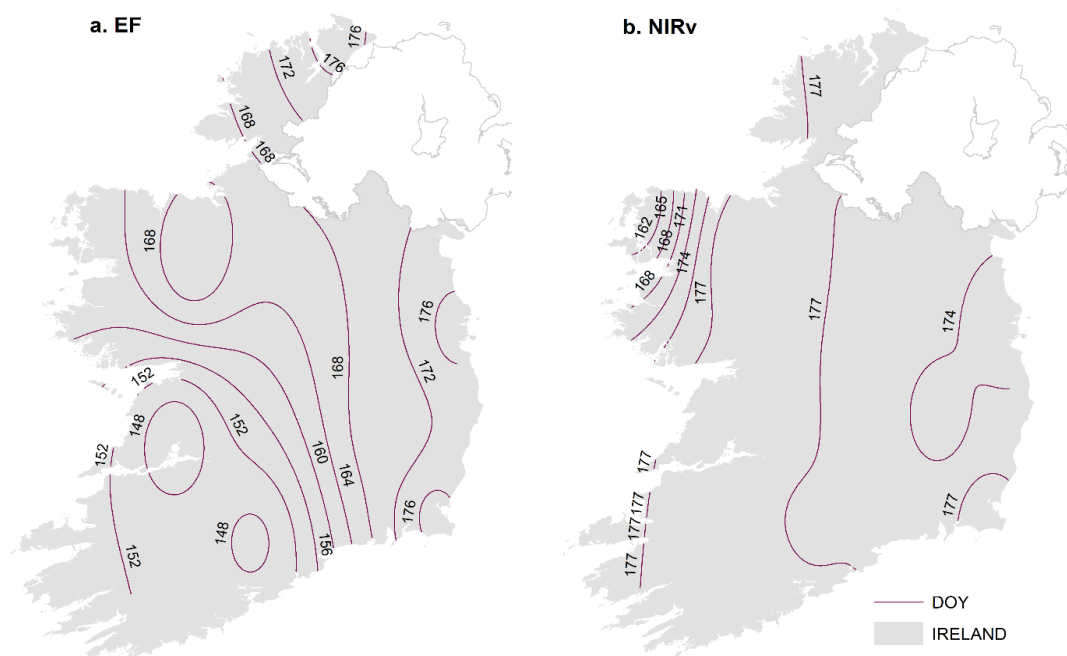


Figure 4.10. Contour maps of the approximate start day of 2018 agricultural drought, based on the estimated critical soil moisture threshold (θ_c) in Table 4.3 for (a) evaporative fraction and (EF), (b) near-infrared reflectance of vegetation (NIRv). DOY is the day of the year.

4.4. Discussion

In this study, we evaluated the use of a land surface scheme that employed readily available meteorological data to assess the impact of the 2018 summer drought on regional land-atmosphere heat and moisture exchanges. Although, previous studies (e.g. Teuling et al., 2010; van Heerwaarden and Teuling, 2014; Stap et al., 2014; Lansu et al., 2020) found contrasting landscape response (Forest and grassland) to land-atmosphere exchange processes during heatwaves and droughts, knowledge of the mechanisms driving the environmental and vegetation response to land surface processes remains limited (e.g. Streck, 2003; Teuling, 2018). Here, we largely focus on grass land cover. Our aim is to evaluate the utility of a physically-based scheme, and multi-source data, to explore the regional characteristics of anomalous land surface processes during the unusually warm and dry conditions experienced in summer 2018.

4.4.1 Changes in land surface processes during severe drought

During extreme weather events such as drought, perturbations in the surface energy budget will drive changes in near-surface temperature and reductions in available soil water. In soils with limited available water (high soil moisture deficit), plant water uptake to meet the increasing atmospheric evaporative demand will be restricted (Teuling, 2018), as a result, available Q_N will be converted to Q_H flux. This describes a positive feedback on Q_H , which can act to amplify drought characteristics. The perturbations of surface exchanges of heat and moisture which impact the patterns of atmospheric temperature are mediated through changes in soil moisture (e.g. Seneviratne et al., 2010; Miralles et al., 2014). Findings from this analysis indicate that an excess in net radiative fluxes (ΔQ_N) was evident from May to July across the country. Changes in leaf area index were relatively small during this period, likely

resulting in very small changes in surface shortwave reflection concomitant with low surface albedo changes, and consequently with negligible impact on Q_N (Teuling and Seneviratne, 2008; Teuling et al., 2010). Rather, the anomalously high Q_N values are associated with higher downward shortwave radiation fluxes resulting from the suppression of cloud formation due to the presence of a high pressure system in the mid-troposphere (e.g Black et al., 2004; Stap et al., 2014).

During the identified peak period of net radiation receipt (middle of June; to start of July), decreasing soil moisture and increasing VPD is evident in the ERA5-Land soil moisture and in situ derived vapour deficit values, respectively (Figure 4.6 d-i). LAI response to the changing land surface characteristics is evident in the east and south east (zone B) and southwest (zone C) regions (Figure 4.6 k-l). While the north west (zone A) displays an increase in VPD and declining soil moisture over this period, the vegetation response is less marked in the LAI response (Figure 4.6b; Figure 4.6j), relative to the climatology, for this region.

On the basis of the land surface scheme, the available Q_N was largely converted to Q_E rather than Q_H during this period in the northwest, which is typical of grasslands even under extremely warm temperatures (Teuling et al., 2010; van Heerwaarden and Teuling, 2014; Stap et al., 2014; Lansu et al., 2020). The preferential channelling of available energy into Q_E is similar for the east (zone B) and the southwest (zone C), but with lower magnitude Q_E anomalies. This enhancement of land-atmosphere Q_E transfer even under water limited conditions was likely facilitated by the integrated effects of higher downward shortwave radiation and increased VPD (associated with higher temperature due to a weak atmospheric moisture advection from the Atlantic Ocean) that characterized the period between mid-June to early July. The lower magnitude Q_E values in the east (zone B) are compensated for by

increasing Q_H – resulting in higher surface temperature - the shift from latent to sensible heat is also apparent in the negative anomalies of LAI in the east and southeast during the month of June (Figure 4.4b). The shift from latent to sensible heat and reduction in LAI during June and July indicate increasing soil moisture deficits, and hence vegetation stress in the region (Figure 4.6e). These results are in broad agreement with Lu et al. (2011) who attributed the 2009-2010 severe surface drying in China to a high rainfall deficits and warmer temperatures, through enhancement in Q_E .

However, the landscapes in the east of the country responded faster to the atmospheric anomaly, evident in the decrease in LAI (Figure 4.4b) and increasing VPD (Figure 4.6h), between June and July. A number of contributing factors are likely to explain this; the southeast is characterised by relatively well drained soils and can experience seasonal soil moisture deficits during ‘normal’ years. The month of April 2018 experienced average, or above average, rainfall across most stations; where soils have storage capacity, such as the imperfectly or poorly drained soils more typical of the southwest and northwest, they provide a temporary storage buffer during periods when rainfall receipts are below average. The arrival of Storm Hector in the middle of June resulted in soil moisture returning to normal levels in the northwest (zone A) (Figure 4.6d) and southwest (zone C) (Figure 4.6f).

Soil drying was more advanced in the east (Figure 4.6e) and increased due to high Q_E during June (Figure 4.7b) with a marked response in vegetation, evident in the negative anomalies of LAI, in the zone during June. By July, with soil moisture depleted evident in the simulated below normal/negative anomalies of Q_E (Figure 4.7b), the positive Q_N anomaly is subsequently partitioned into Q_H and Q_G . The net effect of the altered partitioning of available energy produced a land-atmosphere feedback that further exacerbated the soil

moisture and vegetation stress in this zone. A similar reasoning applies to zone C based on the LSS simulated fluxes (Figure 4.7c) and is supported by the increasing negative anomalies in LAI in the southwest during this month. The periods when the negative impact of high soil moisture deficit outweigh the potential enhancement effects of higher downward shortwave radiation and VPD therefore depend on the antecedent conditions, geographical area and soil characteristics, findings that are consistent with Xiao et al. (2009) and Zhang et al. (2012).

Across the zones, the lower but positive LSS-derived ΔQ_H , relative to other energy components, indicates a weak horizontal advection of warm air in May and June, typical of humid climate. In addition, positive anomalous surface heat and moisture transfers are largely correlated with an increase in net radiative flux during early summer. This suggests that the exchange processes are largely constrained by atmospheric anomalies during the hydrological season. In the east (zone B), the simulated negative ΔQ_E flux in July is explained by reduced evapotranspiration due to water-stress conditions which has propagated into the root zone. In addition, the landscapes that characterize this zone are largely dominated by free-draining soils (Creamer et al., 2014), suggesting low water holding capacity and quicker response of the landscapes to atmospheric anomalies, relative to the rest of the country. Although, the landscapes in southwest zone closely replicate these processes, our analysis shows relatively small positive ΔQ_E in contrast to the former zone in July, suggesting a continued evapotranspiration process even under water shortage.

4.4.2 Role of soil moisture in land-atmosphere exchanges during 2018 summer

Soil moisture can significantly influence terrestrial water, energy and carbon cycle through its control on Q_E at the land-atmosphere interface. This connection can be explored using a soil moisture-evaporative fraction (θ -EF) framework that distinguishes three different stages of

transition from wet to dry evaporative regime (Seneviratne et al., 2010; Teuling et al., 2010): (1) wet regime in which EF is independent of soil moisture (2) transitional regime where soil moisture and EF are linearly coupled and (3) dry regime where EF becomes negligible. Initial exploration of these relationships enable an estimate of the critical soil moisture value (widely referred to as critical soil moisture thresholds) that separate these regimes, and potentially diagnose the mechanisms responsible for the shift from a normal into a water-stress regime, where the land surface state controls the sensitivity of the atmosphere (Seneviratne et al., 2010).

We applied segmented regression analysis on the ERA5-Land θ and estimated EF anomaly to identify the threshold in soil moisture that marks the transition from wet to transitional regime; a similar approach was applied to the NIRv data. In the east, this shift was identified as occurring in late June ($\approx 22^{\text{nd}}$ June), indicating the onset of agricultural drought. The transitional regime was sustained for several days (20) during which θ -EF are linearly coupled (higher $\frac{\delta EF}{\delta \theta}$ sensitivity), providing the mechanism that contributes to ‘hypersensitive’ atmospheric anomalies during these periods, and further exacerbated agricultural drought in the affected areas. In a previous study over grassland above saturated soils in the south of Ireland, Jaksic et al. (2006) reported that measured soil moisture status in both dry and wet years are different, but well above wilting point, so that the impact of soil moisture status on net ecosystem functioning is small and identical for both years. This is consistent with our findings over zones A where the landscape either shows no $\frac{\delta EF}{\delta \theta}$ sensitivity or the θ -EF coupling is too weak to support the theoretical θ -EF framework (Seneviratne et al., 2010). Results from the $\frac{\delta EF}{\delta \theta}$ analysis in the southwest also indicated a weak coupling, however, the land surface response to reduce soil moisture is evident in the vegetation response (Figure 4.4b) – further

work is necessary to explore this. ERA5-Land uses monthly climatology of LAI to generate the global reanalyses data (Boussetta et al., 2013), which may contribute to weak θ -EF signals in these zones.

There is the possibility that ERA5-Land may have underestimate very dry soils as demonstrated in Figure 4.2, consequently resulting in the LSS to underestimate the impact of soil moisture anomalies on land-atmosphere feedback mechanisms. This is consistent with Dirmeyer et al. (2021) who noted that ERA5-Land underestimates the impact of very dry soils on extreme temperatures, over Britain in 2018 summer. A further assessment indicates that the signal in EF is largely driven by Q_H during the transitional regimes, as revealed in the east (Figure 4.9). Therefore, Q_H appears to be the mechanistic factor responsible for the unusual shift in land-atmosphere coupling and consequently amplified agricultural drought during summer 2018. Finally, the assumed volumetric water content at field capacity (θ_{FC}) of $0.3 \text{ m}^3 \text{ m}^{-3}$, necessary to apply the LSS in the absence of measured soil moisture, may also have contributed.

4.5 Conclusion

In this study, we evaluated the use of a physically-based land surface scheme, in combination with readily available ERA5-Land global reanalyses surface soil moisture data, satellite-derived CGLS leaf area index (LAI) and ground-based meteorology, to estimate the surface flux densities and evaporative fraction (EF) to understand the land surface response to the atmospheric forcing during the Summer of 2018. The approach allows us to explore changes in land surface processes and the effect of a soil moisture regime shift on land-atmosphere sensitivities. We demonstrate the application of this framework, utilising data from fourteen

weather stations, across Ireland during the 2018 summer record-breaking heat and drought events.

The study revealed synoptic variability in anomalous land-atmosphere heat and moisture transfers, across the stations and between dates. Drought-induced perturbations in land surface processes are largely not effective until the period between late June/early July and extend to mid-July in some cases. Prior to this period, the processes were constrained by atmospheric anomalies. That is, in the absence of rainfall, the rising evaporative demand due to warmer temperature enhanced latent heat flux (Q_E) via increase in evapotranspiration (ET) rates, leading to the higher soil moisture deficits in July across the country. This is particularly apparent in the east and southeast regions, where the drying soils quickly shifted into a 'transitional' regime in which EF is self-limiting, consequently providing positive land-atmosphere feedback mechanism (increase in land surface temperature and Q_H), beginning from 27th June and further exacerbated agricultural drought in July.

Segmented regression analysis of θ -EF interplay has found significant critical soil moisture threshold ($\theta_c \approx 0.18 \text{ m}^3 \text{ m}^{-3}$, and $\theta_c \approx 0.23 \text{ m}^3 \text{ m}^{-3}$ for θ -NIRv analysis) at which land-atmosphere signals potentially become hypersensitive in the east and southeast zone, based on ERA5-Land. These values also represent the point of onset of drought impact on landscapes and ecosystem functioning in this region. Although, the segmented models also identified soil moisture shift across the rest of the country, the linear θ -EF coupling was too weak to conclude that EF was constrained by land surface state in these areas. While spatial variations in precipitation and local effects of soil and vegetation structures may play a critical role in the differing land responses, it should be noted that ERA5-Land underestimates seasonally dry soil moisture regimes for Irish landscapes, which may have lessened the impact

of soil moisture anomalies on the exchange processes across the region. Nonetheless, the findings of this study are invaluable to speculate the zones and critical soil moisture values under which land-atmosphere exchanges are constrained by the land surface state and further exacerbate surface warming and dryness. This contribution is important, certainly for Ireland, not only because it may help improve the representation of soil moisture factors in Numerical Weather Prediction (NWP) models, but can also help to enhance subseasonal-to-seasonal predictability of drought propagation and early warning systems of summer climate extremes in the future episodes.

5. Mapping High-Resolution Farm-Scale Water Use of Pasture Lands using Sentinel-2 Data: Application for Grass Yield Prediction

Preface

In draft as:

K. A. Ishola, R. M., Fealy, G. Mills, S., Green, R. Fealy. Mapping high-resolution water use efficiency of pasture lands using Sentinel-2 data: Application for grass yield prediction, 1-30pp – In preparation for submission to *International Journal of Applied Earth Observation and Geoinformation*.

In this chapter, the response of plant productivity to climate conditions is assessed at a farm scale using Sentinel-2 products. We focus on mapping evapotranspiration (ET) and gross primary productivity (GPP) that are linked through water use efficiency (WUE) at ecosystem level and are more relevant to agriculture and agricultural applications. ET which is a measure of latent heat flux, a surface energy budget term, is regulated by surface resistance (Chapter 3) when surface-air exchanges are limited by water availability that is distinguished based on the so called critical soil moisture content (Chapter 4). The ET is derived from the validated LSS (Chapters 3-4) at Sentinel-2 scale and GPP is based on Sentinel-2 derived data (fraction of absorbed photosynthetically active radiation FAPAR and near infrared reflectance of radiation NIRv) using physiological models. The chapter/paper (see supplementary information paper 3 for full manuscript to be submitted) broadly addressed the pursuant questions: **Can the validated LSS (Chapters 3-4) be used to examine carbon uptake and water exchanges during dry and wet regimes, and be used to evaluate water use efficiency and grass yield at a farm scale?**

As discussed in Section 1.1, pastoral farming accounts for over 80% exports of agri-food, resulting to growing interests by farmers and other related stakeholders to optimize and sustain growth in farm production in the country. Here, the development of pasture WUE

maps will support the farmers to make informed on-farm decisions akin to water management and productivity.

Abstract

In this study, we used remotely sensed data from MultiSpectral Instrument (MSI) on board Sentinel-2 satellite, in combination with a land surface scheme to generate high-resolution (10 m pixel size) maps of daily actual evapotranspiration (ET), gross primary productivity (GPP), and water-use efficiency (WUE) at ecosystem level. The aim was to investigate the potential of ecosystem WUE as a yield prediction tool for pasture farms. The study was conducted using cloud-free image dates over 2017-2018, covering three selected pasture research farms that broadly represent the farming population across Ireland. Findings (WUE ≈ 1.0 - $1.5 \text{ g C kg}^{-1} \text{ H}_2\text{O}^{-1}$) indicate that the rates of water loss through transpiration are nearly equal to the rates of photosynthetic carbon uptake during the period when the vegetation is most productive across the farms. During severe surface drying and vegetation stress in July of 2018, the study revealed a substantial reduction in ET over grass, possibly due to shallow roots that engendered water restrictions and stomatal closure. As a consequence, ecosystem WUE increased exponentially over grass, much more at Johnstown Castle farm than the other (Athenry and Moorepark) research farms. The observed stronger ET-GPP couplings ($R^2 \approx 0.9$) and lower WUE at the latter farms suggest that these areas are more productive than the former pasture farm, over the analysis period. Additionally, the WUE improved the correlations between ecosystem indicators and grass yields, relative to ET at farm-scale. Therefore, the study demonstrates the utility of remotely sensed Sentinel-2 observations to provide spatially explicit information about the potential of WUE as a tool for distinguishing optimal zones of productivity, and for prediction of grass growth response to climate change.

5.1 Introduction

Terrestrial evapotranspiration (ET) and water-use efficiency (WUE) of plants are important indicators that can assist farmers in understanding the crop water and carbon dynamics for optimization of water use, nutrient management and plant productivity within their farms. These ecosystem indicators are also key for linking terrestrial energy, water, carbon to weather and climate (e.g. Ma et al., 2021). Quantifying these indices at detailed spatial scales can provide an important tool for use in precision agriculture, more sustainable land and water use and both hydrological and climatological applications in a changing climate.

ET dynamics are influenced by a range of factors including surface heterogeneity, vegetation cover/crop type, soil type, soil water availability and atmospheric conditions; management practices can also influence ET (e.g. irrigation or drainage; altered herbivory through pasture management etc). While there are a number of techniques to measure or estimate ET, providing field scale information remains challenging. Satellite remote sensing (RS) techniques serve as a viable and cost effective alternative which have been widely used for estimation of actual ET at different scales (e.g. Anderson et al., 2011; Singh et al., 2020). A number of widely used RS-based ET models rely on the surface energy balance concept in which the ET flux is obtained as a residual of the surface energy balance components (Norman et al., 1995; Bastiaanssen et al., 1998a; Su, 2002; Allen et al., 2007; Anderson et al., 2007; Senay et al., 2013). These models are dependant on land surface temperature (T_s) derived from the radiometric thermal infrared (TIR) spectral signature that are obtained at regional scales and with global coverage, such as from NASA' Landsat Program or the European Space Agency's (ESA) Sentinel-3 mission etc. The Landsat and Moderate Resolution Imaging Spectroradiometer (MODIS) TIR are among the most commonly used products to derive T_s

for use in deriving ET. In spite of their wide spread use, these products are limited in both temporal (16 day repeat measures for Landsat) and spatial (1 km for MODIS) resolution, with obvious implications for field scale agricultural applications. To overcome this, several studies have applied an integrated, multi-sensor approach that fuses both Landsat and MODIS TIR products (Cammalleri et al., 2014; Yang et al., 2017, 2018, 2021).

The ESA's Sentinel-2 products with finer spatial (10, 20 m) and temporal (5 day or less repeat measurements cycle) resolutions has also opened a new prospect towards an explicit characterization of the land surface. Though Sentinel-2 mission does not provide TIR images required for ET modeling using a residual SEB method, the data provided could be fused with TIR data from other RS sources to estimate ET at field scale (Bisquert et al., 2016; Guzinski et al., 2020; Singh et al., 2020). Guzinski and Nieto (2019) evaluated disaggregating coarser (1 km) Sentinel-3 land surface temperature to finer (10 m) Sentinel-2 images using a two-source surface energy balance model (TSEB). They found relative error on surface energy fluxes less than 20% in an agricultural setting. Another study (Vanino et al., 2018) integrated Sentinel-2 derived leaf area index and surface albedo, with FAO-56 Penman-Monteith (PM) equation to estimate potential ET and irrigation water requirements for tomato fields in central Italy. The study indicated the suitability of Sentinel-2 to predict tomato water demand at field level.

As an alternative to calculating ET using the residual method, the PM approach is considered more robust, due to its explicit representation of surface resistance (r_s) (e.g. Mu et al., 2011). The r_s controls the tradeoff between plant water loss through transpiration and carbon assimilation in the process of photosynthesis (Collatz et al., 1991; Ma et al., 2021). This tradeoff can be quantified by the water use efficiency (WUE), defined as the ratio between gross primary productivity (GPP) and actual ET, at canopy and ecosystem level (Medrano et

al., 2009; Lu and Zhuang, 2010; Wagle and Kakani, 2012; Hatfield and Dold, 2019). WUE also provides a means to study plant health and productivity, species distribution, and ecosystem water and carbon cycling (e.g. Lu and Zhuang, 2010; Wagle and Kakani, 2012). Under water stress, r_s increases, leading to a high WUE. While this hypothesis of stomatal control is largely used in ecosystem models (e.g. Ma et al. 2021), the response may be different under extreme drought conditions (e.g. Reichstein et al., 2002, 2003). This fact is supported by Lu and Zhuang (2010) and Zhao et al. (2020) who showed that ecosystem WUE increased under moderate drought but tended to decrease during severe drought, thus, the response of WUE is not monotonous to changes in water availability. The response of WUE during mild/moderate drought reflects patchy stomata closure and the acclimation of plants' physiology to rising water deficits. In the event of extreme drought, the response is linked to absorbed visible light by plants in excess of what is required for photosynthesis, reducing plants' photosynthetic capacity due to impairment of electron transport and carboxylation capacity (Reichstein et al., 2002; Yu et al., 2008; Lu and Zhuang, 2010). Therefore, it is imperative to understand the variability of ecosystem WUE under both wet and dry conditions (e.g. Rammal et al., 2003; Reichstein et al., 2002, 2003, 2007; Medrano et al., 2009; Lu and Zhuang, 2010; Zhao et al., 2020).

Numerous authors have identified a linear relationship between productivity and water-use (e.g. González-Dugo and Mateos, 2008; Kiziloglu et al., 2009; Anderson et al., 2016a, 2016b; Yang et al., 2018; Campos et al., 2018). However, many of these studies are based on ET indices and do not account for the contribution of photosynthesis to plant growth. The use of WUE, which incorporates GPP, to relate with productivity could potentially provide a more robust analysis of grass growth response to water-carbon couplings in a changing climate.

Thus, the two primary objectives of this study are to: (1) estimate high resolution farm-scale daily actual ET and WUE, and; (2) evaluate the relationships between the derived indicators and grass yields, for selected pasture farms across Ireland for both dry and wet years. To achieve these objectives, RS-based Sentinel-2 products are integrated with a validated land surface scheme (LSS), based on PM approach (Chapter 3-4) and light-use efficiency (LUE) scheme (Running and Zhao, 2015; Jiang et al., 2020; Ma et al., 2021) to characterize plant water-use at detailed spatial scale for yield prediction.

5.2 Materials and Methods

5.2.1 *Sample research farms*

Three sample farms (Figure 5.1), broadly representative of farming across the country were chosen for this study, largely due to the availability of on farm grass growth data from these farms. The selected farms are Johnstown Castle, Co. Wexford (52.2875 °N, 6.4961 °W, 51-65 m a.s.l.), Athenry, Co. Galway (53.2822 °N 8.7775 °W, 28-40 m a.s.l.) and Moorepark, Co. Cork (52.1633 °N 8.2472 °W, 25-40 m a.s.l.) (Figure 5.1). These farms are research pasture farms which are managed by Teagasc, the Irish Agriculture and Food Development Authority. The three farms vary in size, soil conditions, topography and climate. At Johnstown Castle, the soil characteristics are fine loam and are classified as imperfectly-drained.; Athenry has fine loam soils and are classified as well-drained, at Moorepark, the soils are coarse loams and are classified as well-drained (Creamer et al., 2014). Based on the long term averages, over 1971-2000, mean daily maximum (minimum) temperature ranges from 16 to 18 °C (8 to 12 °C) in summer and from 7 to 9 °C (1 to 4 °C) in winter across the farms; annual total precipitation is approximately 900 mm at Johnstown Castle, > 1200 mm at Athenry and approximately 1200 mm at Moorepark.

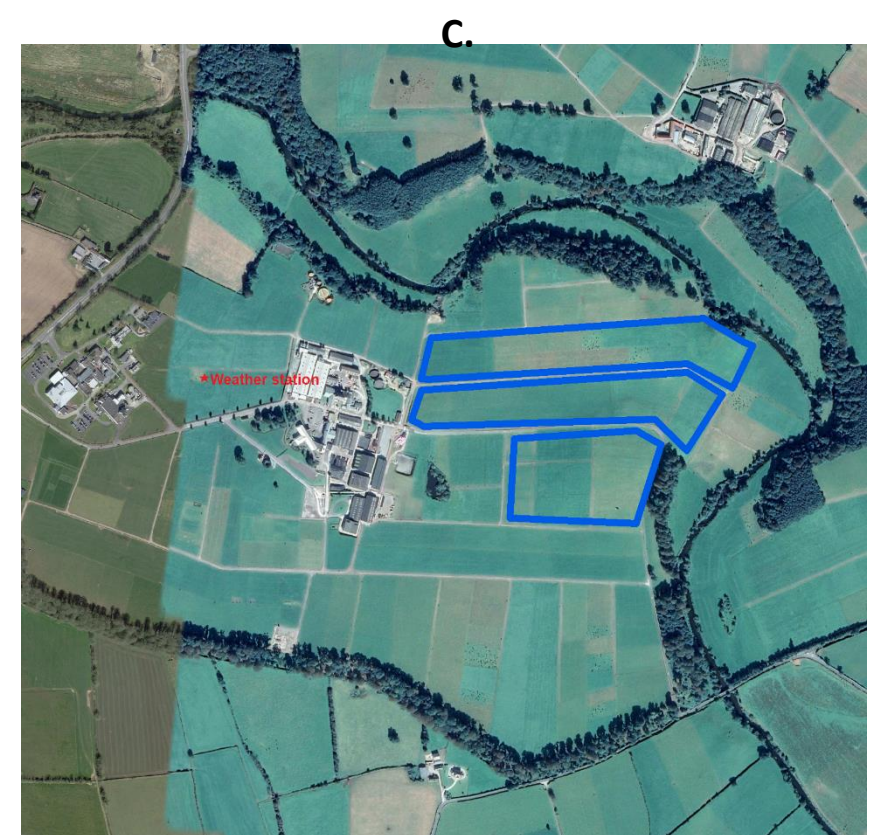
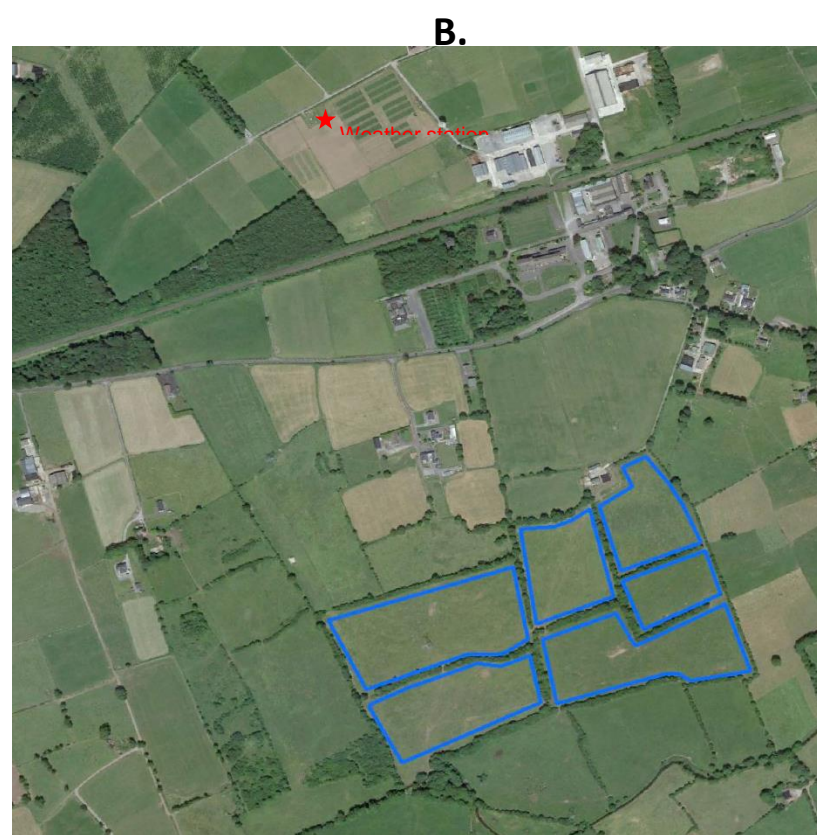
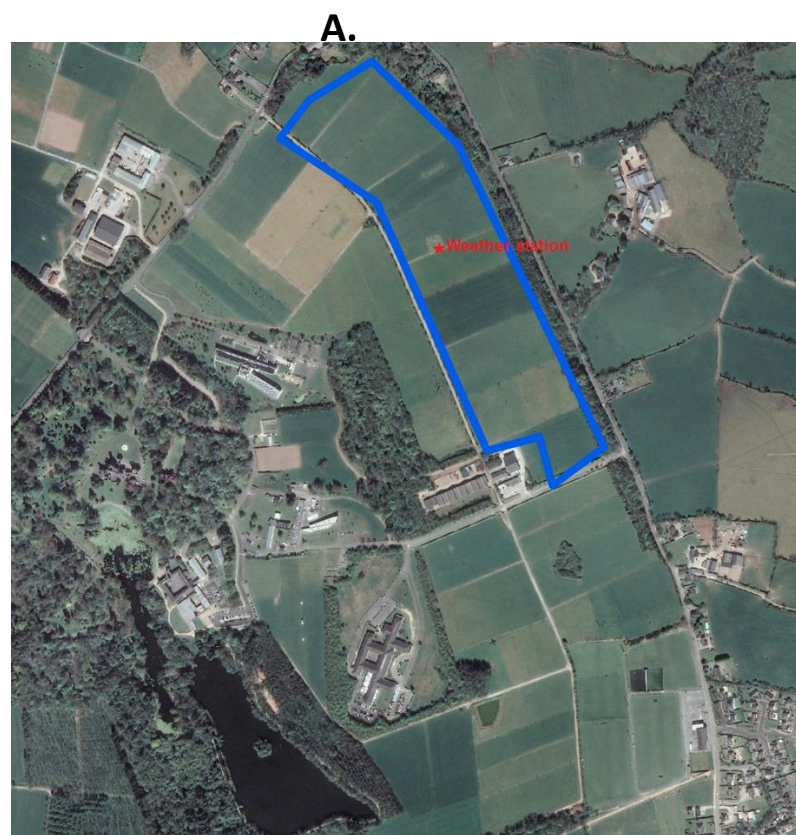
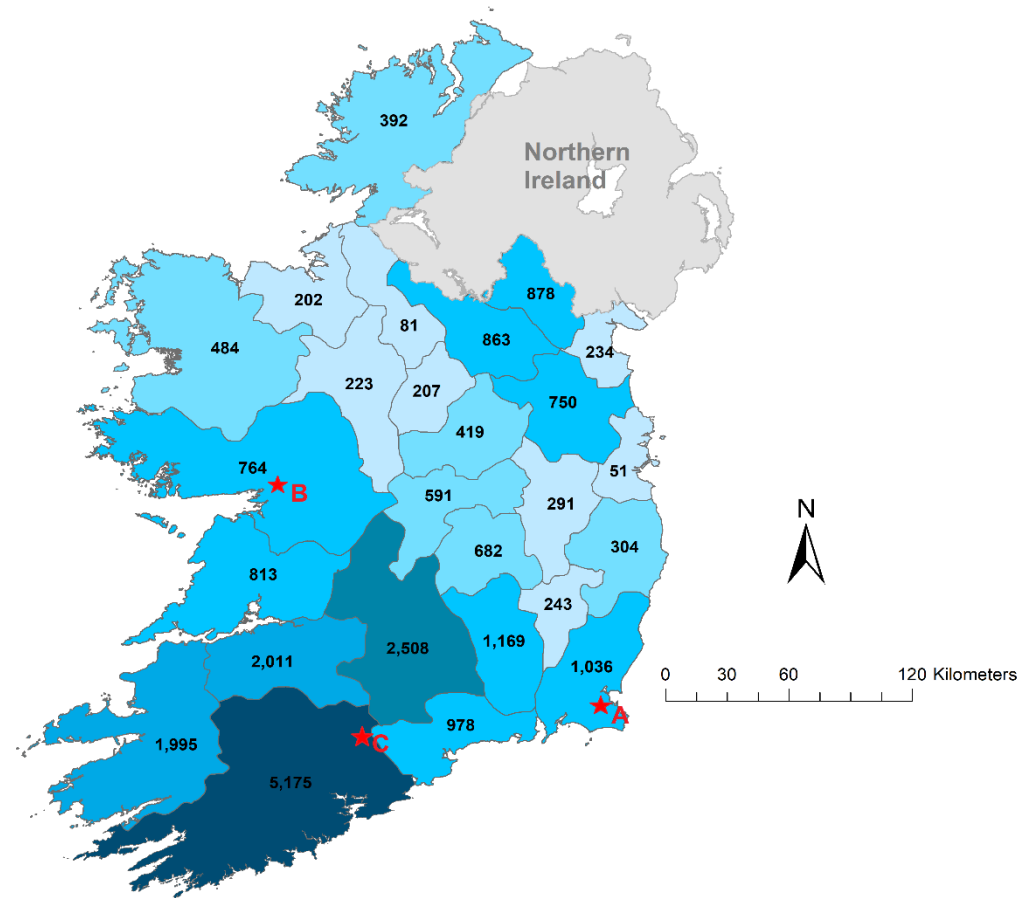


Figure 5.1. The map of Ireland shows the herd population by County in 2019 (Source: Irish Cattle Breeding Federation) (top). Location of the sample research pasture farms and collocated weather stations. (A) Johnstown Castle (B) Athenry and (C) Moorepark. The highlighted plots are the sample grass areas used for analysis of each farm (bottom).

For this study, the mapping size of the sample area for each farm is approximately 13 acres (5 Ha), 9.5 acres (3.8 Ha) and 15.5 acres (6.3 Ha) for Johnstown Castle, Athenry and Moorepark, respectively. Figure 5.1 provides a general overview of herd population/size per county and farm locations. These pasture farms were selected for this study on the basis that: (1) the required on farm grass growth data are available from the farms and; (2) the farms are relatively large and generally serve research purposes on farming across the country. In addition, we used Met Éireann weather stations which are collocated within the research farms (Figure 5.1) and provide long-term meteorological records.

5.2.2 Meteorological forcing data

Meteorological observations are available from automatic weather stations (AWS) adjacent to the selected farms and were obtained from the Irish national meteorological agency, Met Éireann. These stations report on global solar radiation ($Q_{s\downarrow}$, $W m^{-2}$) or sun duration (hours), air temperature ($^{\circ}C$), relative humidity (%), pressure (kPa), wind speed ($m s^{-1}$) and precipitation (mm). At Athenry, where $Q_{s\downarrow}$ observations are not available, observations from the nearest (≈ 50 km) weather station (Claremorris, $53.711^{\circ}N$ $8.991^{\circ}W$) are used, on the basis that the offsite meteorology has negligible impact on model simulations (Ishola et al., 2020; Chapter 3). All observations were obtained for the closest (11.00) hour of satellite overpass for periods corresponding to the cloud-free Sentinel-2 scenes in 2017 and 2018 (see Table 5.2 for available image dates for each farm). These years are selected as the reference wet and dry years, respectively, on the basis that the measured summer total precipitation are higher and lower than the long-term (2010-2019) mean, respectively across the country, as demonstrated in Chapter 4.

We also obtained ERA5-Land (0.1° resolution) hourly volumetric water content at level 1 (0-7 cm) for the same period of study (Hersbach et al., 2020). A previous evaluation of this product shows satisfactory results for different land surface conditions across Ireland (Section 4.2.2).

5.2.3 Grass yield data

To evaluate the relationship between water use and grass yield, pasture growth rate in kilograms Dry Matter per hectare per day (kg DM/ha/day) for the selected farms were obtained from Teagasc's PastureBased Ireland (PBI) database, a web-based tool tailored for Irish grassland management (Hanrahan et al., 2017). The PBI system uses farmers' inputs to derive pasture growth products such as the daily growth rate for paddock/farm, farm cover, etc. The farm level data is used by PastureBase Ireland to generate regional grass growth indices which are published, however, the raw data is not open access. The grass growth data are calculated as the difference between present pasture cover estimate and previous cover estimate per window period, provided that the present is greater than or equal to the previous cover estimate for all grassland paddocks (Hanrahan et al., 2017). The data for 2017 and 2018 were made available for this study.

5.2.4 Satellite derived data

We obtained earth observation data from the European Space Agency's (ESA) Copernicus Sentinel-2 satellite. The Sentinel-2 mission is based on a constellation of Sentinel-2A and 2B satellites, both orbiting the Earth in polar sun-synchronous at an altitude of 786 km (http://www.esa.int/Our_Activities/Observing_the_Earth/Copernicus/Sentinel-2). The Sentinel-2A was launched on the 23rd June, 2015, and Sentinel-2B on the 7th March, 2017. Both satellites are kept 180° apart to optimize coverage, and they capture the Earth, covering the land and coastal areas between 84°N and 84°S, around 10.30 hours every five days over the equator, with higher revisit times over higher latitudes. Both satellites carry a Multi-Spectral Imager (MSI) obtaining data in 13 spectral bands and with varying spatial resolutions, from 10 m in the visible/near infrared bands to 60 m in the atmospheric correction bands. The properties of the MSI spectral bands, in terms of the spectral wavelengths, spatial resolutions and general applications are presented in Table 5.1.

ESA Sentinel-2 Level-1C Top of Atmosphere (ToA) reflectance products are available through the Copernicus open access hub (<http://scihub.copernicus.eu>). The satellite images were obtained for the available cloud-free periods for both a wet (2017) and a dry (2018) year. More details of the satellite specification, tiles and temporal coverage, corresponding to the cloud-free scenes for the selected farms are given in Table 5.2.

Band	Center Wavelength (nm)	Spectral width wavelength (nm)	Spatial resolution (m)	w_B (-)	Application
B1	443	20	60	-	Atmospheric corrections.
B2	490	65	10	0.356	Atmospheric corrections; vegetation senescence, carotenoid, browning and soil background.
B3	560	35	10	-	Vegetation chlorophyll, maximum greening.
B4	665	30	10	0.130	Peak chlorophyll absorption.
B5	705	15	20	-	Fluorescence baseline/Atmospheric corrections; Red edge.
B6	740	15	20	-	Red edge; Aerosols retrieval; Atmospheric corrections.
B7	783	20	20	-	Near infrared edge; Leaf Area Index.
B8	842	115	10	0.373	Leaf Area Index.
B8a	865	20	20	-	Chlorophyll absorption, water vapour absorption, LAI, biomass, aerosols retrieval.
B9	945	20	60	-	Water vapour absorption; Atmospheric corrections.
B10	1375	30	60	-	High cloud (e.g cirrus); Atmospheric corrections.
B11	1610	90	20	0.085	Snow/ice/cloud differences; lignin, above ground biomass, forest.
B12	2190	180	20	0.072	Soil texture and type, soil erosion, biomass.
				-0.0018	

Table 5.1. A summary characteristics of Sentinel-2 Multispectral Imager spectral bands. w_B is the weighting coefficient for estimating shortwave broadband albedo (Liang, 2001)

Johnstown Castle			Athenry			Moorepark		
Date	Julian day	MSI	Date	Julian day	MSI	Date	Julian day	MSI
2017								
08/05*	128	S2A	25/03	84	S2A	12/03	71	S2A
17/06*	168	S2A	11/05*	131	S2A	01/05	121	S2A
20/06	171	S2A	20/06*	171	S2A	11/05*	131	S2A
02/07*	183	S2B	12/11	316	S2B	18/09*	261	S2A
17/07	198	S2A						
20/07	201	S2A						
15/09	258	S2A						
2018								
28/04	118	S2B	20/03	79	S2A	21/04	111	S2B
06/05*	126	S2A	06/05	126	S2A	16/05*	136	S2A
16/05	136	S2A	16/05*	136	S2A	05/07	186	S2A
23/05	143	S2A	28/06*	179	S2A	10/07*	191	S2B
07/06	158	S2B	03/07	184	S2B	03/09*	246	S2A
22/06*	173	S2A	10/07*	191	S2B	28/09	271	S2B
27/06	178	S2B	30/07	211	S2B	18/10	291	S2B
30/06	181	S2B	29/08	241	S2B	28/10	301	S2B
05/07*	186	S2A	28/10	301	S2B			
10/07	191	S2B	25/11	329	S2A			
09/08	221	S2B						
03/09	246	S2A						
13/09	256	S2A						

Table 5.2. Temporal coverage and corresponding instrument type of Sentinel-2 (S2) cloud-free images used over the sample farms, Johnstown Castle (tiles T29UPT and T29UPU); Athenry (tiles T29UNV); Moorepark (tiles T29UNT). *periods used in the plotted maps.

During pre-processing of the products, the occurrence of clouds and cloud shadows that partially cover the downloaded satellite images of the area of interest were removed, leading to a total of 46 images available for further analysis across the three farms. The Level-1C ToA reflectance images were then processed and corrected to Level-2A and Level-2B Bottom of Atmosphere (BoA) reflectance products using ESA Sen2Cor v2.5.5 atmospheric correction processor algorithm (ESA, 2018). The spectral bands of the corrected Level-2A and Level-2B

were resampled from their native pixel size to 10 m pixel size, using Nearest Neighbor resampling methods with band B2 as the reference image. This pixel size is sufficient to effectively discriminate between different land cover types and avoid misrepresentation/misinterpretation of pixels. The data for biophysical parameters, including the Leaf Area Index (LAI), Normalized Difference Vegetation Index (NDVI), Fraction of Absorbed Photosynthesis Active Radiation (FAPAR), near infrared NIR reflectance of vegetation (NIRv) and surface albedo (α), were subsequently derived using the Sentinel Application Platform (SNAP), a tool developed by ESA and tailored to processing Sentinel-2 observations (<http://step.esa.int/main/toolboxes/sentinel-2-toolbox/sentinel-2-toolbox-features/>).

The NIRv, defined as the product of NIR and NDVI (Badgley et al., 2017), has been introduced in Chapter 4. Here, the data were derived by combining the Sentinel spectral Bands 4 (red) and 8 (NIR) using the vegetation radiometric indices processor in the ESA SNAP Toolbox. The integrated SNAP-biophysical processor was also used to map the farm-scale LAI and FAPAR at 10 m resolution. The algorithm used to derive LAI is tailored for Sentinel-2 observations, and it includes an Artificial Neural Network (ANN) model which is trained using simulations from PROSAIL (PROSPECT + SAIL) radiative transfer models (Verhoef, 1984; Jacquemoud and Baret, 1990). The algorithm incorporates B3-B7, B8, B11-B12 bands to derive the biophysical parameter. This approach has proven reliable for LAI estimations for different experimental fields and environments (e.g. Vuolo et al., 2016; Djamai and Fernandes, 2018; Vanino et al., 2018). For a more detailed description of the approach, the reader is referred to Weiss and Baret (2016). A linear model, relating the derived NIRv values to LAI and FAPAR, was

developed for each of the selected farms (Figure 5.2). Both regression model fits show strong linear relationships ($R^2 \approx 0.9$) at the selected farm-scale.

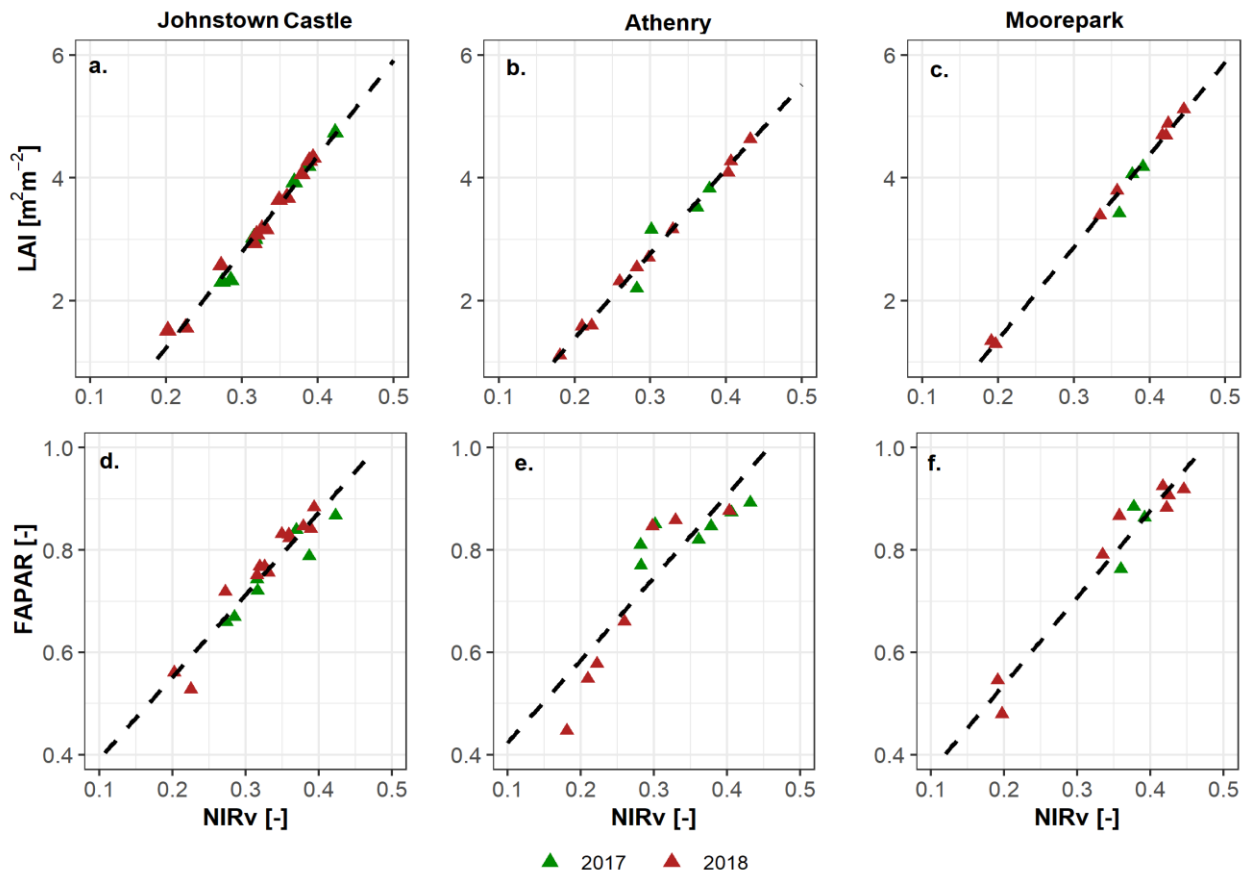


Figure 5.2. Relationships between near infrared reflectance of vegetation (NIRv) and leaf area index, LAI [top]; fraction of absorbed photosynthesis active radiation, FAPAR [bottom] for 2017 [green] and 2018 [red] image dates across the farms. Values are derived from the highlighted sample grass plots in Figure 1.

In addition, broadband surface albedo (α) was derived using the Level-2A/2B reflectance bands obtained from ESA Sen2Cor algorithm. We applied the commonly used linear regression model (Equation 5.1) from Liang (2001) for this purpose. The approach incorporates five different reflectance bands and empirical weighting coefficients (Table 5.1). While the weighting coefficients were derived based on Landsat reflectance data, the corresponding Sentinel-2 bands can be assigned to estimate shortwave broadband albedo,

bearing in mind that some of the spectral wavelengths for the corresponding bands of Landsat and Sentinel-2 may differ considerably (Naegeli et al., 2017). The linear model is given by;

$$\alpha = \sum_{Bi} w_{Bi} \cdot \rho_{Bi}, \quad (5.1)$$

where w_{Bi} is the weighting coefficients for band number Bi (Table 1) and ρ_{Bi} is the Level 2A/2B surface reflectance for band number Bi . Other linear models for Sentinel2-based albedo have also been proposed (e.g. Li et al., 2018). A brief comparison with the model used here shows good agreement in terms of the magnitude and spatial pattern (see Appendix A). The derived surface albedo, LAI and NDVI were used as inputs to represent the dynamics of surface parameters in the LSS while FAPAR and NIRv were used in GPP models (see Section 5.2.6) that are based on LUE theory.

5.2.5 Mapping high resolution daily evapotranspiration

The land surface scheme (LSS) employed here has been described elsewhere (Ishola et al., 2020; Chapters 3-4). In contrast to the previous application of the LSS, where surface conditions are prescribed using specified values, the modification here is that the scheme integrates Sentinel-2 data that is then used to calculate and represent the dynamics of surface parameters, and simulate farm-scale surface energy fluxes at 10 m pixel-size. ET which is a measure of latent heat flux, is part of a surface energy budget understanding of surface-air exchanges.

Daily actual evapotranspiration (ET_{24}) values are more relevant than the instantaneous ET for management applications of water-consumption. Thus, the high resolution farm-scale 24-hr total actual evapotranspiration (ET_{24} , mm day^{-1}) values were estimated by integrating the hourly instantaneous latent heat flux (Q_E) retrieved from the land surface scheme and $Q_{s\downarrow}$.

Although, an evaporative fraction (EF), defined as the ratio of Q_E and available energy ($Q_N - Q_G$) at the land surface (see also Chapter 4) is commonly used to upscale ET from instantaneous to 24-hr total ET, the use of $Q_{S\downarrow}$ has also demonstrated consistent results (e.g. Yang et al., 2018). The latter is preferred here in order to avoid errors inherent in EF assumptions such as the assumption that estimated EF at a specific daytime remains constant assuming clear-sky throughout the daylight hours. This may not apply because only a specific time of the day is required to be cloud-free, while the rest of the day can be clear or cloudy. In addition, the $Q_{S\downarrow}$ upscaling approach is used to avoid biases arising from Q_N and Q_G estimations (van Niel et al., 2012; Cammalleri et al., 2014, Yang et al., 2018). The temporal upscaling of daily ET is given as:

$$ET_{24} = \frac{8.64 \times 10^7 \times Q_E \times Q_{S\downarrow 24}}{Q_{S\downarrow} \times \lambda \rho_w}, \quad (5.2)$$

where λ is the latent heat of vaporization ($2.45 \times 10^6 \text{ J kg}^{-1}$), and ρ_w density of water (1000 kg m^{-3}). $Q_{S\downarrow}$ and $Q_{S\downarrow 24}$ are the instantaneous and daily global radiation, respectively. Q_E is the instantaneous latent heat flux, calculated by the LSS at the closest time (11.00 hour) the respective satellite image for a location was acquired.

5.2.6 Relationship between ecosystem water use and yield

Daily Sentinel2-scale ecosystem WUE ($\text{g C kg}^{-1} \text{ H}_2\text{O}$) is calculated as (e.g. Hatfield and Dold, 2019; Zhou et al., 2020):

$$WUE = \frac{GPP}{ET_{24}}, \quad (5.3)$$

where ET_{24} is the daily actual evapotranspiration (mm day^{-1}) derived from land surface scheme (see section 5.2.5). GPP is the daily Sentinel-2 scale gross primary productivity (g C day^{-1}).

For robust analysis, two approaches were applied to estimate GPP, resulting in two different estimates of WUE. The first approach is based on the MODIS light use efficiency (LUE) scheme (Running and Zhao, 2015; Ma et al., 2021) (hereafter termed 'WUE_{MODIS}'). It is given as:

$$GPP = PAR \times FAPAR \times LUE, \quad (5.3a)$$

where FAPAR is the Sentinel-2 derived fraction of absorbed photosynthetically active radiation derived using the integrated SNAP-biophysical processor. PAR (MJ m^{-2}) is the photosynthetically active radiation per unit time, taken as 45% of measured incoming shortwave radiation ($Q_{s\downarrow}$) (Running and Zhao, 2015; Ma et al., 2021). The employed fractional value is universal and works well in Ireland, based on the evaluation over Johnstown Castle (not shown).

$$PAR = 0.45 \times Q_{s\downarrow}, \quad (5.3b)$$

LUE is calculated as the product of maximum vegetation LUE (LUE_{max} , g C MJ^{-1}) and environmental stressors ($Tmin_{scalar}$ and VPD_{scalar}) of daily minimum temperature ($Tmin$, °C) and daily vapour pressure deficit (VPD , Pa), respectively.

$$LUE = LUE_{max} \times Tmin_{scalar} \times VPD_{scalar} \quad (5.3c)$$

The LUE_{max} (0.86 g C MJ^{-1} for grass) is given in a Biome Parameter Look-up Table (BPLUT) for different ecosystem types (Running and Zhao, 2015). The $Tmin_{scalar}$ and VPD_{scalar} are given as:

$$Tmin_{scalar} = \begin{cases} 1 & Tmin > Tmin_{max} \\ (Tmin - Tmin_{min}) / (Tmin_{max} - Tmin_{min}) & Tmin_{min} \leq Tmin \leq Tmin_{max} \\ 0 & Tmin < Tmin_{min} \end{cases}, \quad (5.3d)$$

$$VPD_{scalar} = \begin{cases} 0 & VPD > VPD_{max} \\ (VPD_{max} - VPD) / (VPD_{max} - VPD_{min}) & VPD_{min} \leq VPD \leq VPD_{max} \\ 1 & VPD < VPD_{min} \end{cases}, \quad (5.3e)$$

where $Tmin_{min}$ (-8 °C) and VPD_{min} (650 Pa) are the daily minimum temperature and VPD at which $LUE = 0$, while $Tmin_{max}$ (12.02 °C) and VPD_{max} (5300 Pa) are daily minimum temperature and VPD at which $LUE = LUE_{max}$. The values were also obtained from BPLUT (Running and Zhao, 2015).

The second approach to estimate LUE is based on NIRv (Jiang et al., 2020) (hereafter termed 'WUE_{NIRv}'). It has been recognized that LUE and FAPAR are strongly related to vegetation indices including NIRv and both exhibit similar biophysical characteristics (e.g. Badgley et al., 2017; Biudes et al., 2021), GPP has also been recognized to show a moderate correlation with LUE (Dechant et al., 2020) and a strong correlation with NIRv (Badgley et al., 2017) (see also Figure 5.2). Thus, Jiang et al. (2020) introduced a simplified version of equation (5.3a) by replacing the last two terms on the right side with a model that is based on a linear relation with NIRv.

$$GPP \approx PAR \times (a \times NIRv + b), \quad (5.3f)$$

where a and b are model coefficients derived from pixel-wise regression fit between Sentinel-2 FAPAR and NIRv. This approach is similar to vegetation index-based models (e.g. Biudes et al., 2021), first introduced by Wu et al. (2010). There are no available GPP measurements for the selected locations, this would have facilitated a cross-comparison and evaluation of the two approaches used in this study. On the basis of both GPP methods outlined, spatial estimates (10 m resolution) of WUE were derived for each of the selected farms.

To understand the relationship between the derived WUE estimates from the procedure described above, and measured grass growth at farm scale, grass Yield-WUE correlations were quantified based on the derived maps for the active growth period (May-August) using the Pearson correlation coefficient. The WUE values were extracted per pixel for sample grass areas within the farms and spatially averaged for each date. The farm level, spatially averaged WUE estimates are then used with the grass yield data (within ± 7 days of image date) to derive a predictive model for each farm. A similar analysis was undertaken for ET₂₄-Yield correlations.

While the output maps showing wider coverage of the farms are presented in the results, further analysis are conducted only for the sample grasslands with highlighted bounding shapes across the farms (see Figure 5.1).

5.3. Results

5.3.1 Analysis of NIRv from Sentinel-2

NIRv maps of the Johnstown Castle farm and corresponding histograms for three selected image dates are shown in Figure 5.3. The Sentinel-2 derived NIRv show large spatial variations, from a low to high reflectance signal, indicating unhealthy to healthy vegetation across the farm. It should be noted that this farm is peculiar for its surface heterogeneity, the field boundaries (highlighted black bounding shape), comprising of 10 paddocks, are used as sample experimental treatments (Figure 5.3a). For the highlighted fields, a substantial proportion of the grasslands show high NIRv values above 0.3 for all the image dates except July when the values are largely below 0.25. Based on the histogram analysis (Figure 5.3b), the NIRv values indicate that a large portion of the vegetation within the farm are healthy, with median NIRv value of approximately 0.3 for both 2017 and 2018 image dates. However,

a large portion of the vegetation are stressed during July 2018 with median NIRv value of approximately 0.2, relative to other image dates.

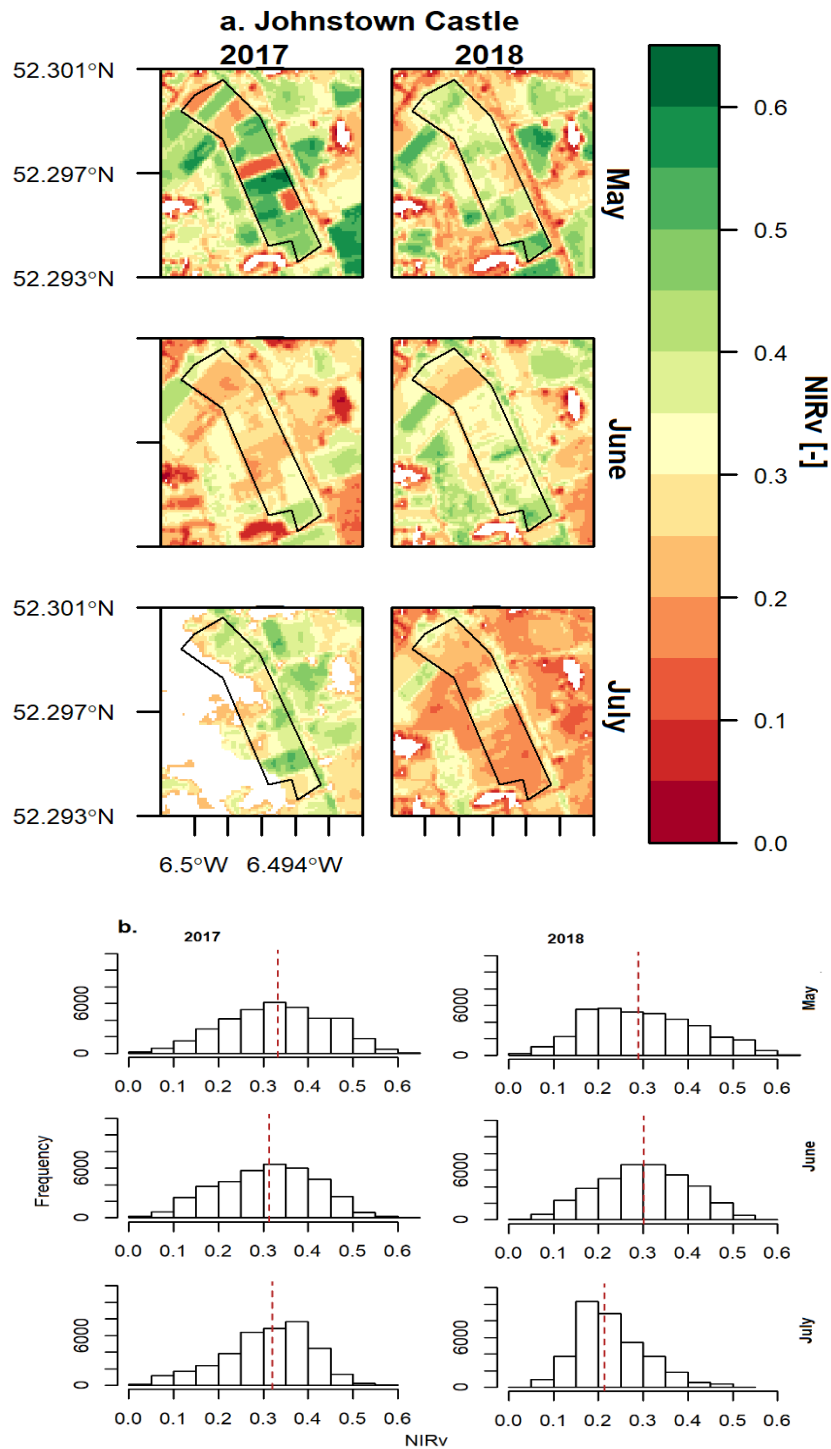


Figure 5.3. (a) Sentinel-2derived near infrared reflectance of vegetation (NIRv) maps and; (b) histogram of NIRv values of selected image dates during 2017 and 2018 for the Johnstown Castle farm. The vertical dashed red lines indicate the median NIRv values.

For the Athenry farm, the NIRv values are relatively high in 2017 maps (Figure 5.4). However in 2018, the values dropped in June and reach their minimum value in July, as clearly revealed in the highlighted (black bounding) grasslands (Figure 5.4a). From the histogram analysis (Figure 5.4b), the median NIRv value is approximately 0.4, suggesting that a substantial portion of the farm is highly productive across May and June of both years. However, a large portion of the land also experienced vegetation stress with median NIRv dropping to approximately 0.23 in July of 2018. While there are some missing satellite image dates from Moorepark farm (Figure 5.5), the results are very similar to the Athenry farm based on both magnitudes and temporal variations.

Comparatively, the results demonstrate that the vegetated landscape at Athenry and Moorepark are healthier and more productive than those of Johnstown Castle for the selected image dates. Additionally, the footprint of water stress on the vegetation signal, as represented by the NIRv analysis is evident during July 2018 across the three farms.

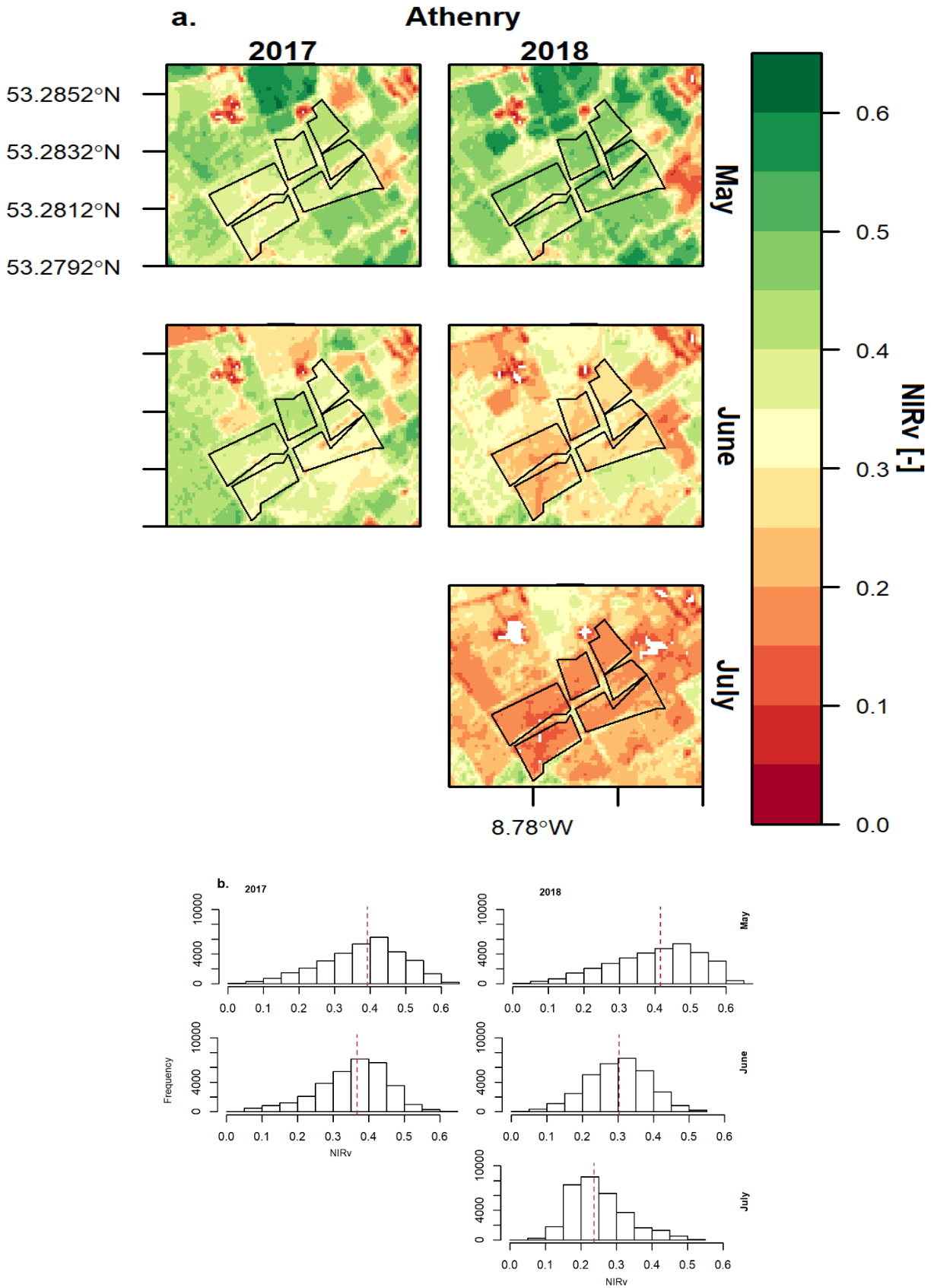


Figure 5.4. (a) Sentinel-2 derived near infrared reflectance of vegetation (NIRv) maps, and; (b) histogram of NIRv values of selected image dates during 2017 and 2018 for Athenry farm. No analysis for July 2017 due to lack of clear-sky Sentinel-2 images. The vertical dashed red lines indicate the median NIRv values

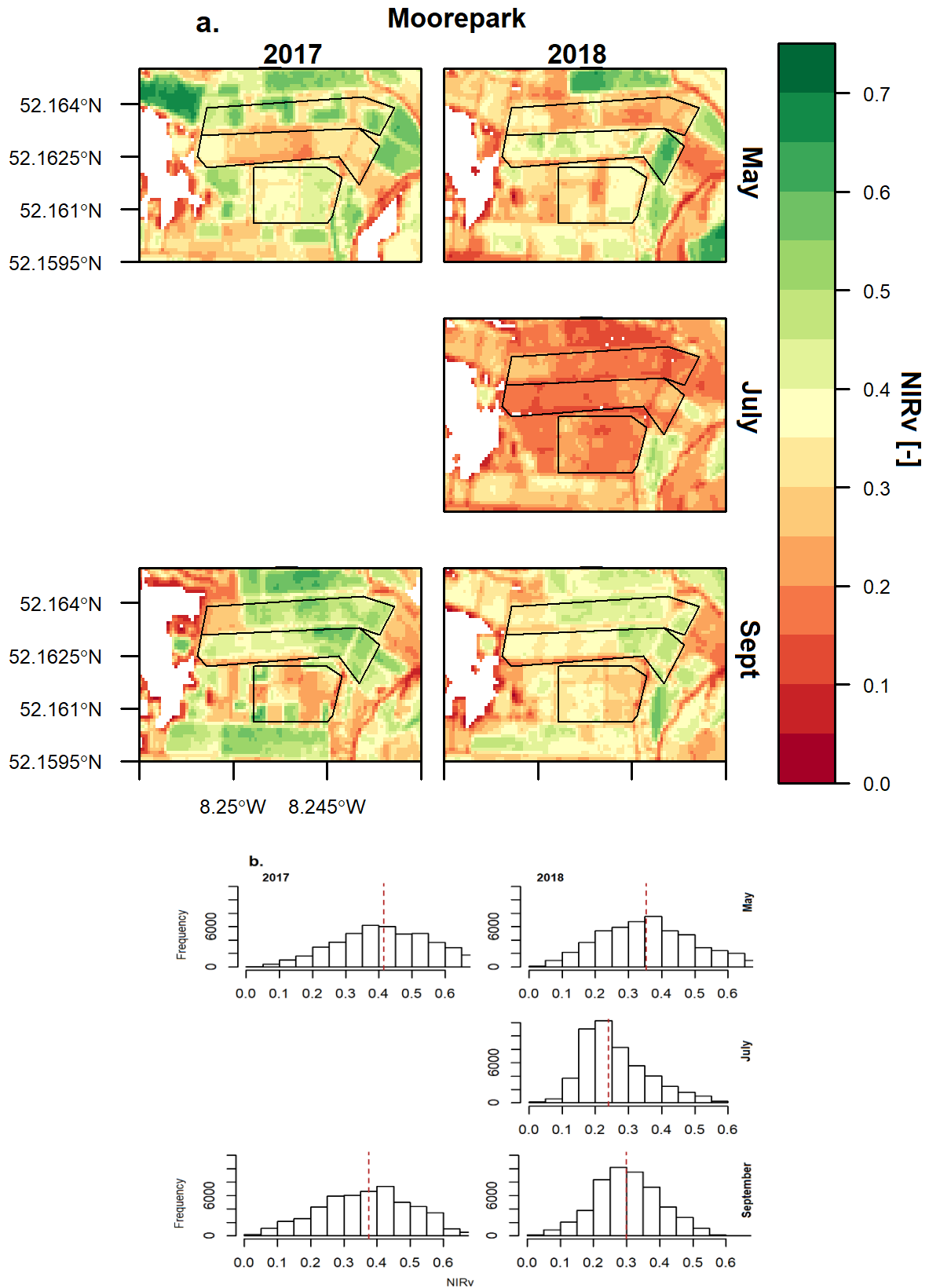


Figure 5.5. (a) Sentinel-2 derived near infrared reflectance of vegetation (NIRv) maps and; (b) histogram of NIRv values of selected image dates during 2017 and 2018 for Moorepark farm. No analysis for June of both years and July 2017 due to lack of clear-sky Sentinel-2 images. The vertical dashed red lines indicate the median NIRv values

5.3.2 Analysis of ET changes

Knowledge of ET dynamics within a farm is essential for agricultural water management and planning. Here, the results of the high resolution ET estimates are presented, along with the relative change for the individual sample farms. The estimates of the relative change in ET in 2018 (expressed in percentage) were derived from the ratio of the difference between 2018 (dry) and 2017 (wet) ET maps, and 2017 map, for a representative selection of dates during analysis period. There are differences in the dates of downloaded Sentinel-2 images for the same month between the years due to cloud cover. Hence, the closest dates (within 7 days difference) between reference wet and dry periods are selected to derive the relative change in ET. The dates used to generate the maps are highlighted in Table 5.2.

5.3.2.1 Johnstown Castle

Figure 5.6 displays a sequence of estimates and boxplots of daily actual ET for the selected dates during May-July in 2017 and 2018 for the Johnstown Castle farm, along with relative change (%) between these years. The maps demonstrate variability in spatial ET changes within the farm. For example, within the highlighted black bounding farm plot (in Figure 5.6a), ET changes are lower (less than 50 % drop in ET) at the centre of the plot relative to rest of the landscape during the growth season. While the ecosystems within the farm largely show maximum ET rates in June, consistent for both years, maximum plant water use ($ET > 5 \text{ mm day}^{-1}$) is higher in 2017 than in 2018 ($4.5 - 5 \text{ mm day}^{-1}$). This is particularly evident in the southwest portion of the farm which is dominated by thick canopy coverage (see Figure 5.1).

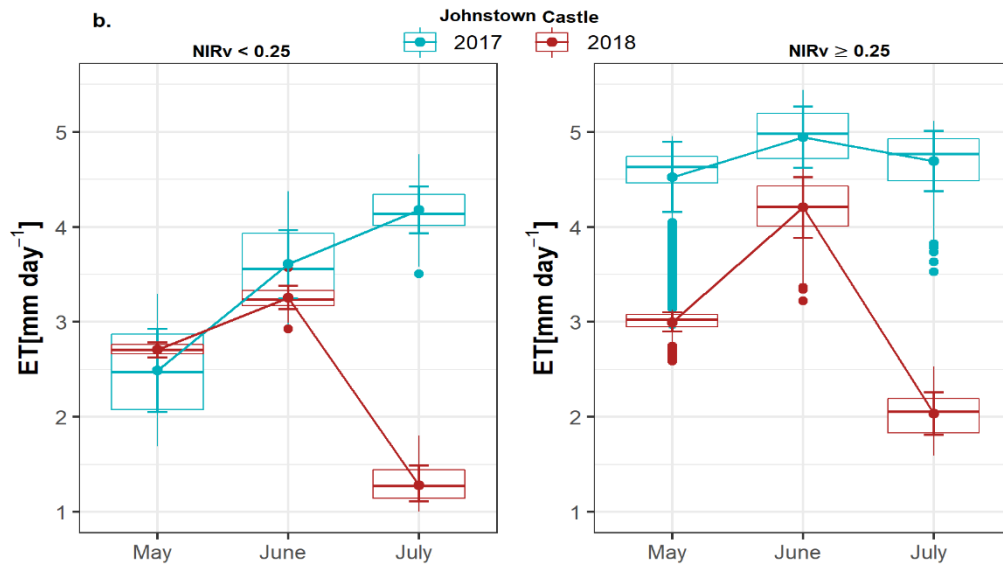
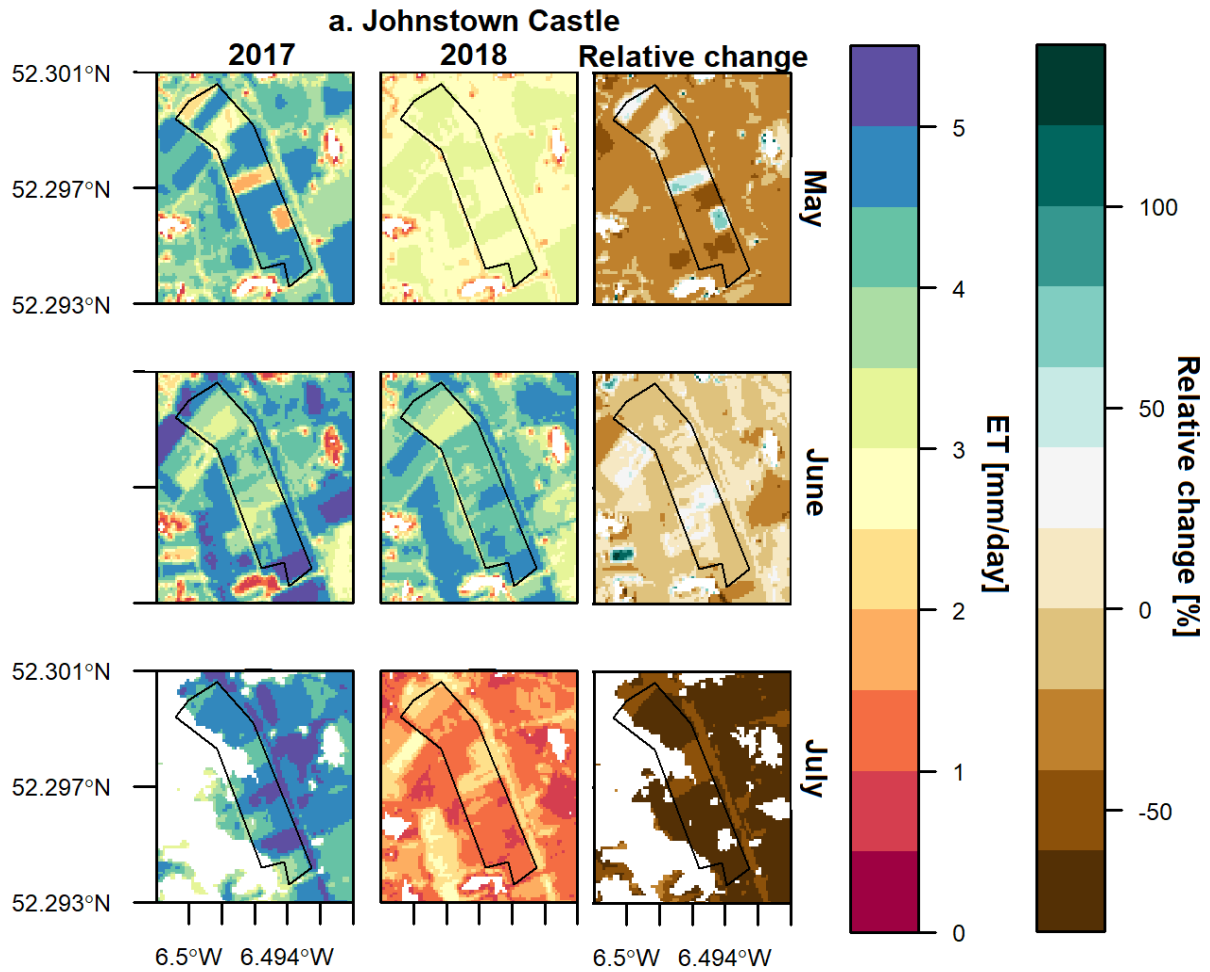


Figure 5.6. The daily evapotranspiration (ET) changes at Senitel-2 scale for three selected image dates during 2017 and 2018 for the Johnstown Castle farm. (a) ET maps, and; (b) the distribution and trend of ET for near infrared reflectance of vegetation (NIRv) pixel values less than 0.25 and for NIRv pixel values greater than or equal to 0.25.

The distribution and trend of ET across the highlighted (black bounding) farm plot are shown in Figure 5.6b. The responses of ET across the plot are distinguished by isolating the vegetation signal using a specified threshold (0.25) of NIRv (see Figures 5.3-5.5). For grasses with $\text{NIRv} < 0.25$, the daily ET increased, reaching maximum rate (median = 4.2 mm day^{-1}) in July of 2017, while 2018 magnitude dropped from maximum rate (median = 3.3 mm day^{-1}) in June to the lowest (median = 1.3 mm day^{-1}) in July. For grasses with high reflectance signal ($\text{NIRv} \geq 0.25$), the changes in ET between the months are small (median is approximately 5 mm day^{-1}) during 2017 but, the highest and lowest (median) ET rates are 4.3 mm day^{-1} in June and 2.1 mm day^{-1} in July of 2018, respectively.

While the patterns of ET are similar in 2018 for both NIRv categories, the 2017 patterns appear to diverge in relation to the $\text{NIRv} < 0.25$ category in July. The observed divergence of ET response between wet and dry years in July suggests the presence of landscapes with high plant water-stress and an increased stomatal resistance that facilitates more energy being partitioned into heat fluxes during July of 2018. Generally, ET is lower for grasses with low reflectance signal ($\text{NIRv} < 0.25$), relative to grasses with high reflectance signal ($\text{NIRv} \geq 0.25$) for both wet and dry years.

5.3.2.2 *Athenry*

The ET maps and patterns over Athenry farm are presented in Figure 5.7. It should be noted that the July map for 2017 is not available due to high cloud amount. As a consequence, the 2018 July image date was contrasted with the map of maximum ET rate in June of 2017, to determine the possible amount of water required to offset the plant water shortage in July, in terms of relative change.

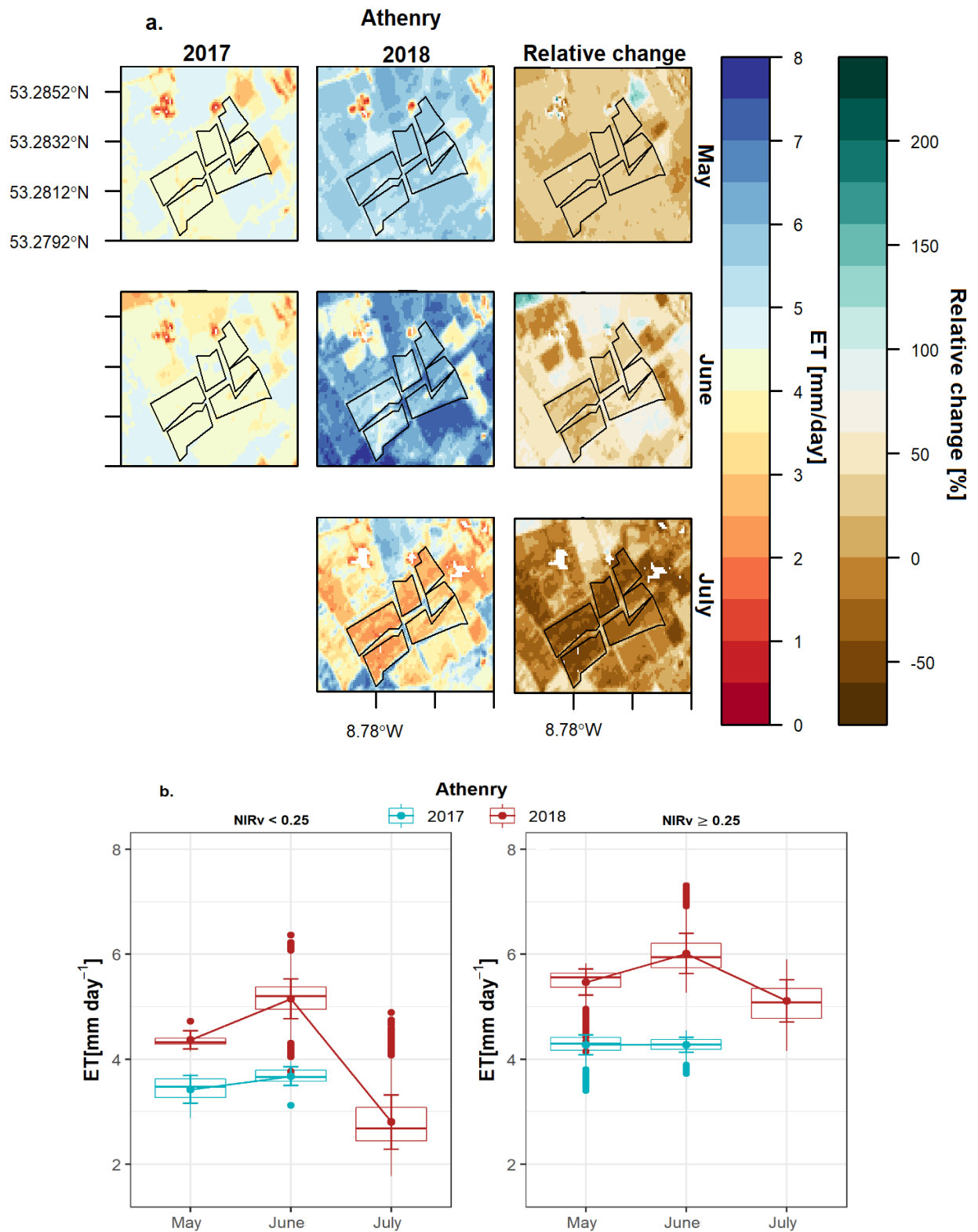


Figure 5.7. The daily evapotranspiration (ET) changes at Sentinel2-scale for three selected image dates during 2017 and 2018 for Athenry farm. (a) ET maps and; (b) the distribution and trend of ET for near infrared reflectance of vegetation (NIRv) pixel values less than 0.25 and for NIRv pixel values greater than or equal to 0.25. No available cloud-free image in July of 2017.

This is done on the basis that ET rate is maximum under non-limiting water availability (wet condition) and high incident radiation for plant use, which is the case for the 2017 June image date (Figure 5.7a).

The ET rates are largely uniform over grass within the farm, maximum at 5-6.5 mm day⁻¹, as shown in the highlighted black bounding shapes. In contrast to Johnstown Castle site, the 2018 ET rates are generally higher (by about 50 %, relative to the 2017 reference wet period) over grass in May and June at Athenry farm, suggesting the importance of higher incident radiation and atmospheric evaporative demand that enhanced the ET processes. Conversely, the ET rates dropped by about 100 % in July of 2018, relative to June reference map, particularly for these grass dominated landscapes within the farm.

For the highlighted sample grasslands in Figure 5.7a, the corresponding trend of ET rate per 10-m pixel are presented in Figure 5.7b. For grasses with low reflectance signal (NIRv < 0.25), ET rates show little difference during May and June image dates (median is approximately 3.5 mm day⁻¹) in 2017. However in 2018, ET rates increased to maximum (median = 5.3 mm day⁻¹) in June and then dropped sharply to the lowest (median = 2.5 mm day⁻¹) in July. These patterns are also similar for grasses with high reflectance signal (NIRv ≥ 0.25) but with higher ET rates.

5.3.2.3 Moorepark

Moorepark site also suffers similar limitation as Athenry farm in terms of missing cloud-free images in June and July of 2017 (Figure 5.8). As a result, the available dates of ET maps are compared in a manner that was described in Section 5.3.2.2. The ET rates (2 – 3.5 mm day⁻¹) are largely uniform over vegetated surfaces in 2017 but enhanced in 2018 across the farm.

The middle black bounding sample grassland shows the maximum ET rates (7 mm day^{-1}) in the West end, relative to the rest of the farm during May of 2018 (Figure 5.8a). The relative increase in ET over grass ranges between 100-200 % in May, and dropped (by more than 50 %) in July.

For the highlighted bounding grasslands (Figure 5.8a), the analysed trends in ET are provided in Figure 5.8b. ET rates show a shallow decreasing slope between May and September of 2017 (note that there are missing June and July images for the year), while also decreased sharply between May and July of 2018, it increased by September of the same year, for grasslands with a low reflectance signal ($\text{NIRv} < 0.25$). For grassland with high reflectance signal ($\text{NIRv} \geq 0.25$), similar patterns of trend are identified but with higher magnitude of ET for both wet and dry years, relative to the results for $\text{NIRv} < 0.25$.

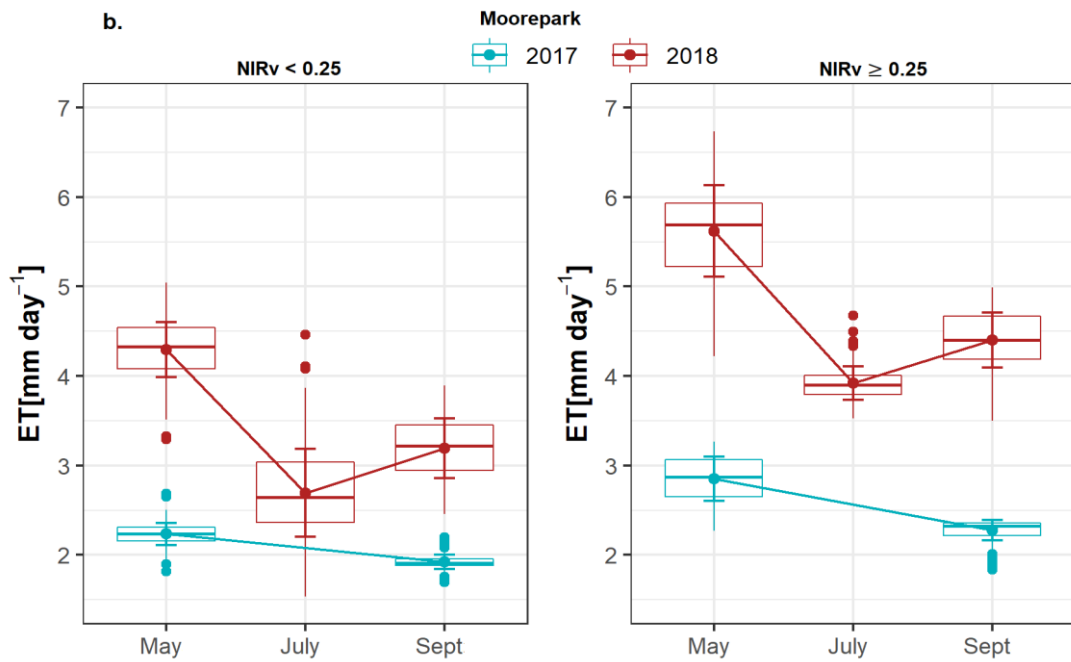
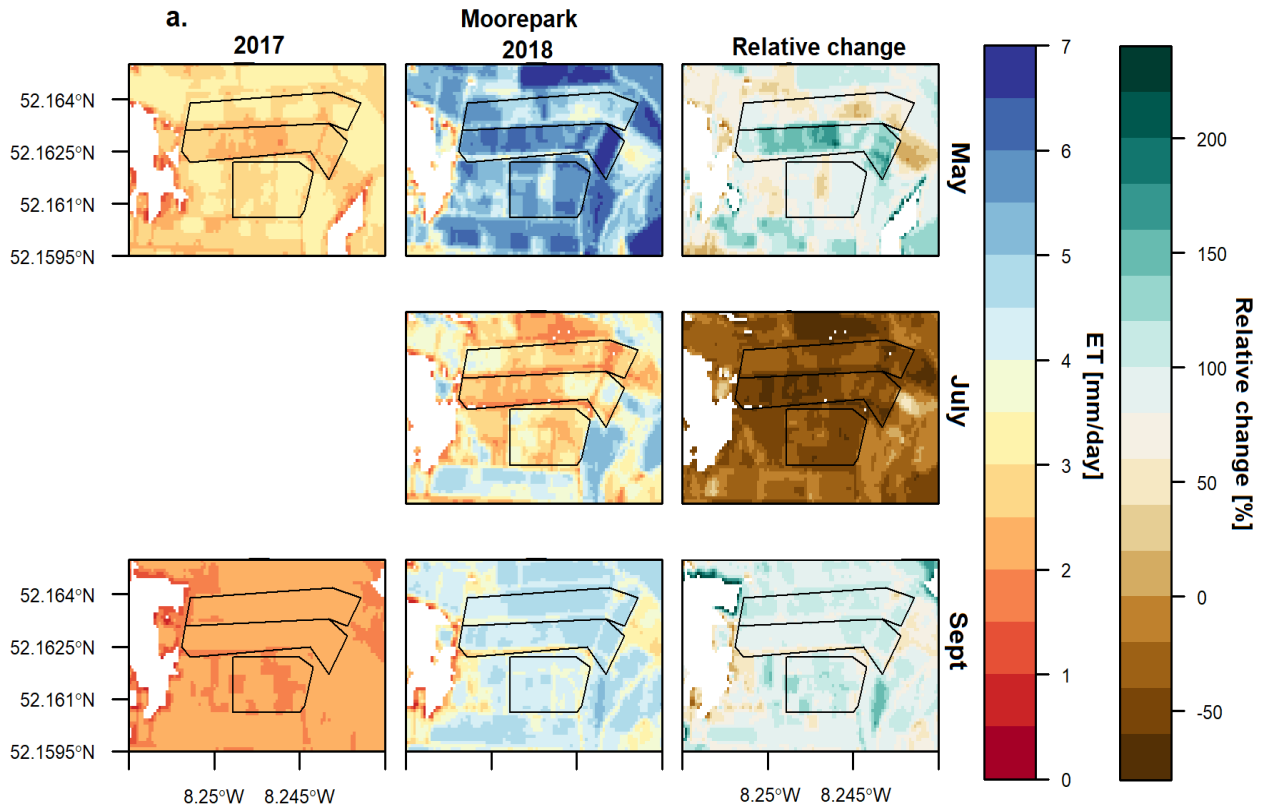


Figure 5.8. The daily evapotranspiration (ET) changes at Senitnel-2 scale for three selected image dates during 2017 and 2018 for Moorepark farm. (a) ET maps and; (b) the distribution and trend of ET for near infrared reflectance of vegetation (NIRv) pixel values less than 0.25 and for NIRv pixel values greater than or equal to 0.25. No available cloud-free image in June and July of 2017 and June of 2018.

5.3.3 Characteristics of ecosystem water use Efficiency across the farms

Water-carbon coupling results at ecosystem level and daily scale are shown in Figure 5.9. The variability in GPP and ET is weakly, but significantly, linked ($R^2 = 0.25$ for MODIS-based GPP and $R^2 = 0.46$ for NIRv-based GPP) over grasslands at Johnstown Castle farm; while much stronger relationships are observed over grasslands at Atheryn ($R^2 = 0.78$ for MODIS-based GPP and $R^2 = 0.91$ for NIRv-based GPP) and Moorepark ($R^2 = 0.63$ for MODIS-based GPP and $R^2 = 0.87$ for NIRv-based GPP) farms.

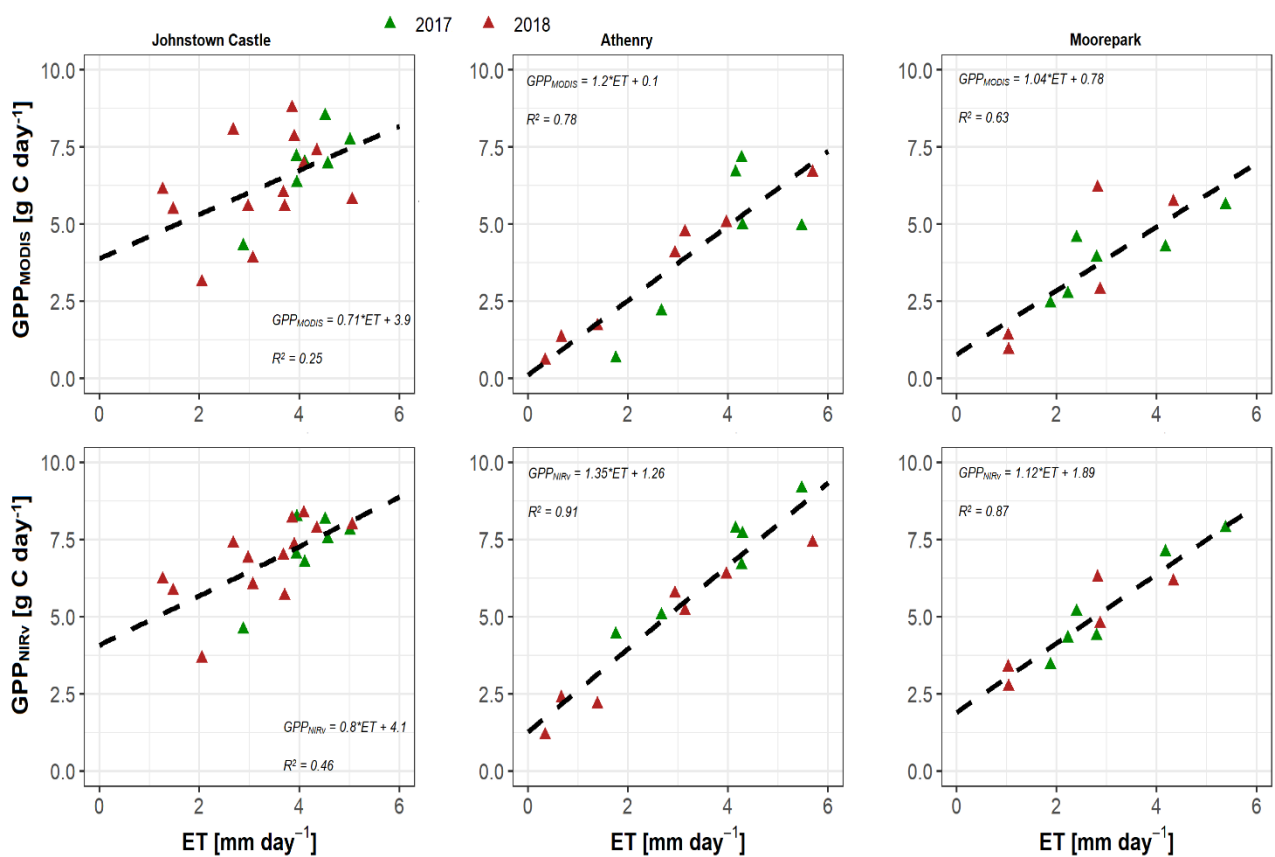


Figure 5.9. Relationships between daily evapotranspiration (ET) and gross primary productivity (GPP) derived from MODIS light use efficiency scheme, GPP_{MODIS} [top]; GPP derived from near infrared reflectance of vegetation, GPP_{NIRv} [bottom] for 2017 [green] and 2018 [red] image dates across the farms. Values are derived from the highlighted sample grass plots in Figure 5.1.

Figure 5.10 shows the ecosystem-level WUE ($\text{g C kg}^{-1} \text{H}_2\text{O}$) estimates for the Johnstown Castle site for the selected image dates in 2017 and 2018. The $\text{WUE}_{\text{MODIS}}$ and WUE_{NIRv} were derived from the approaches described in Section 5.2.6. The results from both approaches are consistent in terms of spatial and temporal changes. The estimated pixel WUE values are generally below 2.0 for grassland during the 2017 growth season and the maximum growth period in 2018 across the farm. This implies that soil water is abundant, leading to an increase in plant transpiration rate that is nearly close to the rate of photosynthetic carbon assimilation.

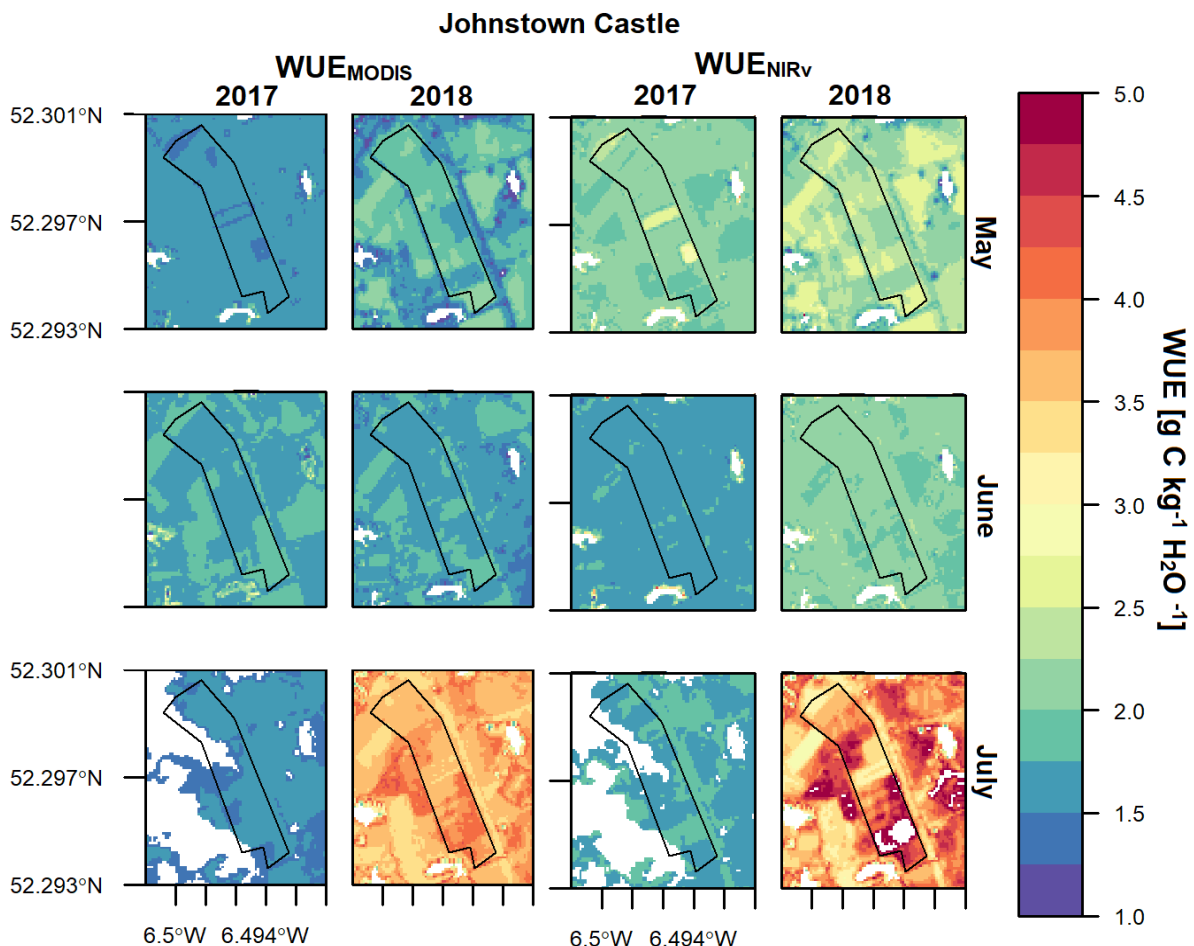


Figure 5.10. The daily water-use efficiency (WUE) maps at Senitnel2-scale for three selected image dates during 2017 and 2018 for Johnstown Castle farm. $\text{WUE}_{\text{MODIS}}$ maps are derived from GPP-based MODIS light use efficiency scheme, while WUE_{NIRv} maps are derived from NIRv-based approach. The WUE maps from both approaches are included to distinguish the model responses between wet and dry conditions, potentially explained by high use efficiency module.

However, the large values (between 4.0 and 5.0) across the grasslands in July suggest an exponential decrease in the rate of water loss through transpiration, possibly due to stomata closure, with small change in photosynthetic carbon fixation, since the GPP slightly decreased during this period (see Figure 5.9)

For Athenry (Figure 5.11), there are observed differences between the magnitudes of WUE_{MODIS} and WUE_{NIRv} . For instance, WUE_{MODIS} values are uniform across farms but progressively increased (0.8-1.8 during 2017 and 0.4-1.6 during 2018) over the course of the season. However, the values of WUE_{NIRv} in 2017 dropped from 2.0 (1.8 for 2018) in May to 1.6 (1.4 for 2018) in June, then increased (maximum rate at 2.6 over grasslands) in July of 2018. Similar differences between WUE_{MODIS} and WUE_{NIRv} , and pattern of changes in WUE are also identified at Moorepark (Figure 5.12). The maximum estimated WUE for Moorepark is between 2.0 and 2.6 for both approaches in July of 2018. The magnitudes of estimated WUE_{NIRv} are largely higher, relative to WUE_{MODIS} for Athenry and Moorepark farms. The different outcomes between both approaches suggest the role of LUE model that stand to constrain the MODIS-based GPP and WUE. The overarching question about which approach has the best capability to reproduce measured GPP and ecosystem WUE at such a high resolution needs further investigation, as this is not evaluated in this study. The WUE variations between dates also reflect the characteristics associated with biological processes and external environmental stressors.

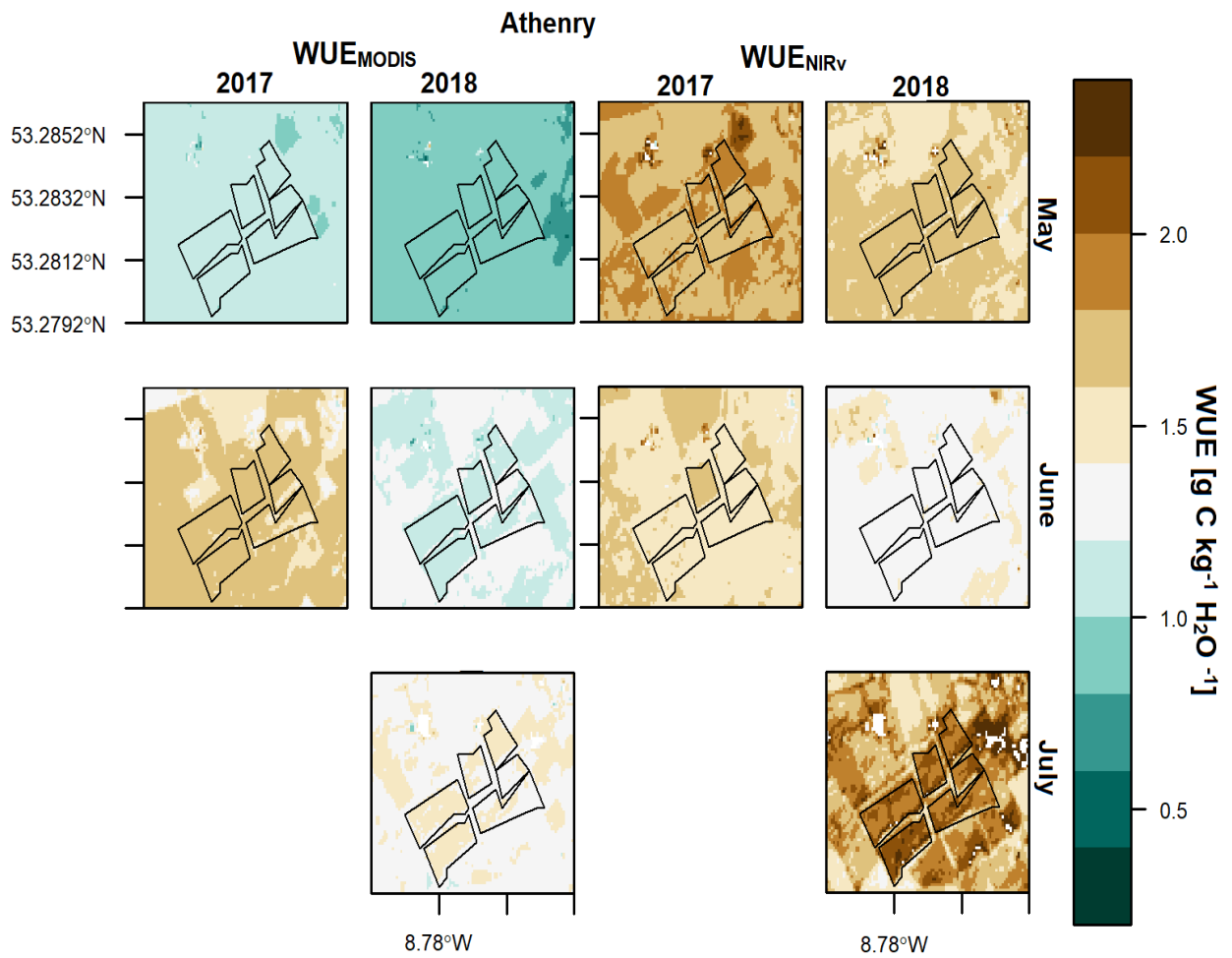


Figure 5.11. The daily water-use efficiency (WUE) maps at Senitnel2-scale for three selected image dates during 2017 and 2018 for Athenry farm. WUE_{MODIS} maps are derived from GPP-based MODIS light use efficiency scheme, while WUE_{NIRv} maps are derived from NIRv-based approach. The WUE maps from both approaches are included to distinguish the model responses between wet and dry conditions, potentially explained by ligh use efficiency module. No available cloud-free image in July of 2017.

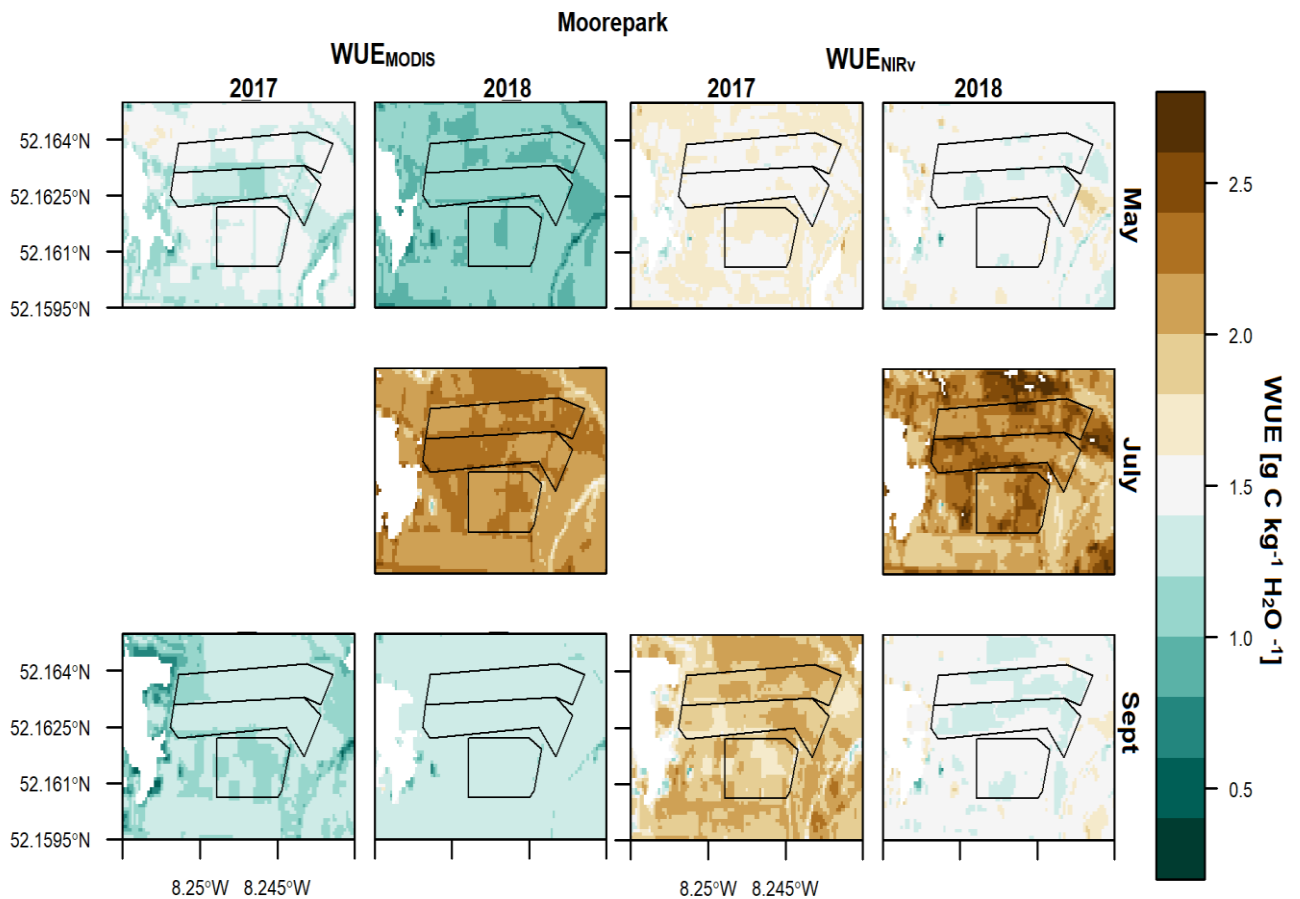


Figure 5.12. The daily water-use efficiency (WUE) maps at Sentinel2-scale for three selected image dates during 2017 and 2018 for Moorepark farm. WUE_{MODIS} maps are derived from GPP-based MODIS light use efficiency scheme, while WUE_{NIRv} maps are derived from NIRv-based approach. No available cloud-free image in June and July of 2017 and June of 2018.

5.3.4 Analysis of WUE-Yield correlations

Relationships between grass growth rate and estimated daily actual ET and ecosystem WUE from the integrated land surface scheme were further investigated for the active growth period (May-August) (Figure 5.13). The first row in Figure 5.13 shows the weekly time series of measured grass growth for 2017 and 2018. The yearly cycle and the peaks of grass growth between May and June are consistent for both years for all the farms. However, there is a clear delay in the start of 2018 growing season, arising from the longer winter and exceptional snow fall that stayed on the ground between late February and middle of March, relative to 2017 for the farms. In addition, Johnstown Castle appears to show lower amplitude of grass

growth, relative to Athenry and Moorepark, consistent with Sentinel-2 derived NIRv (Figures 5.3-5.5).

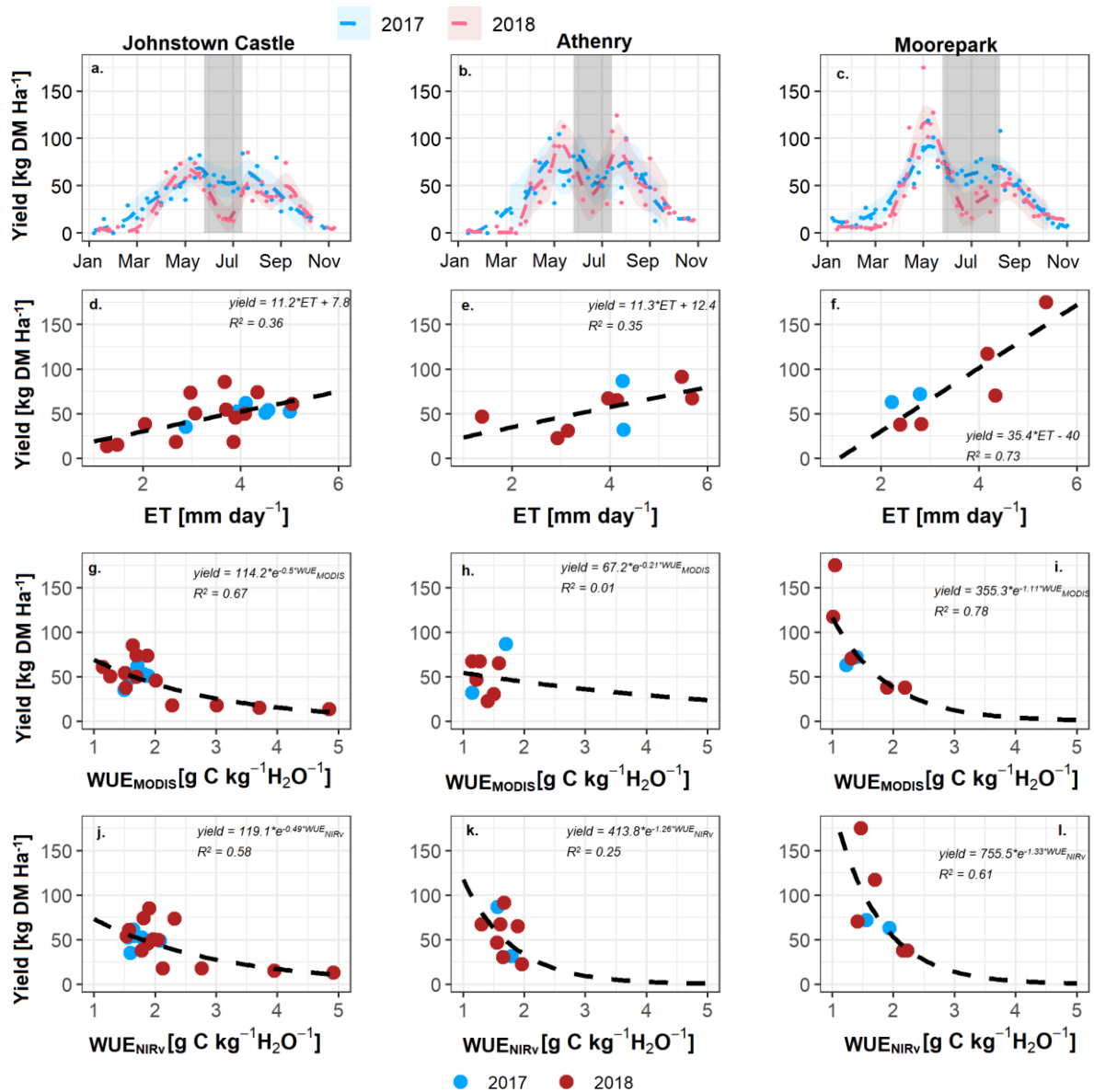


Figure 5.13. Temporal evolution of measured weekly grass yields of 2017 and 2018 across the farms [first row]. Relationships between water-use indicators (daily actual evapotranspiration, ET and water-use efficiency, WUE) at 10-m pixel and grass yields [rows 2-4]. WUE_{MODIS} maps are derived from GPP-based MODIS light use efficiency scheme, while WUE_{NIRv} maps are derived from NIRv-based approach. Scatterplots contain image dates within the period in respective grey box in first row. Values are for highlighted sample grass plots in Figure 5.1.

Comparatively, the grass growth rate dropped substantially during the 2018 mid-growing season, relative to the 2017 reference wet conditions. This is similar for all the farms (Figure 5.13 a-c), and indicates vegetation stress that is likely attributable to the combined negative effect of soil water and environmental stress. The recovery appears to occur at a faster rate or less impact at Athenry compared to the other farms, possibly due to Storm Hector that brought rainfall to the west in mid-summer thereby improving water availability in the area.

The analysis of ET-Yield and ecosystem WUE-Yield relations are provided in Figures 5.13d-f and 5.13g-l, respectively. The ET and WUE pixel values within the selected fields (highlighted black bounding boxes) were extracted and spatially averaged for each date of active growth period indicated in Figure 5.13a-c. The Sentinel-2 scale ET shows relatively weak correlations with grass growth ($R^2 \approx 0.3$) for Johnstown Castle and Athenry (Figure 5.13d-e) but a strong correlation ($R^2 \approx 0.7$) was obtained for Moorepark (Figure 5.13f). The grass growth shows an exponential relationship with ecosystem-level WUE across the farms. For Johnstown Castle, grass growth reveals much stronger correlation ($R^2 \approx 0.6$) with both WUE_{MODIS} and WUE_{NIRv} (Figure 5.13 g, j), while WUE-yield correlation remains relatively weak for Athenry (Figure 5.13 h, k). The WUE-yield correlation is also strong for Moorepark (Figure 5.13 i, l).

Generally, these results demonstrate that ET is much more related to WUE than GPP and thus, influences the plant WUE across the selected farms. The WUE is relatively low with some saturation under high rate of grass growth, but as the WUE increases above a certain point (observed value around $1.5 \text{ g C kg}^{-1} \text{ H}_2\text{O}$), grass growth rate dropped substantially to the lowest and becomes insensitive at higher WUE ($> 2.0 \text{ g C kg}^{-1} \text{ H}_2\text{O}$). Since the 10-m pixel allows discrimination between different land cover types, the results of this study are a good

representation of the landscape of interest (grassland) and provide a potentially useful tool for the assessment of water productivity and grass growth within pasture farms.

5.4. Discussion

Understanding the effects of changes in water availability on ecosystem functioning is essential to quantifying water and carbon budgets of landscapes at detailed spatial scales, particularly under water-limiting conditions. Water and carbon uptakes of ecosystem are generally understood to increase under non-limiting water conditions and decrease under water-limited conditions (e.g. Reichstein et al., 2002; Wagle and Kakani, 2012). However, ecosystem water-carbon couplings (WUE) can exhibit contrasting responses under different intensities of surface dryness or drought, as evidenced from observations and model-based analyses (Reichstein et al., 2002; Medrano et al., 2009; Lu and Zhuang, 2010; Wagle and Kakani, 2012; Zhou et al., 2020; Ma et al., 2021). This evidence needs to be tested at farm-scale for different environments and landscapes, as this will improve the understanding of regional climate change effects on ecosystem functioning (Reichstein et al., 2002). In this light, this study provides explanations to changes in water and photosynthetic carbon uptakes of grassland, quantified by ET and WUE during wet and dry years, and their effects on the measured grass growth rate within a farm in the context of Irish landscapes. The indicators were derived from an integrated land surface scheme at 10-m Sentinel2-scale for three selected pasture farmlands across Ireland.

Findings from this analysis indicate that plant water-uptake based on estimated actual ET are relatively higher during 2017 than 2018 growth periods at Johnstown Castle. Conversely, ET rates are enhanced during 2018 than 2017 growth periods at Athenry and Moorepark (note that the Sentinel-2 image dates of both years do not coincide). These variations of ET rates

between dry and wet years, and between farms can be explained by the integrated effects of changes in land surface and meteorological conditions. Warmer temperatures, facilitating higher atmospheric demand for ET, have been recognized to enhance ET processes over grasslands (Teuling et al., 2010; Stap et al., 2014; Lansu et al., 2020), which is in agreement with the findings from Athenry and Moorepark during May and June of 2018. However, the lower ET rates at Johnstown Castle during these periods demonstrate the role of grassland that shows lower growth rate across the farm, relative to Athenry and Moorepark. Generally, all the farms show substantial shortfalls in ET rates in July of 2018, relative to 2017 reference wet period, as a consequence of restricted plant water availability and higher stomatal resistance. Some types of grass (e.g. perennial C₄) are recognized to be drought-tolerant (e.g. Vignolio et al., 2005) due to their ability to tap water from the soil horizon to maintain high ET under water restrictions. The findings here demonstrate that the grass species within the sample pasture farms are shallow-rooted, and therefore indicate the plant's inability to extract water from the subsurface, leading to a low resilience to soil water shortage (De Boeck et al., 2011; Teuling et al., 2010). These findings also reveal the vulnerability of Irish grasslands to climate change and the need to devise a management option such as irrigation practice that will offset the worst impact of water stress on productivity.

Based on the derived Sentinel-2 scale ET and GPP (from both MODIS LUE- and NIRv-based approaches) for selected sample pasture lands, much stronger water-carbon couplings were identified over Athenry and Moorepark, relative to Johnstown Castle. This is because, the transpiration rates -a component of ET which is strongly connected to GPP (Kuglitsch et al., 2008) - is relatively higher over Athenry and Moorepark, and therefore confirms that these farms are more productive than Johnstown Castle, consistent with grass growth

measurements. Across all the farms, the derived WUE at ecosystem level are low ($1.5 \text{ g C kg}^{-1} \text{ H}_2\text{O}$) and show some saturation under full canopy coverage. This demonstrates that when vegetation is highly productive, the rates of water loss through transpiration are nearly equal to carbon uptake through photosynthesis over grass fields, possibly due to an increased plant access to soil water. This is consistent with Lu and Zhuang (2010) who reported low ecosystem WUE ($1.6 \text{ g C kg}^{-1} \text{ H}_2\text{O}$) for grassland in summer over conterminous USA. Several studies using modelling approaches (e.g. Reichstein et al., 2002; Lu and Zhuang, 2010; Zhao et al., 2020) have demonstrated that ecosystem WUE rises during drought conditions. Our analysis further reveals that the WUE rises above a certain point as the rates of grass growth drop exponentially, which agree with the findings from the previous studies. Although, these studies also noted contrasting pattern of ecosystem WUE using observations during drought (e.g. Wagle and Kakani, 2012), and when the intensity of drought becomes severe based on model results (e.g. Lu and Zhuang, 2010; Zhao et al., 2020).

The land surface scheme used here has been previously calibrated and evaluated over Irish landscapes (see Chapter 3) but, there are some caveats that need to be recognized. The two approaches used for GPP and resulting WUE estimates are based on the concept of LUE scheme (Running and Zhao, 2015; Jiang et al., 2020). The models incorporate different parameter coefficients which differ for land cover types (Prentice et al., 2015) and thus, require robust evaluation for different ecosystem types before applications in precision agriculture. Nevertheless, the use of WUE as a tool for grass growth prediction in this study provides an added advantage to ingest GPP that accounts for the contribution of plant photosynthesis process. The findings in that WUE-grass growth signal over grasslands occur during water-limiting condition, suggest essential information that underpin the

understanding of vegetation stress in relation to biogeochemical processes down to farm scales.

5.5 Conclusion

In this study, we applied a land surface scheme that has been previously evaluated for Irish landscapes to examine grass growth response to changes in ET and water-carbon coupling over pasture farms during wet and dry reference years. The modelling framework integrates high resolution Sentinel-2 products and GPP models that are based on LUE theory to quantify ET, GPP and WUE at farm-scale using three selected pasture farms across Ireland.

The study revealed variations in water-use response between image dates and between pasture farms. During the periods when vegetation is most productive, the rates of water-uptake closely match the rates of carbon-uptake for grasslands. However, ecosystem WUE increased (much more over Johnstown Castle farm, relative to the other research farms) under severe surface drying, due to a substantial reduction in plant water availability and increase in stomatal resistance. The observed stronger water-carbon couplings and lower WUE over Athenry and Moorepark grasslands confirm that these farms are more productive than Johnstown Castle. Additionally, WUE improved the correlations between ecosystem indicators and grass yields, relative to ET at farm-scale. Therefore, the findings demonstrate the potential of WUE as a tool for discriminating between optimal zones of productivity, and for grass growth predictions.

A major limitation of remote sensing-derived information for applications in precision agriculture is the paucity of data due to high low cloud coverage, particularly in Ireland. Nevertheless, the derived maps convey important spatially explicit information that will guide

on-farm decisions in relation to water and nutrient applications and management to maximize productivity, particularly during drought episodes in the future.

6. Conclusions

6.1 Summary

Terrestrial exchanges of heat, gases and momentum are outcomes of a complex set of interconnected processes that link soils, vegetative cover and the atmosphere. To capture these dynamic processes and simulate the associated exchanges that govern microclimate variations and affect vegetation growth and productivity, a physically-based Land Surface Scheme (LSS) is needed. Here, the LSS is based on the surface energy budget (SEB) framework and is used to estimate surface-air energy exchanges (including the latent (Q_E) and sensible heat fluxes (Q_H and Q_G)) and evapotranspiration (ET) to monitor regional agrometeorological conditions and crop productivity. This approach is distinguished from traditional monitoring and simulation approaches that rely on correlations between observed atmospheric and vegetation productivity variables. By contrast, a LSS provides a deeper understanding of the links between the conditions of the soil, the vegetative cover and the atmosphere and allows the integration of a variety of environmental data from multiple sources to generate simulations at high spatial and temporal resolution across Ireland.

Three principal research questions formed the basis of this PhD research:

1. Can a LSS be developed to simulate the terms of the surface energy budget in response to soil, vegetation and atmospheric variations across Ireland?
2. Can a validated LSS be used to explore (and predict) the emergence and development of agricultural drought and its regional characteristics?

3. Can the LSS be used to examine carbon uptake and water exchanges during dry and wet regimes, and be used to evaluate water use efficiency and grass yield at a farm scale?

Any specific extreme weather event could arise from a complex mix of natural and anthropogenic factors, thus an event may not necessarily be caused by human-induced climate change (Seneviratne et al., 2021). However, new knowledge on event attribution has provided strong evidence of strong increases in probability and magnitude of many heat waves (periods of extreme high temperature) and hot droughts (periods of extreme water shortage) in many regions around the world, attributable to human influence (Arias et al., 2021; Seneviratne et al., 2021). In 2018, the continental-scale hot droughts, reaching the island of Ireland was evident on grass yield in summer, particularly the south eastern agricultural area (e.g. Figure 1.5), and such impacts are projected to intensify and become more frequent in the future as the global average temperature continues to rise (e.g. Samaniego et al., 2018). The 2018 event partly sets the aims of this PhD research in focus, particularly as Irish grasslands which are primarily rainfed, have been shown to be vulnerable to climate change.

Each of the research questions were addressed in Chapters 3-5 and a synthesis of key findings from each chapter, contributions to scientific knowledge, and implications for policy in relation to the research questions is provided in the following sections.

6.1.1 Understanding LSS sensitivity and performance over Irish landscapes

Chapter 3 evaluated the applicability of a LSS that incorporates routine weather observations to simulate daytime surface radiation and energy balance components, using two test sites (Johnstown Castle and Dripsey) with different soil drainage characteristics. The sensitivity of

the model to different parameterizations of surface resistance (r_s), and to environmental stressors was evaluated with the primary goal of improving model estimates of fluxes. The effects of using estimated global radiation ($Q_{s\downarrow}$) and of using $Q_{s\downarrow}$ from an off-site weather station on model performance were also examined.

The LSS generated Q_E values that produced a good fit to the observed Q_E values at Dripsey (a site dominated by poorly drained soils and similar to the 'Cabauw' site where the scheme was originally developed). However, the fit between the measured and modeled Q_E values was poor for Johnstown Castle (a site dominated by seasonally dry, imperfectly drained soils). The study highlighted a plausible physical property, the soil moisture coefficient (c_{soil}), responsible for the identified differences in the results, as the soil moisture content drops below the upper limit of critical value ($0.25 \text{ m}^3 \text{ m}^{-3}$) separating the wet from drying soils (Shuttleworth, 1993). The c_{soil} term, which determines the water stored and available to plants for evapotranspiration, represents the important memory of the system and is accounted for only by using a modified Jarvis formulation of r_s (Beljaars and Bosveld, 1997). Calibrating this model property from the original ($6.3 \text{ m}^3 \text{ m}^{-3}$ suits wet soils at Dripsey) to a different optimum soil condition of $4.3 \text{ m}^3 \text{ m}^{-3}$ resulted in Q_H and Q_E values that fit well with the measured values at Johnstown Castle. Therefore, the derived optimum c_{soil} coefficient is suited to both wet and seasonally dry soils and is applied for subsequent model runs in Chapters 4-5.

Additionally, the study demonstrated at Dripsey that the use of off-site meteorology from the nearest weather station, approximately 25 km removed from the sites, and estimated $Q_{s\downarrow}$ and soil water from a similar wet but different precipitation year, produced flux estimates that agree well with the measured values, notwithstanding the inherent uncertainties. Generally,

the de Rooy and Holtslag (1999) scheme used here demonstrated good performance in replicating the measured fluxes through the adjustment of c_{soil} , but the scheme is sensitive to different soil characteristics. Hence, the study suggests that a careful consideration should be given to the treatment of c_{soil} when applying de Rooy and Holtslag (1999) scheme with modified Jarvis r_s parameterization (Beljaars and Bosveld, 1997) over different surface conditions.

6.1.2 Evaluating regional SEB and exchange processes during drought

Chapter 4 evaluates the regional characteristics of surface energy fluxes, simulated by the LSS (Chapter 3) using meteorological data from fourteen automatic weather stations across Ireland in combination with ERA5-Land volumetric water content in the topsoil layer (0-7 cm). The objective here was to explore the role of land surface processes in the amplification of summer climate extremes, using the continental-scale severe drought event of 2018 as a case study. A descriptive analysis of drought during summer of 2018 was initially carried out, combining ground meteorology, global reanalyses soil moisture and satellite-derived leaf area index (LAI). Changes in land-atmosphere exchange processes, and the effects of seasonal shift in soil moisture regime on land-atmosphere sensitivities at regional scale were also investigated. It should be noted that the calibrated c_{soil} value in Section 6.1.1 was based on two grassland sites where in-situ soil moisture measurements were available. However, as ERA5-Land may overestimate soil water in extremely dry surface (Dirmeyer et al., 2021; see also Figure 4.2), the c_{soil} which is sensitive only as soil water drops below critical value, may facilitate underestimation of surface resistance and consequently, underestimate the effects of seasonal shift in soil moisture regime on land-atmosphere sensitivities using the LSS. The regime shift is explored using a soil moisture-evaporative fraction (θ -EF) framework that

distinguishes three different stages of transition from wet to dry evaporative regime (Seneviratne et al., 2010; Teuling et al., 2010): (1) wet regime in which EF is independent of soil moisture (2) transitional regime where soil moisture and EF are linearly coupled and (3) dry regime where EF becomes negligible. A Similar approach was applied to the near-infrared reflectance of vegetation (NIRv) data, as a way of comparing with the EF based approach, and which provides a means of linking soil moisture to vegetation productivity and ecosystem functioning.

The study demonstrates that the impacts of 2018 drought event on land-atmosphere energy exchanges were dominated first by atmospheric anomalies. That is, as the rainfall deficit increased throughout summer months, the observed higher evaporative demand associated with warmer temperature enhanced Q_E exchange with the overlying air, leading to higher soil moisture deficits and subsequent soil moisture constraints in July across the country. This was particularly evident in the East and South-East of the country (defined by mixed grazing agricultural region, less precipitation, warmer temperature and high proportion of fertile well/moderately soils), where the drying soils quickly shifted into a prolonged 'transitional' evaporative regime in which the evaporative fraction (EF) was constrained by the land surface state, consequently providing the mechanisms (increase in land surface temperature and Q_H) that positively feedback into the air, beginning from 27 June and further amplified agricultural drought in July. The Irish climate is principally influenced by the Atlantic Ocean through advection of moist air, as such, the country does not suffer temperature extremes experienced by many other countries. However, the unusually high temperature beginning from 27 June suggests that the advection was very weak, affirming that the land surface is the dominant influence on the atmospheric conditions during these periods. While previous

studies (e.g. Falzoi et al., 2018; Moore et al., 2020) had analysed the 2018 drought, the analysis carried out here was the first attempt in Ireland to link the drought or any previous drought event to landscape processes.

Based on segmented analysis of the role of ERA5-Land soil moisture extremes in surface-air signals, the study identified significant critical soil moisture (θ_c) threshold (0.18 m³ m⁻³ from θ -EF interplay and 0.23 m³ m⁻³ from θ -NIRv analysis) of regime shift into land-atmosphere couplings in the East and Southeast zone. Although, the θ regime shifts were also identified across the rest of the country, the θ -EF signals were too weak to conclude that the surface-air exchanges were constrained by land surface state in these areas.

The parameter θ_c is a key determinant of the landscape transition from wet to dry evaporative regime. Hence, the contributions of this study are essential to speculate the zones and θ_c points under which surface-air couplings are strongest in water-limited regimes across the country. This information is important to facilitate subseasonal-to-seasonal predictability of drought propagation and early warning systems of summer climate extremes in the future episodes

6.1.3 Relating high resolution farm-scale water use to grass yields.

Chapter 5 sought to quantify farm-scale evapotranspiration (ET) and ecosystem water use efficiency (WUE) (here defined as the ratio of photosynthetic gross primary productivity and water loss through ET) at a high spatial resolution, integrating the scheme with a light use efficiency model (Running and Zhao, 2015; Jiang et al., 2020) and Sentinel-2 data. The aim was to evaluate the potential of ET and WUE as viable ecosystem indicators for predicting grass yields within a pasture farm. Changes in farm-scale water use between wet and dry

years were mapped and evaluated for Sentinel-2 cloud-free image dates. The links between measured farm-scale grass yield (pasture growth rate in kilograms Dry Matter per hectare per day, kg DM/ha/day), ET (grass Yield-ET correlation) and WUE (grass Yield-WUE correlation) were also analysed.

The study demonstrated that the rates of water loss through ET is nearly equal to the rates of photosynthetic carbon assimilation of grass, and identified that saturation in ecosystem WUE ($\approx 1.0\text{-}1.5 \text{ g C kg}^{-1} \text{ H}_2\text{O}$) value occurs during the period when vegetation is most productive across the selected pasture research farms (Johnstown Castle, Athenry and Moorepark). During severe surface drying and vegetation stress, experienced during July of 2018, the study found a substantial increase in ecosystem WUE due to the reduction in ET over grass, much more at Johnstown Castle compared to the other research farms. The observed stronger ET-GPP couplings ($R^2 \approx 0.6\text{-}0.9$) and lower ecosystem WUE at Athenry and Moorepark confirm that these farms are more productive than Johnstown Castle, consistent with the measured grass yield data.

The study further demonstrates that the use of WUE rather than ET, improved the correlations between ecosystem indicators and grass yields at farm-scale. Therefore, remotely sensed Sentinel-2 observations can be used in the current LSS to provide spatially explicit information that underpin the understanding of biogeochemical processes down to farm scales, and the use of ecosystem WUE is a better indicator of grass growth response to climate change.

6.2 Research Limitations

This thesis used a LSS, based on the surface energy budget concept (SEB), to provide an improved understanding of regional characteristics of land-atmosphere interactions, changes in water availability at detailed spatial scales, and to improve the estimates of surface energy fluxes. The work also points towards the poor understanding of the role of land surface processes in grass growth response to climate change in Ireland. Chapter 3 adapted a land surface scheme applicable to Irish landscapes and provided a validated model for the remaining chapters. Chapters 4-5 presented a promising path to use high resolution polar-orbiting satellite information in a modelling framework to provide scientific-based evidence relating to biogeochemical processes to support on-farm planning and management activities. The concept used in this work leveraged an existing land surface scheme and readily available in situ, gridded and satellite observations. Based on the findings from Chapters 3-5, the following conclusions are drawn: The LSS provides an alternative to more traditional diagnostic based approaches, and reduces the requirement of a high number of input parameters that often limit the application of land surface models for regional and local scale applications. By evaluation, the LSS performed well across different surface and atmospheric conditions, and led to an improved understanding of specific climate extreme events and how grasslands respond to extreme drought event, which are likely to increase in frequency and intensity as a consequence of climate change. Hence, it provides mechanistic evidence for applications in other regions and in the future. However, this work has some major caveats that should be taken into consideration when interpreting or using the results for decision making. These include,

- Non-closure of surface energy budget from an eddy covariance system

- Inherent errors from global reanalyses soil moisture data
- Uncertainty in estimated gross primary productivity and ecosystem water use efficiency
- Insufficient remotely-sensed cloud-free observations

(i) Surface energy budget closure problem

The surface flux estimates derived from the land surface scheme were evaluated by comparison with eddy covariance (EC) measurements made at two sites in Chapter 3. EC measurements are known to underestimate the turbulent fluxes (Q_H and Q_E) relative to the measured available energy ($Q_N - Q_G$), leading to energy budget closure problem (e.g. Franssen et al., 2010; Stoy et al., 2013). This is mainly because EC systems do not capture the effects of large-scale eddies that are linked to landscape heterogeneity (Foken, 2008). This work did not attempt to evaluate the magnitude of underestimations but since the energy budget closure at the two test sites were consistent with those reported in the previous studies (e.g. Wilson et al., 2002), the impact of non-closure energy balance on the model outputs is assumed to be small and less significant. However, the non-closure (error) term which may be between 10-20 %, should be borne in mind when EC measurements are used to evaluate surface flux estimates from the LSS.

(ii) Errors inherent in global reanalyses soil moisture data

Soil moisture measurements are not routine practice in Ireland, similar to several other countries across the globe; Chapters 4 and 5 relied on ERA5-Land volumetric water content for model runs and other analysis. ERA5 product is limited in that it uses monthly climatology

of LAI to generate the global reanalyses data (Boussetta et al., 2013), which may not adequately capture the synoptic time-scale variability in surface-air signals during severely dry conditions (Dirmeyer et al., 2021). As demonstrated in Chapter 4, ERA5-Land may have underestimated very dry soils, consequently resulting in the land surface scheme to underestimate the impact of soil moisture anomalies on land-atmosphere feedback mechanisms.

(iii) Uncertainty in estimated gross primary productivity and water use efficiency at ecosystem level

Though the outputs from the land surface scheme are evaluated in Chapters 3-4, the estimated gross primary productivity (GPP) and ecosystem WUE values at Sentinel2-scale in Chapter 5 are based on the concept of light use efficiency (LUE) theory (Running and Zhao, 2015; Jiang et al., 2020). The GPP models incorporate different parameter coefficients which differ for land cover types (Prentice et al., 2015) and thus, require robust evaluation for different ecosystem types before applications in precision agriculture. Due to lack of measured GPP in this work, there may likely be uncertainties in the estimated ecosystem WUE due to the possibility of systematic errors inherent in GPP models.

(iv) Insufficient remotely sensed cloud-free observations

A major limitation of remote sensing-derived information for applications in precision agriculture is the paucity of data due to impact of cloud coverage on data availability, particularly in Ireland. Although, more satellite images for cloud-free dates were available, particularly during 2018 drought event, and used in Chapter 5, the sparse or missing images between dates point towards the limitation of this work to provide detailed temporal

information for agricultural applications. The development of integrated multi-sensor fusion technique (e.g. Guzinski et al., 2020; Singh et al., 2020) in recent past refers to a promising path that enables provision of high spatial and temporal resolution information. The potential benefits of radar data (Sentinel 1) require further exploration in countries, such as Ireland, however, it has associated challenges.

6.3 Implications for Policy

This thesis attempted to test the ability of a LSS to improve our understanding of how agricultural lands, particularly pastoral lands would respond to changes in surface climate; by moving away from traditional approaches in which weather variables are directly related to grass yields, to a prognostic approach that allows robust assessments of plants physiological interactions in response to external environmental factors. Considering the research findings and limitations highlighted above, the following are recommended for policy intervention:

i. Create soil moisture monitoring network to complement meteorological observations

Soil moisture variability is recognized to be the major environmental factor influencing the model sensitivity, leading to erroneous simulations of surface heat and water fluxes that govern plant performance and growth, particularly on Irish (well-drained, moderately-drained and imperfectly-drained) soils that often experience seasonally dry regime. Applying this framework would therefore require reliable, consistent and fairly represented national soil moisture network across Irish grasslands above the aforementioned soil drainage characteristics. Such a long-term monitoring network has been initiated and currently

underway within the Irish Agmet group, a working group on Agrometeorology (Hochstrasser et al., 2021) and other large scale projects, including Terrain-AI (terrainai.com). Moreover, this thesis affirmed that the initiative needs policy intervention to further aid wide spread support from related stakeholders towards actualising the primary goal of the projects and; the importance of providing measured soil moisture data to improving model applications in Irish agricultural landscapes cannot be overemphasized.

Soil water availability controls the biophysical interactions of plants. When the soil moisture content is very low (below the wilting point), plants respond by closing their stomata and consequently struggle to survive. Similarly, too much water can be equally detrimental. Therefore, the more insights we gain about soil moisture regimes, the better the decisions to recognise the impacts soil moisture can have on local weather conditions, and the particular conditions that are suited to a plant. In essence, soil moisture information are needed generally not only to evaluate/calibrate a LSS but also to capture the information on the land-atmosphere system, including monitoring impacts of changes in ET, rainfall and temperature patterns that are associated with surface-air coupling and feedback processes in a changing climate. However, soil moisture measurements are lacking at spatial scale and can be unrepresentative of the structure due to soil heterogeneity, limiting the capacity to efficiently capture the dynamic processes. The soil moisture monitoring network will complement the extensive meteorological observation network to capture these information and how they vary spatially and temporally is fundamental to gain an insight into likely future conditions, as the climate projections for Ireland (e.g. Fealy et al., 2018) are likely to threaten Irish agriculture through an increase in the occurrence, frequency and severity of surface drying in the remaining period of 21st century.

ii. Create a network of stations to measure surface-air fluxes, including terrestrial carbon fluxes.

It is critical that model simulations of surface heat, water and carbon fluxes using the modeling framework must be evaluated against ground-based measurements before applying to inform on-farm decisions. However, as demonstrated in this thesis, in-situ measurements of surface fluxes have significant systematic bias that must be recognized when interpreting model simulations. Notwithstanding, measurements which may be obtained using different techniques, are required before the modeling framework can be used to estimate surface heat, water and carbon fluxes. Though the model outputs were evaluated in Chapters 3-4 of this thesis, more test sites may be sampled, to particularly cover measurement of terrestrial carbon fluxes for sustainable period over different soil types. The importance of adding carbon fluxes stems from the findings in Chapter 5 which revealed that integrating water use and photosynthetic carbon fixation of plants can improve the ability of ecosystem indicators to predict grass yields at farm level.

Apart from using flux measurements to improve model outputs, the land-atmosphere system comprises of a highly complex processes that link surface-air exchanges with biological and physiological responses and in fact, requires both the observations (network) and theory (model) to understand its various elements and interactions. Our capacity to offer scientific understanding on landscape processes operating on a wide range of spatial and temporal scales, and to monitor ecosystem response, is predicated on our capability to measure, describe, understand and predict the land-atmosphere fluxes of heat, water and carbon. Eddy covariance (EC) is an effective technique for measuring these fluxes with greater precision, as reliable measurements are required to evaluate model outputs or to effectively integrate with

models to provide evidence for sustainable landscape management. To this end, policy intervention would require significant infrastructure to deploy and maintain EC systems alongside the soil moisture instrument for consistent and reliable observing network across Irish agricultural lands.

iii. Development of short-term spatially refined landscape management actions to support agriculture.

Notwithstanding the limitations associated with the available gridded soil moisture products as highlighted above, the LSS has further demonstrated the ability to explain and improve our understanding of specific extreme climate events such as agricultural drought, as shown in Chapter 4. Findings indicate that Irish grasslands which are primarily rainfed and largely characterized as wet 'evaporative' regime, can switch into a regime in which evapotranspiration is constrained by land surface conditions, particularly water availability. This shift may eventually exacerbate surface drying by increasing warming locally through positive land-atmosphere feedbacks under water restrictions, and these responses can be quicker in the South and South East which are dominated by free draining soils. As the occurrence and severity of these physical processes are expected to be frequent and increase in the future, this thesis demonstrated the vulnerability of Irish grasslands to climate change and the need to devise a short-term adaptation measures that will offset worst impact of such extreme events, as the efforts to mitigate or limit warming would perhaps take a longer period to achieve. Considering the evidence from this thesis, it has become imperative for policy makers to develop efficient spatially refined strategies that will guide/inform on-farm water administration and management since agricultural production across Ireland is likely to switch from rain-fed into more of management practices such as irrigation system, in a

changing climate. Since this modeling framework can provide information relating to the onset of agricultural drought and amounts of water that may be required to offset the impact on Irish grasslands, infrastructure can be deployed to ensure the establishment of irrigation scheduling by the farmers based on the well-informed knowledge of their local agrometeorological conditions. A sprinkler irrigation system is an example of a non-rainfed system that can be employed to provide efficient water administration over agricultural lands. Identification of plant species (e.g. C₄ plants) that are resilient to heat and drought, and/or deep-rooted to access water in the deeper soil profile during water restriction, is also an important adaptation measure that may assist in reducing the impacts of climate extremes on Irish grasslands.

Additionally, there exists an enormous volume of Earth observations (EO) from multiple sources (e.g. Satellite, airborne, etc.) that has not been usefully harnessed to support local/regional and national landscape management. EO data are holistic, continuous and in many cases provide near-real time information over a wider land coverage. As demonstrated in Chapter 5, Satellite data (e.g. Sentinel-2 products) can be integrated to map the farm level biophysical responses and water use at a detailed spatial scale, which are needed by grassland farmers to make informed decisions every day. However, cloud coverage can provide a setback to fully integrate EO for day to day farm management actions across Ireland. The use of airborne (e.g. drones) platforms to capture the landscape is an emerging EO technology that may not be affected by cloud and has seen huge growth within a short period in providing services for Irish farmers. Currently, a new national multidisciplinary project (terrainai.com) is underway with the primary objective of integrating EO data from multiple sources, including airborne, and in-situ data with modeling approaches to improve the knowledge of land use

activity. This type of large-scale contribution with emphasis on integration of EO data can be reinforced to improve day to day on-farm management practices.

6.4 Future work

As previously highlighted, applying the modelling framework in the future may require that the outputs from the models be thoroughly evaluated against the measured surface fluxes to ensure some level of consistency and accuracy. Overall, the current work emphasizes the importance of soil moisture in the current framework. Hence, future work could implement this framework with more reliable soil moisture data to improve estimates of surface fluxes during extremely dry regime. Gross primary productivity (GPP), a carbon budget component, measurements from a number of test sites across Irish landscapes would enable cross-comparison and evaluation of GPP models, and robust analysis of WUE at ecosystem level in the future. The information about grass response to water-carbon coupling in Chapter 5 could perhaps stimulate more diagnostic analyses and motivate the integration of the current framework with carbon components of earth system models. This model integration could lead to a better understanding of the role of landscapes in water, energy and carbon dynamics.

As highlighted in Section 6.3, the integration of EO data is a potential approach to holistically monitor the ecosystem response to environmental changes down to farm levels. Satellite (e.g. Landsat, Sentinel) products may be limited in space and/or time due to clouds over Ireland, however, the gaps can be filled, depending on the number of available images, using algorithms developed (e.g. in the Moderate Resolution Imaging Spectroradiometer, MODIS program) to optimize cloud free products and must be tailored to the particular landscape management in Ireland (Green, 2019). There are multisource satellite fusion approaches (e.g.

Yang et al., 2018; Singh et al., 2020) that can also be employed to provide spatially and temporally consistent landscape information. The essence of multispectral fusion approaches is to integrate low (e.g. MODIS, Sentinel-3) and high (e.g. Sentinel-2, Landsat) spatial resolution satellite products to capture information at finer resolutions (e.g. 20 m and daily) for precision agricultural applications at field/farm scales. Thus, the integration of EO is an area of research that is certainly open for an improvement in the provision of useful land management information at detailed temporal and spatial scales in the future.

There is a wide understanding that certain crops perform better in a particular region, and such growth performance could be attributed to the combined climate factors (e.g., amount of rainfall, length of growing season, frequency of frost damage, etc.) and environmental factors (e.g., soil type, topography, etc.) (van Wart et al., 2013). It is with this knowledge that the concept and definition of agro-environmental zonation emanated with the primary purpose of identifying and delineating areas with similar groups of potentials for planning, management and development (FAO, 1996). The United Nations Food and Agriculture Organization (FAO) defines agro-ecological zones (AEZ) based on the combined characteristics of climate, soil and landform (FAO, 1996). In Ireland, rainfall and temperature characteristics were often used to delimit the growth environment of plants (e.g. Holden and Brereton, 2004), without accounting for the variability in soil conditions which can also define the responses of plants in different regions (Fitzgerald et al., 2005, 2009). Therefore, further research may seek to apply the framework used in this thesis as a way of translating the integrated effects of soil, energy, environment and vegetation conditions into relevant homogenous zones of agri-environment to inform planning and decision making, and consequently harness optimal zones of productivity.

Overall, future work will leverage the knowledge from this thesis to develop modeling capacities and tools for monitoring short and long-term evolution of terrestrial carbon, heat and water exchanges, in response to soil moisture variations and land use. The sixth assessment report of IPCC has established human-induced climate change impact on terrestrial ecosystems (Arias et al., 2022), hence, incorporating land use will provide a pathway to understanding the extent of human footprints on Irish microclimate. The model development will build on existing state-of-the-art global dynamic land surface models (e.g. NOAH-MP, JULES, ORCHIDEE, etc.) that couple different physical processes, including hydrology, surface energy budget and carbon to better represent the behaviour of the system. Additionally, the ongoing large-scale ground-based and airborne monitoring networks (e.g. Terrain-AI and AgMET projects), emerging satellite technology (e.g. the ESA Sentinel, Proba-V and MetOp missions, the OCO mission and the GOME series) and state-of-the-art global reanalyses (e.g. ECMWF ERA5 products) will form an important integration to constrain the models, with emphasis on uncertainties arising from model parameters and structure.

It is therefore hoped that this work should provide valuable insights that will assist interested researchers/experts to further improve our understanding in relation to climate science, hydrology, and agriculture in the future.

Bibliography

- Abtew, W., Melesse, A., 2012. Evaporation and Evapotranspiration: Measurements and Estimation. *Springer Dordrecht*. ISBN: 9400747365, 290 p.
- Agam N, Kustas WP, Anderson MC, Norman JM, Colaizzi PD, Howell TA, Prueger JH, Meyers TP, Wilson, T.B., 2010. Application of the Priestley–Taylor approach in a two-source surface energy balance model, *Journal of Hydrometeorology*, 11, 185–198.
- Aires, L. M. I., Pio, C. A., Pereira, J. S., 2008a. The effect of drought on energy and water vapour exchange above a Mediterranean C3/C4 grassland in Southern Portugal, *Agric. Fores. Met.*, 148, 565-579
- Aires, L. M. I., Pio, C. A., Pereira, J. S., 2008b. Carbon dioxide exchange above a Mediterranean C3/C4 grassland during two climatologically contrasting years, *Global Change Biology*, 14, 539-555.
- Akbar, R., Short Gianotti, D. J., McColl, K. A., Haghighi, E., Salvucci, G. D., & Entekhabi, D., 2018. Estimation of landscape soil water losses from satellite observations of soil moisture. *Journal of Hydrometeorology*, 19, 871–889
- Akumaga, U., Alderman, P. D., 2019. Comparison of Penman-Monteith and Priestley-Taylor evapotranspiration methods for crop modeling in Oklahoma, *Agron. J.*, 111, 1171-1180
- Albergel, C., Dutra, E., Bonan, B., Zheng, Y., Munier, S., Balsamo G., de Rosnay, P., Muñoz-Sabater, J., and Calvet J-C., 2019. Monitoring and Foerecasting the impact of the 2018 summer heatwave on vegetation, *Remote Sensing*, 11, 520, doi:10.3390/rs11050520
- Alexander, L., 2011. Climate science: extreme heat rooted in dry soils, *Nat. Geosci.* 4, 12–13. doi:10.1038/ngeo1045
- Allen, R. G., Pereira, L. S., Raes, D. and Smith, M., 1998. Crop evapotranspiration. Guidelines for computing crop water requirements. *Irrigation and Drainage Paper No. 56*. Rome: FAO.
- Allen, R. G., Tasumi, M., and Trezza, R., 2007. Satellite-based energy balance for mapping evapotranspiration with internalized calibration (METRIC)-Model. *Journal of Irrigation and Drainage Engineering*, 133, 380.
- Allen, R.G., Pereira L.S., Howell T.A., Jensen M.E., 2011. Evapotranspiration information reporting: I Requirements for accuracy in measurement. *Agric. Water Manage.*, 98, 899-920.
- Anderson, M. C., Norman, J. M., Mecikalski, J. R., Otkin, J. A., Kustas, W. P., 2007. A climatological study of evapotranspiration and moisture stress across the continental United States based on thermal remote sensing: 1. Model formulation. *J. Geophys. Res. Atmos.*, 112, 1-17
- Anderson, M. C., Hain, C., Wardlow, B., Pimstein, A., Mecikalski, J. R., Kustas, W. P., 2011. Evaluation of drought indices based on thermal remote sensing of evapotranspiration over the continental United States, *J. Clim.*, 24, 2025-2044

- Anderson, M. C., R. G. Allen, A. Morse, and W. P. Kustas, 2012. Use of Landsat thermal imagery in monitoring evapotranspiration and managing water resources, *Remote Sens. Environ.*, 122, 50– 65
- Anderson, M. C., C.A. Zolin, P.C. Sentelhas, C.R. Hain, K. Semmens, M. Tugrul Yilmaz, F. Gao, J.A. Otkin, R. Tetrault, 2016a. The Evaporative Stress Index as an indicator of agricultural drought in Brazil: an assessment based on crop yield impacts, *Remote Sens. Environ.*, 174, 82-99
- Anderson, M. C., C.R. Hain, F. Jurecka, M. Trnka, P. Hlavinka, W. Dulaney, J.A. Otkin, D. Johnson, F. Gao, 2016b. Relationships between the evaporative stress index and winter wheat and spring barley yield anomalies in the Czech Republic, *Clim. Res.*, 70, 215-230
- Arias, P.A., N. Bellouin, E. Coppola, R.G. Jones, G. Krinner, J. Marotzke, V. Naik, M.D. Palmer, G.-K. Plattner, J. Rogelj, M. Rojas, J. Sillmann, T. Storelvmo, P.W. Thorne, B. Trewin, K. Achuta Rao, B. Adhikary, R.P. Allan, K. Armour, G. Bala, R. Barimalala, S. Berger, J.G. Canadell, C. Cassou, A. Cherchi, W. Collins, W.D. Collins, S.L. Connors, S. Corti, F. Cruz, F.J. Dentener, C. Dereczynski, A. Di Luca, A. Diongue Niang, F.J. Doblas-Reyes, A. Dosio, H. Douville, F. Engelbrecht, V. Eyring, E. Fischer, P. Forster, B. Fox-Kemper, J.S. Fuglestedt, J.C. Fyfe, N.P. Gillett, L. Goldfarb, I. Gorodetskaya, J.M. Gutierrez, R. Hamdi, E. Hawkins, H.T. Hewitt, P. Hope, A.S. Islam, C. Jones, D.S. Kaufman, R.E. Kopp, Y. Kosaka, J. Kossin, S. Krakovska, J.-Y. Lee, J. Li, T. Mauritsen, T.K. Maycock, M. Meinshausen, S.-K. Min, P.M.S. Monteiro, T. Ngo-Duc, F. Otto, I. Pinto, A. Pirani, K. Raghavan, R. Ranasinghe, A.C. Ruane, L. Ruiz, J.-B. Sallée, B.H. Samset, S. Sathyendranath, S.I. Seneviratne, A.A. Sörensson, S. Szopa, I. Takayabu, A.-M. Tréguier, B. van den Hurk, R. Vautard, K. von Schuckmann, S. Zaehle, X. Zhang, and K. Zickfeld, 2021: Technical Summary. In *Climate Change 2021: The Physical Science Basis. Contribution of Working Group I to the Sixth Assessment Report of the Intergovernmental Panel on Climate Change* [Masson-Delmotte, V., P. Zhai, A. Pirani, S.L. Connors, C. Péan, S. Berger, N. Caud, Y. Chen, L. Goldfarb, M.I. Gomis, M. Huang, K. Leitzell, E. Lonnoy, J.B.R. Matthews, T.K. Maycock, T. Waterfield, O. Yelekçi, R. Yu, and B. Zhou (eds.)]. Cambridge University Press. In Press.
- Arya, P. S., 2001. *Introduction to Micrometeorology*, 2nd ed., 420 pp., Academic Press, San Diego, Calif.
- Aubinet, M., A. Grelle, A. Ibrom, Ü. Rannik, J. Moncrieff, T. Foken, A.S. Kowalski, P.H. Martin., 2000. Estimates of the annual net carbon and water exchange of forests: the euroflux methodology. *Adv. Ecol. Res.*, 30, 113-175
- Badgley, G., Field, C. B., and Berry, J. A., 2017. Canopy near-infrared reflectance and terrestrial photosynthesis, *Sci. Adv.*, 3, e1602244, <https://doi.org/10.1126/sciadv.1602244>
- Badgley, G., Anderegg, L. D. L., Berry, J. A., and Field, C. B., 2019. Terrestrial gross primary production: Using NIRV to scale from site to globe, *Global Change Biol.*, 25, 3731–3740, <https://doi.org/10.1111/gcb.147299>
- Baldocchi, D. D., Falge E., Gu L., Olson R., Hollinger D. Y., Running S. W., Anthoni P., Bernhofer Ch., Davis K. J., Evans R., Fuentes J., Goldstein A., Katul G., Law B. E., Lee X., Malhi Y., Meyers T. P., Munger J. W., Oechel W. C., Paw U K. T., Pilegaard K., Schmid H. P., Valentini R., Verma S., Vesala T., Wilson K. B., and Wofsy S. C., 2001. FLUXNET: A New

Tool to Study the Temporal and Spatial Variability of Ecosystem-Scale Carbon Dioxide, Water Vapor, and Energy Flux Densities. *Bulletin of the American Meteorological Society*, 82: 2415-2434

- Baldocchi, D. D., Ryu, Y., Dechant, B., Eichelmann, E., Hemes, K., Ma, S., Sanchez, C. R., Shortt, R., Szutu, D., Valach, A., Verfaillie, J., Badgley, G., Zeng, Y., and Berry, J. A., 2020 Outgoing Near Infrared Radiation from Vegetation Scales with Canopy Photosynthesis Across a Spectrum of Function, Structure, Physiological Capacity and Weather, *J. Geophys. Res.-Biogeo.*, 125, e2019JG005534, <https://doi.org/10.1029/2019JG005534>
- Ball, J., Woodrow, I., and J. Berry, 1987. A model predicting stomatal conductance and its contribution to the control of photosynthesis under different environmental conditions. *Progress in Photosynthesis Research*, IV, 221–224
- Balsamo, G., Viterbo, P., Beljaars, A., van den Hurk, B., Hirschi, M., Betts, A. K., and Scipal, K., 2009. A revised hydrology for the ECMWF model: Verification from field site to terrestrial water storage and impact in the Integrated Forecast System, *J. Hydrometeorol.*, 10, 623–643
- Baret, F., Weiss, M., Lacaze, R., Camacho, F., Makhmarad, H., Pacholczyk, P., Smetse, B., 2013. GEOV1: LAI, FAPAR essential climate variables and FCOVER global time series capitalizing over existing products, Part 1: Principles of development and production, *Remote Sens. Environ.*, 137, 299–309.
- Bastiaanssen, W. G., Ali, S., 2003. A new crop yield forecasting model based on satellite measurements applied across the Indus Basin, *Agric. Ecosyst. Environ.*, 94, 321-340
- Bastiaanssen, W. G. M., Menenti, M., Feddes, R. A., Holtslag, A. A. M., 1998a. A remote sensing surface energy balance algorithm for land (SEBAL). 1. Formulation. *Journal of Hydrology*, 212- 213, 198-212.
- Bastiaanssen, W. G. M., Pelgrum, H., Wang, J., Ma, Y., Moreno, J. F., Roerink, G. J, Vander, W. T., 1998b. The surface energy balance algorithm for land (SEBAL). Part 2: Validation. *J. Hydrol.*, 212–213, 213–229.
- Bateni, S. M., and D. Entekhabi, 2012. Relative efficiency of land surface energy balance components, *Water Resour. Res.*, 48, W04510
- Bauer, P., Thorpe, A., Brunet, G., 2015. The quiet revolution of numerical weather prediction, *Nature*, 525, 47-55
- Beguieria, S., Vicente-Serrano, S. M., Reig, F., Latorre, B., 2014. Standardized precipitation evapotranspiration index (SPEI) revisited: Parameter fitting, evapotranspiration models, tools, datasets and drought monitoring. *Int. J. Climatol.*, 34, 3001–3023
- Beillouin, D., Schauburger, B., Bastos, A., Ciais, P., & Makowski, D., 2020. Impact of extreme weather conditions on European crop production in 2018. *Philos. Trans. R. Soc. Lond B. Biol. Sci.*, 375(1810), 20190510.
- Beljaars, A. C. M. and Bosveld, F. C., 1997. Cabauw Data for the Validation of Land Surface Parameterization Schemes *J. Climate* 10, 1172 – 1193.
- Beljaars, A. C. M., and A. A. M. Holtslag, 1991. On flux parametrization over land surfaces for atmospheric models. *J. Appl. Meteor.*, 30, 327–341.

- Beljaars, A.C.M., P. Viterbo, M. Miller, and A.K. Betts, 1996. The anomalous rainfall over the USA during July 1993: Sensitivity to land surface parametrization and soil moisture anomalies. *Mon. Wea. Rev.*, 124, 362-383
- Beniston, M., 2004. The 2003 heat wave in Europe: A shape of things to come? An analysis based on Swiss climatological data and model simulations. *Geophys. Res. Lett.*, 31, L02022, doi:10.1029/2003GL018857
- Benson, D. O. and Dirmeyer, P. A., 2020. Characterizing the relationship between temperature and soilmoisture extremes and their role in the exacerbation of heatwaves over the Contiguous United States. *J. Clim*, 34, 2175-2187
- Berkowicz, R., and Prahm, L. P., 1982a. Evaluation of the profile method for estimation of surface fluxes of momentum and heat. *Atmospheric Environment*, 16, 2809–2819
- Berkowicz, R., and Prahm, L. P., 1982b. Sensible heat flux estimated from routine meteorological data by the resistance Method. *J. Appl. Meteor.* 21, 1845–1864
- Betts, A.K. and Ball, J.H., 1995. The FIFE surface diurnal cycle climate. *J. Geophys. Res.*, 100, 25679-25693.
- Betts, A.K. and Ball, J.H., 1998. FIFE Surface Climate and Site-Average Dataset 1987–89. *J. Atmos. Sci.*, 55, 1091–1108.
- Bhumralkar, C. M., 1975. Numerical experiments on the computation of ground surface temperature in an atmospheric general circulation model, *Journal of Applied Meteorology*, 14, 1246–1258.
- Bisquert, M., Sanchez, J. M., Lopez-Urrea, R., Caselles, V., 2016. Estimating high resolution evapotranspiration from disaggregated thermal images. *Remote Sensing of Environment*, 187, 423–433.
- Biudes, M. S., Vourlitis, G. L., Valesque, M.C.S., Machado, N. G., Danelichen, V. H., Pavao, V. M., Arruda, P. H. Z., Nogueira, J., 2021. Gross primary productivity of Brazilian Savanna (Cerrado) estimated by different remote sensing-based models. *Agricultural and Forest meteorology*, 307, 108456. <https://doi.org/10.1016/j.agrformet.2021.108456>
- Black, E., Blackburn, M. , Harrison, G., Hoskins, B. and Methven, J., 2004. Factors contributing to the 2003 European heat wave. *Weather*, 59, 217–223.
- Black K., Davis P., Lynch P., Jones M., McGettigan M., Osborne B., 2006. Long-term trends in solar irradiance in Ireland and their potential effects on gross primary productivity. *Agricultural and Forest Meteorology*, 141, 118–132
- Boisvenue, C., Running, S.W., 2013. Controls on provisioning services and forest productivity: Responses and risk under changing environmental conditions. In *Climate Vulnerability*; Pielke, R.A., Ed.; Academic Press: Oxford, UK, pp. 129–149
- Bonan, G. B., Lawrence, P. J., Oleson, K. W., Levis, S., Jung, M., Reichstein, M., Lawrence, D. M., & Swenson, S. C., 2011. Improving canopy processes in the community land model version 4 (CLM4) using global flux fields empirically inferred from FLUXNET data. *Journal of Geophysical Research*, 116, G02014.

- Boudhina, N., Zitouna-Chebbi, R., Mekki, I., Jacob, F., Ben Mechlia, N., Masmoudi, M., & Prévot, L., 2018. Evaluating four gap-filling methods for eddy covariance measurements of evapotranspiration over hilly crop fields. *Geoscientific Instrumentation, Methods and Data Systems*, 7, 151–167.
- Boussetta, S., Balsamo, G., Beljaars, A., Kral, T., and Jarlan, L., 2013. Impact of a satellite-derived leaf area index monthly climatology in a global numerical weather prediction model. *International Journal of Remote Sensing*, 34, 3520–3542. <https://doi.org/10.1080/01431161.2012.716543>
- Brázdil R, Trnka M, Mikšovský J, Řezníčková L, Dobrovolný P., 2015. Spring-summer droughts in the Czech Land in 1805-2012 and their forcings. *International Journal of Climatology*, 35, 1405–1421
- Brereton, A.J., 1992. The impact of weather on grassland farming. In: T. Keane, ed. *Irish farming, weather and environment*. Dublin: AGMET, 125–135.
- Brutsaert, W., 1982. Evaporation into the atmosphere: Theory, history, and applications. *Springer, Dordrecht, the Netherlands*. doi:10.1007/978-94-017-1497-6.
- Buitink, J., Swank, A. M., van der Ploeg, M., Smith, N. E., Benninga, H.-J. F., van der Bolt, F., Carranza, C. D. U., Koren, G., van der Velde, R., and Teuling, A. J., 2020. Anatomy of the 2018 agricultural drought in the Netherlands using in situ soil moisture and satellite vegetation indices, *Hydrol. Earth Syst. Sci.*, 24, 6021–6031, <https://doi.org/10.5194/hess-24-6021-2020>
- Buckley, T. N., 2017. Modeling stomatal conductance, *Plant physiology*, 174, 572-582.
- Buckley, T. N., Mott, K. A., 2013. Modelling stomatal conductance in response to environmental factors, *Plant, Cell and Environment*, 36, 1691-1699.
- Buras, A., Rammig, A., Zang, C. S., 2019. Quantifying impacts of the drought 2018 on European ecosystems in comparison to 2003. *Biogeosciences*, 17, 1655–1672.
- Burba, G., Anderson D., 2010. A Brief Practical Guide to Eddy Covariance Flux Measurements: Principles and Workflow Examples for Scientific and Industrial Applications. LiCor Corporation, Lincoln, NE. [https://www.licor.com/env/pdf/eddy_covariance/Brief Intro Eddy Covariance.pdf](https://www.licor.com/env/pdf/eddy_covariance/Brief_Intro_Eddy_Covariance.pdf) (last accessed July 26, 2020, 214 pp.)
- Businger, J. A., 1966. Transfer of Momentum and Heat in the planetary boundary layer. *Proc. Symp. Arctic Heat Budget and Atmospheric Circulation*, the RAND Corporation, 305 – 331
- Businger, J. A., Wyngaard, J. C., Izumi, Y., Bradley, E. F., 1971. Flux-profile relationships in atmospheric surface layer *Journal of the Atmospheric Sciences*, 28 (2), 181-189
- Calvet, J. C., Noilhan, J., J.-L. Roujean, P. Bessemoulin, M. Cabelguenne, A. Olioso, and J.-P. Wigneron, 1998. An interactive vegetation SVAT model tested against data from six contrasting sites, *Agric. For. Meteorol.*, **92**, 73–95
- Cammalleri, C., Anderson, M. C., Gao, F., Hain, C. R., Kustas, W. P., 2014. Mapping daily evapotranspiration at field scales over rainfed and irrigated agricultural areas using remote sensing data fusion. *Agric. For. Meteorol.*, 186, 1-11.

- Campioli, M., Malhi, Y., Vicca, S., Luyssaert, S., Papale, D., Penuelas, J., Reichstein, M., Migliavacca, M., Arain, M. A., Janssens, I. A., 2016. Evaluating the convergence between eddy-covariance and biometric methods for assessing carbon budgets of forests. *Nat Commun.*, 7, 13717
- Campos, I., Neale, C. M. U., Arkebauer, T. J., Suyker, A. E., Goncalves, I. Z., 2018. Water productivity and crop yield: A simplified remotes sensing driven operational approach, *Agric Fores. Meteor.*, 249, 501-511.
- Canadell, J.G., P.M.S. Monteiro, M.H. Costa, L. Cotrim da Cunha, P.M. Cox, A.V. Eliseev, S. Henson, M. Ishii, S. Jaccard, C. Koven, A. Lohila, P.K. Patra, S. Piao, J. Rogelj, S. Syampungani, S. Zaehle, and K. Zickfeld, 2021. Global Carbon and other Biogeochemical Cycles and Feedbacks. In *Climate Change 2021: The Physical Science Basis. Contribution of Working Group I to the Sixth Assessment Report of the Intergovernmental Panel on Climate Change* [Masson-Delmotte, V., P. Zhai, A. Pirani, S.L. Connors, C. Péan, S. Berger, N. Caud, Y. Chen, L. Goldfarb, M.I. Gomis, M. Huang, K. Leitzell, E. Lonnoy, J.B.R. Matthews, T.K. Maycock, T. Waterfield, O. Yelekçi, R. Yu, and B. Zhou (eds.)]. Cambridge University Press. In Press.
- Casty C, Wanner H, Luterbacher J, Esper J, Böhm R., 2005. Temperature and precipitation variability in the European Alps since 1500. *Int. J. Climatol.* 25: 1855–1880, doi: 10.1002/joc.1216.
- Chen, F., and J. Dudhia, 2001. Coupling an advanced land surface–hydrology model with the Penn State–NCAR MM5 modeling system. Part I: Model implementation and sensitivity. *Mon. Wea. Rev.*, 129, 569–585.
- Chen, F., K. Mitchell, J. Schaake, Y. Xue, H.L. Pan, V. Koren, Q. Y. Duan, M. Ek, Betts A., 1996. Modeling of land surface evaporation by four schemes and comparison with FIFE observations. *J. Geophys. Res.*, 101:7251–7268.
- Chen, T. H., A. Henderson-Sellers, P. C. D. Milly, A. J. Pitman, A. C. M. Beljaars, J. Polcher, F. Abramopoulos, A. Boone, S. Chang, F. Chen, Y. Dai, C. E. Desborough, R. E. Dickinson, L. Du“ Menil, M. Ek, J. R. Garratt, N. Gedney, Y. M. Gusev, J. Kim, R. Koster, E. A. Kowalczyk, K. Laval, J. Lean, D. Lettenmaier, X. Liang, J.-F. Mahfouf, H.-T. Mengelkamp, K. Mitchell, O. N. Nasonova, J. Noilhan, A. Robock, C. Rosenzweig, J. Schaake, C. A. Schlosser, J.-P. Schulz, Y. Shao, A. B. Shmakin, D. L. Verseghy, P. Wetzel, E. F. Wood, Y. Xue, Z.-L. Yang, and Q. Zeng, 1997. Cabauw experimental results from the Project for Intercomparison of Land surface Parameterization Schemes (PILPS). *J. Climate*, 10, 1194–1215.
- Chirouze, J., Boulet, G., Jarlan, L., Fieuzal, R., Rodriguez, J. C., Ezzahar, J., Er-Raki, S., Bigeard, G., Merlin, O., Garatuza-Payan, J., Watts, C., and Chehbouni, G., 2014. Intercomparison of four remote-sensing-based energy balance methods to retrieve surface evapotranspiration and water stress of irrigated fields in semi-arid climate, *Hydrol. Earth Syst. Sci.*, 18, 1165–1188
- Ciais, P., Reichstein, M., Viovy, N., Granier, N.A., Ogée, J., Allard, V., Buchmann, N., Aubinet, M., Bernhofer, C., Carrara, A., Chevallier, F., De Noblet, N., Friend, A., Friedlingstein, P., Grünwald, T., Heinesch, B., Keronen, P., Knohl, A., Krinner, G., Loustau, D., Manca, G.,

- Matteucci, G., Miglietta, F., Ourcival, J.M., Pilegaard, K., Rambal, S., Seufert, G., Soussana, J.F., Sanz, M.J., Schulze, E.D., Vesala, T., Valentini, R., 2005. Unprecedented European-level reduction in primary productivity caused by the 2003 heat and drought. *Nature*, 437, 529–533.
- Colaizzi, P. D., S. R. Evett, T. A. Howell, and J. A. Tolk, 2006. Comparison of five models to scale daily evapotranspiration from one-time-of day measurements, *Trans. ASABE*, 49(5), 1409–1417.
- Collatz, G. J., Ball, J. T., Grivet, C., and Berry, J. A., 1991. Physiological and environmental regulation of stomatal conductance, photosynthesis and transpiration: A model that includes a laminar boundary layer. *Agricultural and Forest Meteorology*, 54, 107–136.
- Conefrey, T., 2018. Irish Agriculture: Economic Impact and Current Challenges. *Economic Letter*, 8, 1-19
- Conti, S., Meli, P., Minelli, G., Solimini, R., Toccaceli, V., Vichi, M., Beltrano, C., Perini L., 2005. Epidemiologic study of mortality during the Summer 2003 heat wave in Italy. *Environ. Res.*, 98, 390–399.
- Consoli, S., D’Urso, G., and Toscano, A., 2006. Remote sensing to estimate ET-fluxes and the performance of an irrigation district in southern Italy, *Agric. Water Manage.*, 81, 295–314.
- Cox, P. M., R. A. Betts, C. D. Jones, S. A. Spall, and I. J. Totterdell, 2000. Acceleration of global warming due to carbon-cycle feedbacks in a coupled climate model, *Nature*, 408, 184–187
- Creamer, R.E., Simo, I., Reidy, Carvalho, J., Fealy, R., Hallett, S., Jones, R., Holden, 829 A., Holden, N., Hannam, J., Massey, P., Mayr, T., McDonald, E., O’Rourke, S., Sills, P., Truckell, I., Zawadzka, J. and Schulte, R.P.O. 2014. Irish Soil Information System. Synthesis Report (2007-S-CD-1-S1). EPA STRIVE Programme, Wexford.
- CSO, 2012. Census of Agriculture 2010 – Final Results. <https://www.cso.ie/en/media/csoie/releasespublications/documents/agriculture/2010/full2010.pdf> , last accessed 04 July, 2021.
- Daccache, A., Weatherhead, E.K., Stalham, M.A., Knox, J.W., 2011. Impacts of climate change on irrigated potato production in a humid climate, *Agricultural and Forest Meteorology*, 151, 1641-1653
- Deardorff, J. W., 1978. Efficient prediction of ground surface temperature and moisture, with inclusion of a layer of vegetation,” *Journal of Geophysical Research*, 83, 1889–1903.
- Denissen, J. M., Teuling, A. J., Reichstein, M. & Orth, R., 2020. Critical soil moisture derived from satellite observations over Europe. *J. Geophys. Res. Atmos.*, 125, e2019
- Denissen, J. M. C., Orth, R., Wouters, H., Miralles, D. G., van Heerwaarden, C. C., de Arellano, J. V.-G., Teuling, A. J., 2021. Soil moisture signature in global weather balloon soundings, *npj Climate and Atmospheric Science*, 4, 13.
- De Boeck, H. J., Dreesen, F. E., Janssens, I. A. and Nijs, I., 2011. Whole-system responses of experimental plant communities to climate extremes imposed in different seasons. *New Phytologist*, 189: 806-817.

- De Bruin, H. A. R., and A. A. M. Holtslag, 1982. A simple parameterization of the surface fluxes of sensible and latent heat during daytime compared with the Penman–Monteith concept. *J. Appl. Meteor.*, 21, 1610–1621
- De Bruin, H. A. R., Kohsiek, W. and van den Hurk, J. J. M., 1993. A verification of some methods to determine the fluxes of momentum, sensible heat, and water vapour using standard deviation and structure parameter of scalar meteorological quantities, *Bound-Layer Meteor.*, 63, 231–257.
- De Bruin, H.A.R., Hartogensis, O.K., Allen, R.G., Kramer, J.W.J.L., 2005. Note on the regional advection perturbations in an irrigated desert (RAPID) experiment. *Theor. Appl. Climatol.* 80, 143–152.
- Dechant, B., Ryu, Y., Badgley, G., Zeng, Y., Berry, J. A., Zhang, Y., Goulas, Y., Li, Z., Zhang, Q., Kang, M., Li, J. and Moya, I., 2020. Canopy structure explains the relationship between photosynthesis and sun-induced chlorophyll fluorescence in crops, *Remote Sens. Environ.*, 241, 111733. <https://doi.org/10.1016/j.rse.2020.111733>
- De Rooy, W. C. and Holtslag, A. A. M., 1999. Estimation of surface radiation and energy flux densities from single-level weather data. *J. Appl. Meteor.*, 38, 526– 540.
- Dickinson, R. E., P. Kennedy, and A. Henderson-Sellers, 1993. Biosphere-Atmosphere Transfer Scheme (BATS) Version 1e As Coupled to the NCAR Community Climate Model, Climate and Global Dynamics Division, National Center for Atmospheric Research, Boulder, Colo, USA.
- Dillon E., Moran B., Lennon J., Donnellan T. 2018. Teagasc National Farm Survey 2018 Results. <https://www.teagasc.ie/publications/2019/National-Farm-Survey-Preliminary-Results-2018.php>, Last accessed November, 2019.
- Dirmeyer, P. A., 2011. The terrestrial segment of soil moisture-climate coupling. *Geophysical Research Letters*, 38, L16702
- Dirmeyer, P. A., Balsamo, G., Blyth, E. M., Morrison, R., and Cooper, H. M., 2021. Land-atmosphere interactions exacerbated the drought and heatwave over northern Europe during summer 2018. *AGU Advances*, 2, e2020AV000283. <https://doi.org/10.1029/2020AV000283>
- Djamai, N., and Fernandes, R., 2018. Comparison of SNAP-derived Sentinel-2A L2A Product to ESA Product over Europe. *Remote Sensing* 10: 926. doi:10.3390/rs10060926
- Dodds, P. E., Meyer, W. S., Barton, A., Annette, B., CSIRO, 2005. A review of methods to estimate irrigated reference crop evapotranspiration across Australia. *CRC Irrig. Futur.* Tech. Rep. 54
- Dole, R., Hoerling, M., Perlwitz, J., Eischeid, J., Pegion, P., Zhang, T., Quan, X-W., Xu, T., Murray D., 2011. Was there a basis for anticipating the 2010 Russian heat wave? *Geophys. Res. Lett.* 3, L06702. doi: 10.1029/2010GL046582
- Domínguez-Castro F, Vicente-Serrano SM, Tomás-Burguera M, Peña-Gallardo M, Beguería S, El Kenawy A, Luna Y, Morata A., 2019. High spatial resolution climatology of drought events for Spain: 1961–2014. *International Journal of Climatology*, 39, 5046–5062.
- Draper, C., R. Reichle, and R. Koster, 2018. Assessment of MERRA-2 land surface energy flux estimates. *J. Climate*, 31, 671–691

- Driesen, E., Van den Ende, W., De Proft, M., Saeys, W., 2020. Influence of Environmental Factors Light, CO₂, Temperature, and Relative Humidity on Stomatal Opening and Development: A Review. *Agronomy*, 10(12), 1975
- Duan Q., Schaake J., Andreassian V., Franks S., Goteti G., Gupta H.V., Gusev Y.M., Habets, F., Hall, A., Hay, L., Hogue, T., Huang, M., Leavesley, G., Liang, X., Nasonova, O. N., Noilhan, J., Oudin, L., Sorooshian, S., Wagener, T., Wood, E. F., 2006. Model Parameter Estimation Experiment (MOPEX): an overview of science strategy and major results from the second and third workshops," *Journal of Hydrology*, 320, 3–17
- Duveiller, G., J. Hooker, A. Cescatti, 2018. The mark of vegetation change on Earth's surface energy balance. *Nat. Commun.*, 9, 679
- Dwyer, N. and Walsh, S., 2012. 'Soil moisture' in Dwyer (ed), The status of Ireland's climate. Environmental Protection Agency, Wexford, Ireland, 115-117.
- Dyer, A. J., 1967. The turbulent transport of heat and water vapour in an unstable atmosphere. *Quart. J. Roy. Meteor. Soc.*, 96, 132 - 137
- Dyer, A. J., 1974. A review of flux-profile relationships, *Bound.-Layer Meteor.*, 7, 363 - 372
- Engman, E. T., Gurney, R. J., 1991. Remote Sensing in Hydrology. Chapman and Hall, London, UK
- Ek, M. B., K. E. Mitchell, Y. Lin, Rogers, E., Grunmann, P., Koren, V., Gayno, G., Tarpley, J. D., 2003. Implementation of Noah land surface model advances in the National Centers for Environmental Prediction operational mesoscale Eta model, *Journal of Geophysical Research: Atmospheres*, 108, 8851.
- ESA, 2018. Sen2Cor software release note. Available online from <http://step.esa.int/thirdparties/sen2cor/2.5.5/docs/S2-PDGS-MPC-L2A-SRN-V2.5.5.pdf>, Accessed date: 07 November, 2020.
- EUROSTAT, 2015. Land cover statistics. Available online at https://ec.europa.eu/eurostat/statistics-explained/index.php/Land_cover_statistics#Land_cover_in_the_EU_Member_States.
- Falge, E., Baldocchi, D., Olson, R., Anthoni, P., Aubinet, M., Bernhofer, C., Burba, G., Ceulemans, R., Clement, R., Dolman, H., Granier, A., Gross, P., Grünwald, T., Hollinger, D., Jensen, N.- O., Katul, G., Keronen, P., Kowalski, A., Ta Lai, C., Law, B. E., Meyers, T., Moncrieff, J., Moors, E., William Munger, J., Pilegaard, K., Rannik, Ü., Rebmann, C., Suyker, A., Tenhunen, J., Tu, K., Verma, S., Vesala, T., Wilson, K., and Wofsy, S., 2001. Gap filling strategies for long term energy flux data sets, *Agr. Forest Meteorol.*, 107, 71–77
- Falzoi, S., Gleeson, E., Lambkin, K., Zimmermann, J., Marwaha, R., O'Hara, R., Green, S., Fratianni S., 2019. Analysis of the severe drought in Ireland in 2018. *Weather*, 99 (99), 1- 6. doi:10.1002/wea.3587
- FAO, 1996. Agro-ecological Zoning. Guidelines. FAO Soils Bulletin 73, 78 pp.
- Fealy, R., Bruyère, C., Duffy, C., 2018. Regional climate model simulations for Ireland for the 21st century, EPA Research Report No. 244, https://www.epa.ie/publications/research/climate-change/Research_Report_244.pdf, last accessed 05 July 2021.

- Feldman, A. F., Short Gianotti, D. J., Trigo, I. F., Salvucci, G. D. & Entekhabi, D., 2019. Satellite-based assessment of land surface energy partitioning-soil moisture relationships and effect of confounding variables. *Water Resour. Res.*, 55, 10657–10677
- Fink, A. H, Brücher, T, Krüger, A, Leckebusch, G. C, Pinto, J. G. and Ulbrich, U., 2004. The 2003 European summer heatwaves and drought – synoptic diagnosis and impacts. *Weather*, 59, 209–16
- Fischer, G., Shah, M., Tubiello, F. N., Van Velhuizen, H., 2005. Socio-economic and climate change impacts on agriculture: an integrated assessment, 1990–2080 *Phil. Trans. R. Soc. Lond. B*, 360, 2067-2083
- Fischer, E. M., Seneviratne, S. I., Lüthi, D. & Schär, C., 2007a. Contribution of land–atmosphere coupling to recent European summer heat waves. *Geophys. Res. Lett.* 34, L06707
- Fischer, E. M., Seneviratne, S. I., Vidale, P. L., Lüthi, D. & Schär, C., 2007b. Soil moisture–atmosphere interactions during the 2003 European summer heat wave. *J. Clim.* 20, 5081–5099
- Fisher, R. A., Koven, C. D., 2020. Perspectives on the future of land surface models and the challenges of representing complex terrestrial systems, *J. Adv. Model. Earth. Sys.*, 12, e2018MS001453
- Fitzgerald, J. B., Brereton, A. J., Holden, N. M., 2005. Assessment of regional variation in climate on the management of dairy cow systems in Ireland using a simulation model, *Grass Forage Sci.*, 60, 283-296
- Fitzgerald, J. B., Brereton, A. J., Holden, N. M., 2009. Assessment of the adaptation potential of grass-based dairy systems to climate change in Ireland—The maximised production scenario, *Agricultural and Forest Meteorology*, 149, 244-255
- Flexas, J., & Medrano, H., 2002. Drought-inhibition of photosynthesis in C3 plants: Stomatal and non-stomatal limitations revisited. *Annals of Botany*, 89, 183–189.
- Foken, T., 2006. 50 years of the Monin–Obukhov similarity theory. *Bound.-Layer Meteor.*, 119, 431–447
- Foken, T., 2008. The Energy Balance Closure Problem: An Overview. *Ecological Applications* 18, 1351–1367. <https://doi.org/10.1890/06-0922.1>
- Franssen, H.J.H., Stöckli, R., Lehner, I., Rotenberg, E., Seneviratne, S.I., 2010. Energy balance closure of eddy-covariance data: A multisite analysis for European FLUXNET stations. *Agricultural and Forest Meteorology* 150, 1553–1567. <https://doi.org/10.1016/j.agrformet.2010.08.005>
- Galinski, A. E., Thomson, D. J., 1995. Comparison of three schemes for predicting surface sensible heat flux. *Boundary-Layer Meteor.*, 72, 345-370
- García-Gutiérrez, V., Stöckle, C., Gil, P. M., and Meza, F. J., 2021. Evaluation of Penman-Monteith Model Based on Sentinel-2 Data for the Estimation of Actual Evapotranspiration in Vineyards. *Remote Sensing*, 13, 478
- García-Herrera, R, Díaz, J, Trigo, R. M, Luterbacher, J. and Fischer, E. M., 2010. A review of the European summer heatwave of 2003. *Crit. Rev. Environ. Sci. Technol.*, 40, 267–306

- Gardiner M. J. and Radford T., 1980. Soil Associations of Ireland and their land use potentials. *Soil Survey Bulletin* 36. <https://www.teagasc.ie/media/website/environment/soil/General.pdf>, last accessed July, 2018
- Garrat, J. R., 1980. Surface influence upon vertical profiles in the atmospheric near-surface layer. *Quart. J. Roy. Met. Soc.*, 106, 803-819.
- Garratt, J. R., Hicks, B. B., 1990. Micrometeorological and PBL experiments in Australia, *Boundary-Layer Meteorology*, 50, 11-29
- Gebremichael M., Wang J., Sammis T.W., 2010. Dependence of remote sensing evapotranspiration algorithm on spatial resolution, *Atmospheric Research*, 96, 489-495.
- Gentine, P., P. D’Odorico, B. R. Lintner, G. Sivandran, and G. Salvucci, 2012. Interdependence of climate, soil, and vegetation as constrained by the Budyko curve. *Geophys. Res. Lett.*, 39, L19404
- Gentine, P., Green, J. K., Guerin, M., Humphrey, V., Seneviratne, S. I., Zhang, Y., Zhou, S., 2019. Coupling between the terrestrial carbon and water cycles-a review. *Environ. Res. Lett.*, 14, 083003
- Gerling, L., Weber, T. K. D., Reineke, D., Durner, W., Martin, S., Weber, S., 2019. Eddy covariance-based surface-atmosphere exchange and crop coefficient determination in a mountainous peatland. *Ecohydrology*, 12, e2047
- Gobbo S, Lo Presti S, Martello M, Panunzi L, Berti A, Morari F., 2019. Integrating SEBAL with in-Field Crop Water Status Measurement for Precision Irrigation Applications—A Case Study. *Remote Sensing*, 11, 2069
- Gocic M, Trajkovic S. 2014. Spatiotemporal characteristics of drought in Serbia. *Journal of Hydrology*, 510, 110–123
- González-Dugo, M. P., and Mateos, L., 2008. Spectral vegetation indices for benchmarking water productivity of irrigated cotton and sugarbeet crops, *Agric. Water Manag.*, 95, 48-58.
- Graf, A., Klosterhalfen, A., Arriga, N., Bernhofer, C., Bogen, H., Bornet, F., Brüggemann, N., Brümmer, C., Buchmann, N., Chi, J., Chipeaux, C., Cremonese, E., Cuntz, M., Dušek, J., El-Madany, T. S., Fares, S., Fischer, M., Foltýnová, L., Gharun, M., Ghiasi, S., Gielen, B., Gottschalk, P., Grünwald, T., Heinemann, G., Heinesch, B., Heliasz, M., Holst, J., Hörtnagl, L., Ibrom, A., Ingwersen, J., Jurasinski, G., Klatt, J., Knohl, A., Koepsch, F., Konopka, J., Korkiakoski, M., Kowalska, N., Kremer, P., Kruijt, B., Lafont, S., Léonard, J., De Ligne, A., Longdoz, B., Loustau, D., Magliulo, V., Mammarella, I., Manca, G., Mauder, M., Migliavacca, M., Mölder, M., Neiryneck, J., Ney, P., Nilsson, M., Paul-Limoges, E., Peichl, M., Pitacco, A., Poyda, A., Rebmann, C., Roland, M., Sachs, T., Schmidt, M., Schrader, F., Siebicke, L., Šigut, L., Tuittila, E.-S., Varlagin, A., Vendrame, N., Vincke, C., Völksch, I., Weber, S., Wille, C., Wizeemann, H.-D., Zeeman, M., and Vereecken, H., 2020.

- Altered energy partitioning across terrestrial ecosystems in the European drought year 2018, *Philos. T. R. Soc. B*, 375, 20190524, <https://doi.org/10.1098/rstb.2019.0524>
- Green, S., 2019. Investigation into the bio-physical constraints on farmer turn-out-date decisions using remote sensing and meteorological data. PhD Thesis, University College Cork. <http://hdl.handle.net/10468/7795>.
- Gu, L., Meyers, T., Pallardy, S. G., Hanson, P. J., Yang, B., Heuer, M., Hosman, K. P., Riggs, J. S., Sluss, D., and Wullschleger, S. D., 2006. Direct and indirect effects of atmospheric conditions and soil moisture on surface energy partitioning revealed by a prolonged drought at a temperate forest site. *Journal of Geophysical Research*, 111, D16102.
- Guzinski, R., Nieto, H., 2019. Evaluating the feasibility of using Sentinel-2 and Sentinel-3 satellites for high-resolution evapotranspiration estimations. *Remote Sensing of Environment*, 221, 157- 172
- Guzinski, R., Nieto, H., Sandholt, I., Karamitilios, G., 2020. Modeling High-Resolution Actual Evapotranspiration through Sentinel-2 and Sentinel-3 Data Fusion. *Remote Sensing*, 12, 1433. <https://doi.org/10.3390/rs12091433>
- Haghighi, E., Short Gianotti, D. J., Akbar, R., Salvucci, G. D. and Entekhabi, D., 2018 Soil and atmospheric controls on the land surface energy balance: a generalized framework for distinguishing moisture-limited and energy-limited evaporation regimes. *Water Resour. Res.* 54, 1831–1851
- Hanrahan, L., Geoghegan, A., O'Donovan, M., Griffith, V., Ruelle, E., Wallace, M., Shalloo, L., 2017. PastureBase Ireland: A grassland decision support system and national database, *Comput. Electron. Agric.*, 136, 193-201
- Hatfield, J. L., Dold, C., 2019. Water-Use Efficiency: Advances and Challenges in a Changing Climate, *Frontiers in Plant Science*, 10, 103.
- Hatfield, J. L., Boote, K. J., Kimball, B. A., Ziska, L. H., Izaurralde, R. C., Ort, D., Thomson, A. M., Wolfe, D. W., 2011. Climate impacts on agriculture: implications for crop production. *Agron. J.* 103, 351–370
- Haymann N., Lukyanov, V., Tanny, J., 2019. Effects of variable fetch and footprint on surface renewal measurements of sensible and latent heat fluxes in cotton. *Agric. For. Meteorol.*, 268, 63 – 73.
- He, M., Kimball, J. S., Yi, Y., Running, S. W., Guan, K., Moreno, A., Wu, X., Maneta, M., 2019. Satellite data-driven modelling of field-scale evapotranspiration in croplands using the MOD16 algorithm framework, *Remote Sensing of Environment*, 230, 111201.
- Henderson-Sellers, A., A. J. Pitman, P. K. Love, P. Irannejad, and T. H. Chen, 1995. The project for intercomparison of land surface parameterization schemes (PILPS): phases 2 and 3, *Bulletin of the American Meteorological Society*, 76, 489–503.
- Henry, C., John, G.P., Pan, R., Bartlett, M. K., Fletcher, L. R., Scoffoni, C., Sack, L., 2019. A stomatal safety-efficiency trade-off constrains responses to leaf dehydration. *Nat. Commun.*, **10**, 3398
- Hersbach, H., Dee, D., 2016. ERA-5 reanalysis is in production, ECMWF newsletter, 147, *Spring.*, 7 p.

- Hersbach, H., Bell, B., Berrisford, P., Hirahara, S., Horányi, A., Muñoz-Sabater, J., Nicolas, J., Peubey, C., Radu, R., Schepers, D., Simmons, A., Soci, C., Abdalla, S., Abellan, X., Balsamo, G., Bechtold, P., Biavati, G., Bidlot, J., Bonavita, M., De Chiara, G., Dahlgren, P., Dee, D., Diamantakis, M., Dragani, R., Flemming, J., Forbes, R., Fuentes, M., Geer, A., Haimberger, L., Healy, S., Hogan, R. J., Hólm, E., Janisková, M., Keeley, S., Laloyaux, P., Lopez, P., Lupu, C., Radnoti, G., de Rosnay, P., Rozum, I., Vamborg, F., Villaume, S., and Thépaut, J.-N., 2020. The ERA5-Land Global Reanalysis, *Q. J. Roy. Meteor. Soc.*, 146, 1999–2049, <https://doi.org/10.1002/qj.3803>
- Heusinkveld, B.G., Jacobs, A.F.G., Holtslag, A.A.M., Berkowicz, S.M., 2004. Surface energy balance closure in an arid region: role of soil heat flux. *Agric. Forest. Meteorol.* 122, 21 – 37.
- Hirschi, M., Seneviratne, S. I., Alexandrov, V., Boberg, F., Boroneant, C., Christensen, O. B., Formayer, H., Orłowsky, B., Stepanek, P., 2011. Observational evidence for soil-moisture impact on hot extremes in southeastern Europe. *Nature Geosci.* 4, 17–21.
- Hochstrasser, T., Jarman, C., Finkle, K., Murphy, P., Fenton, O., Richards, K., Daly, E., Saunders, M., Cummins, T., Whetton, R., O’Loughlin, F., 2021. Towards establishing an Irish National Soil Moisture Monitoring Network, EMS Annual Meeting Abstract, 18, 273. <https://doi.org/10.5194/ems2021-273>
- Högström, U., 1988. Non-dimensional wind and temperature profiles in the atmospheric surface-layer—a re-evaluation, *Boundary-Layer Meteorology*, 42, 55-78
- Högström, U., Bergstrom, H., 1996. Organized turbulence structures in the near-neutral atmospheric surface layer *Journal of the Atmospheric Sciences*, 53, 2452-2464
- Holden, N. M., Brereton, A. J., 2002. An assessment of the potential impact of climate change on grass yield in Ireland over the next 100 years, *Irish J. Agric. Food Res.*, 41, 213-226
- Holden, N. M., Brereton, A. J., 2003a Climate change and the introduction of maize and soybean to Ireland, *Irish J. Agric. Food Res.*, 42, 1-15
- Holden, N. M., Brereton, A. J., 2003b. The impact of climate change on Irish Agriculture. In: Sweeney, J. (Ed.), *Climate Change and Ireland: Scenarios and Impacts for Ireland*. Environmental Protection Agency, Johnstown Castle, Wexford, 33–80.
- Holden, N. M., Brereton, A. J., 2004. Definition of agroclimatic regions in Ireland using hydro-thermal and crop yield data, *Agric. For. Meteorol.*, 122, 175-191
- Holden, N. M., Brereton, A. J., Fealy, R., Sweeney, J., 2003. Possible change in Irish climate and its impact on barley and potato yields, *Agricultural and Forest Meteorology*, 116, 181-196
- Holmes, T. R., C. R. Hain, W. T. Crow, M. C. Anderson, and W. P. Kustas, 2018. Microwave implementation of two-source energy balance approach for estimating evapotranspiration. *Hydrol. Earth Syst. Sci.*, 22, 1351–1369
- Holtslag, A. A. M., and A. P. Van Ulden, 1983. A simple scheme for daytime estimates of the surface fluxes from routine weather data. *J. Climate Appl. Meteor.*, 22, 517–529.
- Holtslag, A. A. M., and H. A. R. De Bruin, 1988. Applied modeling of the nighttime surface energy balance over land. *J. Appl. Meteor.*, 27, 689– 704.

- Hopkins, A., 2000. Grass : its production and utilization. Published for the British Grassland Society by Blackwell Science, Oxford ; Malden, MA, 440 p
- Hu, E., Babcock, E. L., Bialkowski, S. E., Jones, S. B., & Tuller, M., 2014. Methods and Techniques for Measuring Gas Emissions from Agricultural and Animal Feeding Operations. *Critical Reviews in Analytical Chemistry*, 44(3), 200–219
- Hunt, E., Svoboda, M., Wardlow, B., Hubbard, K., Hayes, M.J. and Arkebauer, T., 2014. Monitoring the effects of rapid onset of drought on non-irrigated maize with agronomic data and climate-based drought indices. *Agricultural and Forestry Meteorology*, 191, 1–1, 11
- Hurtado-Uria, C., Hennessy, D., Shalloo, L., O'Connor, D., and Delaby, L., 2013a. Relationships between meteorological data and grass growth over time in the south of Ireland. *Ir. Geogr.* 46, 175–201
- Hurtado-Uria, C., Hennessy, D., Shalloo, L., Schulte, R. P. O., Delaby, L., and O'Connor, D., 2013b. Evaluation of three grass growth models to predict grass growth in Ireland. *J. Agric. Sci.* 151, 91–104
- Idso, S. B., 1981. A set of equations for full spectrum and 8 to 14 μm and 10.5 to 12.5 μm thermal radiation from cloudless skies. *Water Resour. Res.*, 17, 295– 304.
- IPCC, 2014: Summary for policymakers. In: Climate Change 2014: Impacts, Adaptation, and Vulnerability. Part A: Global and Sectoral Aspects. Contribution of Working Group II to the Fifth Assessment Report of the Intergovernmental Panel on Climate Change [Field, C.B., V.R. Barros, D.J. Dokken, K.J. Mach, M.D. Mastrandrea, T.E. Bilir, M. Chatterjee, K.L. Ebi, Y.O. Estrada, R.C. Genova, B. Girma, E.S. Kissel, A.N. Levy, S. MacCracken, P.R. Mastrandrea, and L.L.White (eds.)]. Cambridge University Press, Cambridge, United Kingdom and New York, NY, USA, pp. 1-32.
- Jacobs, C., 1994. Direct impact of atmospheric CO₂ enrichment on regional transpiration. Ph.D. dissertation, Wageningen Agricultural University, 179 pp. [Available from Dept. of Meteorology, Duivendall 2, Wageningen Agricultural University, 6701 AP Wageningen, the Netherlands.]
- Jacob, F., Olioso, A., Gu, X. F., Su, Z., Seguin, B., 2002. Mapping surface fluxes using airborne visible, near infrared, thermal infrared remote sensing data and a spatialized surface energy balance model, *Agronomie*, 22, 669-680
- Jacovides, C., Kerkides, P., Papaioannou, G., 1991. Evapotranspiration and sensible heat flux estimation above grass: Comparison of methods and correlation of several attributes to routinely measured data. *Water Res. Manag.*, 5, 305-319.
- Jacquemoud, S., Baret, F., 1990. PROSPECT: a model of leaf optical properties spectra. *Remote Sens. Environ.* 34, 75–91.
- Jaksic, V., G. Kiely, J. Albertson, R. Oren, and G. Katul, 2006. Net ecosystem exchange of grassland in contrasting wet and dry years, *Agric. For. Meteorol.*, 139, 324-334
- Jarvis, P., 1976. The interpretation of leaf water potential and stomatal conductance found in canopies in the field. *Philos. Trans. Roy. Soc. London B*, 273, 593–610.

- Jiang, C., Guan, K., Wu, G., Peng, B., Wang, S., 2020. A daily, 250 m, and real-time gross primary productivity product (2000 – present) covering the Contiguous United States. *Earth System Science Data*, 13, 281-298.
- Jung, M., Reichstein, M., Ciais, P., Seneviratne, S. I., Sheffield, J., Goulden, M. L., Bonan, G., Cescatti, A., Chen, J., de Jeu, R., Dolman, A. J., Eugster, W., Gerten, D., Gianelle, D., Gobron, N., Heinke, J., Kimball, J., Law, B. E., Montagnani, L., Mu, Q., Mueller, B., Oleson, K., Papale, D., Richardson, A. D., Rouspard, O., Running, S., Tomelleri, E., Viovy, N., Weber, U., Williams, C., Wood, E., Zaehle, S., and Zhang, K., 2010. Recent decline in the global land evapotranspiration trend due to limited moisture supply, *Nature*, 467, 951–954.
- Jung, M., Koirala, S., Weber, U., Ichii, K., Gans, F., Camps-Valls, G., Papale, D., Schwalm, C., Tramontana, G., and Reichstein, M. 2019. The FLUXCOM ensemble of global land-atmosphere energy fluxes, *Scientific Data*, 6, 74, <https://doi.org/10.1038/s41597-019-0076-8>
- Kaimal, J., Finnigan, J., 1994. Atmospheric Boundary Layer Flows: Their Structure and Measurement. Oxford University Press, Oxford, UK.
- Keane, T. and Collins, J.F. (Eds.), 2004. Climate, Weather and Irish Agriculture, AGMET, UCD, Belfield, Dublin 4.
- Khan, A., Stockle, C. O., Nelson, R. L., Peters, T., Adam, J. C., Lamb, B., Chi J., Waldo, S., 2019. Estimating biomass and yield using METRIC evapotranspiration and simple growth algorithms, *Agronomy Journal*, 111, 536-544.
- Kiely, G., Leahy, P., Lewis, C., Sottocornola, M., Laine, A., Koehler, A.-K., 2018. GHG fluxes from Terrestrial Ecosystems in Ireland. Research report No. 227.EPA Research Programme, Wexford.https://www.epa.ie/pubs/reports/research/climate/Research_Report_227.pdf, last accessed, 07 Feb., 2019
- Kim, J., and S. B. Verma, 1991. Modeling canopy stomatal conductance in a temperate grassland ecosystem. *Agric. For. Meteorol.*, 55, 149–166.
- Kiziloglu, F. M., Sahin, U. Kuslu, Y., Tunc, T., 2009. Determining water-yield relationship, water use efficiency, crop and pan coefficients for silage maize in a semiarid region. *Irrigation Science*, 27, 129-137.
- Knist, S., Goergen, K., Buonomo, E., Christensen, O.B., Colette, A., Cardoso, R.M., Fealy, R., Fernandez, J., Garcia-Diez, M., Jacob, D., Kartsios, S., Katragkou, E., Mayer, S., van Meijgaard, E., Nikulin, G., Soares, P.M.M., Sobolowski, S., Szepszo, G., Teichmann, C., Vautard, R., Warrach-Sagi, K., Wulfmeyer, V. and Simmer, C., 2017. Land atmosphere coupling in EURO-CORDEX evaluation experiments. *Journal of Geophysical Research Atmospheres*, 122, 79–103.
- Kornhuber, K., Osprey, S., Coumou, D., Petri, S., Petoukhov, V., Rahmstorf, S., and Gray, L., 2019. Extreme weather events in early summer 2018 connected by a recurrent hemispheric wave-7 pattern. *Environmental Research Letters*, 14, 054002. <https://doi.org/10.1088/1748-9326/ab13bf>
- Kørup, K., Lærke, P. E., Baadsgaard, H., Andersen M. N., Kristensen, K., Munnich, C., Didion, T., Jensen, E. S., Martensson, L.-M., Jørgensen, U., 2017. Biomass production and water

- use efficiency in perennial grasses during and after drought stress, *GCB-Bioenergy*, 10, 12-27.
- Koster, R. D., Sud Y.C., Guo, Z., Dirmeyer, P. A., Bonan, G., Oleson, K. W., Chan, E., Versegny, D., Cox, P., Davies, H., Kowalczyk, E., Gordon, C. T., Kanae, S., Lawrence, D., Liu, P., Mocko, D., Lu, C-H., Mitchell, K., Malyshev, S., McAvaney, B., Oki, T., Yamada, T., Pitman, A., Taylor, C. M., Vasic, R., Xue, Y., 2006. GLACE: The Global Land–Atmosphere Coupling Experiment. Part I: Overview, *J. Hydrometeorol.*, 7, 590– 610
- Krinner, G., N. Viovy, N. de Noblet-Ducoudré, J. Ogée, J. Polcher, P. Friedlingstein, P. Ciais, S. Sitch, and I. C. Prentice (2005), A dynamic global vegetation model for studies of the coupled atmosphere-biosphere system, *Global Biogeochemical Cycles*, 19, GB1015, doi:10.1029/2003GB002199
- Kuglitsch, F. G., Reichstein, M., Beer, C., Carrara, A., Ceulemans, R., Granier, A., Janssens, I. A., Koestner, B., Lindroth, A., Loustau, D., Matteucci, G., Montagnani, L., Moors, E. J., Papale, D., Pilegaard, K., Rambal, S., Rebmann, C., Schulze, E. D., Seufert, G., Verbeeck, H., Vesala, T., Aubinet, M., Bernhofer, C., Foken, T., Grünwald, T., Heinesch, B., Kutsch, W., Laurila, T., Longdoz, B., Miglietta, F., Sanz, M. J., and Valentini, R., 2008. Characterisation of ecosystem water-use efficiency of european forests from eddy covariance measurements, *Biogeosciences Discuss.*, 5, 4481–4519
- Kumar, S. V., C. D. Peters-Lidard, Y. Tian, P. R. Houser, J. Geiger, S. Olden, L. Lighty, J. L. Eastman, B. Doty, and P. Dirmeyer, 2006. Land information system: An interoperable framework for high resolution land surface modeling, *Environmental modelling & software*, 21, 1402–1415
- Kustas, W. P., Norman, J. M., Schmugge, T. J., and Anderson, M. C., 2004. Mapping surface energy fluxes with radiometric temperature. In Quattrochi, D., and Luvall, J. (eds.), *Thermal Remote Sensing in Land Surface Processes*. Boca Raton: CRC Press, pp. 205–253.
- Lang, D., Zheng, J., Shi, J., Liao, F., Ma, X., Wang, W., Chen, X., Zhang, M., 2017. A Comparative Study of Potential Evapotranspiration Estimation by Eight Methods with FAO Penman–Monteith Method in Southwestern China. *Water*, 9, 734
- Lansu, E. M., van Heerwaarden, C. C., Stegehuis, A. I., Teuling, A. J., 2020. Atmospheric aridity and apparent soil moisture drought in European forest during heatwaves. *Geophysical Research Letters*, 47, e2020GL087091. <https://doi.org/10.1029/2020GL087091>
- Lathuilliere, M. J., M. S. Johnson, and S. D. Donner, 2012. Water use by terrestrial ecosystems: Temporal variability in rainforest and agricultural contributions to evapotranspiration in Mato Grosso, Brazil, *Env. Res. Lett.*, 7, 024024
- Leuning, R., 2007. The correct form of the Webb, Pearman and Leuning equation for eddy fluxes of trace gases in steady and non-steady state, horizontally homogeneous flows. *Boundary-Layer Meteorol.* 123, 263–267.
- Li, S., Hao, X., Du, T., Tong, L., Zhang, J., Kang, S., 2013. A coupled surface resistance model to estimate crop evapotranspiration in arid region of northwest China, *Hydrological Processes*, 28, 2312-2323

- Li, Y., M. Zhao, S. Motesharrei, Q. Mu, E. Kalnay, S. Li, 2015. Local cooling and warming effects of forests based on satellite observations, *Nat. Commun.*, 6, 6603
- Li, J., Y.-P. Wang, Q. Duan, X. Lu, B. Pak, A. Wiltshire, E. Robertson, and T. Ziehn, 2016. Quantification and attribution of errors in the simulated annual gross primary production and latent heat fluxes by two global land surface models, *J. Adv. Model. Earth Syst.*, 8, 1270–1288.
- Li, Z., Erb, A., Sun, Q., Liu, Y., Shuai, Y., Wang, Z., Boucher, P., Schaaf, C., 2018. Preliminary assessment of 20-m surface albedo retrievals from Sentinel-2A surface reflectance and MODIS/VIIRS surface anisotropy measures. *Remote Sensing of Environment*, 217, 352-365.
- Li, J., Chen, F., Lu, X., Gong, W., Zhang, G., & Gan, Y., 2020a. Quantifying contributions of uncertainties in physical parameterization schemes and model parameters to overall errors in noah-MP dynamic vegetation modeling. *Journal of Advances in Modeling Earth Systems*, 12(7), e2019MS001914
- Li, M., Wu, P., Ma, Z., 2020b. A comprehensive evaluation of soil moisture and soil temperature from third generation atmospheric and land reanalysis data sets. *International Journal of Climatology*, 1 – 23, DOI: 10.1002/joc.6549
- Li, J., Tam, C. Y., Tai, A. P. K., Lau, N.C., 2021. Vegetation-heatwave correlations and contrasting energy exchange responses of different vegetation types to summer heatwaves in the Northern Hemisphere during the 1982-2011 period, *Agric. Fores. Meteor.*, 296, 108208.
- Liang, S., 2001. Narrowband to broadband conversions of land surface albedo I: Algorithms, *Remote Sensing of Environment*, 76, 213-238
- Liang, S., Li, X., Wang, J., 2012. Chapter 19- Terrestrial Evapotranspiration, *Adv. Rem. Sens.*, 557-588. <https://doi.org/10.1016/B978-0-12-385954-9.00018-6>
- Liu, E. K., Mei, X. R., Yan, C. R., Gong, D. Z., Zhang, Y. Q., 2016 Effects of water stress on photosynthetic characteristics, dry matter translocation and WUE in two winter wheat genotypes. *Agric. Water Manag.*, 167, 75–85
- Liu, S., Proudman, J., Mitloehner, F. M., 2021. Rethinking methane from animal agriculture, *CABI Agriculture and Bioscience*, 2:22, <https://doi.org/10.1186/s43170-021-00041-y>
- Long, D., and V. P. Singh, 2013. Assessing the impact of end-member selection on the accuracy of satellite-based spatial variability models for actual evapotranspiration estimation, *Water Resour. Res.*, 49, 2601–2618
- Lu, X., Zhuang, Q., 2010. Evaluating evapotranspiration and water-use efficiency of terrestrial ecosystems in the conterminous United States using MODIS and AmeriFlux data. *Remote Sensing of Environment*, 114, 1924-1939.
- Lu, E., Luo, Y., Zhang, R., Wu, Q. and Liu, L., 2011. Regional atmospheric anomalies responsible for the 2009–2010 severe drought in China. *J. Geophys. Res.*, 116, D21114
- Lu, J., R. Tang, H. Tang, and Z.-L. Li, 2014. A new parameterization scheme for estimating surface energy fluxes with continuous surface temperature, air temperature, and surface net radiation measurements, *Water Resour. Res.*, 50, 1245–1259

- Ma, M., Ren, L., Yuan, F., Jiang, S., Liu, Y., Kong, H., Gong, L., 2014. A new standardized Palmer drought index for hydro-meteorological use. *Hydrol. Process* 28, 5645–5661
- Ma, N., Y. Zhang, C.-Y. Xu, and J. Szilagyi, 2015. Modeling actual evapotranspiration with routine meteorological variables in the data-scarce region of the Tibetan Plateau: Comparisons and implications, *J. Geophys. Res. Biogeosci.*, 120, 1638–1657
- Ma, Z., Wu, B., Yan, N., Zhu, W., Xu, J., 2021. Coupling water and carbon processes to estimate field-scale maize evapotranspiration with Sentinel-2 data. *Agricultural and Forest Meteorology*, 306, 108421, <https://doi.org/10.1016/j.agrformet.2021.108421>
- Magnusson, L., Ferranti, L., Vamborg, F., 2018. Forecasting the 2018 European heatwave. *ECMWF Newsletter*, 157, 4.
- Manabe, S., 1969. Climate and the ocean circulation," *Monthly Weather Review*, vol. 97, 739–774
- Martens, B., Schumacher, D. L., Wouters, H., Muñoz-Sabater, J., Verhoest, N. E. C., and Miralles, D. G., 2020. Evaluating the land-surface energy partitioning in ERA5, *Geosci. Model Dev.*, 13, 4159– 4181, <https://doi.org/10.5194/gmd-13-4159-2020>.
- Mauder, M., Desjardins, R.L., MacPherson, I., 2007. Scale analysis of airborne flux measurements over heterogeneous terrain in a boreal ecosystem. *J. Geophys. Res.* 112, D13112
- McCabe, M. F., Wood, E. F., 2006. Scale influences on the remote estimation of evapotranspiration using multiple satellite sensors, *Remote Sens. Environ.*, 105, 271–285
- McDonnell, J., Lambkin, K., Fealy, R. , Hennessy, D. , Shalloo, L. and Brophy, C., 2018. Verification and *bias* correction of ECMWF forecasts for Irish weather stations to evaluate their potential usefulness in grass growth modelling. *Met. Apps*, 25, 292-301.
- McEniry, J., Crosson, P., Finneran, E., McGee, M., Keady, T.W.J. and O’Kiely, P., 2013. How much grassland biomass is available in Ireland in excess of livestock requirements?. *Irish Journal of Agricultural and Food Research*, 52, 67–80
- McGloin, R., Šigut, L., Fischer, M., Foltýnová, L., Chawla, S., Trnka, M., Pavelka, M., Marek, M. V., 2019. Available energy partitioning during drought at two Norway spruce forests and a European beech forest in central Europe. *Journal of Geophysical Research: Atmospheres*, 124, 3726-3742.
- McKee, T.B., N.J. Doesken and J. Kleist., 1993. The relationship of drought frequency and duration to time scale. In: Proceedings of the Eighth Conference on Applied Climatology, Anaheim, California, 17–22 January 1993. Boston, *American Meteorological Society*, 179–184. *Research: Atmospheres*, 124, 3726–3742
- McVeigh, P., Sottocornola, M., Foley, N., Leahy, P. and Kiely, G., 2014. Meteorological and functional response partitioning to explain the interannual variability of CO₂ exchange at an Irish Atlantic Blanket Bog. *Agricultural and Forest Meteorology*. 194, 8–19.
- Medrano, H., Flexas, J., Galmes, J., 2009. Variability in water use efficiency at the leaf level among Mediterranean plants with different growth forms. *Plant and Soil*, 317, 17–29.
- Meehl, G., and Tebaldi, C., 2004. More intense, more frequent and longer lasting heat waves in the 21st century. *Science*, 305, 994–997.

- Meresa, H., Murphy, C., Fealy, R., 2021. Climate change impact on the hydrometeorological drought propagation, EGU General Assembly Conference Abstracts, EGU21-8285. <https://doi.org/10.5194/egusphere-egu21-8285>, 2021
- Met Eireann, 2020. Climatological drought and dry spells 2020. https://www.met.ie/cms/assets/uploads/2020/04/20200429_dryperiods.pdf, last accessed July 2020
- Met Eireann Report, 2018a. 2018, A summer of heatwaves and droughts. Available online at <https://www.met.ie/cms/assets/uploads/2018/09/summerfinal3.pdf>, last accessed November, 2019.
- Met Eireann Report, 2018b. Weather Statement for Spring 2018. <https://www.met.ie/climate/past-weather-statements>, last accessed May 2021
- Minacapilli, M., S. Consoli, D. Vanella, G. Ciraolo, and A. Motisi, 2016. A time domain triangle method approach to estimate actual evapotranspiration: Application in a Mediterranean region using MODIS and MSG-SEVIRI products. *Remote Sens. Environ.*, 174, 10–23
- Miralles, D. G., M. J. van den Berg, A. J. Teuling, and R. A. M. de Jeu, 2012. Soil moisture-temperature coupling: A multiscale observational analysis, *Geophys. Res. Lett.*, **39**, L21707
- Miralles D. G., Gentine, P., Seneviratne S. I., Teuling A. J., 2019. Land-atmosphere feedbacks during droughts and heatwaves: state of the science and current challenges. *Ann. N. Y. Acad. Sci.* 1436, 19 – 35. doi: 10.1111/nyas.13912
- Miralles, D. G., Teuling, A. J., van Heerwaarden, C. C., & de Arellano, J.-G., 2014. Mega-heatwave temperatures due to combined soil desiccation and atmospheric heat accumulation. *Nature Geoscience*, 7(5), 345
- Mishra, V., J.F. Cruise, J.R. Mecikalski, C.R. Hain, M.C. Anderson, 2013. A remote-sensing driven tool for estimating crop stress and yields, *J. Remote Sens.*, 5, 3331-3356
- Mladenova, I. E., J.D. Bolten, W.T. Crow, M.C. Anderson, C.R. Hain, D.M. Johnson, R. Mueller, 2017. Intercomparison of soil moisture, evaporative stress, and vegetation indices for estimating corn and soybean yields over the U.S, *IEEE J. Sel. Top. Appl. Earth Obs. Remote Sens.*, 10, 1328-1343
- Mohan, M. and Siddiqui, T. A., 1998. Applied Modeling of Surface Fluxes under Different Stability Regimes. *J. Appl. Meteor.*, 37, 1055–1067.
- Moncrieff, J., Valentini, R., Greco, S., Seufert, G. and Ciccioli, P., 1997a. Trace gas exchange over terrestrial ecosystems: methods and perspectives in micrometeorology. *Journal of Experimental Botany*, 48, 1133–1142.
- Moncrieff, J.B., Massheder, J.M., Debruin, H., Elbers, J., Friborg, T., Heusinkveld, B., Kabat, P., Scott, S., Soegaard, H., Verhoef, A., 1997b. A system to measure surface fluxes of momentum, sensible heat, water vapour and carbon dioxide. *Journal of Hydrology*, 189, 589–611
- Monin A. S. and Obukhov A.M., 1954. 'Osnovnye zakonomernosti turbulentnogo peremeshivaniya v prizemnom sloe atmosfery (Basic Laws of Turbulent Mixing in the Atmosphere Near the Ground)'. *Trudy geofiz. inst. AN SSSR* 24, 163–187

- Monteith, J., 1965. Evaporation and environment, *Symp. Soc. Exp. Bio.*, 19, 205-224.
- Monteith, J.L., 1972. Solar radiation and productivity in tropical ecosystems. *J. Appl. Ecol.*, 9, 747–766
- Monteith, J., 1981. Evaporation and surface temperature. *Q. J. R. Meteorol. Soc.*, 107, 1–27.
- Moore, P., 2020. Summer 2018. Available online at <https://www.met.ie/cms/assets/uploads/2020/06/Summer2018.pdf>, last accessed February, 2021
- Moran, M. S., Rahman, A. F., Washburne, J. C., Goodrich, D. C., Weltz, M. A., Kustas, W. P., 1996. Combining Penman-Monteith equation with measurements of surface temperature and reflectance to estimate evaporation rates of semiarid grasslands, *Agric. Fores. Meteor.*, 80, 87-109.
- Mu, Q., Zhao, M., Running, S. W., 2011. Improvements to a MODIS global terrestrial evapotranspiration algorithm. *Remote Sensing of Environment*, 115, 1781-1800
- Mu, Q., F.A. Heinsch, M. Zhao, S.W. Running, 2007. Development of a global evapotranspiration algorithm based on MODIS and global meteorology data. *Remote Sens. Environ.*, 111, 519-536
- Muggeo, V. M. R., 2003. Estimating regression models with unknown break-points. *Statistics in Medicine*, 22, 3055–3071. <https://doi.org/10.1002/sim.1545>
- Muggeo, V. M. R., 2021. Regression models with break-points/change-points estimation. An R ‘segmented’ package version 1.3-3, last accessed 10 March, 2021.
- Murphy, C., Wilby, R.L., Matthews, T.K., Horvath, C., Crampsie, A., Ludlow, F., Noone, S., Brannigan, J., Hannaford, J., McLeman, R., Jobbova, E., 2020. The forgotten drought of 1765 – 1768: Reconstructing and re-evaluating historical droughts in the British and Irish isles. *International Journal of Climatology*, 1 – 23, DOI: 10.1002/joc.6521
- Naegeli, K., Damm, A., Huss, M., Shaepman, M., Wulf, H., and Hoelze, M., 2017. Cross comparison of albedo products for glacier surfaces derived from airborne and satellite (Sentinel2 and Landsat 8) optical data, *Remote Sens.*, 9, 110, <https://doi.org/10.3390/rs9020110>
- Nickerson, E. C., and V. E. Smiley, 1975. Surface energy budget parameterizations for urban scale models. *J. Appl. Meteor.*, 14, 297–300.
- Niyogi, D., and S. Raman, 1997. Comparison of four different stomatal resistance schemes using FIFE data. *J. Appl. Meteor.*, 36, 903–917.
- Niyogi, D. S., Raman, S., Alapaty, K., 1998. Comparison of Four Different Stomatal Resistance Schemes using FIFE Data. Part II: Analysis of Terrestrial Biospheric-Atmospheric Interactions. *J. Appl. Met. Clim.*, 37, 1301-1320.
- Ní Choncubhair, Ó., B. Osborne, J. Finnan, G. Lanigan, 2017. Comparative assessment of ecosystem C exchange in *Miscanthus* and reed canary grass during early establishment, *GCB Bioenergy*, 9, 280 – 298, doi: 10.1111/gcbb.12343.
- Niu, G. Y., Yang, Z. L., Mitchell KE, Chen F, Ek MB, Barlage M, Kumar A, Manning K, Niyogi D, Rosero E, Tewari, M., Xia, Y., 2011. The community Noah land surface mode I with multiparameterization options (Noah-MP): 1. Model description and evaluation with

- local-scale measurements. *J. Geophys. Res.*, 117, D08107, doi:10.1029/2004GL019836.
- Nolan, P., 2015. Ensemble of regional climate model projections for Ireland. EPA Research Report No. 159, https://www.epa.ie/publications/research/climate-change/EPA-159_Ensemble-of-regional-climate-model-projections-for-Ireland.pdf, last accessed 05 July 2021.
- Noone S, Broderick C, Duffy C., Matthews, T., Wilby, R. L., Murphy, C., 2017. A 250-year drought catalogue for the Island of Ireland (1765–2015). *Int. J. Climatol.* 37, 239–254
- Otkin, J.A., Svoboda, M., Hunt, E.D., Ford, T.W., Anderson, M.C., Hain, C. and Basara, J.B., 2018. Flash droughts: a review and assessment of the challenges imposed by rapid-onset droughts in the United States. *Bulletin of American Meteorological Society*, 99, 911–919.
- Palmer, W. C., 1965. Meteorological drought, vol 30. US Department of Commerce, Weather Bureau, Washington
- Pan, H. L., and L. Mahrt, 1987. Interaction between soil hydrology and boundary-layer development, *Boundary Layer Meteorol.*, 38, 185- 202
- Papale, D., Reichstein, M., Aubinet, M., Canfora, E., Bernhofer, C., Longdoz, B., Kutsch, W., Rambal, S., Valentini, R., Vesala, T. and Yakir, D. 2006. Towards a standardized processing of Net Ecosystem Exchange measured with eddy covariance technique: algorithms and uncertainty estimation, *Biogeosciences*, 3, 571-583
- Paulson, C. A., 1970. The Mathematical Representation of Wind Speed and Temperature Profiles in the Unstable Atmospheric Surface Layer. *J Appl. Meteor.*, 9, 857–861.
- Peel, M. C., Finlayson, B. L., and McMahon, T. A., 2007. Updated world map of the Köppen-Geiger climate classification, *Hydrol, Earth Syst. Sci.*, 11, 1633–1644.
- Peichl, M., Carton, O. and Kiely, G., 2012. Management and climate effects on carbon dioxide and energy exchanges in a maritime grassland, *Agric. Ecosys. Environ.*, 158, 132 – 146.
- Peichl, M., Leahy, P., and Kiely, G., 2011. Six-year stable annual uptake of carbon dioxide in intensively managed humid temperate grassland. *Ecosystems* 14, 112–126
- Peichl, M., Carton, O., Kiely, G., 2012. Management and Climate Effects on Carbon dioxides and Energy Exchanges in a Maritime Grasslands. *Agric Ecosy. Environ.*, 158, 132 - 146
- Penman, H. L. 1948. "Natural evaporation from open water, bare soil and grass." *Proc. Roy. Soc. London*, A193, 120-146
- Phelan, P., Morgan, E. R., Rose, H., Grant, J. and O'Kiely, P. 2016. Predictions of future grazing season length for European dairy, beef and sheep farms based on regression with bioclimatic variables. *The Journal of Agricultural Science*, 154, 5, 765
- Philip, S. Y., Kew, S. F., Hauser, M., Guillod, B. P., Teuling, A. J., Whan, K., Uhe, P., & van Oldenborgh, G. J., 2018. Western us high June 2015 temperatures and their relation to global warming and soil moisture. *Climate Dynamics*, 50, 2587–2601

- Pitman, A. J., 2003. The evolution of, and revolution in, land surface schemes designed for climate models," *International Journal of Climatology*, 23, 479–510.
- Popova, Z., Kercheva, M., Pereira, L.S., 2006. Validation of the FAO methodology for computing ETo with limited data. Application to South Bulgaria. *Irrigation and Drainage* 55, 201–215.
- Porter, J.R., Xie, L., Challinor, A.J., Cochran, K., Howden, M., Iqbal, M.M., Lobell, D.B., Travasso, M.I.. 2014. Chapter 7. Food Security and Food Production Systems. Climate Change 2014: Impacts, Adaptation and Vulnerability. Working Group II Contribution to the IPCC 5th Assessment Report. Geneva, Switzerland
- Potop, V., Boroneanț, C., Možný, M., Štěpánek, P., Skalák, P., 2014. Observed spatiotemporal characteristics of drought on various time scales over the Czech Republic. *Theoretical and Applied Climatology*, 115, 563–581
- Prentice, I. C., Dong, N., Gleason, S. M., Maire, V., and Wright, I. J., 2014. Balancing the costs of carbon gain and water transport: Testing a new theoretical framework for plant functional ecology. *Ecology Letters*, 17, 82–91.
- Prentice, I. C., Liang, X., Medlyn, B. E., Wang, Y. P., 2015. Reliable, robust and realistic: the three R's of next-generation land-surface modelling, *Atmospheric Chemistry and Physics*, 15, 5987-6005
- Priestley, C H. B., Taylor, R. J., 1972. On the assessment of surface heat flux and evaporation using large-scale parameters, *Mon. Weather Rev.*, 100, 81-92
- Quesada, B., Vautard, R., Yiou, P., Hirschi, M. & Seneviratne, S. I., 2012. Asymmetric European summer heat predictability from wet and dry southern winters and springs. *Nature Clim. Change* 2, 736–741
- Qiu, B., Xue, Y., Fisher, J. B., Guo, W., Berry, J. A., Zhang, Y., 2018. Satellite chlorophyll fluorescence and soil moisture observations lead to advances in the predictive understanding of global terrestrial coupled carbon-water cycles. *Global Biogeochemical Cycles*, 32, 360–375.
- Quintana-Seguí, P., Barella-Ortiz, A., Regueiro-Sanfiz, S., Miguez-Macho, G., 2020. The Utility of Land-Surface Model Simulations to Provide Drought Information in a Water Management Context Using Global and Local Forcing Datasets. *Water Resour Manage* 34, 2135–2156.
- Raupach, M. R., Thom, A. S., Edwards, I., 1980. A wind tunnel study of turbulent flow close to regular arrayed rough surfaces. *Boundary-Layer Met.*, 18, 373-397
- Reichstein, M., Tenhunen, J. D., Rouspard, O., Ourcival, J. M., Rambal, S., Miglietta, F., Peressotti, A., Pecchiari, M., Tirone, G., Valentini, R., 2002. Severe drought effects on ecosystem CO₂ and H₂O fluxes at three Mediterranean evergreen sites: Revision of current hypotheses? *Global Change Biology*, 8, 999–1017.
- Reichstein, M., Tenhunen, J., Rouspard, O., Ourcival, J. -M., Rambal, S., Miglietta, F., Peressotti, A., Pecchiari, M., Tirone, G., Valentini, R., 2003. Inverse modeling of seasonal drought effects on canopy CO₂/H₂O exchange in three Mediterranean ecosystems. *Journal of Geophysical Research*, 108(D23), 4726.

- Reichstein, M., Ciais, P., Papale, D., Valentini, R., Running, S., Viovy, N., Cramer, W., Granier, A., Ogée, J., Allard, V., Aubinet, M., Bernhofer, C., Buchmann, N., Carrara, A., Grünwald, T., Heimann, M., Heinesch, B., Knohl, A., Kutsch, W., Loustau, D., Manca, G., Matteucci, G., Miglietta, F., Ourcival, J., Pilegaard, K., Pumpanen, J., Rambal, S., Schaphoff, S., Seufert, G., Soussana, J., Sanz, M., Vesala, T. and Zhao, M., 2007. Reduction of ecosystem productivity and respiration during the European summer 2003 climate anomaly: a joint flux tower, remote sensing and modelling analysis. *Global Change Biology*, 13, 634–651.
- Rigden, A. J., and G. D. Salvucci, 2015. Evapotranspiration based on equilibrated relative humidity (ETRHEQ): Evaluation over the continental U.S., *Water Resour. Res.*, 51, 2951–2973
- Ronda, R. J., H. A. R. de Bruin, and A. A. M. Holtslag, 2001. Representation of the canopy conductance in modeling the surface energy budget for low vegetation. *J. Appl. Meteor.*, 40, 1431–1444.
- Rösner, B., Benedict, I., van Heerwaarden, C., Weerts, A., Hazeleger, W., Bissolli, P., and Trachte, K., 2019. The long heat wave and drought in Europe in 2018. *Bulletin of the American Meteorological Society*, 100(9), S222–S223.
- Running, S. W., Zhao, M., 2015. User's Guide Daily GPP and Annual NPP (MOD17A2/A3) Products. NASA Earth Observing System MODIS Land Algorithm. Available online from https://www.nts.gov/files/modis/MOD17UsersGuide2015_v3.pdf , last accessed 10 January, 2021.
- Russell, G., 1980. Crop evaporation, surface resistance and soil water status. *Agric. Meteorol.*, 21, 213–226.
- Samaniego L, Thober S, Kumar R, Wanders N, Rakovec O, Pan M, Zink M, Sheffield J, Wood E. F and Marx A., 2018. Anthropogenic warming exacerbates European soil moisture droughts *Nat. Clim. Change*, 8, 421–6.
- Schaaf, C. and Wang, Z., 2015. MCD43A4 MODIS/Terra+ Aqua BRDF/Albedo Nadir BRDF Adjusted Ref Daily L3 Global-500 m V006 [Data set], NASA EOSDIS Land Processes DAAC, <https://doi.org/10.5067/MODIS/MCD43A4.006>
- Schaake, J. C., Koren, V. I., Duan, Q.-Y., Mitchell, K., Chen, F., 1996. Simple water balance model for estimating runoff at different spatial and temporal scales. *J. Geophys. Res.-Atmos.*, 101, 7461–7475.
- Schayes, G., 1982. Direct determination of diffusivity profiles from synoptic reports. *J. Atmos. Sci.*, 27, 1122–1137.
- Schuldt, B., Buras, A., Arend, M., Vitasse, Y., Beierkuhnlein, C., Damm, A., Gharun, M., Grams, T.E.E., Hauck, M., Hajek, P., Hartmann, H., Hiltbrunner, E., Hoch, G., Holloway-Phillips, M., Korner, C., Larysch, E., Lubbe, T., Nelson, D. B., Rammig, A., Rigling, A., Rose, L., Ruehr, N. K., Schumann, K., Weiser, F., Werner, C., Wohlgemuth, T., Zang, C. S., Kahmen, A., 2020. A first assessment of the impact of the extreme 2018 summer drought on Central European forests. *Basic and Applied Ecology*, 45, 86–103.

- Schulte, R.P.O., Diamond, J., Finkele, K., Holden, N. M., Brereton, A. J., 2005. Predicting the soil moisture conditions of Irish grasslands. *Irish Journal of Agricultural and Food Research*, 44, 95–110
- Sellers, P. J., F. G. Hall, G. Asrar, D. E. Strebel, and R. E. Murphy, 1992. An overview of the first international satellite land surface climatology project (ISLSCP) field experiment (FIFE), *Journal of Geophysical Research: Atmospheres*, 97, 18345–18371.
- Sellers, P. J., Hall, F. G., Kelly, R. D., Black, A., Baldocchi, D., Berry, J., Ryan, M., Ranson, K. J., Crill, P. M., and Lettenmaier, D. P., 1997. BOREAS in 1997: Experiment overview, scientific results, and future directions, *J. Geophys. Res.-Atmos.*, 102, 28731–28769.
- Smith, F. B., 1990. Atmospheric structure. *Proc. Air Pollution Modelling for Environmental Impact Assessment*, Trieste, Italy, International Centre for Theoretical Physics, 201–236.
- Senay, G.B., Bohms, S., Singh, R. K. Gowda, P. H., Velpuri, N. M., Alemu, H., Verdin, J. P., 2013. Operational evapotranspiration mapping using remote sensing and weather datasets: a new parameterization for the SSEB approach. *JAWRA Journal of the American Water Resources Association*, 49, 577–591.
- Senay, G.B., Schauer, M., Friedrichs, M., Velpuri, N. M., Singh, R. K., 2017. Satellite-based water use dynamics using historical Landsat data (1984–2014) in the southwestern United States. *Remote Sensing of Environment*, 202, 98–112
- Seneviratne, S.I., Corti, T., Davin, E. L., Hirschi, M., Jaeger, E. B., Lehner, I., Orlowsky B., Teuling, A. J., 2010. Investigating soil moisture–climate interactions in a changing climate: a review. *Earth Sci. Rev.*, 99, 125–161.
- Seneviratne, S. I., X. Zhang, M. Adnan, W. Badi, C. Dereczynski, A. Di Luca, S. Ghosh, I. Iskandar, J. Kossin, S. Lewis, F. Otto, I. Pinto, M. Satoh, S. M. Vicente-Serrano, M. Wehner, B. Zhou, 2021, Weather and Climate Extreme Events in a Changing Climate. In: *Climate Change 2021: The Physical Science Basis. Contribution of Working Group I to the Sixth Assessment Report of the Intergovernmental Panel on Climate Change* [Masson-Delmotte, V., P. Zhai, A. Pirani, S. L. Connors, C. Péan, S. Berger, N. Caud, Y. Chen, L. 50 Goldfarb, M. I. Gomis, M. Huang, K. Leitzell, E. Lonnoy, J. B. R. Matthews, T. K. Maycock, T. Waterfield, 51 O. Yelekçi, R. Yu and B. Zhou (eds.)]. Cambridge University Press. In Press
- Sentelhas P. C., Gillespie T. J., Santos E. A., 2010. Evaluation of FAO Penman–Monteith and alternative methods for estimating reference evapotranspiration with missing data in southern Ontario, Canada. *Agric. Water Manag.* 97:635–644
- Sherratt, D.J, and Wheeler, H.S., 1984. The use of surface resistance-soil moisture relationships in soil water budget models. *Agric. For. Meteorol.*, 31, 143--157.
- Shi, Q. and Liang, S., 2014. Surface-sensible and latent heat fluxes over the Tibetan Plateau from ground measurements, reanalysis, and satellite data. *Atmos. Chem. Phys.*, 14, 5659–5677.
- Shindell, D. T., 2016. Crop yield changes induced by emissions of individual climate-altering pollutants, *Earth's Future*, 4, 373-380.

- Shrestha, P., Sulis, M., Simmer, C., and Kollet, S., 2018. Effects of horizontal grid resolution on evapotranspiration partitioning using TerrSysMP, *J. Hydrol.*, 557, 910–915
- Shuttleworth, W. J., 1993. Evaporation. D. R. Maidment (Ed.), *Handbook of Hydrology*, McGraw-Hill Inc, New York, pp. 4.1 – 4.53.
- Singh, R. K., Khand, K., Kagone, S., Schauer, M., Senay, G. B., Wu, Z., 2020. A novel approach for next generation of water-use mapping using Landsat and Sentinel-2 satellite data. *Hydrological Sciences*, 65, 2508-2519.
- Sobrino, J. A., M. Gomez, J. C. Jimenez-Muoz, and A. Olioso, 2007. Application of a simple algorithm to estimate daily evapotranspiration from NOAA-AVHRR images for the Iberian Peninsula, *Remote Sens. Environ.*, 110, 139–148.
- Sottocornola, M. and Kiely, G., 2010a. Hydro-meteorological controls on the CO₂ exchange variation in an Irish blanket bog. *Agricultural and Forest Meteorology*, 150, 287–297.
- Sottocornola, M. and Kiely, G., 2010b. Energy fluxes and evaporation mechanisms in an Atlantic blanket bog in southwestern Ireland. *Water Resources Research*, 46, W11524
- Spiliotopoulos M., Holden N.M. and Loukas A., 2017. Mapping evapotranspiration coefficients in a temperate maritime climate using the METRIC model and Landsat TM. *Water*. 9, 1 – 15.
- Stap L. B., van den Hurk B. J. J. M., van Heerwaarden C. C., Neggers R. A. J., 2014. Modeled Contrast in the response of the surface energy balance to heatwaves for forest and grassland. *J. Hydromet.*, 15, 973 – 989.
- Steduto, P., Raes, D., Hsiao, T.C., Fereres, E., Heng, L.K., Howell, T.A., Evett, S.R., Rojas-Lara, B.A., Farahani, H.J., Izzi, G., Oweis, T. Y., Wani, S. P., Hoozeveer, J., Geerts, S., 2009. Concepts and applications of AquaCrop: The FAO crop water productivity model. In *Crop Modeling and Decision Support*; Springer: Berlin, Germany, 175–191
- Stewart, J. B., 1988. Modeling surface conductance of pine forest. *Agric. For. Meteorol.*, 43, 19–35.
- Stewart, J. B., and Gay, L. W., 1989. Preliminary modeling of transpiration from FIFE site in Kansas, USA. *Agric. For. Meteorol.*, 48, 305– 316.
- Stockle, C.O., Martin, S.A., Campbell, G.S., 1994. CropSyst, a cropping systems simulation model: Water/nitrogen budgets and crop yield. *Agric. Syst.*, 46, 335–359
- Stöckle, C.O., Kjelgaard, J., Bellochi, G., 2004. Evaluation of estimates weather data for calculating Penman–Monteith reference crop evapotranspiration. *Irrigation Science*, 23, 39–46.
- Stoy, P.C., Mauder, M., Foken, T., Marcolla, B., Boegh, E., Ibrom, A., Arain, M.A., Arneth, A., Aurela, M., Bernhofer, C., Cescatti, A., Dellwik, E., Duce, P., Gianelle, D., van Gorsel, E., Kiely, G., Knohl, A., Margolis, H., McCaughey, H., Merbold, L., Montagnani, L., Papale, D., Reichstein, M., Saunders, M., Serrano-Ortiz, P., Sottocornola, M., Spano, D., Vaccari, F., Varlagin, A., 2013. A data-driven analysis of energy balance closure across FLUXNET research sites: The role of landscape scale heterogeneity. *Agricultural and Forest Meteorology* 171–172, 137–152. <https://doi.org/10.1016/j.agrformet.2012.11.004>

- Streck, N. A., 2003. Stomatal response to water vapor pressure deficit: An unsolved issue. *Current Agricultural Science and Technology*, 9, 317–322.
- Stull, R. B., 1988. An introduction to boundary layer meteorology. *Atmospheric and Oceanic Sciences library*, 13, 667 pp., doi:10.1007/978-94-009-3027-8
- Su, Z., 2002. The Surface Energy Balance System (SEBS) for estimation of turbulent heat fluxes. *Hydrology and Earth System Sciences Discussions*, 6, 85-100
- Su H., McCabe M.F., Wood E. F., Su Z., Prueger J., 2005. Modeling evapotranspiration during SMACEX: comparing two approaches for local and regional scale prediction. *Journal of Hydrometeorology*, 6, 910–922
- Su, H., E.F. Wood, M.F. McCabe, Z. Su, 2007. Evaluation of remotely sensed evapotranspiration over the CEOP EOP-1 reference sites, *J. Meteorol. Soc. Jpn.*, 85A, 439-459
- Sulman, B. N., Roman, D. T., Yi, K., Wang, L., Phillips, R. P., Novick, K. A., 2016. High atmospheric demand for water can limit forest carbon uptake and transpiration as severely as dry soil. *Geophysical Research Letters*, 43, 9686–9695
- Swinbank, W. C., 1963. Longwave radiation from clear skies. *Quart. J. Roy. Meteor. Soc.*, 89, 339–448.
- Tadesse, T., G.B. Senay, G. Berhan, T. Regassa, S. Beyene, 2015. Evaluating a satellite-based seasonal evapotranspiration product and identifying its relationship with other satellite-derived products and crop yield: A case study for Ethiopia, *Int. J. Appl. Earth Obs. Geoinf.*, 40, 39-54
- Tang, R., Li, Z.L., and Tang, B., 2010. An application of the Ts–VI triangle method with enhanced edges determination for evapotranspiration estimation from MODIS data in arid and semi-arid regions: implementation and validation. *Remote Sensing of Environment*, 114, 540–551
- Tang, R. L., Z.-L. Li, and X. M. Sun, 2013. Temporal upscaling of instantaneous evapotranspiration: An intercomparison of four methods using eddy covariance measurements and MODIS data, *Remote Sens. Environ.*, 138, 102–118
- Tardieu, F., 2013. Plant response to environmental conditions: assessing potential production, water demand, and negative effects of water deficit, *Frontiers in Physiology*, 4, 1-11.
- Teagasc, 2021. Agriculture in Ireland. <https://www.teagasc.ie/rural-economy/rural-economy/agri-food-business/agriculture-in-ireland/>, last accessed 04 July, 2021.
- Teuling, A. J., 2018. A hot future for European droughts. *Nature Climate Change*, 8, 364 – 365.
- Teuling, A., Seneviratne, S. I., 2008. Contrasting spectral changes limit albedo impact on land–atmosphere coupling during the 2003 european heat wave. *Geophys. Res. Lett.*, 35, L03401.
- Teuling, A. J., S. I. Seneviratne, C. Williams, and P. A. Troch., 2006. Observed timescales of evapotranspiration response to soil moisture, *Geophys. Res. Lett.*, 33, L23403
- Teuling, A. J., Seneviratne, S. I., Stöckli, R., Reichstein, M., Moors, E., Ciais, P., Luysaert S., van den Hurk B., Ammann C., Bernhofer C., Dellwik E., Gianelle D., Gielen B., Grunwald T., Klumpp K., Montagnani L., Moureaux C., Sottocornola M., Wohlfahrt G., 2010.

- Contrasting response of European forest and grassland energy exchange to heatwaves. *Nature Geoscience*, 3(10), 722–727.
- Todd B, Macdonald N, Chiverrell RC, Caminade C, Hooke JM. 2013. Severity, duration and frequency of drought in SE England from 1697 to 2011. *Climatic Change*, 121, 673–687
- Twine, T. E., Kustas, W. P., Norman, J. M., Cook, D. R., Houser, P. R., Meyers, T. P., Prueger, J. H., Starks, P. J., Wesely, M. L., 2000. Correcting eddy-covariance flux underestimates over a grassland. . *Agricultural and Forest Meteorology*, 103(3), 279-300
- van de Boer, A., Moene, A. F. , Schu"ttemeyer, D., 2013. Sensitivity and uncertainty of analytical footprint models according to a combined natural tracer and ensemble approach. *Agric. Forest. Meteor.*, 169, 1–11.
- van de Boer, A., Moene, A. F. , Graf, A., Simmer, C. and Holtslag, A. A. M., 2014a. Estimation of the refractive index structure parameter from single-level daytime routine weather data. *Applied Optics*, 1 – 20, DOI:10.1364/AO.53.005944
- van de Boer, A., Moene, A. F. , Graf, A., Schu"ttemeyer, D., and Simmer, C., 2014b. Detection of entrainment influences on surface-layer measurements and extension of Monin-Obukhov similarity theory, *Bound-Layer Meteor*, 152, 19 – 44
- van den Hurk, B.J.J.M. , Viterbo, P., Beljaars, A.C.M. and Betts, A.K., 2000. Offline validation of the ERA40 surface scheme. Technical report ECMWF, 43p.
- van den Hurk, B.J.J.M. , Viterbo, P. and Los, S.O., 2003. Impact of Leaf Area Index seasonality on the annual land surface evaporation in a global circulation model. *J Geophys. Res.* 108(D6), 4191
- van Heerwaarden, C. C. and Teuling, A. J., 2014 Disentangling the response of forest and grassland energy exchange to heatwaves under idealized land–atmosphere coupling, *Biogeosciences*, 11, 6159–6171.
- van Heerwaarden, C. C., Vila-Guerau de Arellano, J., Gounou, A., Guichard, F., & Couvreux, F., 2010. Understanding the daily cycle of evapotranspiration: A method to quantify the influence of forcings and feedbacks. *Journal of Hydrometeorology*, 11, 1405– 1422.
- Van Loon AF. 2015. Hydrological drought explained. *WIREs Water*, 2, 359–392
- Van Loon AF, Gleeson T, Clark J, Dijk Van, AIJM Stahl K, Hannaford J, Di Baldassarre G, Teuling AJ, Tallaksen LM, Uijlenhoet R, Hannah DM, Sheffield J, Svoboda M, Verbeiren B, Wagener T, Rangecroft S, Wanders N, Van Lanen HAJ., 2016. Drought in the Anthropocene. *Nat. Geosci.*, 9, 89–91
- Van Niel, T. G., McVicar, T. R., Roderick, M.L. , Van, Dijk, A.I.J.M. , Beringer, J., Hutley, L.B., Van Gorsel, E., 2012. Upscaling latent heat flux for thermal remote sensing studies: comparison of alternative approaches and correction of bias, *J. Hydrol.*, 468–469, 35-46.
- Van Ulden, A. P., Holtslag, A. A. M., 1983. The stability of the atmospheric surface layer during nighttime. *Preprints Sixth Symp. on Turbulence and Diffusion*. Boston, Amer. Meteor. Soc., 257-260
- van Ulden, A. P., and A. A. M. Holtslag, 1985. Estimation of atmospheric boundary layer parameters for diffusion applications. *J. Climate Appl. Meteor.*, 24, 1196–1207.

- Van Wart, J., van Bussel L.G.J., Wolf J., Licker R., Grassini P., Nelson A., Boogaard H., Gerber, J., Mueller, N. D., Claessens, L., van Ittersum, M. K., Cassman, K. G., 2013. Use of agro-climatic zones to upscale simulated crop yield potential. *Field Crops Research*, 143, 44-55.
- Vanino, S., Nino, P., De Michele, C., Falanga Bolognesi, S., D'Urso, G., Di Bene, C., Pennelli, B., Vuolo, F., Farina, R., Pulighe, G., Napoli, R., 2018. Capability of Sentinel2 data for estimating maximum evapotranspiration and irrigation requirements for tomato crop in Central Italy. *Remote Sens. Environ.* 215, 452–470
- Verger, A., Baret, F., Weiss, M., 2014. Near real time vegetation monitoring at global scale. *IEEE J. Sel. Top. Appl. Earth Obs. Remote Sens.*, 7, 3473–3481.
- Verhoef, W., 1984. Light scattering by leaf layers with application to canopy reflectance modelling. The SAIL model. *Remote Sens. Environ.* 16, 125–141
- Vicente-Serrano SM, Begueria S, López-Moreno J. I., 2010. A multiscalar drought index sensitive to global warming: The standardized precipitation evapotranspiration index. *J. Clim.*, 23, 1696–1718
- Vicente-Serrano, S. M., Domínguez-Castro, F., Murphy, C., Hannaford, J., Reig, F., Peña-Angulo, D., Trambly, Y., Trigo, R. M., Mac Donald, N., Luna, M. Y., Mc Carthy, M., Van der Schrier, G., Turco, M., Camuffo, D., Noguera, I., García-Herrera, R., Becherini, F., Della Valle, A., Tomas-Burguera, M., El Kenawy, A., 2020. Long-term variability and trends in meteorological droughts in Western Europe (1851–2018), *International Journal of Climatology*, 1 – 28, DOI: 10.1002/joc.6719
- Vickers, D., Mahrt, L., 1997. Quality control and flux sampling problems for tower and aircraft data. *Journal of Atmospheric and Oceanic Technology*, 14, 512–526.
- Vignolio, O.R., Biel, C., de Herralde, F., Araujo-Alves, J.P.L., Save, R., 2005. Use of water-stress tolerant *Lotus creticus* and *Cynodon dactylon* in soil revegetation on different slopes in a Mediterranean climate. *Ann. Bot. Fenn.* 42, 195–205.
- Viterbo, 2002. The role of the land surface in the climate system. ECMWF Meteorology Training Course Lecture Series, <https://www.ecmwf.int/sites/default/files/elibrary/2002/16961-role-land-surface-climate-system.pdf> (last accessed 09 May, 2019), 19 pp.
- Viterbo, P., and A. Beljaars, 1995. An improved land-surface parameterization scheme in the ECMWF model and its validation. *J. Climate*, 8, 2716–2748.
- Viterbo, P., A.C.M. Beljaars, J.-F. Mahfouf, and J. Teixeira, 1999. The representation of soil moisture freezing and its impact on the stable boundary layer. *Quart. J. Roy. Meteor. Soc.*, 125, 2401-2426
- Vuolo, F., Żóltak, M., Pipitone, C., Zappa, L., Wenng, H., Immitzer, M., Weiss, M., Baret, F., Atzberger, C., 2016. Data service platform for sentinel-2 surface reflectance and value-added products: system use and examples. *Remote Sens.*, 8, 938.

- Wagle, P., Kakani, V. G., 2012. Growing season variability in evapotranspiration, ecosystem water use efficiency, and energy partitioning in switchgrass. *Ecohydrology*, 7, 64-72.
- Walsh S., 2012. A summary of climate averages for Ireland, 1981 – 2010. MET Eireann CLIMATOLOGICAL NOTE No. 14, Dublin. <https://www.met.ie/climate-ireland/SummaryClimAvgs.pdf>, last accessed Oct., 2018.
- Wan, Z., Hook, S., Hulley, G., 2015. *MOD11A1 MODIS/Terra Land Surface Temperature/Emissivity Daily L3 Global 1km SIN Grid V006* [Data set]. NASA EOSDIS Land Processes DAAC. <https://doi.org/10.5067/MODIS/MOD11A1.006>, last accessed 2021-01-29
- Wang, K. and Dickinson R. E., 2012. A review of global terrestrial evapotranspiration: observation, modeling, climatology, and climatic variability. *Rev. Geophys.* 50 10.1029/2011rg000373
- Wang, X. Y., Yao, Y. J., Zhao, S. H., Jia, K., Zhang, X. T., Zhang, Y. H., Zhang, L., Xu, J., Chen, X., 2017. MODIS-based estimation of terrestrial latent heat flux over North America using three machine learning algorithms. *Remote Sensing*, 9, 1326.
- Wang, M., Sun, R., Zhu, A., and Xiao, Z., 2020. Evaluation and Comparison of Light Use Efficiency and Gross Primary Productivity Using Three Different Approaches. *Remote Sensing*, 12, 1003.
- Webb, E., Pearman, G., Leuning R., 1980. Correction of flux measurements for density effects due to heat and water-vapor transfer. *Q. J. Roy. Meteor. Soc.*, 106, 85–100.
- Weiss, M., Baret, F., 2016. S2 ToolBox level 2 products: LAI, FAPAR, FCOVER version 1.1. Available from http://step.esa.int/docs/extra/ATBD_S2ToolBox_L2B_V1.1.pdf, last accessed 07 November 2020, 53 pp.
- Wilby RL, Noone S, Murphy C, Matthews T, Harrigan S, Broderick C. 2015a. An evaluation of persistent meteorological drought using a homogeneous Island of Ireland precipitation network. *Int. J. Climatol.* 36: 2854–2865
- Wilby RL, Prudhomme C, Parry S, Muchan KGL. 2015b. Persistence of hydrometeorological droughts in the United Kingdom: a regional analysis of multi-season rainfall and river flow anomalies. *J. Extr. Events.* 2: 1550006
- Wieringa, J., 1980. A revaluation of the Kansas mast influence on measurements of stress and cup anemometer overspeeding *Boundary-Layer Meteorology*, 18, 411-430
- Williams, A. P., Cook, E. R., Smerdon, J. E., Cook, B. I., Abatzoglou, J. T., Bolles, K., Baek, S. H., Badger, A. M., Livneh, B., 2020. Large contribution from anthropogenic warming to an emerging North American megadrought. *Science*, 368, 314–318
- Wilson, K., Goldstein, A., Falge, E., Aubinet, M., Baldocchi, D., Berbigier, P., Bernhofer, C., Ceulemans, R., Dolman, H., Field, C., Grelle, A., Ibrom, A., Law, B.E., Kowalski, A., Meyers, T., Moncrieff, J., Monson, R., Oechel, W., Tenhunen, J., Valentini, R., Verma, S., 2002. Energy balance closure at FLUXNET sites. *Agricultural and Forest Meteorology*, FLUXNET 2000 Synthesis 113, 223–243. [https://doi.org/10.1016/S0168-1923\(02\)00109-0](https://doi.org/10.1016/S0168-1923(02)00109-0)
- Wingler, A., Hennessy, D., 2016. Limitation of grassland productivity by low temperature and seasonality of growth, *Frontiers in Plant Science*, 7, 1130.

- World Bank, 2012. Agriculture and food. Available at <https://www.worldbank.org/en/topic/agriculture/overview>, last accessed August, 2021.
- Wu, C., Zheng, N., Gao, S., 2010. Gross primary production estimation from MODIS data with vegetation index and photosynthetically active radiation in maize *J. Geophys. Res.*, 115 (D12), 1-11
- Wutzler, T., Lucas-Moffat, A., Migliavacca, M., Knauer, J., Sickel, K., Šigut, L., Menzer, O., and Reichstein, M., 2018. Basic and extensible post-processing of eddy covariance flux data with REdyProc, *Biogeosciences*, 15, 5015–5030
- Xiao, J., Zhuang, Q., Liang, E., Shao, X., McGuire, A. D., Moody, A., Kicklighter, D. W., Melillo, J. M., 2009. Twentieth-century droughts and their impacts on terrestrial carbon cycling in China. *Earth Interact.* 13, 1–31.
- Xing, Z., Chow, L., Meng, F., Rees, H. W., Monteith, J., Lionel, S., 2008. Testing reference evapotranspiration estimation methods using evaporation pan and modeling in Maritime region of Canada. *J. Irrig. Drain. Eng. ASCE* 134, 417–424
- Xu, Y.-P., S. Pan, G. Fu, Y. Tian, and X. Zhang, 2014. Future potential evapotranspiration changes and contribution analysis in Zhejiang Province, East China, *J. Geophys. Res. Atmos.*, 118, 2174–2192
- Xue, Y., P. J. Sellers, J. L. Kinter, and J. Shukla, 1991. A simplified biosphere model for global climate studies, *Journal of Climate*, 4, 345–364.
- Yang, Y., Anderson, M. C., Gao, F., Hain, C. R., Semmens, K. A., Kustas, W. P., Noormets, A., Wynne, R. H., Thomas, V. A., Sun, G., 2017. Daily Landsat-scale evapotranspiration estimation over a forested landscape in North Carolina, USA using multi-satellite data fusion, *Hydrol. Earth Syst. Sci.*, 1017-1037.
- Yang, Y., Anderson, M.C., Gao, F., Wardlow, B., Hain, C.R., Otkin, J.A., Alfieri, J., Yang, Y., Sun, L., Dulaney, W., 2018. Field-scale mapping of evaporative stress indicators of crop yield: an application over Mead, NE, USA. *Remote Sens. Environ.* 210, 387–402.
- Yang, Y., Anderson, M.C., Gao, F., Johnson, D. M., Yang, Y., Sun, L., Dulaney, W., Hain, C. R., Otkin, J. A., Prueger, J., Meyers, T. P., Bernacchi, C. J., Moore, C. E., 2021. Phenological corrections to a field-scale, ET-based crop stress indicator: An application to yield forecasting across the U.S. Corn Belt. *Remote Sensing of Environment*, 257, 112337. <https://doi.org/10.1016/j.rse.2021.112337>
- Yu, G. R., Song, X., Wang, Q. F., Liu, Y. F., Guan, D. X., Yan, J. H., Sun, S., Zhang, L., Wen, X., 2008. Water-use efficiency of forest ecosystems in eastern China and its relations to climatic variables. *New Phytologist*, 177, 927–937
- Zaitchik, B. F., Macalady, A. K., Bonneau, L. R. and Smith, R. B., 2006. Europe’s 2003 heat wave: A satellite view of impacts and land–atmosphere feedbacks. *Int. J. Climatol.* 26, 743–769.
- Zhang, K., J.S. Kimball, R.R. Nemani, S.W. Running, 2010. A continuous satellite-derived global record of land surface evapotranspiration from 1983 to 2006, *Water Resour. Res.*, 46, W09522

- Zhang, L., Xiao, J., Li, J., Wang, K., Lei, L. and Guo, H., 2012. The 2010 spring drought reduced primary productivity in southwestern China. *Environmental research Letters*, 7, 1748-9326.
- Zhang, B., Y. Xia, B. Long, M. Hobbins, X. Zhao, C. Hain, Y. Li, M.C. Anderson, 2020. Evaluation and comparison of multiple evapotranspiration data models over the contiguous United States: Implications for the next phase of NLDAS (NLDAS-Testbed) development, *Agric. For. Meteorol.*, 280, 107810
- Zhao, W., Li, A., 2015. A review on land surface processes modelling over complex terrain, *Advances in Meteorology*, 607181, <https://doi.org/10.1155/2015/607181>.
- Zhao, J., Xu, T., Xiao, J., Liu, S., Mao, K., Song, L., Yao, Y., He, X., Feng, H., 2020. Responses of Water Use Efficiency to Drought in Southwest China. *Remote Sensing*, 12, 199
- Zheng, D., van der Velde, R., Su, Z., Wang, X., Wen, J., Booij, M. J., Chen, Y., 2015. Augmentations to the Noah model physics for application to the Yellow River source area. Part II: Turbulent heat fluxes and soil heat transport. *Journal of Hydrometeorology*, 16, 2677– 2694
- Zhu, W., Jia, S., Lv, A., 2017. A universal Ts-VI triangle method for the continuous retrieval of evaporative fraction from MODIS products. *Journal of Geophysical Research: Atmospheres*, 122, 10,206– 10,227
- Zscheischler, J., Westra, S., Hurk, B. J. J. M. van den, Seneviratne, S. I., Ward, P. J., Pitman, A., Agha Kouchak, A., Bresch, D. N., Leonard, M., Wahl, T., and Zhang, X., 2018. Future climate risk from compound events. *Nature Climate Change*, 8, 469–477.

Appendix A: Comparison of shortwave broadband albedo models

The linear regression model used to estimate shortwave broadband albedo (α) in Chapter 5 is given as:

$$\alpha = \sum_{Bi} w_{Bi} \cdot \rho_{Bi}, \quad (\text{A1})$$

where w_{Bi} is the weighting coefficients for band number Bi (Table A1) and ρ_{Bi} is the Level 2A/2B surface reflectance for band number Bi .

The Liang (2001) weighting coefficients used in Chapter 5 were derived based on Landsat reflectance data, but the corresponding Sentinel-2 bands were assigned (Table A1). The estimated α values are compared (see Figure A1) with those derived using recent Sentinel-2 based weighting coefficients (Table A1) (Li et al., 2018).

Band	w_B [-]	
	Liang (2001)	Li et al. (2018)
B1		-
B2	0.356	0.2688
B3	-	0.0362
B4	0.130	0.1501
B5		-
B6		-
B7		-
B8	0.373	-
B8a	-	0.3045
B9		-
B10		-
B11	0.085	0.1644
B12	0.072	0.0356
	-0.0018	-0.0049

Table A1. Weighting coefficient (w_B) by spectral band for estimating shortwave broadband albedo, based on Liang (2001) and Li et al. (2018).

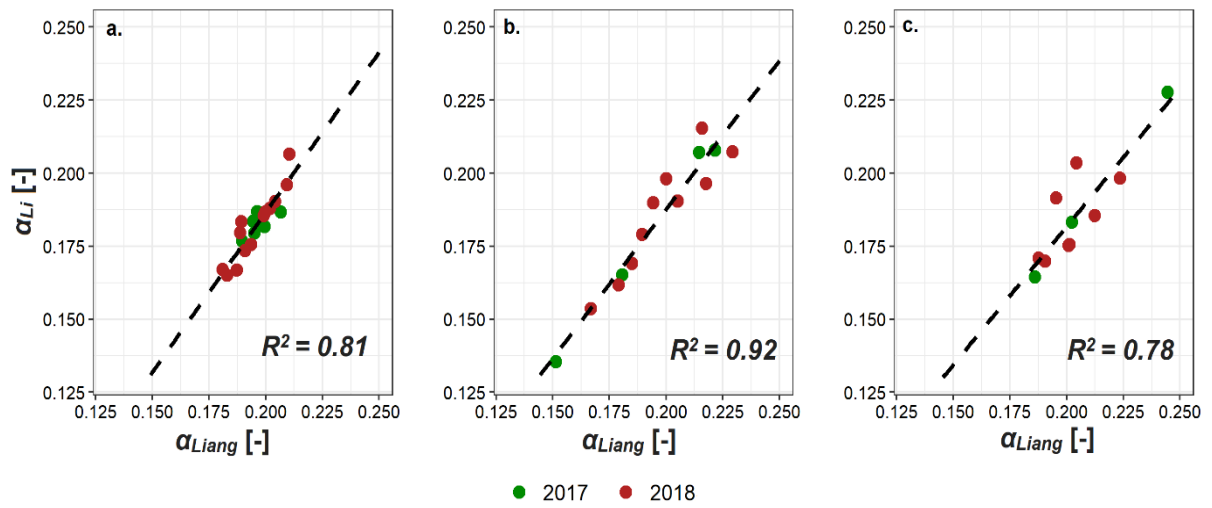


Figure A1. Comparison between Liang (2001) based shortwave broadband albedo (α_{Liang}), and Li et al. (2018) based shortwave broadband albedo (α_{Li}) using the weighting coefficients (w_B) in Table A1 for (a) Johnstown Castle, (b) Athenry and (c) Moorepark, farms over the analysis period.

Appendix B: Python script used for simulating surface fluxes

Python script used in Chapters 3-4 for estimating surface radiation and energy fluxes. The script is also available on github, <https://github.com/kazeemIshola/SURFLEX>.

```
##### Define the required libraries #####

import math

from math import e

import matplotlib.pyplot as plt

import scipy.interpolate as sci

from scipy.stats import *

from matplotlib.pyplot import *

import numpy as np

from sklearn.metrics import mean_squared_error

from math import sqrt

import pandas as pd

import datetime

import matplotlib.dates as dates

#####

##### Function to convert air temperature from celsius to kelvin #####

def Tk(tc):

    x = tc + 273.15

    return(x)

#####

##### Function to compute water vapour fractional conductance #####
```

```

def Fdq(dq):
    y = 1/(1 + 0.16*((dq) - 3))
    y = [1 if i > 1 else i for i in y]
    return(y)

#####

##### Function to compute radiation fraction #####

def Fs(S):
    z = (770*S)/(1000*S + 230*(1000 - 2*S))
    return(z)

#####

##### Function to compute soil moisture response #####

def Fm(sm):
    u = [0.1 if i < 0.1 else i for i in sm]
    u = np.array([1 + 4.3*(i - 0.3) if i < 0.3 else 1 for i in u])
    return(u)

#####

#omit error values #####

np.seterr(divide='ignore', invalid='ignore')

#####

##### Function for the first loop i.e for neutral condition. #####

def it_1(ws,t24h,tc,P,S,rh):
    psc = (1005*P*462)/(287*2450000) #(0.001005*P)/(0.622*2.45)
    eslope = 4098*((0.6108*np.exp((17.27*tc)/(tc+237.3)))/(tc+237.3)**2)
    ustar=(ws*k)/(math.log(10/zom,math.e))

```

```

ra=(math.log(z/zoh,math.e)/(k*ustar))

#rc=(10**4)*((es-ea)/P)*rd_rv          ###dRH99

#rc=70                                  ###FAO

rc=25.9/(Fdq(dq)*Fs(S)*Fm(sm))        ###BB97

K=(1-a)*S

er=1.2*((ea*10)/Tk(tc))**0.143

Lin = (er*stef*Tk(tc)**4 ) #+ 60*N

R= (eslope+(psyc*(1+(rc/ra))))

A = ((eslope+psyc)*R)-(eslope*(eslope+psyc))

B = -1*(eslope+psyc)

C = (eslope+psyc)*R

D=K+Lin+(3*0.94*stef*Tk(tc)**4)+(Ag*t24h)-((4*0.94*stef*Tk(tc)**3)+Ag)*(Tk(tc)+adiab*2)

E = ((4*0.94*stef*Tk(tc)**3)+Ag)*(ra/den_cp)

H = (A*D+B)/(C+A*E)

tvs=(-1*H)/(den_cp*ustar)

L=(Tk(tc)*ustar**2)/(k*9.8*tvs)

return(ra,H,L)

#####

#### Function for the second loop i.e for stability correction. #####

def it_2(ws,t24h,tc,P,S,rh,H,L):

    psyc = (1005*P*462)/(287*2450000)

    eslope = 4098*((0.6108*np.exp((17.27*tc)/(tc+237.3)))/(tc+237.3)**2)

    stab_u=[(2*np.log((1+((1-(16*(z/i)))**0.25))/2))+(np.log((1+((1-(16*(z/i)))**0.25)**2)/2))-
    (2*np.arctan((1-(16*(z/i)))**0.25))+(np.pi/2) if i < 0 else -5*(z/i) for i in L]

    stab_t=[2*np.log((1+((1-(16*(zoh/i)))**0.25)**2)/2) if i < 0 else -5*(zoh/i) for i in L]

```

```

ustar_new=(ws*k)/(math.log(10/zom,math.e)-(stab_u*(10/L))+(stab_u*(zom/L)))
ra=(1/(ustar_new*k))*(math.log(z/zoh,math.e)-(stab_t*(z/L))+(stab_t*(zoh/L)))
ra = np.array([1000 if i > 1000 else i for i in ra])

#rc=(10**4)*((es-ea)/P)*rd_rv          ##dRH99
#rc=70                                ###FAO
rc=25.9/(Fdq(dq)*Fs(S)*Fm(sm))        ###BB97

K=(1-a)*S
er=1.2*((ea*10)/Tk(tc))**0.143
Lin = (er*stef*Tk(tc)**4) #+ 60*N
R= (eslope+(psyc*(1+(rc/ra))))
A = ((eslope+psyc)*R)-(eslope*(eslope+psyc))
B = -1*(eslope+psyc)
C = (eslope+psyc)*R
D=K+Lin+(3*0.94*stef*Tk(tc)**4)+(Ag*t24h)-((4*0.94*stef*Tk(tc)**3)+Ag)*(Tk(tc)+adiab*2)
E = ((4*0.94*stef*Tk(tc)**3)+Ag)*(ra/den_cp)
H = (A*D+B)/(C+A*E)
tvs=(-1*H)/(den_cp*ustar_new)
L=(Tk(tc)*ustar_new**2)/(k*9.8*tvs)
return(ra,H,L,ustar_new,Lin)

#####

##### import input data in csv format (.csv) from the local directory #####

data=pd.read_csv("C:/Users/...../test.csv")

data = data.convert_objects(convert_numeric=True)

#####

##### define the input and validation variables in the data #####

```

```

date=data.iloc[:, 0]      #date
S=data.iloc[:, 1]        #global solar radiation (W m-2)
tc=data.iloc[:, 2]       #near-surface temperature at observation height (2 m) (°C)
P=data.iloc[:, 3]        # msl pressure (kPa)
rh=data.iloc[:, 4]       # Relative humidity (%)
ws=data.iloc[:, 5]       # Wind speed (m s-1)
t24h=data.iloc[:, 6]     # mean air temperature in the last 24hr (24hr moving average) (°K)
sm=data.iloc[:, 7]       # Measured soil moisture content at top 20 cm (m3 m-3)
Rn_obs=data.iloc[:, 8]   # Measured total radiative flux (W m-2)
H_obs=data.iloc[:, 9]    # Measured Sensible heat flux (W m-2)
Le_obs=data.iloc[:, 10]  # Measure Latent heat flux (W m-2)

#####

##### define initial coefficients #####

a=0.23                    ##surface albedo for grass
z=2                       ##observation height (m)
zom=0.01                  ## surface roughness length for momentum (m)
zoh=0.1*zom              ## surface roughness length for heat (m)
k=0.41                    ## von Karma constant
Ag=9                      ## soil heat flux coefficient (W m-2 K-1)
adiab=0.01                ##dry adiabatic lapse rate (K m-1)
den=1.225                 ## density of dry air (kg m-3)
cp=1005                   ##specific heat capacity of dry air (J kg-1 K-1)
den_cp=den*cp
Lv=2450000                ## latent heat of vaporization (J kg-1)
rd=287                    ## specific gas constant for dry air (J kg-1 K-1)

```

```

rv=462          ## specific gas constant for vapour (J kg-1 K-1)

rd_rv=rd/rv

stef=5.67*10**-8  ## stefan boltzmann's constant (W m-2 K-1)

#####

###Compute moisture deficit #####

es = 0.6108*(np.exp((17.27*tc)/(tc+237.3)))      ###saturated vapour pressure (kPa)

ea = rh/100 * es                                #####actual vapour pressure (kPa)

dq = (621.9907*es/(P-es)) - (621.9907*ea/(P-ea))  ###moisture deficit (kPa)

#VPD = es-ea

#####

#### iteration 1 loop setup #####

loop_setup=it_1(ws,t24h,tc,P,S,rh)

#####

#### iteration2: loop action #####

loop_action=it_2(ws,t24h,tc,P,S,rh,loop_setup[2],loop_setup[1])

loop_action_2=it_2(ws,t24h,tc,P,S,rh,loop_action[2],loop_action[1])

loop_action_3=it_2(ws,t24h,tc,P,S,rh,loop_action_2[2],loop_action_2[1])

loop_action_4=it_2(ws,t24h,tc,P,S,rh,loop_action_3[2],loop_action_3[1])

loop_action_5=it_2(ws,t24h,tc,P,S,rh,loop_action_4[2],loop_action_4[1])

loop_action_6=it_2(ws,t24h,tc,P,S,rh,loop_action_5[2],loop_action_5[1])

#####

#### define output objects #####

L=loop_action_6[2]      # Obukhov length (m)

H=loop_action_6[1]     # estimated Sensible heat flux (W m-2)

ra=loop_action_6[0]    # estimated aerodynamic resistance (s m-1)

```

```

ustar=loop_action_6[3]      # estimated friction velocity (m s-1)
Lin=loop_action_6[4]      # estimated longwave radiation downward (W m-2)

#####

##### Compute fluxes #####

eslope = 4098*((0.6108*np.exp((17.27*tc)/(tc+237.3)))/(tc+237.3)**2)

er=1.2*((ea*10)/Tk(tc))**0.143      # apparent atmospheric emissivity
psyc =(1005*P*462)/(287*2450000)    # psychrometric constant (kPa K-1)
K=(1-a)*S      # net shortwave radiation (W m-2)
ts=(Tk(tc)+((H*ra)/den_cp)+(z*0.01)) # Land surface temperature (°K)
Lou=(0.94*stef*ts**4) + (1-0.94)*Lin # longwave radiation upward (W m-2)
Go = Ag*(ts-t24h)      # Soil heat flux (W m-2)

Rn = (K + (er-1)*(er*stef*Tk(tc)**4)) - (0.94*stef*4*Tk(tc)**3*(ts-Tk(tc))) # estimated net
radiative flux (W m-2)

#####

##### Compute latent heat flux with different parameterizations of rc #####

#rc= (10**4)*((es-ea)/P)*rd_rv      ### dRH99 (de Rooy and Holtslag, 1999)
#rc=70      ### FAO (Allen et al., 1998)
rc=25.9/(Fdq(dq)*Fs(S)*Fm(sm))      ### BB97 (Beljaars and Bosveld, 1997)

Le = (eslope*(Rn - Go) + ((den_cp*(es-ea))/ra)) / (eslope + psyc*(1 + rc/ra)) ## PM approach
#Le = Rn - Go - H      ##### Balance method

#####

##### export data in csv format to local directory #####

my_data=np.vstack((date,Rn, H, Le, Go, rc,ts))

my_data=my_data.T

df= pd.DataFrame(my_data)

```

```

colnames=['date','Rn','H','Le','G','rc','ts']
df.to_csv('C:/Users/...../flux_test.csv',
          index=False, header=colnames)          # write output to csv

#####

#####

##### Sample RMSE and bias calculation for Le #####

mask = ~np.isnan(Le_obs) & ~np.isnan(Le)

rms = sqrt(mean_squared_error(Le_obs[mask], Le[mask]))

bias = sum(Le[mask] - Le_obs[mask])/8760

#####

##### Sample scatterplots between measured and estimated Le #####

slope, intercept, r_value, p_value, std_err = stats.linregress(Le_obs[mask], Le[mask])

print(r_value,slope,intercept,p_value)

fig = plt.figure()

ax = fig.add_subplot(111)

plt.plot(Le_obs,Le, '.',c="black",label="BB97")

plt.plot(Le_obs, slope*Le_obs + intercept, '-',c="r",label="r = 0.82")

#label axes

xlabel("Measured QE (W m^-2)")

ylabel("Estimated QE (W m^-2)")

ax.text(0.1, 0.9,',', horizontalalignment='center',
        verticalalignment='center',
        transform=ax.transAxes)

plt.legend()

plt.show()

```

```
fig.savefig('C:/Users/...../Le.png',dpi=600,transparent=True)
```

```
#####
```

Appendix C: R script used for estimating terrestrial evapotranspiration, gross primary productivity and water use efficiency at Sentinel-2 scale

R script used in Chapter 5 for estimating evapotranspiration, gross primary productivity and water use efficiency based on integrated land surface scheme, light use efficiency scheme, and Sentinel-2 data

```
##### Define the required libraries #####

library(raster)

library(rgdal)

#####

##### import input meteorological data, and surface parameters : Sentinel-2 derived surface
##### albedo, LAI and NDVI

albedo <- brick("C:/Users/17252302/Downloads/Sentinel2/Moorepark/Albedo_all.tif")

LAI <- brick("C:/Users/17252302/Downloads/Sentinel2/Moorepark/LAI_all.tif")

NDVI <- brick("C:/Users/17252302/Downloads/Sentinel2/Moorepark/NDVI_all.tif")

df <- read.table(file.choose(), header=T, sep=',', fill = T)

#####

##### Retain only pixels with vegetation cover for surface parameters #####

cld_mask = brick("C:/Users/17252302/Downloads/Sentinel2/Moorepark/Cloud_mask.tif")

cld_mask[cld_mask!=4] <- NA ##### mask only for vegetation

albedo = mask(albedo, cld_mask)

LAI = mask(LAI, cld_mask)

NDVI= mask(NDVI, cld_mask)

#####

##### Function for conditional statement for raster layers #####

rastercon=function(condition, trueValue,falseValue){
```

```

return (condition*trueValue+(!condition)*falseValue)
}

#####

##### Surfex function for estimating surface fluxes #####

Surfex <- function(S, Ta, pp, RH, u, sT, sm, albedo, LAI, NDVI, DEM, iter.max = 20, t1=1, Rg_24, ETref,
model= "SURFLEX")

{
  if(!class(albedo) == "RasterLayer") stop( "albedo is not a raster object")

  if(!class(LAI) == "RasterLayer") stop( "LAI is not a raster object")

  if(!class(NDVI) == "RasterLayer") stop( "NDVI is not a raster object")

  #####

##### Define the required coefficients #####

z=2          ### observation height

k=0.4        ### von Karma constant

Ag=9         ### soil heat flux coefficient

adiab=0.01

den = (1000*pp)/(1.0*((Ta)*287)) #####Ta in degree kelvin

cp=1005

den_cp=den*cp

Lv= 1000000*((2.495-(0.00236*(Ta-273.15))))

rd=287

rv=462

rd_rv=rd/rv

stef=5.67E-08

Tac=Ta-273.15

es=0.6108*exp(((17.27*(Ta-273.15))/((Ta-273.15)+237.3)))

ea=RH/100*es

dq=(621.9907*es/(pp-es)) - (621.9907*ea/(pp-ea))

```

```

psyc=(cp*pp*rv)/(rd*Lv)
eslope=(4098*(0.6108*exp((17.27*Tac)/(Tac+237.3)))/(Tac+237.3))^2
#####
##### surface roughness parameters #####
print(paste("Computing surface momentum and thermal roughness lengths"))
zom = 0.123 * (LAI/24)
zoh = 0.1 * zom
#####
##### surface and atmospheric emissivity #####
print(paste("Computing surface and atmospheric emissivities"))
er=1.2*((ea*10)/Ta)^0.143
e0=rastercon(NDVI<0 & albedo<0.47, 0.985, rastercon(LAI>=3, 0.98, 0.95+(LAI*0.01)))
#####
##### soil moisture stress function parameters #####
print(paste("Computing environmental stress functions"))
Fdq = rastercon((1/(1+0.16*(dq-3)))>1,1,1/(1+0.16*(dq-3)))
Fs=(770*S)/(1000*S+230*(1000-2*S))
Fm = rastercon(sm<0.3,1+4.3*(sm-0.3), rastercon(1+4.3*(sm-0.3)<0,0,1))
#####
##### Compute the first guess for friction velocity and Obukhov length #####
print(paste("Computing u_star, ra, H and L for neutral condition "))
u200=u*(log(200/2)/log(10/2))
ustar=(u200*k)/(log(200/zom))
ra=(log(z/zoh)/(k*ustar))
ra= rastercon(ra >1000,1000,ra)
rc=(0.47 * 110/LAI)/(Fdq*Fs*Fm)
K=(1-albedo)*S

```

```

Lin = (er*stef*Ta^4) #+ 60*N
R= (eslope+(psyc*(1+(rc/ra))))
A = ((eslope+psyc)*R)-(eslope*(eslope+psyc))
B = -1*(eslope+psyc)
C = (eslope+psyc)*R
D = K+Lin+(3*e0*stef*Ta^4)+(Ag*sT)-((4*e0*stef*Ta^3)+Ag)*(Ta+adiab*2)
E = ((4*e0*stef*Ta^3)+Ag)*(ra/den_cp)
H = (A*D+B)/(C+A*E)
tvs=(-1*H)/(den_cp*ustar)
L=(Ta*ustar^2)/(k*9.8*tvs)
#####
##### Correct for atmospheric stability in an iterative process #####
print(paste("Computing u_star, ra, H and L with stability correction"))
i=1
while (i<=iter.max)
{
  print(paste("Monin-Obukhov length iteration",i,"of",iter.max))
  x_bus200=(1-(16*(200/L)))^0.25
  x_bus01=(1-(16*(zoh/L)))^0.25
  x_bus=(1-(16*(2/L)))^0.25
  stab_u200=rastercon(L<0,(2*log((1+x_bus200)/2)))+(log((1+x_bus200^2)/2))-
(2*atan(x_bus200))/(pi/2),rastercon(L>0,-5*(200/L),0))
  stab_t01=rastercon(L<0,2*log((1+x_bus01^2)/2),rastercon(L>0,-5*(zoh/L),0))
  stab_t=rastercon(L<0,2*log((1+x_bus^2)/2),rastercon(L>0,-5*(2/L),0))
  ustar_new = (u200*k)/(log(200/zom)-stab_u200)
  ra=(1/(ustar_new*k))*(log(z/zoh) - stab_t + stab_t01)
  ra= rastercon(ra >1000,1000,ra)
  rc=(0.47 * 110/LAI)/(Fdq*Fs*Fm)

```

```

K=(1-albedo)*S
er=1.2*((ea*10)/Ta)^0.143
Lin = (er*stef*Ta^4) #+ 60*N
R= (eslope+(psyc*(1+(rc/ra))))
A = ((eslope+psyc)*R)-(eslope*(eslope+psyc))
B = -1*(eslope+psyc)
C = (eslope+psyc)*R
D = K+Lin+(3*e0*stef*Ta^4)+(Ag*sT)-((4*e0*stef*Ta^3)+Ag)*(Ta+adiab*2)
E = ((4*e0*stef*Ta^3)+Ag)*(ra/den_cp)
H = (A*D+B)/(C+A*E)
tvs=(-1*H)/(den_cp*ustar_new)
L=(Ta*ustar_new^2)/(k*9.8*tvs)
i=i+1
}

#####

##### compute outputs #####

print(paste("Computing the final outputs"))

Ts=(Ta+((H*ra)/den_cp)+(DEM*0.01))

Lou=(e0*stef*Ts^4) + (1-e0)*Lin

Go = Ag*(Ts-sT)

Rn = (K + (er-1)*(er*stef*Ta^4)) - (e0*stef*4*Ta^3*(Ts-Ta))

#G= Rn*((Ts-273.15)*(0.0038+0.0074*albedo)*(1-0.98*NDVI^4))

#Go = rastercon(LAI < 0.5, (Rn*(1.8*(Ts-273.15)/Rn) + 0.084), Rn*(0.05 +(0.18*exp(-0.521*LAI))))

Le = (eslope*(Rn - Go) + ((den_cp*(es-ea))/ra)) / (eslope + psyc*(1 + rc/ra))

#Le = Rn-H-Go

ETint = (t1*3600*Le)/Lv ##### instantaneous ET

```

```

EF= Le/(Rn-Go)

Rn_24 <- ((1-albedo)*(Rg_24) - (110*(0.75+0.00002*DEM)))

#ET_24 <- (86400000*1*EF*Rn_24)/(1000*Lv)

ET_24 <- (86400000*1*Le*Rg_24)/(S*1000*Lv) ##### 24-hr ET

ESI = ET_24/ETref

Factor = list(EF=EF, ET_24=ET_24, ra = ra, rc = rc, Rn=Rn, H=H, Go=Go, Le=Le, ETins = ETint,
              Ts = Ts, Lou = Lou, Lin = Lin)

factor$call<-match.call()

class(factor)<-model

factor

}

#####

##### Run the Surfex model and write the outputs in specified folders #####

for (i in 1:12){

  m <- Surfex(S=df[i,2], Ta=df[i,4], pp=df[i,5], RH=df[i,6], u=df[i,7], sT=df[i,8], sm=df[i,9],

              ETref = df[i,10], Rg_24 = df[i,13],DEM=df[1,14],albedo[[i]],LAI[[i]],NDVI[[i]],

              iter.max=20, t1=1, model="SURFLEX")

  writeRaster(m$Rn,filename = paste0("C:/Users/17252302/Downloads/Sentinel2/OP-
  JC/JC/output/Rn/", "Rn_",stringr::str_pad(string = i,width = 4,side = "left",pad=0)), format ="GTiff",
  overwrite=T)

  writeRaster(m$H,filename = paste0("C:/Users/17252302/Downloads/Sentinel2/OP-
  JC/JC/output/H/", "H_",stringr::str_pad(string = i,width = 4,side = "left",pad=0)), format ="GTiff",
  overwrite=T)

  writeRaster(m$Le,filename = paste0("C:/Users/17252302/Downloads/Sentinel2/OP-
  JC/JC/output/Le/", "LE_",stringr::str_pad(string = i,width = 4,side = "left",pad=0)), format ="GTiff",
  overwrite=T)

  writeRaster(m$Go,filename = paste0("C:/Users/17252302/Downloads/Sentinel2/OP-
  JC/JC/output/G/", "G_",stringr::str_pad(string = i,width = 4,side = "left",pad=0)), format ="GTiff",
  overwrite=T)

  writeRaster(m$ETins,filename = paste0("C:/Users/17252302/Downloads/Sentinel2/OP-
  JC/JC/output/ETins/", "ETins_",stringr::str_pad(string = i,width = 4,side = "left",pad=0)), format
  ="GTiff", overwrite=T)

```

```
writeRaster(m$ET_24,filename = paste0("C:/Users/17252302/Downloads/Sentinel2/OP-
JC/JC/output/ET_24/", "ET24_",stringr::str_pad(string = i,width = 4,side = "left",pad=0)), format
="GTiff", overwrite=T)
```

```
writeRaster(m$Ts,filename = paste0("C:/Users/17252302/Downloads/Sentinel2/OP-
JC/JC/output/Ts/", "Ts_",stringr::str_pad(string = i,width = 4,side = "left",pad=0)), format ="GTiff",
overwrite=T)
```

```
writeRaster(m$ESI,filename = paste0("C:/Users/17252302/Downloads/Sentinel2/OP-
JC/JC/output/ESI/", "ESI_",stringr::str_pad(string = i,width = 4,side = "left",pad=0)), format ="GTiff",
overwrite=T)
```

```
writeRaster(m$EF,filename = paste0("C:/Users/17252302/Downloads/Sentinel2/OP-
JC/JC/output/EF/", "EF_",stringr::str_pad(string = i,width = 4,side = "left",pad=0)), format ="GTiff",
overwrite=T)
```

```
}
```

```
#####
```

```
### Estimate GPP and Water use efficiency #####
```

```
VPD_sc=list(); T_sc=list(); GPP=list(); es=list(); ea=list(); VPD=list()
```

```
K=list(); par=list(); GPP=list(); lue=list()
```

```
ET = list.files("C:/Users/17252302/Downloads/Sentinel2/OP-JC/JC/output/ET_24/",pattern="tif",
full.names=T) #### load in ET raster layers
```

```
fpar = list.files("C:/Users/17252302/Downloads/Sentinel2/.....",pattern="tif",
full.names=T) #### load in FAPAR raster layers
```

```
nirv = list.files("C:/Users/17252302/Downloads/Sentinel2/.....",pattern="tif", full.names=T)
#### load in NIRv raster layers
```

```
ET= stack(ET)
```

```
fpar= stack(fpar)
```

```
nirv= stack(nirv)
```

```
s = stack(fpar, nirv)
```

```
for (i in 1:20) {
```

```
  #Using a simplified NIRv-based approach for GPP estimation Jian et al.(2020)
```

```
  fun=function(x) { if (is.na(x[1])){ NA } else { lm(x[1:20] ~ x[21:40])$coefficients[2] }}
```

```
  a <- calc(s, fun) # a is slope and s is the raster stack of both variables
```

```
  fun=function(x) { if (is.na(x[1])){ NA } else { lm(x[1:20] ~ x[21:40])$coefficients[1] }}
```

```
  b <- calc(s, fun) # b is the intercept
```

```

K[[i]] = df[i,12] #incoming shortwave radiation

par[[i]] = 0.45 * K[[i]]

GPP[[i]] = par[[i]] * (a*nirv[[i]]+b)

#####

# Using LUE scheme Running and Zhao (2015)

# es[i] =(0.6108*exp((17.27*df[i,5])/(df[i,5]+237.3)))*1000

# ea[i] =df[i,6]/100*es[[i]]

# VPD[i] = es[[i]]-ea[[i]]

# VPDmx = 5300; VPDmn=650; Tmx=12.02; Tmn=-8.0; luemx=0.000860*1000 ### Running and
##Zhao (2015) BLUPT for grass

#VPD_sc[i] = min((VPDmx - VPD[[i]])/(VPDmx - VPDmn),1)

#T_sc[i] = min((df[i,3] - Tmn)/(Tmx - Tmn),1)

#lue[i] = luemx * VPD_sc[[i]] * T_sc[[i]]

#K[[i]] = df[i,12]

#par[[i]] = 0.45 * K[[i]]

#GPP[[i]] = lue[[i]] * par[[i]] * fpar[[i]]

}

GPP=stack(GPP)

WUE = GPP/ET

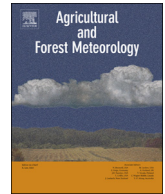
writeRaster(GPP, "C:/Users/17252302/...../GPP", "GTiff", overwrite=T)

writeRaster(WUE, "C:/Users/17252302/...../WUE", "GTiff", overwrite=T)

#####

```

Supplementary Information



Improving a land surface scheme for estimating sensible and latent heat fluxes above grasslands with contrasting soil moisture zones

Kazeem A. Ishola^{a,b,d,*}, Gerald Mills^c, Reamonn M. Fealy^d, Órlaith Ní Chonchubhair^e, Rowan Fealy^{a,b}

^a Irish Climate Analysis and Research Units (ICARUS), Maynooth University, Ireland

^b Department of Geography, Maynooth University, Co. Kildare, Ireland

^c School of Geography, University College Dublin, Co. Dublin, Ireland

^d Teagasc Agrifood Business and Spatial Analysis Department, Ashtown, Co. Dublin, Ireland

^e Teagasc Environmental Research Centre, Johnstown Castle, Co. Wexford, Ireland

ARTICLE INFO

Keywords:

Surface resistance
Surface-atmosphere exchange
Surface-layer schemes
Agriculture

ABSTRACT

Knowledge of soil–vegetation–atmosphere energy exchange processes is essential for examining the response of agriculture to changes in climate in both the short and long term. However, there are relatively few sites where all the flux measurements necessary for evaluating these responses are available; where they exist, data are often incomplete and/or of limited duration. At the same time, there is often an extensive observation network available that has gathered key meteorological data (sunshine, wind, rainfall, etc.) over decades. Simulating the terms of the surface energy balance (SEB) using available meteorological, soil and vegetation data can improve our understanding of how agricultural systems respond to climate and how this response will vary spatially. Here, we employ a physically-based scheme to simulate the SEB fluxes over a mid-latitude, maritime temperate environment using routine weather observations. The latent heat flux is a critical SEB term as it incorporates the response of the plant to environmental conditions including available energy and soil water. This response is represented in modeling schemes through surface resistance (r_s), which is usually expressed as a function of near-surface water vapor alone. In this study, we simulate the SEB over two grassland sites, where eddy flux observations are available, representing imperfectly- and poorly- drained soils. We employ three different formulations of r_s , representing varying degrees of sophistication, to estimate the surface fluxes. Due to differences in soil moisture characteristics between the sites, we ultimately focused our attention on an r_s formulation that accounted for soil water retention capacity, based on the Jarvis conductance model; the results at both hourly and daily intervals are in good agreement, with RMSE values of $\approx 40 \text{ W m}^{-2}$ for sensible and latent heat fluxes at both sites. The findings show the potential value of using routine weather observations to generate the SEB where flux observations are not available and the importance of soil properties in estimating surface fluxes. These findings could contribute to the assessment of past and future climate change on grassland ecosystems.

1. Introduction

Information on the exchange of heat and moisture at the Earth's surface is needed to evaluate the performance of climate models in simulating land-atmosphere interactions (e.g. Knist et al., 2017) and for applications in a number of areas, such as agricultural productivity, soil moisture and hydrology, boundary-layer development, etc. (de Bruin et al., 1993; van den Hurk et al., 2000; Chen and Dudhia, 2001; Jung et al., 2010; Lathuilliere et al., 2012; van de Boer et al., 2013, 2014b). Typically, these exchanges are expressed in terms of the surface energy balance (SEB, see Appendix 1) which stipulates that net

radiation (Q_N) is expended as sensible heat flux by conduction with the soil (Q_G) and as sensible (Q_H) and latent (Q_E) heat fluxes by turbulence with the overlying atmosphere. However, measurements of these flux densities are not routine practice, partly due to the complexity of turbulence measurement and the relative cost of instrumentation (Haymann et al., 2019). To overcome this challenge, past and recent studies have developed physically-based schemes to simulate these exchanges based on routine meteorological observations (de Bruin and Holtslag, 1982; Holtslag and van Ulden, 1983; Holtslag and de Bruin, 1988; Viterbo and Beljaars, 1995; Chen et al., 1996; Beljaars and Bosveld, 1997; Mohan and Siddiqui, 1998; de Rooy and Holtslag, 1999;

* Corresponding author at: Irish Climate Analysis and Research Units (ICARUS), Maynooth University, Ireland.

E-mail address: kazeem.ishola.2018@mumail.ie (K.A. Ishola).

Nomenclature

A_g	soil heat transfer coefficient ($\text{W m}^{-2} \text{K}^{-1}$)	r_a	aerodynamic resistance (s m^{-1})
c_p	specific heat capacity of air ($\text{J kg}^{-1} \text{K}^{-1}$)	r_s	the surface resistance (s m^{-1})
c_{soil}	soil moisture coefficient ($\text{m}^3 \text{m}^{-3}$).	$r_{s, min}$	minimum stomatal resistance (s m^{-1})
e	vapor pressure (kPa)	s	slope of saturated vapor pressure curves (kPa K^{-1})
F_M	soil moisture stress function	S_r	global radiation coefficient (W m^{-2})
F_S	solar radiation stress function	T_a	air temperature at z_a (K)
$F_{\Delta q}$	air moisture deficit function	T_s	surface temperature (K)
F_T	near-surface temperature function	T_{24}	24-h moving average of T_a (K)
f_r	an empirical site-specific constant	u	wind speed at 10 m (m s^{-1})
g	acceleration due to gravity (m s^{-2})	u_*	friction velocity (m s^{-1})
h_s	moisture deficit coefficient (kg kg^{-1})	z_a	observation height, 2 m.
k	von Kàrmàn constant	z_{oH}	surface roughness length for heat (m)
L	Obukhov length (m)	z_{om}	surface roughness length for momentum (m)
LAI	leaf area index ($\text{m}^2 \text{m}^{-2}$)	α	surface albedo
N	cloud amount (oktas)	γ	psychrometric constant (kPa K^{-1})
P	mean sea level pressure (kPa)	Γ_d	dry adiabatic lapse rate (K m^{-1})
Q_E	latent heat flux (W m^{-2})	Δq_a	specific humidity deficit at z_a (kg kg^{-1}).
Q_G	soil heat flux (W m^{-2})	Δq_s	specific humidity deficit at the surface (kg kg^{-1})
Q_H	sensible heat flux (W m^{-2})	ε	surface emissivity
Q_N	net radiation (W m^{-2})	ε_a	atmospheric emissivity
$Q_{L\downarrow}$	incoming longwave radiation (W m^{-2})	θ	volumetric soil moisture in the root zone ($\text{m}^3 \text{m}^{-3}$)
$Q_{L\uparrow}$	outgoing longwave radiation (W m^{-2})	θ_{CT}	critical soil moisture ($\text{m}^3 \text{m}^{-3}$)
$Q_{S\downarrow}$	global solar radiation (W m^{-2})	θ_{FC}	field capacity ($\text{m}^3 \text{m}^{-3}$)
$Q_{S\uparrow}$	outgoing shortwave radiation (W m^{-2})	θ_{ST}	saturation point ($\text{m}^3 \text{m}^{-3}$)
$Q_{\Delta S}$	soil heat storage (W m^{-2})	θ_{WP}	wilting point ($\text{m}^3 \text{m}^{-3}$)
RH	relative humidity (%)	θ_*	temperature scale (K)
R_d	specific gas constant for dry air ($\text{J kg}^{-1} \text{K}^{-1}$)	ρ	density of dry air (kg m^{-3})
R_v	specific gas constant for water vapor ($\text{J kg}^{-1} \text{K}^{-1}$)	σ	stefan Boltzmann's constant ($\text{W m}^{-2} \text{K}^{-1}$)
		ψ_H	dimensionless stability term for heat
		ψ_M	dimensionless stability term for momentum

van de Boer et al., 2014a; Lu et al., 2014). Although the choice of scheme is dependent on the availability of input meteorological parameters, the analytic context is usually based on the Monin–Obukhov Similarity Theory (MOST), which uses vertical profiles of air temperature, humidity and wind to simulate the fluxes of heat, vapor and momentum, respectively, within the atmospheric surface layer (Appendix 1). However, issues remain with these schemes. For example, Chen et al. (1997) found large discrepancies between schemes that have been partly attributed to the dependence on empirical constants derived from site specific data.

de Rooy and Holtslag (1999) proposed and evaluated a scheme for estimating SEB fluxes using a minimal number of input parameters derived from single-level routine weather observations. The methodology was developed based on observations made over short grass in Cabauw, the Netherlands, and has not been evaluated elsewhere. More recently, van de Boer et al. (2014a) proposed a modified version of this scheme which was evaluated at two locations over different land cover types. This modified scheme accounts for the dependency of each flux on air, rather than surface, temperature as in de Rooy and Holtslag (1999). In addition, it employs a modified formulation for surface resistance (r_s) a key parameter in the estimation of Q_E as it accounts for soil moisture content and the transfer of soil water to the atmosphere by evapotranspiration. There are different methods of parameterizing r_s (Kim and Verma, 1991; Jacobs, 1994) but one of the most widely used is that of Jarvis (1976), which incorporates environmental controls, including atmospheric (radiation, temperature, vapor pressure deficit, CO_2 concentration), vegetation (Leaf Area Index) and soil (soil water) factors (e.g. Stewart, 1988; Beljaars and Bosveld, 1997; Niyogi and Raman, 1997; de Rooy and Holtslag, 1999; van de Boer et al., 2014a). Where it is assumed that there is no moisture stress, the dependence of r_s on soil water content has either been excluded (van de Boer et al., 2014a) or assumed to be negligible (de Rooy and Holtslag, 1999). However, under conditions of increasing soil

moisture stress, water availability acts to regulate r_s (Russell, 1980; Sherratt and Wheeler, 1984) and consequently plays a prominent role in modulating heat and moisture fluxes (Sherratt and Wheeler, 1984; Betts and Ball, 1995; 1998; Senevirante et al., 2010). Increased r_s due to limited water availability affects evapotranspiration and is a major factor controlling the productivity of terrestrial ecosystems (Ciais et al., 2005; De Boeck et al., 2011; Reichstein et al., 2007; Teuling et al., 2006; Zhang et al., 2012). The parameterization of r_s has also been identified as playing a significant role in contributing to model uncertainties in estimating Q_E and gross primary production (GPP) in land surface models (Li et al., 2016).

In this study we examine the influence of available soil moisture on the simulation of energy fluxes using the de Rooy and Holtslag (1999) scheme. We identify two grassland sites in Ireland that have the same precipitation regime but are distinguished by their soil characteristics and are defined as imperfectly- and poorly- drained soils. Our primary objectives are to; (1) examine whether the de Rooy and Holtslag (1999) scheme is transferrable to Irish sites; (2) evaluate if meteorological data from one location can be employed to estimate the measured surface fluxes at a nearby location and; (3) evaluate the response of surface fluxes to three different parameterizations of surface resistance (r_s).

The study seeks to extend the value of flux estimates to places where such observations are not available and contribute to the improvement and applicability of land surface schemes over grassland ecosystems.

2. Data and methods

2.1. Background climate

The climate of Ireland is dominated by westerly airflow off the North Atlantic and consequently exhibits a maritime temperate climate (Peel et al., 2007). Based on the long term averages over the period from 1981 to 2010, Ireland typically experiences cool summers with

daily maximum ranging from 18 to 20 °C and mild winters (8 °C); minimum temperatures fall below 0 °C on approximately 40 (10) days per year at inland (coastal) areas. Annual average rainfall is just over 1200 mm, which is distributed nearly evenly throughout the year. The highest rainfall is typically recorded in upland regions on the west coast. Rainfall amounts decline moving eastwards, associated with airflow interactions with topography. However, topographic variations across the island are relatively small – the average elevation is 118 m a.s.l. and the highest peak is just over 1000 m a.s.l. A summary description of the climatology of the region is reported in Walsh (2012).

The climate in Ireland provides conditions suitable for the year-round grass growth, particularly along coastal margins in the south of the country which records a median grass growing season length of 330 days (Keane and Collins, 2004). Consequently, grassland land-cover is the most important crop and accounts for more than 90% of the land under agricultural production (McEniry et al., 2013) and 56% of the total land area (EUROSTAT, 2015). Due to the year-round precipitation, excessive soil moisture is generally more problematic for grass production than water deficits (McDonnell et al., 2018), particularly on poorly drained soils. However, soil moisture deficits are periodically experienced during the summer months, typically in the east and south east of the country (Dwyer and Walsh, 2012), associated with the

location of well drained soils (Fig. 1). In terms of soil characteristics, the General Soil Map of Ireland classifies the south-east as mostly free-draining sandy soils, with limestone-rich soils in the south and midlands, and acid and peat soils on mountains, hills and the western seaboard (Gardiner and Radford, 1980). More detailed soil properties combining previous and existing soil survey information for Ireland is available from Creamer et al. (2014).

2.2. Site descriptions

Two sites are employed in this study representing imperfectly drained (Johnstown Castle, Co. Wexford) and poorly drained (Dripsey, Co. Cork) soil characteristics; Table 1 provides summary information on each site and Fig. 1 shows the site locations. Both sites have available eddy covariance (EC) flux tower measurements.

Details on the vegetation and soil characteristics associated with the flux tower footprints are as follows:

- i) Johnstown Castle: Two main types of soil (Gleys and Brown Earths), have been reported within the flux site footprint (Peichl et al., 2012). The soil within the flux footprint (< 150 m) is moderately to imperfectly drained Gley (FAO classification: Gleyic Cambisol). The

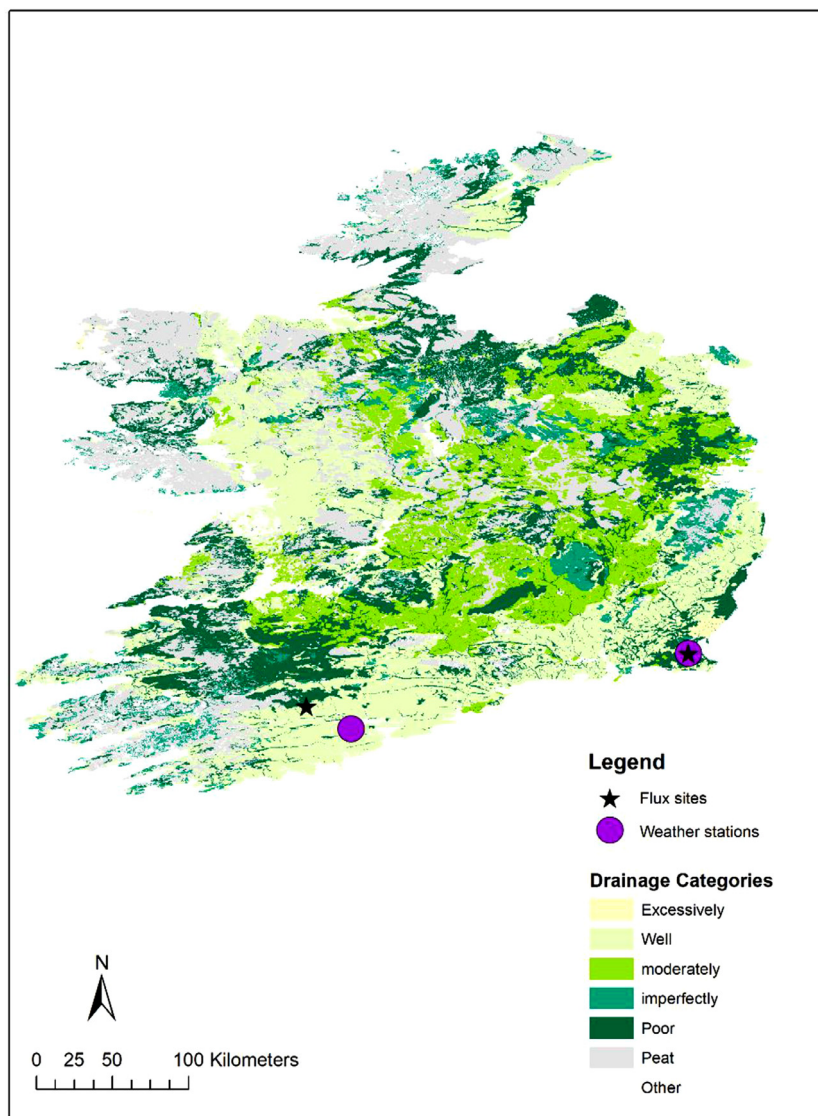


Fig 1. Map of soil drainage classes of Ireland (Irish Soil Information System by Teagasc for EPA, Creamer et al., 2014), showing the locations of test sites.

Table 1

Descriptions of grassland eddy covariance flux and synoptic stations used in this study. Meteorological data from Cork Airport (51.84°N, 8.48°W) at an elevation of 155 m were used for Dripsey. Johnstown Castle has a co-located weather station. The soil moisture properties are field capacity (θ_{FC}), saturation level (θ_{ST}) and wilting point (θ_{WP}), in order.

Station	Lat/Long (°)	Elevation (m)	Soil description	Moisture properties (θ_{FC} , θ_{ST} , θ_{WP})	Drainage class	Time period
Johnstown Castle	52.29°N, 6.49°W	58	A combination of gley, brown earths and free draining fine siliceous loam soils.	32% 59% 17%	Imperfect	2013
Dripsey	51.98°N, 8.75°W	186	Gley water-logged soils.	32% 45% 12%	Poor	2010

soils transition to moderately or well drained Brown Earths (Cambisol) at the outer edge of the flux footprint. The soil class in this area therefore varies from moderately to imperfectly drained, and the land cover is grass.

- ii) Dripsey: The EC footprint is over grass cover on a soil type that impedes water movement and can become waterlogged (Kiely et al., 2018) and is classed as a poorly drained Gley soil.

More detailed descriptions on the soil properties, climatology and EC footprints at Dripsey and Johnstown Castle are reported in Kiely et al. (2018) and Peichl et al. (2012), respectively.

Detailed information on vegetation height and leaf area index (LAI) are not available for the periods corresponding with flux measurements made at Dripsey, but Kiely et al. (2018) reported LAI values ranging from $\approx 2 \text{ m}^2 \text{ m}^{-2}$ in winter to $\approx 6 \text{ m}^2 \text{ m}^{-2}$ in summer. At Johnstown Castle, LAI is estimated from measurements of grass dry matter yield concurrent with the EC observations and an allometric relationship established with leaf area index meter readings. Modeled LAI values range between 0.1 (winter) and $6.8 \text{ m}^2 \text{ m}^{-2}$ (summer) for this site, with an average LAI of $2.2 \text{ m}^2 \text{ m}^{-2}$.

2.3. Data

We employ available routine weather observations to parameterize surface fluxes of heat and moisture over the two grassland sites described above. In the following sections, the observed flux data available for each site is discussed followed by a description of the available meteorological and soil water data. A summary of the Eddy-covariance and meteorological parameters used as input to, and evaluation of, the scheme employed is presented in Table 2.

2.3.1. Eddy-covariance measurements

Sensible and latent heat fluxes: Half-hourly EC flux measurements of Q_H and Q_E are available from the European Fluxes Database Cluster (<http://www.europe-fluxdata.eu/>) (Papale et al., 2006) for Dripsey (Kiely et al., 2018) for the period 2010. In order to avoid any potential

bias, we only employed non gap-filled data (Level 2 data). Half-hourly EC flux measurements of Q_H and Q_E were also obtained for Johnstown Castle for 2013 (Unpublished results). The instrumentation at both sites consists of an open-path infra-red gas analyser (IRGA) for measuring H_2O density and CO_2 concentration, in combination with a 3D sonic anemometer. The EC data were logged at 10 Hz and averaged over 30-minutes intervals (see Table 2 for a list of instruments at each site).

Data processing procedures at both sites were similar and are documented elsewhere: Sottocornola and Kiely (2010a, 2010b) for Dripsey; and Ní Chonchubhair et al. (2017) for Johnstown Castle. These procedures include spike removal (Vickers and Mahrt, 1997), the Webb–Pearman–Leuning correction (Webb et al., 1980; Moncrieff et al., 1997a), sonic anemometer tilt correction using the double rotation method (Kaimal and Finnigan, 1994) and spectral attenuation corrections after Moncrieff et al. (1997b). Some data filtering procedures, which differ from the above approaches, were applied to Dripsey and are described in Kiely et al. (2018). Here, poor quality data based on quality control flags (QC = 2) were removed and flux observations recorded when precipitation exceeded 1 mm were removed as these are likely to generate errors in Q_E measurements using open-path sensors (e.g. Ma et al., 2015). A statistical examination of the processed data for all sites showed typical ranges of -100 – 400 W m^{-2} for Q_H and Q_E ; individual observations outside of these ranges were excluded from further analysis (following Ma et al., 2015).

Following these pre-processing steps, a significant percent (original plus filtered) of flux data at each site was classed as missing: 24% and 32% of Q_H and Q_E , respectively at Johnstown Castle and 28% and 31% of Q_H and Q_E at Dripsey. While the proportion of data gaps from Johnstown Castle mainly arose from the quality control procedures, the higher proportion of missing data from Dripsey was due to a combination of both the number of missing values in the original data and the quality control processes, outlined above. After the filtering processes, the proportion of nighttime data slightly exceeded the daytime data at both sites. At Johnstown Castle, approximately 51% (2941 h) and 49% (2939 h) of Q_E data remained for nighttime and daytime (08:00–18:00) hours, respectively. Similarly, 53% (3188 h) and 47% (2851 h) of data

Table 2

Descriptions of meteorology and eddy-covariance parameters used as forcings and for validation, respectively.

Variables	Usage		Instrumentation
	Forcing	Validation	
Q_N		x	NR-Lite (Johnstown) and CNR1 (Dripsey) (Kipp & Zonen, Delft, The Netherlands)
Q_{S1}	x		
T_a	x		
u	x		
P	x		
RH	x		
Precipitation			
Sunshine hours			
Q_{Hb} , Q_{Eb}		x	IRGA gas analyzers, LI-7500 (LI-COR, Lincoln, NE) at 6 m for Dripsey and; 2.28 m (1 st Jan. – 26 th Feb.), 2.72 m (26 th Feb. – 23 rd Oct.), 2.85 m (23 rd Oct. – 31 st Dec.) for Johnstown.
θ	x		CS616 (Johnstown) and CS615 (Dripsey) (Campbell Scientific, Shepherd, UK)

for Dripsey were available for analysis.

Net radiation: Half-hourly measurements of Q_N from Dripsey for 2010 are available from the European Fluxes Database Cluster (Papale et al., 2006). For Johnstown Castle, Q_N measurements for 2013 are available from previously unpublished research (see Section 2.3.1). Hourly values of Q_N in the range -100 and 700 W m^{-2} were selected for the subsequent analysis (following Shi and Liang, 2014).

The energy budget closure is an efficient approach to evaluate the consistency of scalar flux densities measured by EC systems (Twine et al., 2000). The approach relates available energy ($Q_N - Q_G$) to turbulent fluxes ($Q_H + Q_E$) in order to determine the magnitude of non-closure of measured fluxes by EC systems. EC measurements are known to underestimate the turbulent fluxes (Q_H and Q_E) and overestimate Q_N resulting in non-closure of the energy balance (EBC) (Wilson et al., 2002; Foken, 2008; Franssen et al., 2010; Stoy et al., 2013). Other potential reasons for non-closure are discussed extensively in the literature and include; the failure to measure heat storage terms as part of measurement programmes (e.g. Heusinkveld et al., 2004); large-scale turbulent circulations over heterogeneous landscapes that are not captured by EC methods (Mauder et al., 2007; Stoy et al., 2013); the assumption of no advection and; inaccurate Q_N measurements (e.g. Foken, 2008). Over the sites available for the present study, the hourly energy budget closure (ignoring the Q_G and Q_{AS} terms) is approximately 69 % at Johnstown Castle and 60% at Dripsey (Fig. 2). These closure values are comparable with previously reported values, which lie within 53 – 99 % (e.g. Wilson et al., 2002).

2.3.2. Meteorological data

On-site hourly meteorological observations for the same period of EC measurements are available for Johnstown Castle but at Dripsey these data are only available at Cork Airport (155 m a.s.l), which is approximately 25 km from the site. Both meteorological stations conform to World Meteorological Organization (WMO) guidelines and report on global solar radiation ($Q_{s\downarrow}$, W m^{-2}) or sun duration (hours), air temperature ($^{\circ}\text{C}$), relative humidity (%), pressure (kPa), wind speed (m s^{-1}) and precipitation (mm). As cloud amount (oktas) was only available from Cork Airport, it was excluded from the subsequent analysis; this value was set ≈ 0 in the calculation of $Q_{L\downarrow}$. Global solar radiation was not available from Cork Airport, therefore hourly $Q_{s\downarrow}$ data was estimated for this site based on observations of sunshine duration following Allen et al. (1998) and Ishola et al. (2018). The hourly meteorological observations correspond with the periods for which the flux data are available at the two sites.

2.3.3. Soil water data

Soil water content, measured as the volumetric water content (θ , $\text{m}^3 \text{ m}^{-3}$) in the upper 20 cm of the soil, was measured at both sites at half-hourly intervals using CS615/CS616 time domain reflectometers (Table 2). At Johnstown Castle, these measurements are contemporaneous with the available EC flux measurements. At Dripsey,

measurements are only available for 2004 and 2005, which coincides with periods when flux measurements are either not available or gap-filled (European Fluxes Database Cluster Level 3 and 4 data). While the general meteorological conditions at Dripsey during 2004 and 2005 were wetter than those experienced in 2010 (1174 mm; 1183 mm and 974 mm, respectively), the cumulative precipitation during 2005 was very similar in profile to 2010, up to October, after which the soils would have been close to or at field capacity.

2.4. Methods

2.4.1. Surface flux estimation

The scheme to estimate the fluxes of heat, moisture and momentum from limited routine weather data was adapted from de Rooy and Holtslag (1999). The scheme was originally developed over a grassland ecosystem using extensive and well-documented datasets from Cabauw, the Netherlands, and covering a variety of weather conditions. The scheme computes the turbulent fluxes (Q_H and Q_E) through a set of sequential calculations (Fig. 3). The required inputs are: air temperature T_a (K) at observation height z_a (2 m), relative humidity RH (%), wind speed u (m s^{-1}) at 10 m, mean sea level pressure P (kPa), global solar radiation $Q_{s\downarrow}$ (W m^{-2}) and cloud amount N (oktas).

In the initial step, the variables that can be obtained directly from the inputs, such as the 24-h mean of 2-m temperature, T_{24} (K), vapor pressure, e (kPa), specific humidity deficit, Δq_a (g kg^{-1}), psychrometric constant, γ (kPa K^{-1}), and the slope of the saturated vapor pressure curve, s (kPa K^{-1}), are estimated. An iterative procedure then estimates the following parameters: friction velocity, u_* (m s^{-1}), aerodynamic resistance, r_a ($\text{s}^{-1} \text{ m}$), Q_H (W m^{-2}), and subsequently temperature scale θ_* (K) and Obukhov length L (m), using flux profile relations (Paulson, 1970). The profile method adopts the MOST to describe the profile relationships of important scaling quantities, u_* , θ_* and L ; r_a is also expressed in terms of a flux-profile relationship. In this study, the empirical stability correction functions used in the profile method are based on those derived for unstable surface layer by Paulson (1970) and Dyer (1974), which relate the fluxes of heat and momentum to their non-dimensional vertical gradients.

The friction velocity, u_* , aerodynamic resistance r_a and sensible heat, Q_H are calculated as follows:

$$u_* = \frac{uk}{\left[\ln\left(\frac{z_a}{z_{om}}\right) - \psi_m\left(\frac{z_a}{L}\right) + \psi_m\left(\frac{z_{om}}{L}\right) \right]}, \quad (1)$$

$$r_a = \frac{1}{ku_*} \left[\ln\left(\frac{z_a}{z_{oH}}\right) - \psi_H\left(\frac{z_a}{L}\right) + \psi_H\left(\frac{z_{oH}}{L}\right) \right], \quad (2)$$

and

$$Q_H = \frac{(X - Y)(A - B) + C}{X + Z(X - Y)}, \quad (3)$$

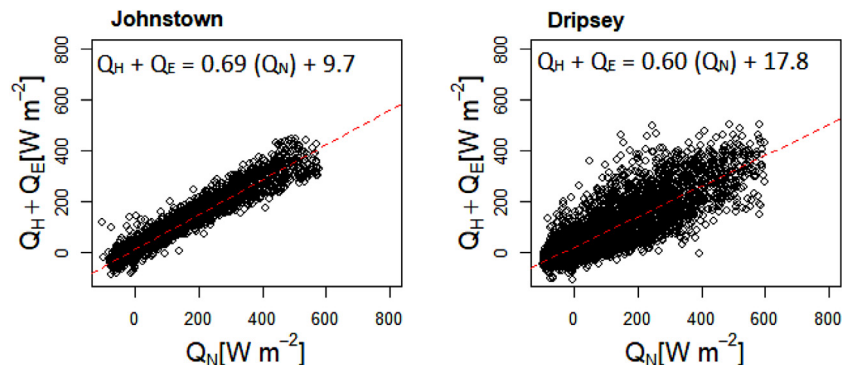


Fig. 2. The hourly Surface energy balance closure at both sites.

$$r_s = 70 \text{ s m}^{-1} \quad (8)$$

A more physically-based formulation was proposed by de Rooy and Holtslag (1999) based on a statistical relationship between r_s and the vapor density deficit (Δq) in the overlying air,

$$r_s = a + b \frac{e_s - e_a}{p} \frac{R_d}{R_v} = 10 \Delta q, \quad (9)$$

where, a (0 s m^{-1}) and b ($10 \text{ s kg m}^{-1} \text{ g}^{-1}$) are empirical constants and p is pressure such that $\frac{e_s - e_a}{p}$ is dimensionless. The remaining terms are constants, R_d is specific gas constant for dry air ($287 \text{ J kg}^{-1} \text{ K}^{-1}$) and R_v is specific gas constant for water vapor ($462 \text{ J kg}^{-1} \text{ K}^{-1}$).

Jarvis (1976) proposed a formulation for stomatal conductance, the inverse of surface resistance, that accounts for plant growth through the inclusion of environmental factors and a minimum surface resistance ($r_{s, \min}$), specific to plant type and leaf area index (LAI),

$$r_s = \frac{r_{s, \min}}{\text{LAI}} F_S F_{\Delta q} F_T F_M, \quad (10)$$

where $r_{s, \min}$ represents the optimum conditions for evapotranspiration as a function of solar radiation (F_S), water vapor ($F_{\Delta q}$), air temperature (F_T) and soil moisture (F_M) (Jarvis, 1976; Stewart, 1988). For short grass, the value of $r_{s, \min}$ is 110 s m^{-1} . Although the LAI of short grass changes seasonally (van den Hurk et al., 2000), a fixed value of $2 \text{ m}^2 \text{ m}^{-2}$ is commonly used (e.g. Beljaars and Bosveld, 1997; de Rooy and Holtslag, 1999; van den Hurk et al., 2000; 2003; van de Boer et al., 2014a).

Beljaars and Bosveld (1997) modified the Jarvis–Stewart approximation by removing the air temperature term (F_T), due to its correlation with radiation, and included a scaling factor (f_r), to adjust r_s to a particular surface (van de Boer et al., 2014a), as follows, (Beljaars and Bosveld, 1997).

$$r_s = f_r \frac{r_{s, \min}}{\text{LAI}} F_S^{-1} F_{\Delta q}^{-1} F_M^{-1} \quad (11)$$

Based on observations over the Cabauw grassland site which has poorly drained soils, Beljaars and Bosveld (1997) derived an optimized value for f_r of 0.47. Values for $r_{s, \min}$ and LAI are as stated above.

The response function F_S to $Q_{s\downarrow}$ is described (following Beljaars and Bosveld, 1997; van de Boer et al., 2014a) as:

$$F_S = \frac{Q_{s\downarrow}(S_{rm} - S_r)}{S_{rm}Q_{s\downarrow} + S_r(S_{rm} - 2Q_{s\downarrow})}, \quad (11a)$$

where the empirical coefficients S_{rm} and S_r are given as 1000 W m^{-2} and 230 W m^{-2} , respectively.

The response function $F_{\Delta q}$ to atmospheric moisture deficit is calculated as,

$$F_{\Delta q} = \frac{1}{(1 + h_s \Delta q)}, \quad (11b)$$

where Δq is the difference between the water vapor deficit at the

reference height (2 m) and surface (Chen and Dudhia, 2001). Following Beljaars and Bosveld (1997) and van de Boer et al. (2014a) we adopt a fixed value of 3 g kg^{-1} for the vapor deficit at the surface. Different values of h_s have been adopted in the literature (e.g. Stewart and Gay, 1989; Chen et al., 1996; van den Hurk et al., 2000; Chen and Dudhia, 2001, Ronda et al., 2001), however, 0.16 kg g^{-1} is employed here as it has previously been used over grassland land cover (Beljaars and Bosveld, 1997; van de Boer et al., 2014a).

F_M is a soil moisture response function and is given as,

$$F_M = 1 \text{ for } \theta > \theta_{FC}, \quad (11c)$$

$$F_M = 1 + c_{soil}(\theta - \theta_{FC}) \text{ for } \theta < \theta_{FC}, \quad (11d)$$

where θ ($\text{m}^3 \text{ m}^{-3}$) is the volumetric soil moisture in the root zone and θ_{FC} ($\text{m}^3 \text{ m}^{-3}$) is the volumetric water content at field capacity specific to soil type (Table 1). We initially employ a value of $6.3 \text{ m}^3 \text{ m}^{-3}$ for c_{soil} (following Beljaars and Bosveld, 1997); this parameter alters the relationship (i.e. slope) between conductance and soil moisture and consequently the sensitivity of F_M to changes in soil moisture.

2.4.3. Simulating fluxes at the test sites

To address our three primary objectives, here we evaluate the de Rooy and Holtslag (1999) scheme against the measured fluxes at the Johnstown Castle and Dripsey grassland sites. In particular, we focus on the different formulations for surface resistance (r_s) and their ability to estimate surface fluxes at i) a site that exhibits similar soil moisture properties to the Cabauw site, over which the scheme was originally developed, and ii) a site with differing soil moisture properties.

In the following section we use abbreviations to represent the different formulations used to obtain r_s :

- 1 FAO to identify r_s obtained using Eq. (8)
- 2 dRH99 to identify r_s obtained using Eq. (9) and,
- 3 BB97 to identify r_s obtained using Eq. (11)

The analysis is carried out for daytime only ($Q_{s\downarrow} > 10 \text{ W m}^{-2}$) when the majority of evapotranspiration takes place. At Johnstown Castle, we employ data from the nearby meteorological station and θ from the Eddy-covariance flux site as input to the scheme. At Dripsey, we employ data from Cork Airport, which is 25 km distant and is the closest suitable meteorological station. Due to the absence of soil moisture measurements for the period of study, we employ soil moisture data from 2005 as a surrogate to test the BB97 formulation in estimating r_s and Q_E at this site. We justify this on the basis that the cumulative precipitation during 2005, when the volumetric water content measurements are available, and 2010, when the flux measurements were obtained, display a similar profile during the period when soil moisture is likely to be most influential. Section 3.1 presents the results of the analysis.

Beljaars and Bosveld (1997) derived values for the f_r , S_r , h_s and c_{soil} coefficients employed in BB97 based on their model fit to the measured

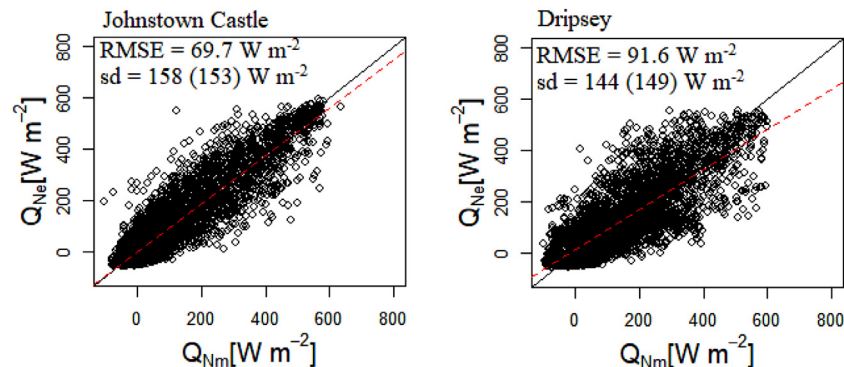


Fig 4. Relationship between daytime hourly measured (Q_{Nm}) and estimated (Q_{Ne}) net radiation flux over both sites.

data at Cabauw. To assess the influence of these specified values on r_s and consequently Q_E at both sites, we undertook a local sensitivity analysis, employing a one-at-a-time technique. For each coefficient value altered, the remaining values are held at their original, specified values. We initially perturbed the values of f_r , S_r , h_s and c_{soil} at Johnstown Castle, where all the required measured input variables are available. For consistency and robustness of model evaluation, we conducted a similar sensitivity analysis for the Dripsey site, employing soil moisture data from 2005. Finally, we employ the optimized values derived from the sensitivity analysis to derive estimated Q_H and Q_E at Johnstown Castle, where the default values for BB97 failed to replicate the measured fluxes; results from the sensitivity analysis are presented in Section 3.2.

3. Results

The de Rooy and Holtslag (1999) scheme is used, with different approximations of r_s , to simulate hourly radiation and turbulent fluxes at each observation site. The estimated hourly Q_N , Q_H and Q_E and daily averaged Q_H and Q_E fluxes were compared with the observed fluxes at each site using a number of statistical measures including root mean square error (RMSE), bias, standard deviation (sd) and correlation coefficient (r), and results are presented below.

3.1. Evaluation of radiation and estimated surface fluxes

3.1.1. Net radiation

Fig. 4 shows the relationship between estimated and measured (daytime) hourly Q_N values for both sites. The estimated (measured) Q_N values are: between -90 and 600 $W\ m^{-2}$ (-100 and 635 $W\ m^{-2}$) at Johnstown Castle and; between -66 and 553 $W\ m^{-2}$ (-100 and 600 $W\ m^{-2}$) at Dripsey. At Johnstown Castle, the model tended to overestimate negative values of Q_N and underestimate large positive values. At Dripsey, the underestimation of Q_N is likely attributable to its reliance on Q_{S1} which was derived based on hourly sun duration obtained from a distant meteorological site. Overall model performance at the two sites indicates: a $RMSE = 69.7$ $W\ m^{-2}$ ($sd = 158$ and 153 $W\ m^{-2}$ for the estimated and measured values, respectively) at Johnstown Castle and; a $RMSE = 91.6$ $W\ m^{-2}$ ($sd = 144$ and 149 $W\ m^{-2}$ for the estimated and measured values) at Dripsey. These results are broadly comparable with other similar studies. For example, Holtslag and van Ulden (1983) derived a linear relationship between Q_{S1} , solar elevation and total cloud cover, in combination with other components of the surface radiation budget, to estimate Q_N under both clear and cloudy sky conditions at Cabauw and obtained a $RMSE$ of 63 $W\ m^{-2}$ for Q_N under all conditions.

3.1.2. Sensible heat fluxes

Table 4 shows the performance metrics for the estimated hourly Q_H for both sites using the three formulations for r_s outlined above. Of these, dRH99 was found to perform the best across all metrics and both sites, but particularly at Johnstown Castle, displaying the lowest RMSE and bias and highest r values. BB97 performs the poorest at Johnstown Castle, displaying the highest RMSE and bias compared to the other two methods. In contrast, at Dripsey, BB97 produces metrics that are very similar to dRH99.

Figs. 5 and 6 display the scatterplots of measured and estimated hourly Q_H , using the three formulations of r_s , at Johnstown Castle and Dripsey, respectively; they also show the daily cycle of Q_H , during daylight hours, averaged for the month of July for the respective year of observation. At Johnstown Castle, BB97 significantly overestimates Q_H (which is evident in the July graph) while both dRH99 and FAO match the measured values more closely (Fig. 5). In general, large positive hourly values of Q_H are underestimated at Dripsey but daytime values during July are very close (Fig. 6). Of the three r_s methods, dRH99, at both sites, and BB97, at Dripsey, produced results that are most

comparable with Holtslag and van Ulden (1983) who employed a modified Priestly-Taylor approach to estimate Q_H and Q_E above a short-grass covered surface at Cabauw; they reported a $RMSE$ of 34 $W\ m^{-2}$ between measured and estimated Q_H .

3.1.3. Latent heat fluxes

Table 5 shows the statistics for the estimated and measured Q_E values for both sites. Although the FAO method employs a constant r_s value, it produced the best fit at Johnstown Castle ($RMSE = 34.9$ $W\ m^{-2}$, $bias = -6.7$ $W\ m^{-2}$ and $r = 0.85$) (Table 5), followed by dRH99 ($RMSE = 43.1$ $W\ m^{-2}$, $bias = 11.7$ $W\ m^{-2}$ and $r = 0.84$). Employing the default Beljaars and Bosveld (1997) values, BB97 performed very poorly at this site ($RMSE = 56.1$ $W\ m^{-2}$, $bias = -29.9$ $W\ m^{-2}$ and $r = 0.62$). At Dripsey, FAO produced the best fit in terms of RMSE and r value ($RMSE = 38.9$ $W\ m^{-2}$ and $r = 0.84$), but displayed the highest bias ($bias = -11.8$ $W\ m^{-2}$) of the three methods. dRH99 performed the poorest at this site, with the highest RMSE and lowest r value ($RMSE = 48.7$ $W\ m^{-2}$ and $r = 0.78$) relative to the other two methods. BB97 resulted in the lowest bias value of all methods ($bias = -2.1$ $W\ m^{-2}$), and an RMSE and r value comparable to FAO ($RMSE = 41.2$ $W\ m^{-2}$ and $r = 0.83$).

Figs. 7 and 8 show scatterplots of hourly measured and estimated Q_E , based on the different r_s formulations, for Johnstown Castle and Dripsey, respectively; they also shows the daily cycle of Q_E for daylight hours, averaged for the month of July. While FAO produced the lowest RMSE and bias values at Johnstown Castle (Table 5), both FAO and dRH99 are shown to overestimate Q_E , evident during the mid-day hours in July, when radiation is most intense; BB97 significantly underestimates Q_E , evident during July (Fig. 7). At Dripsey, all r_s methods underestimate Q_E , with the largest underestimates associated with FAO. Holtslag and van Ulden (1983), in their study over Cabauw, report a $RMSE$ of 56 $W\ m^{-2}$ between measured and estimated Q_E ; results for all r_s methods used here are consistent with this finding.

3.2. Surface resistance

To explore the difference in performance between the r_s formulations, we examined the calculated r_s ranges during daytime hours for both dRH99 and BB97. From Table 6, the range in r_s values are larger for BB97 than for dRH99, at both sites. The large difference in estimated r_s values between dRH99 and BB97 result in a marked contrast in the estimated Q_E values at Johnstown (Fig. 7). In contrast, the difference in the range of r_s values at Dripsey between methods is smaller; smaller differences are also apparent in the estimated Q_E between these methods at this site. To further examine this, we focus our attention on BB97 to understand the role of the environmental response factors in regulating r_s and consequently Q_E at both sites.

3.2.1. Sensitivity of Q_E to soil and environmental factors

A sensitivity analysis on BB97 was conducted by altering the values of f_r , S_r , h_s and c_{soil} , individually, and leaving the remaining coefficients unchanged.

At Johnstown, the estimated Q_E was found to be largely insensitive, within the range of values tested, to alterations in either h_s , associated

Table 4

Performance assessment of daytime ($Q_{S1} > 10$ $W\ m^{-2}$) Q_H based on different r_s , over both stations. The italicized values show the r_s method that give the best agreement between estimated and measured Q_H . RMSE and Bias ($W\ m^{-2}$).

r_s , method	Dripsey			Johnstown Castle		
	RMSE	Bias	r	RMSE	Bias	r
dRH99	38.2	9.4	0.78	36.1	8.3	0.83
BB97	39.8	11.9	0.77	51.8	23.4	0.83
FAO	44.7	16.7	0.77	43.8	15.9	0.82

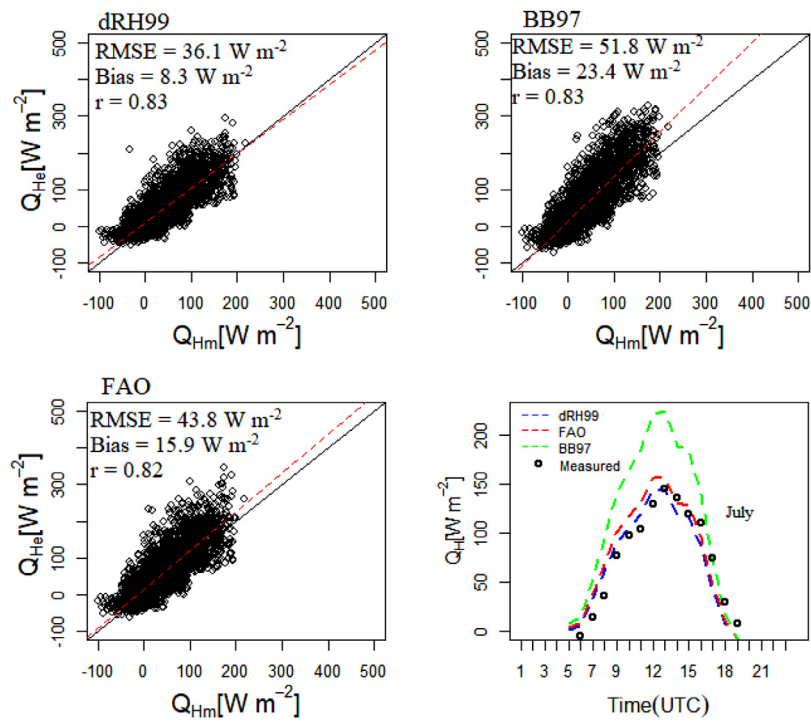


Fig 5. Relationship between daytime hourly measured (Q_{Hm}) and estimated (Q_{He}) sensible heat flux applying the Scheme with different r_s models over Johnstown Castle. The line plot is the diurnal cycle of Q_H , averaged for July, 2013.

with the atmospheric moisture deficit function ($F_{\Delta q}$), or S_r , associated with the radiation function (F_s) (Fig. 9, top) during January or July. In contrast, during July, r_s and consequently Q_E was found to be very sensitive to changes in c_{soil} , associated with the soil moisture function (F_M) (Fig. 9, bottom left). When the default value ($6.3 \text{ m}^3 \text{ m}^{-3}$) for c_{soil} was employed, the average daytime value of r_s increased significantly ($\approx 600 \text{ s m}^{-1}$), suppressing the estimated Q_E values (Fig. 7). When

$c_{soil} = 0 \text{ m}^3 \text{ m}^{-3}$, equivalent to setting $F_M = 1$, the estimated Q_E increases to near its potential, in response to low daytime r_s ($< 50 \text{ s m}^{-1}$) values. Setting c_{soil} values within the range of $2.3\text{--}4.3 \text{ m}^3 \text{ m}^{-3}$ resulted in Q_E estimates with the lowest bias, relative to measured values. A similar response was found for f_r ; estimated Q_E decreased from its potential ($f_r = 0$) with increasing f_r . A $c_{soil} = 4.3 \text{ m}^3 \text{ m}^{-3}$ was ultimately selected, based on the bias value

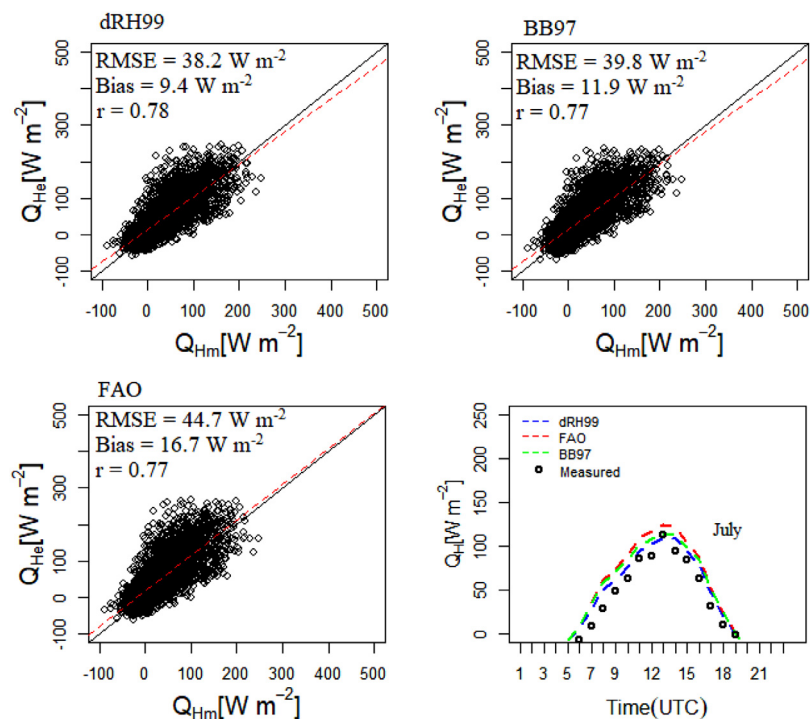


Fig 6. Relationship between daytime hourly measured (Q_{Hm}) and estimated (Q_{He}) sensible heat flux applying the Scheme with different r_s models over Dripsey. The line plot is the diurnal cycle of Q_H , averaged for July, 2010.

Table 5

Performance assessment of daytime ($Q_{s_i} > 10 \text{ W m}^{-2}$) Q_E based on different r_s , over both stations. The italicized values show the r_s method that give the best agreement between estimated and measured Q_E . RMSE and Bias (Wm^{-2}).

r_s method	Dripsey			Johnstown Castle		
	RMSE	Bias	r	RMSE	Bias	r
dRH99	48.7	5.6	0.78	43.1	11.7	0.84
BB97	<i>41.2</i>	<i>-2.1</i>	<i>0.83</i>	56.1	-29.9	0.62
FAO	38.9	-11.8	0.84	<i>34.9</i>	<i>-6.7</i>	<i>0.85</i>

(0.9 W m^{-2}) for the month of July.

At Dripsey, changes to h_s , S_r and c_{soil} had little or no impact on r_s and consequently Q_E (Fig. 10, top and bottom left), during either January or July. Similar to the findings at Johnstown, r_s was found to increase with increasing f_r so that the corresponding Q_E decreases, evident during the mid-day hours in both January and July.

3.2.2. Estimation of surface fluxes using adjusted coefficients

Fig. 11 (top) shows the hourly measured and estimated fluxes of Q_E and Q_H and averaged hourly day time values for July (Fig. 11, bottom). The use of adjusted values (Table 7) at Johnstown improves the RMSE and bias for Q_E ($RMSE = 37.8 \text{ W m}^{-2}$, $bias = -9.7 \text{ W m}^{-2}$) and Q_H ($RMSE = 41.7 \text{ W m}^{-2}$, $bias = 15.3 \text{ W m}^{-2}$) and the r value for Q_E ($r = 0.82$). The diurnal cycle (Fig. 11, bottom) shows clearly that Q_E is significantly improved, matching more closely with the measured values during July. Overall, the magnitudes of daytime hourly estimated (measured) Q_H were within the range -60 and 320 W m^{-2} (-100 and 220 W m^{-2}), while that of Q_E were within -100 and 350 W m^{-2} (-20 and 310 W m^{-2}). At Dripsey, using the original BB97 values which proved to be optimum for this site, the surface fluxes were estimated within the range -68 and 235 W m^{-2} for Q_H and within -11 and 330 W m^{-2} for Q_E .

Averaged daily Q_H were estimated between -50 W m^{-2} and 170 W m^{-2} at both sites; daily Q_E values ranged between -15 W m^{-2}

and 190 W m^{-2} at both sites (Fig. 12, top). While both sites showed similar exchanges of Q_H , at both hourly and daily time scales Q_E was higher than Q_H . This indicates that the surface conditions at these sites were wet, in general, resulting in lower Δq_a and r_s and consequently, higher Q_E . The broader pattern shows the seasonal variation in the fluxes, which are low in winter and peak in summer (Fig.12, bottom).

4. Discussion

4.1. Physical control of parameterized surface resistance and surface fluxes

In this study, we evaluated the land surface parameterization scheme of de Rooy and Holtslag (1999) as a means of deriving surface energy fluxes using routine meteorological data. Although the scheme was developed using observations made over short grass grown on poorly drained soil, they suggested it could be adjusted for use elsewhere if the surface parameters, particularly surface resistance (r_s), are modified to local conditions by using appropriate parameterization schemes. Beljaars and Bosveld (1997) indicate that r_s can vary owing to a range of environmental factors, including soil moisture, photosynthetically active radiation (PAR) and near-surface moisture deficit. Here, we focus on three different methods (namely FAO, dRH99 and BB97) of representing r_s , representing varying levels of sophistication, within the scheme.

The FAO method requires no information on atmospheric and site conditions and assigns a fixed value for r_s . Estimates using this method performed relatively well in estimating Q_E but poorly in estimating Q_H at both sites. The dRH99 method incorporates the near-surface moisture deficit but did not perform as well as FAO for Q_E , but did better than FAO for Q_H at both sites. The most sophisticated method (BB97), using the standard values for the environmental response factors (i.e. f_r , S_r , h_s and c_{soil}), provided a good fit to both Q_H and Q_E at Dripsey but performed poorest of all methods at Johnstown.

These results may seem counterintuitive, as the FAO method with the least information performs well, relative to the other methods with regard to Q_E . In part this can be explained by the constrained nature of

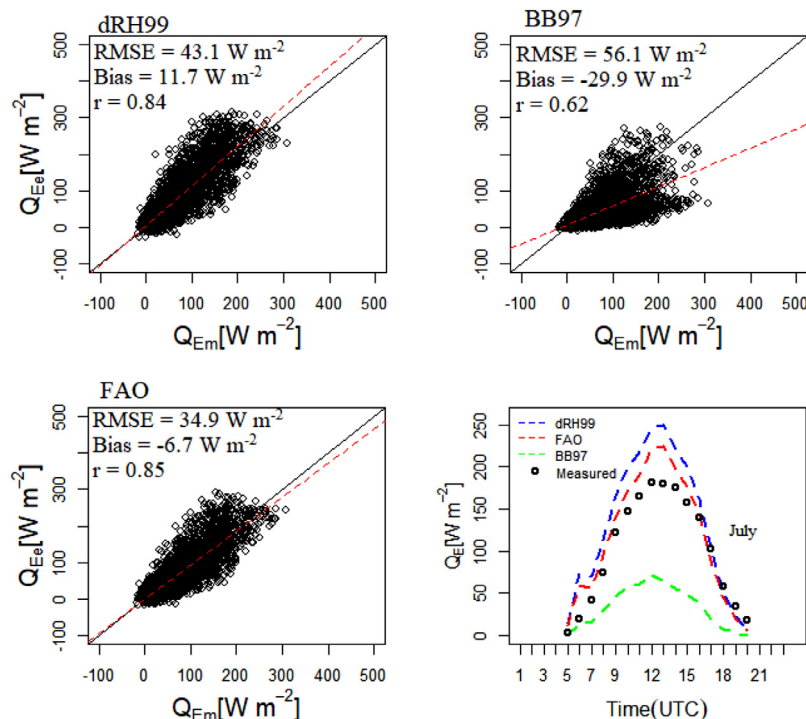


Fig 7. Relationship between daytime hourly measured (Q_{Em}) and estimated (Q_{Ee}) latent heat flux applying the Scheme with different r_s models over Johnstown Castle. The line plot is the diurnal cycle of Q_E , averaged for July, 2013.

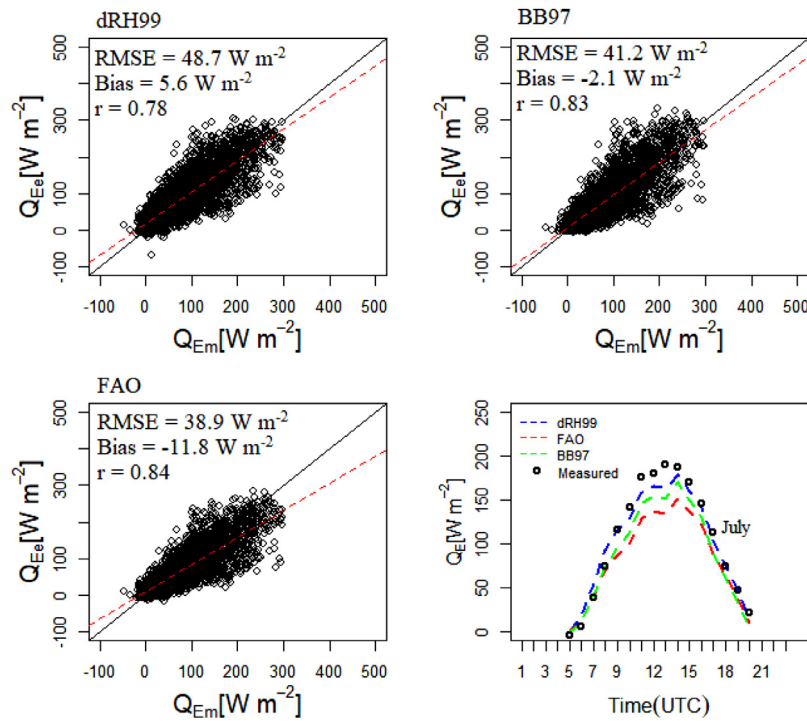


Fig 8. Relationship between daytime hourly measured (Q_{Em}) and estimated (Q_{Ee}) latent heat flux applying the Scheme with different r_s models over Dripsey. The line plot is the diurnal cycle of Q_E , averaged for July, 2010.

Table 6

Range of estimated r_s ($s m^{-1}$) during mid-day time ($Q_{S1} > 10 W m^{-2}$ and $Q_{S1} > 100 W m^{-2}$) over the selected stations. BB97 is based on the scheme using the default parameter values (i.e. Beljaars and Bosveld, 1997) for BB97; BB97 (optimized) is based on the updated optimized values for Johnstown Castle, employed in this study.

r_s method	Johnstown Castle		Dripsey	
	$Q_{S1} > 10 W m^{-2}$	$Q_{S1} > 100 W m^{-2}$	$Q_{S1} > 10 W m^{-2}$	$Q_{S1} > 100 W m^{-2}$
dRH99	0–100	0–100	0–90	0–90
BB97	25–15800	25–2613	25–1300	25–175
BB97 (optimized)	25–2450	20–400	–	–

the energy budget, which allocates the energy available (that is, $Q_N - Q_G$) into Q_H and Q_E . As FAO underestimates Q_H , more energy is channeled into Q_E . Similarly the improved performance of dRH99 for Q_H results in a weaker result for Q_E . However, the intriguing result is for the most sophisticated method (BB97), which includes many of the physical controls on r_s , performs well at Dripsey using standard values but poorly at Johnstown for both Q_H and Q_E . As both Johnstown Castle and Dripsey experience similar meteorological conditions (e.g. Fig. 4), we hypothesized that this is due to the soil moisture characteristics (Table 1), which are not considered by dRH99.

Fig. 13 shows the average daily values of soil moisture (θ) of Dripsey and Johnstown for the years available. Seneviratne et al. (2010) classified evapotranspiration regimes into types. A wet regime is defined as energy-limited, and occurs when θ lies above a critical soil moisture level (θ_{CT}). When θ falls below θ_{CT} (typically between 0.5 and 0.8 of θ_{FC}) (Seneviratne et al. 2010; after Shuttleworth, 1993) the regime is classed as moisture-limited and 'transitional'. At Dripsey, daily θ varies between 0.25 to 0.4 $m^3 m^{-3}$ over the two year period and only drops below θ_{FC} for short periods; from the 6th June to the 8th August during 2004 (≈ 64 days) and from the 28th June to the 23rd July during 2005 (≈ 26 days). At Johnstown, θ varies between 0.12 to 0.47 $m^3 m^{-3}$ over the measurement period;

however, θ falls below θ_{CT} for an extended period from the 23rd May to the 30th September during 2013 (≈ 131 days). Consistent with the soil drainage characteristics, the heavier soils at Dripsey maintain sufficient moisture throughout the year; this meets the definition of a wet regime where Q_E is constrained by the available energy. At Johnstown, in the absence of precipitation, the soil moves from a wet to a transitional regime and Q_E becomes moisture-limited. This suggests that the impact of the different methods for obtaining r_s values will be most evident during transitional soil moisture regimes. BB97 is the only method that can incorporate these effects into the calculation of surface resistance (r_s).

The sensitivity analysis identified the c_{soil} coefficient, which acts to modify the plants ability to access soil moisture below field capacity (θ_{FC}) as a critical variable. A value of $c_{soil} \approx 6.3 m^3 m^{-3}$ was estimated by Beljaars and Bosveld (1997) based on observations at a poorly-drained site (Cabauw), similar to the Dripsey site, which fits the characteristics of an energy-limited evapotranspiration regime. However, we found that a value of $c_{soil} \approx 4.3 m^3 m^{-3}$ was better suited to the imperfectly-drained soils at Johnstown, which often experiences a transitional regime. The adjusted c_{soil} value reduced the range of r_s values (Table 6) and improved results for both hourly and daily Q_H and Q_E estimates (Figs. 11 and 12). These results indicate that r_s depends very strongly on soil moisture regimes, particularly during a transitional period where θ falls below θ_{CT} , so that the use of a constant value or a linear relation where air moisture response is the only driver of r_s may prove inferior. This supports the conclusion of Beljaars and Bosveld (1997), who established that all the environmental response parameters are important for stomatal control during dry periods, in order to obtain a good flux simulation.

The estimates of surface energy fluxes generated by the de Rooy and Holtslag (1999) scheme using the BB97 method that adjusts to soil moisture conditions, generates both hourly ($RMSE \approx 40 W m^{-2}$) and daily ($RMSE \approx 24 W m^{-2}$) statistics that are comparable with other similar studies. For instance, Holtslag and van Ulden (1983), using calculated Q_{S1} as an input into their scheme, obtained half-hourly measures of $RMSE \approx 34 W m^{-2}$ for Q_H during daytime over grassland

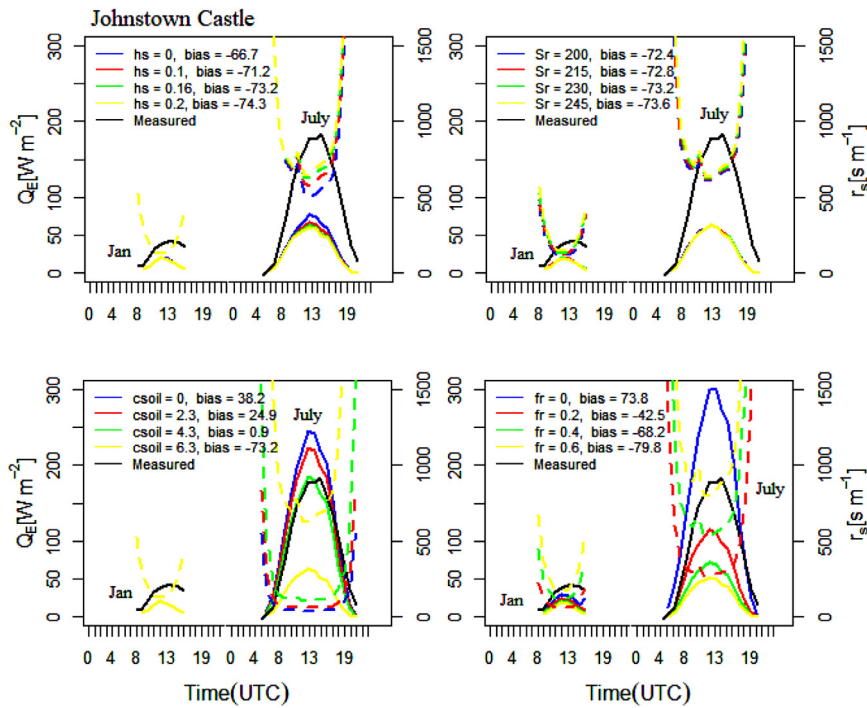


Fig 9. Sensitivity of daytime r_s and Q_E to environmental factors, averaged for January and July over Johnstown Castle. h_s (g kg^{-1}), S_r (W m^{-2}), c_{soil} ($\text{m}^3 \text{m}^{-3}$) and f_r is dimensionless. The calculated biases for January ($\approx -14 \text{ W m}^{-2}$) are similar for all factors. The dashed and solid lines are r_s and Q_E , respectively.

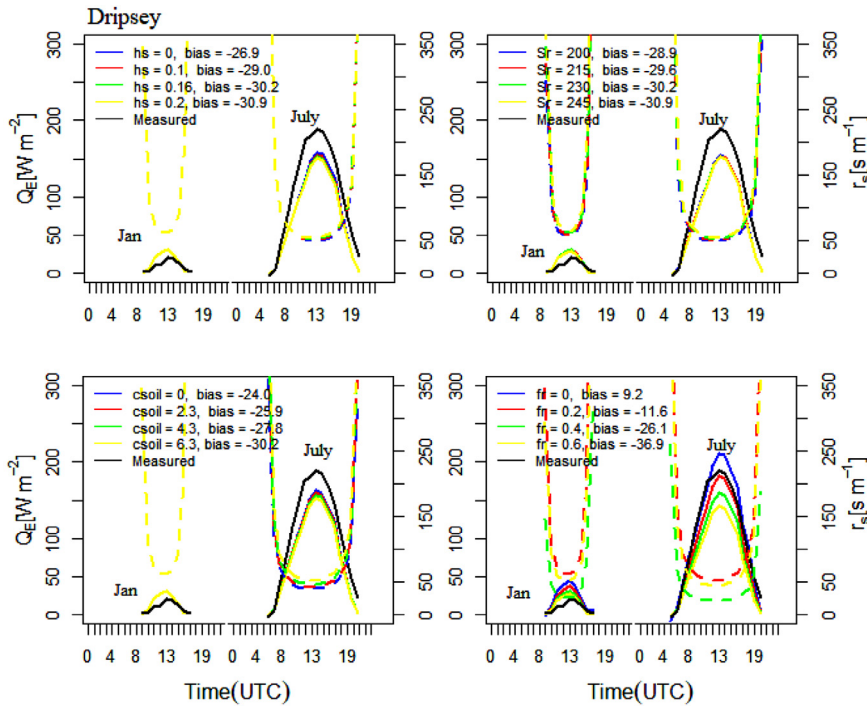


Fig 10. Sensitivity of daytime r_s and Q_E to environmental factors, averaged for January and July over Dripsey. h_s (g kg^{-1}), S_r (W m^{-2}), c_{soil} ($\text{m}^3 \text{m}^{-3}$) and f_r is dimensionless. The calculated biases for January ($\approx -9 \text{ W m}^{-2}$) are similar for all factors. The dashed and solid lines are r_s and Q_E , respectively.

at Cabauw, the Netherlands. The errors of estimated Q_E using different spatial evapotranspiration (ET) models including mapping ET at high resolution with internalized calibration (METRIC) (Allen et al., 2007), surface energy balance systems (SEBS) model (Su, 2002), two-source energy balance (TSEB) model (Norman et al., 1995), triangle model, and surface energy balance algorithm for land (SEBAL) (Bastiaanssen et al., 1998) are within the range $\approx 30\text{--}80 \text{ W m}^{-2}$ (Long and Singh, 2013), which also correspond to results in this study.

Estimated daily ET fluxes using an upscaled evaporative fraction (EF) scheme have also been found to range between 5 and 40 W m^{-2} (Colaizzi et al., 2006; Sobrino et al., 2007; Tang et al., 2013).

4.2. Uncertainties in surface heat flux simulations

It is important to recognize several potential sources of error in this work and their likely effect on the findings.

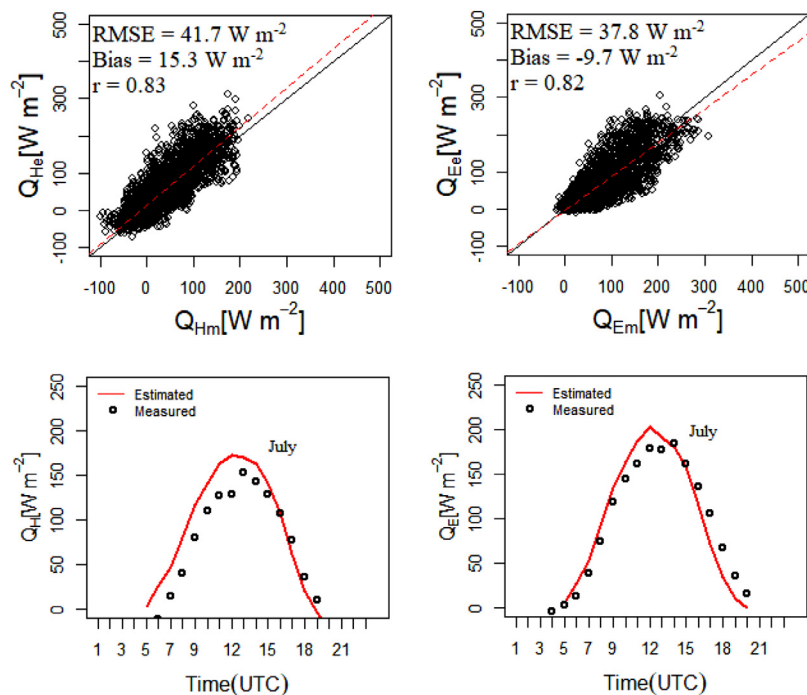


Fig 11. Relationship between daytime hourly measured and estimated Q_H [left] and Q_E [right] fluxes for 2013, applying the Scheme with optimized ($c_{soil} = 4.3 \text{ m}^3 \text{ m}^{-3}$) r_s over Johnstown Castle.

Table 7

Adapted empirical coefficients of optimized r_s for Q_E estimation under different surface conditions.

Soil Drainage Characteristics	Variable	Optimized value	Units
Imperfectly drained (Johnstown Castle)	f_r	0.47	-
	r_{smin}	110	s m^{-1}
	LAI	2	$\text{m}^2 \text{ m}^{-2}$
	h_s	0.16	g kg^{-1}
	c_{soil}	4.3	$\text{m}^3 \text{ m}^{-3}$
	S_r	230	W m^{-2}
Poorly drained (Dripsey)	f_r	0.47	-
	r_{smin}	110	s m^{-1}
	LAI	2	$\text{m}^2 \text{ m}^{-2}$
	h_s	0.16	g kg^{-1}
	c_{soil}	6.3	$\text{m}^3 \text{ m}^{-3}$
	S_r	230	W m^{-2}

Energy budget closure: The energy flux estimates generated here using the de Rooy and Holtslag scheme are evaluated by comparison with EC measurements made at two sites. It is important to acknowledge that there are likely to be errors in the measured fluxes that can be assessed as part of energy budget closure (see Section 2.3.1). Here, the closure is measured as $Q_N - (Q_H + Q_E)$ and the results for both sites (Fig. 2) are consistent with those reported in the previous studies (e.g. Wilson et al., 2002). The major reason for the non-closure here is the absence of substrate heat flux (Q_G) observations but there are also likely to be errors associated with the measured terms (Heusinkveld et al., 2004). EC measurements are known to underestimate the turbulent sensible (Q_H) and latent (Q_E) heat fluxes mainly because they do not capture the effects of large-scale eddies that are linked to landscape heterogeneity (Foken, 2008). We do not attempt to evaluate the magnitude of the underestimates in this work but Foken (2008) indicates that these may be between 10% and 20%. This should be borne in mind when evaluating the estimated turbulent fluxes using BB97, which employ adjusted parameters to improve the fit to observations.

Meteorological observations: The de Rooy and Holtslag (1999) scheme requires inputs on solar radiation, air temperature, humidity,

etc. to estimate fluxes. Ideally, these meteorological observations are complete and available at the site of study. This was not the case for Dripsey, where the scheme used data obtained for a site 25 km distant (Cork Airport) where observations of solar radiation (Q_{S1}) and cloud cover were not available. The study estimated Q_{S1} from sunshine hours using a modified Angstrom-model but could not account for the impact of clouds on Q_{L1} ; as a result, estimated Q_N is likely to be lowered, especially at night. This error will affect all surface energy fluxes but, given the focus on daytime evaporation, the impact is likely to be small. While the estimated Q_G values were not evaluated in this study, de Rooy and Holtslag (1999) also highlighted that, an overestimation of Q_G may result in negative bias in $Q_N - Q_G$ that is used to estimate Q_E .

Finally, we should acknowledge that the need to estimate radiation components (rather than using observations) will result in errors that will impact on the turbulent flux estimates produced by the different methods.

5. Summary and conclusion

This paper applied an existing physically-based scheme for estimating surface energy fluxes over two independent sites with contrasting soil moisture characteristics. The radiative and non-radiative components were parameterized from limited routine weather observations for daytime conditions over grass-covered surfaces at Johnstown Castle and Cork Airport in Ireland. The parameterized fluxes were further evaluated against observed EC flux measurements at Johnstown Castle and Dripsey (25 km from Cork Airport). Our main objectives are to test whether the original de Rooy and Holtslag (1999) scheme, which was derived at a grassland site in the Netherlands (Cabauw) can be transferred to other grassland sites and take into account different soil characteristics. The study focused in particular on the role of surface resistance (r_s) in regulating the daytime turbulent heat fluxes of Q_H and Q_E . Three methods of varying sophistication (FAO, dRH99 and BB97) were applied to the estimation scheme at the two test sites, which represent poorly (Dripsey) and imperfectly (Johnstown) drained soils. While BB97 and dRH99 produced a good fit to observed Q_E values at Dripsey (a site that is similar to Cabauw), the fit at Johnstown was

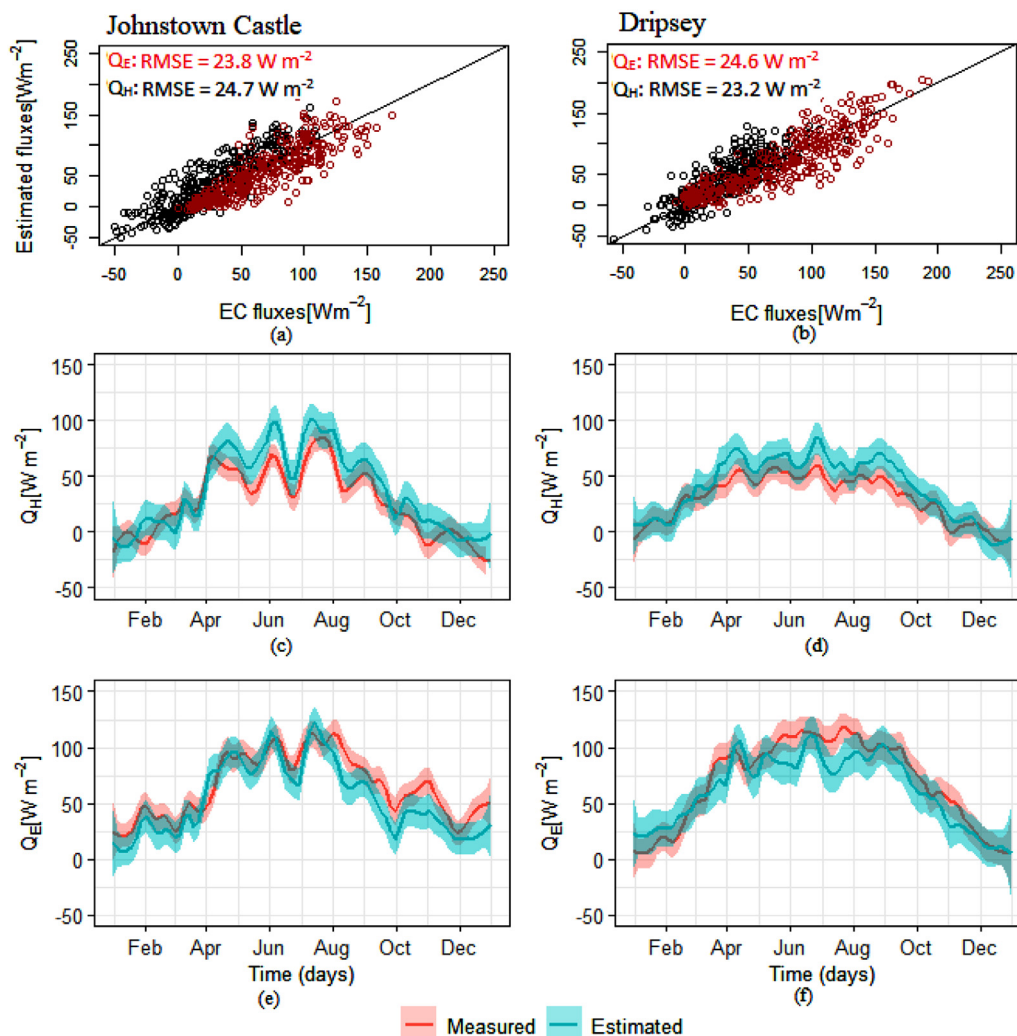


Fig 12. Relationship between parameterized and measured averaged daily Q_H and Q_E over the selected sites. The daily variations of Q_E and Q_H in the course of a year are shown in the middle (c,d) and bottom (e,f) panels, respectively. The shaded portions are the 5th and 95th percentiles of uncertainty bound as calculated by LOESS regression

poor. The differences in results were attributed to soil moisture characteristics and only BB97 accounts for this property. A critical variable in this method of deriving r_s is the soil moisture coefficient (c_{soil}), which accounts for the water available to plants for evapotranspiration; the

value of c_{soil} used in BB97 ($6.6 \text{ m}^3 \text{ m}^{-3}$) was suited to the wet soil conditions at Dripsey but not at Johnstown. This study finds that $c_{soil} \approx 4.3 \text{ m}^3 \text{ m}^{-3}$ resulted in Q_H and Q_E values that agree well with the measured values over imperfectly drained soil.

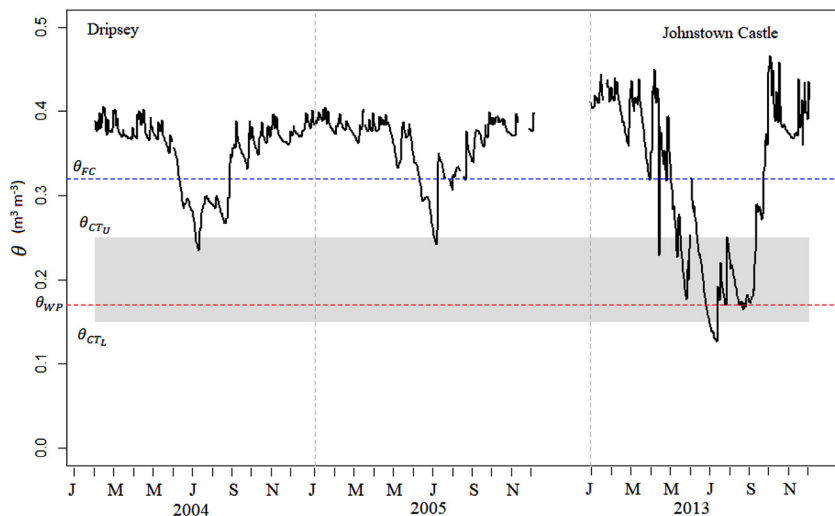


Fig 13. Averaged diurnal variations of the measured θ of the top layer of the soil from 2004 to 2005 at Dripsey and for the year 2013 at Johnstown Castle. The gaps indicate periods with missing values. The horizontal dashed line is the threshold of θ at field capacity [blue] and wilting point [red], and the grey box is the (upper and lower critical θ at $0.25 \text{ m}^3 \text{ m}^{-3}$ and $0.15 \text{ m}^3 \text{ m}^{-3}$, respectively) bound of transitional soil moisture regime for both sites (after Shuttleworth, 1993). (For interpretation of the references to color in this figure legend, the reader is referred to the web version of this article.)

An additional finding from this work was that the use of off-site meteorology, similar to the site of interest, can be reliably employed to estimate the measured surface fluxes at a location; we demonstrated this at Dripsey, where the nearest suitable meteorological station was located ≈ 25 km away. Notwithstanding the uncertainties associated the estimation of $Q_{s\downarrow}$ from sun hours and the use of soil water from a similar precipitation year (i.e. 2005), the estimated fluxes agree well with the measured values at this site. In the absence of direct soil moisture measurements and based on the soil drainage characteristics at Dripsey, the use of $F_M = 1$ in combination with standard optimal coefficients of BB97 is likely to produce similar results to dRH99.

The surface energy imbalance is always characterized to be partly a consequence of an underestimation of turbulent heat fluxes by EC techniques. Given the measures of observed surface energy balance closure at the test sites which, while they do not account for Q_G , are consistent with previous studies, we can conclude that the uncertainty of the parameterization scheme associated with the systematic bias of EC measurements of turbulent heat fluxes is relatively smaller. Notwithstanding the problems of surface energy balance closure of EC measurements, the estimated fluxes improved significantly through the adjustment of a c_{soil} adjusted to account for the soil moisture conditions. Generally, the [de Rooy and Holtslag \(1999\)](#) scheme demonstrated good performance in replicating the measured fluxes over grass-covered surfaces exhibiting different soil moisture characteristics and using routine weather observations for daytime weather conditions at both

sites. On the basis of the analysis conducted here, we therefore conclude that the land surface scheme is sensitive to soil types that exhibit different drainage characteristics; whether the optimized coefficient for c_{soil} in this study is more generally applicable, remains to be tested. The python code for this application is obtainable from the first author.

Declaration of Competing Interest

The authors declare that they have no known competing financial interests or personal relationships that could have appeared to influence the work reported in this paper.

Acknowledgments

The authors are grateful to Met Éireann, the Irish Meteorological Service, for providing routine weather observations. We thank the Dripsey FLUXNET site investigators for sharing the flux data used in this work. We acknowledge the help and advice of Prof. Bert Holtslag, Dr. Bert Heusinkveld and Dr. Arnold Moene. This study is funded by the Teagasc Irish Agriculture and Food Development Authority under Walsh Fellowship Programme (project: 2016076). We also thank the anonymous reviewers for their constructive comments to improving the quality of the study.

Appendix

A.1. Surface energy budget

The SEB is the energy conservation at the earth's surface. It describes the ability to partition the net radiation (Q_N) into surface sensible (Q_H) and latent (Q_E) heat exchange with the overlying atmosphere, and soil heat with the subsurface (Q_G) assuming no heat is stored or released within the canopy. The SEB equation can be written as;

$$Q_N = Q_H + Q_E + Q_G \quad (A1)$$

On a typical day, Q_N is positive during the day and increases toward mid-day when the sun is highest, at night it becomes negative. Consequently, the surface is the source of energy to the atmosphere leading to rising air temperature and humidity, and to the subsurface (raising soil temperature), during the daytime. However, during night-time, the surface serves as a sink as the energy flows in reverse order.

The non-radiative terms in (A1) are related to vertical gradients of air temperature (Q_H), humidity (Q_E) and soil temperature (Q_G) and the respective transfer properties. In the atmosphere, transfer is regulated by the near-surface airflow and stability while conductivity controls heat exchange in the soil. An expanded discussion of these components and application to the study region has been presented in [Keane and Collins \(2004\)](#).

A.2. Radiation terms

Q_N is parameterized based on the components of surface radiation as represented in equation A2.

$$Q_N = Q_{S\downarrow} - Q_{S\uparrow} + Q_{L\downarrow} - Q_{L\uparrow} \quad (A2)$$

The magnitude of $Q_{S\downarrow}$ depends on the Sun's altitude, clarity of the atmosphere and the latitude. This parameter is basically available by means of observations or model estimation ([Holtslag and van Ulden, 1983](#); [Ishola et al., 2018](#); for application to the study area). The $Q_{S\uparrow}$ is a fraction of $Q_{S\downarrow}$ reflected back to the atmosphere and is a function of the surface albedo ($\alpha = \frac{Q_{S\uparrow}}{Q_{S\downarrow}}$). A parameterization of surface albedo based on solar elevation has been investigated ([Beljaars and Bosveld, 1997](#); [de Rooy and Holtslag, 1999](#)), but for the purpose of simplicity, the recommended normal surface albedo value for short grass ($\alpha = 0.23$; [Oke, 1978](#)) is adopted in this study. The longwave terms in (A2) depend on the air (T_a) and surface (T_s) temperature and their respective emissivity.

A simple approximation of the incoming longwave radiation in relation to T_a at a reference height (1–2 m) has been reported ([Swinbank, 1963](#)). However, this simple empirical relation does not account for the influence of cloud cover thus, the adopted model in this study was that optimized by [Holtslag and van Ulden \(1983\)](#);

$$Q_{L\downarrow} = \varepsilon_a \sigma T_a^4 + c_1 \left(\frac{N}{8} \right) \quad (A3a)$$

$$\varepsilon_a = 1.2 \left(\frac{e}{T_a} \right)^{0.143} \quad (A3b)$$

c_1 is an empirical constants (60 W m^{-2}). A number of approximations have been proposed for ε_a , relating it to T_a and N ([Idso, 1981](#); [Holtslag and de Bruin, 1988](#)), and water vapor pressure (mbar) and T_a ([Brutsaert, 1982](#)). Here, we adopted the latter as shown in (A3a) for estimation of ε_a ([de Rooy and Holtslag, 1999](#)).

The estimation of $Q_{L\uparrow}$ depends primarily on the surface emissivity (ε) and T_s ,

$$Q_{L\uparrow} = \varepsilon\sigma T_s^4 + (1 - \varepsilon)Q_{L\downarrow} \quad (\text{A3c})$$

The literature indicates that, ε ranges from 0.9 – 0.95 for long to short grass (Oke, 1978) and 0.94 is used here (de Rooy and Holtslag, 1999). The T_s is critical for estimating $Q_{L\uparrow}$ and all of the non-radiative terms in the SEB and is discussed in the next section.

A.3. Surface temperature

Monin–Obukhov Similarity Theory (MOST) describes the profile relationships of scaling quantities, u_* , θ_* and L (Schayes, 1982; Berkowicz and Prahm, 1982; Holtslag and van Ulden, 1983; Manju and Sharma, 1987; Mohan and Siddiqui, 1998; de Rooy and Holtslag, 1999; van de Boer et al., 2014a). The temperature and wind speed profiles are given as,

$$\Delta\theta = \theta_a - \theta_s = \frac{\theta_*}{k} \left[\ln\left(\frac{z_a}{z_{oH}}\right) - \psi_H\left(\frac{z_a}{L}\right) + \psi_H\left(\frac{z_{oH}}{L}\right) \right] \quad (\text{A4})$$

$$u = \frac{u_*}{k} \left[\ln\left(\frac{z_a}{z_{om}}\right) - \psi_m\left(\frac{z_a}{L}\right) + \psi_m\left(\frac{z_{om}}{L}\right) \right] \quad (\text{A5})$$

In this study, the potential temperature θ_a is given, by adjusting the air temperature adiabatically for the height above the ground, as; $\theta_a = T_a + \frac{gz_a}{c_p}$ (de Rooy and Holtslag, 1999). Both z_{oH} and z_{om} (m) lengths are taken such that the downward-extrapolated profiles of (A4) produce effective temperature at the radiation level and the profiles of (A5) result in zero value for wind speed. de Rooy and Holtslag (1999) noted that for homogenous surfaces the local z_{oH} and z_{om} depend only on the local surface cover thus, the corresponding lengths used in this study are 0.01 m and 0.001 m for z_{om} and z_{oH} , respectively. ψ_H and ψ_m are the stability correction terms for heat and momentum (Beljaars and Holtslag, 1991). Using Businger-Dyer representations of similarity functions (Businger 1966, Dyer, 1967), Paulson (1970) has derived stability functions. The functions relate the fluxes of momentum and heat to their non-dimensional vertical gradients. The reader is referred to this paper for information on the derived stability functions in an unstable surface layer.

The scaling parameters in (A6) and (A7) are related with sensible heat flux Q_H and Obukhov length L (m) by;

$$\theta_* = -\frac{Q_H}{u_*\rho c_p} \quad (\text{A6})$$

$$L = \frac{u_*^2 T_a}{k\theta_* g} \quad (\text{A7})$$

The L is a dimensional height above the surface where the turbulence generated by buoyancy (heat production) equals the mechanically (shear) generated turbulence, describing a layer where stratification influence is negligible (Foken, 2006). Below this layer, shear production dominates over buoyancy. It is a parameter that helps to characterize the dynamic and thermodynamic processes within the atmospheric boundary layer and, in turn, the conditions of stability and instability of the surface layer. L is zero for neutral stratification and positive (negative) for stable (unstable) stratifications.

Estimation of scaling parameters requires the determination of the vertical gradients of wind and temperature from measurement at different levels, which are not available at typical meteorological stations where instruments are at one level (2 m above the earth's surface). Here, MOST is coupled with the radiative energy terms (described in Section 1) to solve a series of Eqs. ((A5)–(A7) and (A10)) by iteration; details are provided in de Rooy and Holtslag (1999).

The first step in the iterative procedure assumes neutral stability such that the last two terms on the right side of (A5) become zero and the initial values of u_* , Q_H and L are estimated. The procedure is repeated but with the inclusion of stability correction terms until the value of Q_H changes little ($\leq 10^{-5} \text{ W m}^{-2}$) with each subsequent iteration, which typically occurs after 5–6 steps (Mohan and Siddiqui, 1998). The resulting Q_H is then used to estimate surface temperature T_s using the relation in (A8).

$$T_s - T_a = \frac{Q_H r_a}{\rho c_p} + z_a \Gamma_d, \quad (\text{A8})$$

where r_a is the aerodynamic resistance (Section 4) and Γ_d is the dry adiabatic lapse rate (0.01 K m^{-1})

A.4. The soil heat flux

A number of relations describing the soil heat flux (Q_G) have been investigated against measured values in the literature (Nickerson and Smiley, 1975; Deardorff, 1978; Schayes, 1982; de Rooy and Holtslag, 1999; van de Boer, 2014a). de Rooy and Holtslag (1999) verified the simple approximation of Q_G proposed in van Ulden and Holtslag (1985) for short grass (A9) using the daily mean T_a ,

$$Q_G = -A_g(T_{24} - T_s) \quad (\text{A9})$$

where T_{24} is the 24-h mean of 2-m temperature (K), T_s is the estimated surface temperature (K), A_g is an empirical constant for soil heat transfer ($9 \text{ W m}^{-2} \text{ K}^{-1}$). This is the approximation used here.

A.5. The sensible and latent heat fluxes

The basic formulation of Q_H and Q_E fluxes has been simplified by the Penman–Monteith equation where the parameterized available energy ($Q_N - Q_G$) was partitioned (Monteith, 1981).

$$Q_H = \frac{r_a \gamma (Q_N - Q_G) - \rho c_p (\Delta q_a - \Delta q_s)}{(s + \gamma) r_a} \quad (A10)$$

$$Q_E = \frac{r_a s (Q_N - Q_G) + \rho c_p (\Delta q_a - \Delta q_s)}{(s + \gamma) r_a + \gamma r_s} \quad (A11)$$

The Penman–Monteith concept has been widely recommended for estimating Q_E at different locations (Allen et al., 1998).

The aerodynamic (r_a) and surface (r_s) resistances capture the atmospheric and canopy controls on the transfer of heat and moisture, respectively. The canopy can regulate the availability of soil water at the surface via stomates and distinguishes the evaporative term in the SEB. Aerodynamic resistance can be approximated using M-O similarity theory,

$$r_a = \frac{1}{k u_*} \left[\ln \left(\frac{z_a}{z_{oH}} \right) - \psi_H \left(\frac{z_a}{L} \right) + \psi_H \left(\frac{z_{oH}}{L} \right) \right] \quad (A12)$$

and is included in the iteration loop described in Section 2.

References

- Allen, R.G., Pereira, L.S., Raes, D., Smith, M., 1998. Crop Evapotranspiration. Guidelines for Computing Crop Water Requirements. FAO, Rome Irrigation and Drainage Paper No. 56.
- Allen, R.G., Tasumi, M., Trezza, R., 2007. Satellite-based energy balance for mapping evapotranspiration with internalized calibration (METRIC)—Model. *J. Irrig. Drain. Eng.* 133 (4), 380–394.
- Bastiaanssen, W.G.M., Menenti, M., Feddes, R.A., Holtslag, A.A.M., 1998. A remote sensing surface energy balance algorithm for land (SEBAL) 1. formulation. *J. Hydrol.* 212–213, 198–212.
- Beljaars, A.C.M., Holtslag, A.A.M., 1991. On flux parametrization over land surfaces for atmospheric models. *J. Appl. Meteorol.* 30, 327–341.
- Beljaars, A.C.M., Bosveld, F.C., 1997. Cabauw data for the validation of land surface parameterization schemes. *J. Clim.* 10, 1172–1193.
- Berkowicz, R., Prahm, L.P., 1982. Evaluation of the profile method for estimation of surface fluxes of momentum and heat. *Atmos. Environ.* 16, 2809–2819.
- Betts, A.K., Ball, J.H., 1995. The FIFE surface diurnal cycle climate. *J. Geophys. Res.* 100, 25679–25693.
- Betts, A.K., Ball, J.H., 1998. FIFE surface climate and site-average dataset 1987–89. *J. Atmos. Sci.* 55, 1091–1108.
- Brutsaert, W., 1982. *Evaporation into the Atmosphere: Theory, History, and Applications*. Springer, Dordrecht, the Netherlands. <https://doi.org/10.1007/978-94-017-1497-6>.
- Businger, J.A., 1966. Transfer of momentum and heat in the planetary boundary layer. In: *Proceedings of Symposium on Arctic Heat Budget and Atmospheric Circulation*. the RAND Corporation, pp. 305–331.
- Ciais, P., Reichstein, M., Viovy, N., Granier, N.A., Ogee, J., Allard, V., Buchmann, N., Aubinet, M., Bernhofer, C., Carrara, A., Chevallier, F., De Noblet, N., Friend, A., Friedlingstein, P., Grünwald, T., Heinesch, B., Kerónen, P., Knohl, A., Krinner, G., Loustau, D., Manca, G., Matteucci, G., Miglietta, F., Ourcival, J.M., Pilegaard, K., Rambal, S., Seufert, G., Soussana, J.F., Sanz, M.J., Schulze, E.D., Vesala, T., Valentini, R., 2005. Unprecedented European-level reduction in primary productivity caused by the 2003 heat and drought. *Nature* 437, 529–533.
- Chen, F., Dudhia, J., 2001. Coupling an advanced land surface–hydrology model with the Penn State–NCAR MM5 modeling system. Part I: Model implementation and sensitivity. *Mon. Weather Rev.* 129, 569–585.
- Chen, F., Mitchell, K., Schaake, J., Xue, Y., Pan, H.L., Koren, V., Duan, Q.Y., Ek, M., Betts, A., 1996. Modeling of land surface evaporation by four schemes and comparison with FIFE observations. *J. Geophys. Res.* 101, 7251–7268.
- Chen, T.H., Henderson-Sellers, A., Milly, P.C.D., Pitman, A.J., Beljaars, A.C.M., Polcher, J., Abramopoulos, F., Boone, A., Chang, S., Chen, F., Dai, Y., Desborough, C.E., Dickinson, R.E., Du Menil, L., Ek, M., Garratt, J.R., Gedney, N., Gusev, Y.M., Kim, J., Koster, R., Kowalczyk, E.A., Laval, K., Lean, J., Lettenmaier, D., Liang, X., Mahfouf, J.-F., Mengelkamp, H.-T., Mitchell, K., Nasonova, O.N., Noilhan, J., Robock, A., Rosenzweig, C., Schaake, J., Schlosser, C.A., Schulz, J.-P., Shao, Y., Shmakin, A.B., Verseghy, D.L., Wetzel, P., Wood, E.F., Xue, Y., Yang, Z.-L., Zeng, Q., 1997. Cabauw experimental results from the Project for Intercomparison of Land surface Parameterization Schemes (PILPS). *J. Clim.* 10, 1194–1215.
- Colaizzi, P.D., Evett, S.R., Howell, T.A., Tol, J.A., 2006. Comparison of five models to scale daily evapotranspiration from one-time-of-day measurements. *Trans. ASABE* 49 (5), 1409–1417.
- Creamer, R.E., Simo, I., Reidy, Carvalho, J., Fealy, R., Hallett, S., Jones, R., Holden, A., Holden, N., Hannam, J., Massey, P., Mayr, T., McDonald, E., O'Rourke, S., Sills, P., Truckell, I., Zawadzka, J., Schulte, R.P.O., 2014. Irish Soil Information System. Synthesis Report (2007-S-CD-1-S1). EPA STRIVE Programme, Wexford.
- Deardorff, J., 1978. Efficient prediction of ground surface temperature and moisture with inclusion of a layer of vegetation. *J. Geophys. Res.* 83, 1889–1903.
- De Boeck, H.J., Dreesen, F.E., Janssens, I.A., Nijs, I., 2011. Whole-system responses of experimental plant communities to climate extremes imposed in different seasons. *New Phytologist* 189, 806–817.
- De Bruin, H.A.R., Holtslag, A.A.M., 1982. A simple parameterization of the surface fluxes of sensible and latent heat during daytime compared with the Penman–Monteith concept. *J. Appl. Meteorol.* 21, 1610–1621.
- De Bruin, H.A.R., Kohsiek, W., van den Hurk, J.J.M., 1993. A verification of some methods to determine the fluxes of momentum, sensible heat, and water vapour using standard deviation and structure parameter of scalar meteorological quantities. *Bound-Layer Meteorol.* 63, 231–257.
- De Rooy, W.C., Holtslag, A.A.M., 1999. Estimation of surface radiation and energy flux densities from single-level weather data. *J. Appl. Meteorol.* 38, 526–540.
- Dwyer, N., Walsh, S., 2012. Soil moisture. Dwyer (ed). *The Status of Ireland's Climate*. Environmental Protection Agency, Wexford, Ireland, pp. 115–117.
- Dyer, A.J., 1967. The turbulent transport of heat and water vapour in an unstable atmosphere. *Q. J. R. Meteorol. Soc.* 96, 132–137.
- Dyer, A.J., 1974. A review of flux-profile relationships. *Bound-Layer Meteorol.* 7, 363–372.
- EUROSTAT, 2015. Land Cover Statistics. Available Online at https://ec.europa.eu/eurostat/statistics-explained/index.php/Land_cover_statistics#Land_cover_in_the_EU_Member_States.
- Foken, T., 2006. 50 years of the Monin–Obukhov similarity theory. *Bound-Layer Meteorol.* 119, 431–447.
- Foken, T., 2008. The energy balance closure problem: an overview. *Ecol. Appl.* 18, 1351–1367. <https://doi.org/10.1890/06-0922.1>.
- Franssen, H.J.H., Stöckli, R., Lehner, I., Rotenberg, E., Seneviratne, S.I., 2010. Energy balance closure of eddy-covariance data: a multisite analysis for European FLUXNET stations. *Agric. For. Meteorol.* 150, 1553–1567. <https://doi.org/10.1016/j.agrformet.2010.08.005>.
- Gardiner, M.J., Radford, T., 1980. Soil Associations of Ireland and their land use potentials. *Soil Surv. Bull.* 36, 39–124. Available online at <https://www.teagasc.ie/media/website/environment/soil/General.pdf>.
- Haymann, N., Lukyanov, V., Tanny, J., 2019. Effects of variable fetch and footprint on surface renewal measurements of sensible and latent heat fluxes in cotton. *Agric. For. Meteorol.* 268, 63–73.
- Heusinkveld, B.G., Jacobs, A.F.G., Holtslag, A.A.M., Berkowicz, S.M., 2004. Surface energy balance closure in an arid region: role of soil heat flux. *Agric. For. Meteorol.* 122, 21–37.
- Holtslag, A.A.M., Van Ulden, A.P., 1983. A simple scheme for daytime estimates of the surface fluxes from routine weather data. *J. Clim. Appl. Meteorol.* 22, 517–529.
- Holtslag, A.A.M., De Bruin, H.A.R., 1988. Applied modeling of the nighttime surface energy balance over land. *J. Appl. Meteorol.* 27, 689–704.
- Idso, S.B., 1981. A set of equations for full spectrum and 8 to 14 μm and 10.5 to 12.5 μm thermal radiation from cloudless skies. *Water Resour. Res.* 17, 295–304.
- Ishola, K.A., Fealy, R., Mills, G., Fealy, R., Green, S., Jimenez-Casteneda, A., Adeyeri, O.E., 2018. Developing regional calibration coefficients for estimation of hourly global solar radiation in Ireland. *Int. J. Sustain. Energy* 38 (3), 297–311. <https://doi.org/10.1080/14786451.2018.1499645>.
- Jacobs, C., 1994. Direct Impact of Atmospheric CO2 Enrichment on Regional Transpiration. Wageningen Agricultural University, pp. 179.
- Jarvis, P., 1976. The interpretation of leaf water potential and stomatal conductance found in canopies in the field. *Philos. Trans. R. Soc. Lond. B* 273, 593–610.
- Jung, M., Reichstein, M., Ciais, P., Seneviratne, S.I., Sheffield, J., Goulden, M.L., Bonan, G., Cescatti, A., Chen, J., de Jeu, R., Dolman, A.J., Eugster, W., Gerten, D., Gianelle, D., Gobron, N., Heinke, J., Kimball, J., Law, B.E., Montagnani, L., Mu, Q., Mueller, B., Oleson, K., Papale, D., Richardson, A.D., Rouspard, O., Running, S., Tomelleri, E., Viovy, N., Weber, U., Williams, C., Wood, E., Zaehe, S., Zhang, K., 2010. Recent decline in the global land evapotranspiration trend due to limited moisture supply. *Nature* 467, 951–954.
- Kaimal, J., Finnigan, J., 1994. *Atmospheric Boundary Layer Flows: Their Structure and Measurement*. Oxford University Press, Oxford, UK.
- Keane, T., Collins, J.F. (Eds.), 2004. *Climate, Weather and Irish Agriculture*. AGMET, UCD, Belfield, Dublin, pp. 4.
- Kiely, G., Leahy, P., Lewis, C., Sottocornola, M., Laine, A., Koehler, A.-K., 2018. GHG Fluxes from Terrestrial Ecosystems in Ireland. Research report No. 227. EPA Research Programme, Wexford. Available online at https://www.epa.ie/pubs/reports/research/climate/Research_Report_227.pdf.
- Kim, J., Verma, S.B., 1991. Modeling canopy stomatal conductance in a temperate grassland ecosystem. *Agric. For. Meteorol.* 55, 149–166.
- Knist, S., Goergen, K., Buonomo, E., Christensen, O.B., Colette, A., Cardoso, R.M., Fealy, R., Fernandez, J., Garcia-Diez, M., Jacob, D., Kartsios, S., Katragkou, E., Mayer, S., van Meijgaard, E., Nikulin, G., Soares, P.M.M., Sobolowski, S., Szepszo, G.,

- Teichmann, C., Vautard, R., Warrach-Sagi, K., Wulfmeyer, V., Simmer, C., 2017. Land atmosphere coupling in EURO-CORDEX evaluation experiments. *J. Geophys. Res. Atmos.* 122, 79–103.
- Lathuilliere, M.J., Johnson, M.S., Donner, S.D., 2012. Water use by terrestrial ecosystems: temporal variability in rainforest and agricultural contributions to evapotranspiration in Mato Grosso. *Brazil* 7 (2), 024024.
- Li, J., Wang, Y.-P., Duan, Q., Lu, X., Pak, B., Wiltshire, A., Robertson, E., Ziehn, T., 2016. Quantification and attribution of errors in the simulated annual gross primary production and latent heat fluxes by two global land surface models. *J. Adv. Model. Earth Syst.* 8, 1270–1288.
- Long, D., Singh, V.P., 2013. Assessing the impact of end-member selection on the accuracy of satellite-based spatial variability models for actual evapotranspiration estimation. *Water Resour. Res.* 49 (5), 2601–2618.
- Lu, J., Tang, R., Tang, H., Li, Z.-L., 2014. A new parameterization scheme for estimating surface energy fluxes with continuous surface temperature, air temperature, and surface net radiation measurements. *Water Resour. Res.* 50, 1245–1259.
- Ma, N., Zhang, Y., Xu, C.-Y., Szilagyi, J., 2015. Modeling actual evapotranspiration with routine meteorological variables in the data-scarce region of the Tibetan Plateau: Comparisons and implications. *J. Geophys. Res. Biogeosci.* 120, 1638–1657.
- Manju, K., Sharma, O.P., 1987. Estimation of turbulence parameters for application in air pollution modelling. *Mausam* 38, 303–308.
- Mauder, M., Desjardins, R.L., MacPherson, I., 2007. Scale analysis of airborne flux measurements over heterogeneous terrain in a boreal ecosystem. *J. Geophys. Res.* 112, D13112.
- McDonnell, J., Lambkin, K., Fealy, R., Hennessy, D., Shalloo, L., Brophy, C., 2018. Verification and bias correction of ECMWF forecasts for Irish weather stations to evaluate their potential usefulness in grass growth modelling. *Meteorol. Appl.* 25, 292–301.
- McEniry, J., Crosson, P., Finneran, E., McGee, M., Keady, T.W.J., O'Kiely, P., 2013. How much grassland biomass is available in Ireland in excess of livestock requirements? *Irish J. Agric. Food Res.* 52, 67–80.
- Mohan, M., Siddiqui, T.A., 1998. Applied modeling of surface fluxes under different stability regimes. *J. Appl. Meteorol.* 37, 1055–1067.
- Moncrieff, J., Valentini, R., Greco, S., Seufert, G., Ciccioli, P., 1997a. Trace gas exchange over terrestrial ecosystems: methods and perspectives in micrometeorology. *J. Exp. Bot.* 48 (310), 1133–1142.
- Moncrieff, J.B., Massheder, J.M., Debruin, H., Elbers, J., Friborg, T., Heusinkveld, B., Kabat, P., Scott, S., Soegaard, H., Verhoef, A., 1997b. A system to measure surface fluxes of momentum, sensible heat, water vapour and carbon dioxide. *J. Hydrol.* 189, 589–611.
- Monteith, J., 1981. Evaporation and surface temperature. *Q. J. R. Meteorol. Soc.* 107, 1–27.
- Nickerson, E.C., Smiley, V.E., 1975. Surface energy budget parameterizations for urban scale models. *J. Appl. Meteorol.* 14, 297–300.
- Niyogi, D., Raman, S., 1997. Comparison of four different stomatal resistance schemes using FIFE data. *J. Appl. Meteorol.* 36, 903–917.
- Ní Chonubhair, Ó., Osborne, B., Finnan, J., Lanigan, G., 2017. Comparative assessment of ecosystem C exchange in *Miscanthus* and reed canary grass during early establishment. *GCB Bioenergy* 9, 280–298. <https://doi.org/10.1111/gcb.12343>.
- Norman, J.M., Kustas, W.P., Humes, K.S., 1995. A two-source approach for estimating soil and vegetation energy fluxes in observations of directional radiometric surface temperature. *Agric. For. Meteorol.* 77, 263–293.
- Oke, T.R., 1978. *Boundary Layer Climates*. Methuen, pp. 372.
- Papale, D., Reichstein, M., Aubinet, M., Canfora, E., Bernhofer, C., Longdoz, B., Kutsch, W., Rambal, S., Valentini, R., Vesala, T., Yakir, D., 2006. Towards a standardized processing of net ecosystem exchange measured with eddy covariance technique: algorithms and uncertainty estimation. *Biogeosciences* 3, 571–583.
- Paulson, C.A., 1970. The mathematical representation of wind speed and temperature profiles in the unstable atmospheric surface layer. *J. Appl. Meteorol.* 9, 857–861.
- Peel, M.C., Finlayson, B.L., McMahon, T.A., 2007. Updated world map of the Köppen-Geiger climate classification. *Hydrol. Earth Syst. Sci.* 11, 1633–1644.
- Peichl, M., Carton, O., Kiely, G., 2012. Management and climate effects on carbon dioxide and energy exchanges in a maritime grasslands. *Agric. Ecosyst. Environ.* 158, 132–146.
- Reichstein, M., Ciais, P., Papale, D., Valentini, R., Running, S., Viovy, N., Cramer, W., Granier, A., Oge, J., Allard, V., Aubinet, M., Bernhofer, C., Buchmann, N., Carrara, A., Grünwald, T., Heimann, M., Heinesch, B., Knohl, A., Kutsch, W., Loustau, D., Manca, G., Matteucci, G., Miglietta, F., Ourcival, J., Pilegaard, K., Pumpanen, J., Rambal, S., Schaphoff, S., Seufert, G., Soussana, J., Sanz, M., Vesala, T., Zhao, M., 2007. Reduction of ecosystem productivity and respiration during the European summer 2003 climate anomaly: a joint flux tower, remote sensing and modelling analysis. *Global Change Biol.* 13, 634–651.
- Ronda, R.J., de Bruin, H.A.R., Holtslag, A.A.M., 2001. Representation of the canopy conductance in modeling the surface energy budget for low vegetation. *J. Appl. Meteorol.* 40, 1431–1444.
- Russell, G., 1980. Crop evaporation, surface resistance and soil water status. *Agric. Meteorol.* 21, 213–226.
- Schayes, G., 1982. Direct determination of diffusivity profiles from synoptic reports. *J. Atmos. Sci.* 27, 1122–1137.
- Seneviratne, S.I., Corti, T., Davin, E.L., Hirschi, M., Jaeger, E.B., Lehner, I., Orlowsky, B., Teuling, A.J., 2010. Investigating soil moisture-climate interactions in a changing climate: a review. *Earth Sci. Rev.* 99 (3–4), 125–161.
- Sherratt, D.J., Wheeler, H.S., 1984. The use of surface resistance-soil moisture relationships in soil water budget models. *Agric. For. Meteorol.* 31, 143–157.
- Shi, Q., Liang, S., 2014. Surface-sensible and latent heat fluxes over the Tibetan Plateau from ground measurements, reanalysis, and satellite data. *Atmos. Chem. Phys.* 14, 5659–5677.
- Shuttleworth, W.J., 1993. Evaporation. In: Maidment, D.R. (Ed.), *Handbook of Hydrology*. McGraw-Hill Inc, New York, pp. 4.1–4.53.
- Sobrinho, J.A., Gomez, M., Jimenez-Muoz, J.C., Olioso, A., 2007. Application of a simple algorithm to estimate daily evapotranspiration from NOAA-AVHRR images for the Iberian Peninsula. *Remote Sens. Environ.* 110 (2), 139–148.
- Sottocornola, M., Kiely, G., 2010a. Hydro-meteorological controls on the CO₂ exchange variation in an Irish blanket bog. *Agric. For. Meteorol.* 150 (2), 287–297.
- Sottocornola, M., Kiely, G., 2010b. Energy fluxes and evaporation mechanisms in an Atlantic blanket bog in southwestern Ireland. *Water Resour. Res.* 46 (11), W11524.
- Stewart, J.B., 1988. Modeling surface conductance of pine forest. *Agric. For. Meteorol.* 43, 19–35.
- Stewart, J.B., Gay, L.W., 1989. Preliminary modeling of transpiration from FIFE site in Kansas, USA. *Agric. For. Meteorol.* 48, 305–316.
- Stoy, P.C., Mauder, M., Foken, T., Marcolla, B., Boegh, E., Ibrom, A., Arain, M.A., Arneth, A., Aurela, M., Bernhofer, C., Cescatti, A., Dellwik, E., Duce, P., Gianelle, D., van Gorsel, E., Kiely, G., Knohl, A., Margolis, H., McCaughey, H., Merbold, L., Montagnani, L., Papale, D., Reichstein, M., Saunders, M., Serrano-Ortiz, P., Sottocornola, M., Spano, D., Vaccari, F., Varlagin, A., 2013. A data-driven analysis of energy balance closure across FLUXNET research sites: the role of landscape scale heterogeneity. *Agric. For. Meteorol.* 171–172, 137–152. <https://doi.org/10.1016/j.agrformet.2012.11.004>.
- Su, Z., 2002. The Surface Energy Balance System (SEBS) for estimation of turbulent heat fluxes. *Hydrol. Earth Syst. Sci.* 6 (1), 85–99.
- Swinbank, W.C., 1963. Longwave radiation from clear skies. *Q. J. R. Meteorol. Soc.* 89, 339–448.
- Tang, R.L., Li, Z.-L., Sun, X.M., 2013. Temporal upscaling of instantaneous evapotranspiration: an intercomparison of four methods using eddy covariance measurements and MODIS data. *Remote Sens. Environ.* 138, 102–118.
- Teuling, A.J., Seneviratne, S.I., Williams, C., Troch, P.A., 2006. Observed timescales of evapotranspiration response to soil moisture. *Geophys. Res. Lett.* 33, L23403.
- Twine, T.E., Kustas, W.P., Norman, J.M., Cook, D.R., Houser, P.R., Meyers, T.P., Prueger, J.H., Starks, P.J., Wesely, M.L., 2000. Correcting eddy-covariance flux underestimates over a grassland. *Agric. For. Meteorol.* 103 (3), 279–300.
- van de Boer, A., Moene, A.F., Schu'temeyer, D., 2013. Sensitivity and uncertainty of analytical footprint models according to a combined natural tracer and ensemble approach. *Agric. Forest. Meteorol.* 169, 1–11.
- van de Boer, A., Moene, A.F., Graf, A., Simmer, C., Holtslag, A.A.M., 2014a. Estimation of the refractive index structure parameter from single-level daytime routine weather data. *Appl. Opt.* 1–20. <https://doi.org/10.1364/AO.53.005944>.
- van de Boer, A., Moene, A.F., Graf, A., Schu'temeyer, D., Simmer, C., 2014b. Detection of entrainment influences on surface-layer measurements and extension of Monin-Obukhov similarity theory. *Bound-Layer Meteorol.* 152, 19–44.
- van den Hurk, B.J.J.M., Viterbo, P., Beljaars, A.C.M. and Betts, A.K., 2000. Offline Validation of the ERA40 Surface Scheme. Technical Report ECMWF, 43 p.
- van den Hurk, B.J.J.M., Viterbo, P., Los, S.O., 2003. Impact of Leaf Area Index seasonality on the annual land surface evaporation in a global circulation model. *J. Geophys. Res.* 108 (D6), 4191.
- van Ulden, A.P., Holtslag, A.A.M., 1985. Estimation of atmospheric boundary layer parameters for diffusion applications. *J. Clim. Appl. Meteorol.* 24, 1196–1207.
- Vickers, D., Mahrt, L., 1997. Quality control and flux sampling problems for tower and aircraft data. *J. Atmos. Ocean. Technol.* 14, 512–526.
- Viterbo, P., Beljaars, A., 1995. An improved land-surface parameterization scheme in the ECMWF model and its validation. *J. Clim.* 8, 2716–2748.
- Webb, E., Pearman, G., Leuning, R., 1980. Correction of flux measurements for density effects due to heat and water-vapor transfer. *Q. J. R. Meteorol. Soc.* 106, 85–100.
- Walsh S., 2012. A Summary of Climate Averages for Ireland, 1981 – 2010. MET Eireann Climatological Note No. 14, Dublin. Available Online at <https://www.met.ie/climate-ireland/SummaryClimAvgs.pdf>.
- Wilson, K., Goldstein, A., Falge, E., Aubinet, M., Baldocchi, D., Berbigier, P., Bernhofer, C., Ceulemans, R., Dolman, H., Field, C., Grelle, A., Ibrom, A., Law, B.E., Kowalski, A., Meyers, T., Moncrieff, J., Monson, R., Oechel, W., Tenhunen, J., Valentini, R., Verma, S., 2002. Energy balance closure at FLUXNET sites. *Agric. For. Meteorol. FLUXNET 2000 Synth.* 113, 223–243. [https://doi.org/10.1016/S0168-1923\(02\)00109-0](https://doi.org/10.1016/S0168-1923(02)00109-0).
- Zhang, L., Xiao, J., Li, J., Wang, K., Lei, L., Guo, H., 2012. The 2010 spring drought reduced primary productivity in southwestern China. *Environ. Res. Lett.* 7 (4), 1748–9326.

1 **A model framework to investigate the role of anomalous land surface processes in the amplification**
2 **of summer drought across Ireland during 2018**

3 Kazeem A. Ishola^{1,3*}, Gerald Mills², Reamonn M. Fealy³, Rowan Fealy¹

4 ¹ *Irish Climate Analysis and Research Units (ICARUS), Department of Geography, Maynooth University, Ireland.*

5 ² *School of Geography, University College Dublin, Co. Dublin, Ireland.*

6 ³ *Teagasc Agrifood Business and Spatial Analysis Department, Ashtown, Co. Dublin, Ireland.*

7 Correspondence: [*kazeem.ishola.2018@mumail.ie](mailto:kazeem.ishola.2018@mumail.ie)

8 **Abstract**

9 Due to its latitude and ample year-round rainfall, Ireland is typically an energy limited regime in the
10 context of soil moisture availability and evapotranspiration. However, during the summer of 2018,
11 regions within the country displayed significant soil moisture deficits, associated with anomalous
12 atmospheric forcing conditions, with consequent impacts on the surface energy balance. Here, we
13 explore the utility of a physically based land surface scheme coupled with observational, global
14 gridded reanalysis and satellite-derived data products to analyse the spatial and temporal evolution
15 of the 2018 summer drought event in Ireland over grassland, which represent the dominant
16 agricultural land-cover. While the surface-air energy exchanges were initially dominated by
17 atmospheric anomalies, soil moisture constraints became increasingly important in regulating these
18 exchanges, as the accumulated rainfall deficit increased throughout the summer months. This was
19 particularly evident over the freer draining soils in the east and southeast of the country. From late
20 June 2018, we identify a strong linear coupling between soil moisture and both evapotranspiration
21 and vegetation response, suggesting a shift from an energy limited evapotranspiration regime into a
22 dry or soil water limited regime. Applying segmented regression models, the study quantifies a critical
23 soil moisture threshold as a key determinant of the transition from wet to dry evaporative regimes.
24 These findings are important to understand the soil moisture context under which land-atmosphere
25 couplings are strongest in water-limited regimes across the country and should help improve the
26 treatment of soil parameters in weather prediction models, required for sub-seasonal and seasonal
27 forecasts, consequently enhancing early warning systems of summer climate extremes in the future.

28 **Keywords.** Drought; Land-atmosphere interactions; Evaporative fraction; Soil moisture; Climate
29 extremes; Surface energy budget

30 **1. Introduction**

31 During the past two decades, regions across Europe have experienced hot summers and drought
32 events, which varied in terms of the development, frequency, intensity and impacts (e.g., Buras et al.,
33 2019). Droughts are typically categorised as either meteorological (high rainfall deficits), hydrological
34 (extremely low groundwater, lakes, streamflow, etc.), agricultural (high soil moisture deficits, affecting
35 vegetation) or socioeconomic, when the demand for water exceeds the supply (van Loon et al., 2015;
36 Falzoi et al., 2019). A meteorological drought precedes agricultural drought through reduction in soil
37 water storage and the water available for uptake by roots (Buitink et al., 2020); but to fully understand
38 the development of these events, other factors such as changes to soil and biophysical properties,
39 must be taken into account. While there have been many studies on agricultural droughts across

40 Europe (e.g. Noone et al., 2017; Falzoi et al., 2019; Buitink et al., 2020; van Hateren et al., 2021), there
41 have been few investigations in Ireland, where such events are rare.

42 The 2018 European summer (April to August) was associated with a higher near-surface temperature
43 and lower rainfall receipts relative to the long-term (1981-2010) mean (Magnusson et al., 2018). These
44 conditions were created by a large and persistent anticyclonic system located over central and
45 northern Europe, which blocked the normal passage of Atlantic storms (Buras et al., 2019; Kornhuber
46 et al., 2019; Rösner et al., 2019; Dirmeyer et al., 2021). The resulting heatwave and drought were
47 extreme, surpassing previous records with several stations across Europe reporting record breaking
48 daily maximum temperatures (Buras et al., 2019; Rösner et al., 2019; Dirmeyer et al., 2021). Ireland,
49 situated on the western maritime fringe of Europe, experienced unusually warm and dry conditions
50 (Moore, 2020) that impacted on grass growth productivity and farm income (Dillon et al., 2018). These
51 impacts were preconditioned by the cold ground temperature arising from the exceptional snow fall
52 that was associated with cold airmass advecting around high pressure from Siberia towards the
53 country dubbed the 'Beast from the East', from the end of February and lasted for about a week,
54 causing a very late onset of grass growth season by about a month relative to an average year (Dillon
55 et al., 2018).

56 When drought and heatwave events evolve simultaneously they can reinforce each other. The
57 occurrence of these 'compound' events and the associated land-air exchanges have been observed
58 across Europe over the last few decades (e.g., 2003, 2010, 2015, 2018). For instance, Black et al. (2004)
59 demonstrated that the events of August 2003 across Europe were exacerbated by the persistence of
60 the anticyclonic blockage that enhanced net radiative flux and reduced water availability, such that
61 the surface-air sensible heat flux was increased leading to elevated air temperatures (that is, a positive
62 feedback) and increased atmospheric water demand. Compound events can result in a wide range of
63 impacts including water scarcity, tree mortality, agricultural loss, wildfires and air pollution with
64 deleterious effects on ecosystems, human health and well-being and agricultural productivity (Fink et
65 al., 2004; Conti et al., 2005; García-Herrera et al., 2010; Dole et al., 2011; Alexander, 2011; Zscheischler
66 et al., 2018; Miralles et al., 2019; Schuldt et al., 2020).

67 The transition from meteorological to agricultural drought is closely linked to the plant available soil
68 moisture (θ) during the growing season. Broadly speaking, evapotranspiration (ET) can be categorised
69 into energy- and water-limited regimes. In the latter, increasing soil moisture deficits and atmospheric
70 evaporative demands causes vegetation to close stomata to limit water loss to the atmosphere; the
71 associated decrease in the latent heat flux with surplus energy being channelled into sensible heat
72 initiates the positive feedback with near surface air temperature described above (Seneviratne et al.,
73 2010; Miralles et al., 2019). The transition from energy- to water-limited regimes occurs at a critical
74 soil moisture (θ_c) value and landscapes can switch between regimes over the course of a year
75 depending on precipitation, available surface energy, atmospheric demand and the status of
76 vegetative cover (Knist et al., 2017).

77 The evaporative fraction (EF), defined as the ratio of latent heat flux and available energy at the land
78 surface and can be expressed as a function of θ (Seneviratne et al., 2010; Buitink et al., 2020;
79 Denissen et al., 2021), has previously been used to evaluate vegetative productivity. Buitink et al.
80 (2020) used a similar framework but replaced the EF with satellite-derived ecosystem indicators, near
81 infrared reflectance of vegetation (NIRv) and vegetation optical depth (VOD), to allow for a more
82 precise analysis of how productivity was related to θ during the 2018 drought event at two sites in the

83 Netherlands. Other studies have also derived values for θ_c based on observations and model outputs
84 using alternative theoretical frameworks (Akbar et al., 2018; Haghghi et al., 2018; Feldman et al.,
85 2019; Denissen et al., 2020). Determining θ_c is also critical for predicting the timescales of plant
86 responses, ET decay and consequently the emergence and progression of agricultural drought.

87 This research uses a simple land surface scheme, which employs readily available meteorological and
88 surface data, to investigate the role of land-atmosphere exchange processes across Ireland during the
89 2018 summer drought. The study seeks to analyse (i) the evolution of the 2018 drought at sub seasonal
90 and regional scales; (ii) the anomalies in simulated land-atmosphere energy exchanges; and, (iii) the
91 role of soil moisture in modulating land-atmosphere exchange processes. We combine a physically-
92 based land surface scheme with observational data, along with readily accessible global gridded
93 reanalysis and satellite-derived data products to address these objectives. The scheme used here has
94 previously been established as having the capability to reproduce measured surface fluxes (de Rooy
95 and Holtslag, 1999; Ishola et al., 2020). The method outlined offers the potential for improving
96 management strategies, particularly during anomalous warm and dry events, and for delineating areas
97 with differential drought responses.

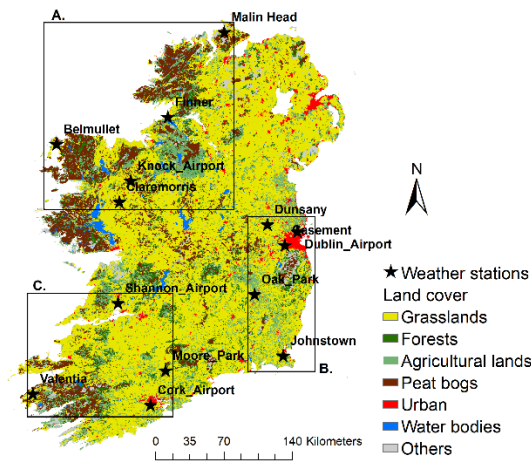
98

99 **2. Materials and Methods**

100 *2.1 Study area*

101 The Island of Ireland (Figure 1) has a maritime temperate climate (Peel et al., 2007) with a long-term
102 (1981-2010) mean daily maximum temperature of between 18 and 20 °C in summer. In winter, daily
103 minimum temperatures occasionally drop below 0 °C, but average winter temperatures are generally
104 around 8 °C. Ireland receives an annual average rainfall of over 1200 mm, distributed throughout the
105 year. The spatial distribution of rainfall follows a west to east gradient; higher rainfall receipts (~1000
106 – 1400 mm) typically occur on the west coast and particularly in the upland regions where receipts
107 can exceed 2000 mm largely associated with topographic interactions with the prevailing maritime
108 air. Lower rainfall amounts are experienced in the east of the country (~750-1000 mm) (Met Éireann).
109 A summary description of the climatology of the region is reported in Walsh (2012).

110 The most important biome in Ireland is that of grassland, which accounts for 56% of the total land
111 area (McEniry et al., 2013) and more than 90% of agricultural land cover (Figure 1). Due to the
112 favourable growing conditions, grass growth can occur throughout the year, particularly along the
113 coastal margins in the south of the country. The low cost of grass production here offers a significant
114 competitive advantage to farmers and positively impacts on the low economic margins associated
115 with agricultural production. However, grass growth is more problematic in the wet soils in the west
116 and north of the country due to the heavier (clayey) soils (Keane and Collins, 2004), compared to the
117 more freely draining soils that characterize the east and southeast region (McDonnell et al., 2018;
118 Creamer et al., 2014). Detailed soil properties and information for Ireland is available from Creamer
119 et al. (2014).



120

121 **Figure 1.** Map of the study area showing the locations of selected weather stations and the dominant land cover
 122 types from 2018 CORINE Land cover product. The boxes A, B and C comprise of the stations grouped on the basis
 123 of similar precipitation regimes and agricultural regions.

124 *2.2 Observational data*

125 Hourly meteorological observations were obtained from fourteen automatic weather stations (AWS)
 126 across Ireland (Table 1 and Figure 1) from the Irish national meteorological service, Met Éireann.
 127 These stations are sited over short grass cover, consistent with World Meteorological Organisation
 128 (WMO) guidelines and report on global solar radiation ($Q_{s\downarrow}$, $W\ m^{-2}$) or sun duration (hours), air
 129 temperature ($^{\circ}C$), relative humidity (%), pressure (kPa), wind speed ($m\ s^{-1}$) and precipitation (mm).
 130 Cloud amount is required as an input but, as the observations are only available at relatively few
 131 stations, we subsequently exclude the cloud input in the land surface scheme to ensure consistency
 132 in approach across all stations. For stations where only sunshine hours are available, including Knock
 133 Airport, Casement (Aerodrome), Shannon Airport and Cork Airport, hourly $Q_{s\downarrow}$ data were estimated
 134 for these stations based on observations of sunshine duration following Allen et al. (1998) and Ishola
 135 et al. (2018). The hourly meteorological observations were obtained for the summer months of May
 136 to August – the period over which the 2018 drought began and subsequently intensified. Due to the
 137 differences in the start of operations of a number of the AWS, we focus the main analysis on the most
 138 recent decade (2010-2019) to ensure consistent temporal coverage of meteorological data across all
 139 stations.

140 *2.3 Gridded meteorological data*

141 Gridded daily total precipitation data for Ireland was also obtained from Met Éireann for the period
 142 from 1999 to 2019. This data, available at $1\ km^2$ grid resolution, was generated using interpolation
 143 techniques applied to in-situ rainfall data from over 500 rainfall stations distributed across the
 144 Republic of Ireland (Walsh, 2012).

145 The land surface scheme employed here requires soil moisture measurements but these are not part
 146 of routine observational practice in Ireland, as in many other countries, and therefore we employed
 147 gridded reanalysis soil moisture data from the European Centre for Medium Range Weather

148 Forecasting (ECMWF) ERA5-Land data, obtained from the C3S Copernicus Climate Data Store. ERA5-
 149 Land is the latest global reanalysis product from ECMWF, which employs improved historical
 150 observations and is run at a finer spatial resolution (atmosphere 0.25°; land 0.1°) relative to its
 151 predecessor, ERA-Interim (Hersbach and Dee, 2016). This product has also been evaluated at the
 152 global scale (e.g., Li et al., 2020). We used ERA5-Land hourly volumetric water content (θ) ($\text{m}^3 \text{m}^{-3}$) in
 153 the top soil layer (0-7 cm), for the period 1999 to 2019.

154

Station	Lat/Long (°N, °W)	Elevation (m)	Soil type	Drainage class	Region	Zone
Belmullet	54.228, 10.007	9	Peat	Poor	Northwest	
Claremorris	53.711, 8.991	69	Coarse loam	Well	Northwest	
Finner	54.494, 8.243	33	Coarse loam	Poor	North	A
Knock Airport	53.906, 8.817	201	Fine loam	Imperfect	Northwest	
Malin Head	55.372, 7.339	20	Peat	Poor	North	
Casement	53.306, 6.439	91	Fine loam	Moderate	East	
Dublin Airport	53.428, 6.241	71	Fine loam	Moderate	East	
Dunsany	53.499, 6.699	83	Fine loam	Moderate	East	B
Johnstown Castle	52.292, 6.489	52	Fine loam	Imperfect	Southeast	
Oak Park	52.861, 6.915	62	Fine loam	Moderate	Southeast	
Cork Airport	51.847, 8.486	155	Fine loam	Well	South	
Moorepark	52.164, 8.264	46	Coarse loam	Well	South	C
Shannon Airport	52.689, 8.918	15	Loam	Well	Southwest	
Valentia	51.929, 10.239	24	Coarse loam	Well	Southwest	

155 **Table 1.** Characteristics of the selected grassland synoptic stations. The soil types and drainage categories are
 156 based on the data from Irish Soil Information System (Creamer et al., 2014). The grouped zones, A, B and C,
 157 comprise of stations with similar precipitation regimes.

158

159 2.4 Satellite-derived data products

160 The leaf area index (LAI) quantifies the greenness of plants and can be observed per unit horizontal
 161 surface area from space. LAI was obtained from the Copernicus Global Land Service (CGLS), which is
 162 derived from SPOT-VGT and PROBA-V, prior to and from 2014, respectively.. The CGLS LAI product,
 163 beginning in 1999, employed SPOT-VGT; the method by Baret et al. (2013) has been used to retrieve
 164 LAI from PROBA-V. Here, we use the CGLS LAI GEOV2 product which is at 1 km² spatial and 10-day
 165 temporal resolution (Albergel et al., 2019). The product development is outlined by Verger et al.
 166 (2014).

167 The land surface temperature (T_s) is a critical parameter that governs the land-atmosphere coupling
 168 and can be used to evaluate model derived estimates of surface energy fluxes. We acquired T_s from
 169 the Moderate Resolution Imaging Spectroradiometer (MODIS) (MOD11A1, version 6) from the Land
 170 Processes Distributed Active Archive Center (LP DAAC) (Wan et al., 2015). In addition, the near-
 171 infrared radiation reflected by vegetation (NIRv) is an important index for monitoring ecosystem
 172 functioning and has previously been employed to link soil moisture induced vegetation stress with
 173 gross primary productivity (GPP) at various scales during drought events (Badgley et al., 2017; 2019;
 174 Baldocchi et al., 2020; Buitink et al., 2020). The NIRv index is derived from the product of the

175 normalized difference vegetation index (NDVI) and near infra-red (NIR) reflectance ($NIR_v = NDVI \times NIR$)
 176 (e.g., Badgley et al., 2017). We obtained daily MODIS (MCD43A4, version 6) red (620-670 nm) and NIR
 177 (841-876 nm) nadir-adjusted reflectance images from the same source (Schaaf and Wang, 2015). The
 178 MODIS T_s and reflectance images are available at 1 km and 500 m resolutions, respectively and were
 179 obtained for the period of 2010 to 2019 to correspond with the period of AWS measurements outlined
 180 in Section 2.2. The T_s data obtained was derived from the Terra satellite which acquires data every 1
 181 to 2 days and passes from north to south over the Equator in the morning, while reflectance data are
 182 derived from 16-day composites of MODIS Terra and Aqua satellite products. A summary description
 183 of data used is provided in Table 2.

184

Product	Variable	Resolution (Spatial, temporal)	Temporal coverage	Source
In situ	Global solar radiation/sunshine duration, 2-m temperature, relative humidity, m.s.l pressure, wind speed	Hourly	2010–2019	Met Éireann
Gridded	Precipitation	1 km ² , Daily	1999-2019	Met Éireann
	ERA5-Land surface volumetric water content (0-7cm)	0.1°, Hourly	1999-2019	Hersbach and Dee (2016)
Satellite	GEOV2 Leaf area index	1 km ² , 10-day	1999-2019	Verger et al. (2014)
	MOD11A1 land surface temperature	1 km, Daily	2010-2019	Wan et al. (2015)
	MCD43A4 nadir-adjusted red and near-infrared reflectances	500 m, Daily	2010-2019	Schaaf and Wang (2015)

185 **Table 2.** A summary description of in-situ, gridded and satellite-derived data products used in this study.

186

187 *2.5 Framework of Land-atmosphere heat and moisture exchanges*

188 Land-atmosphere interactions are best understood within a surface energy budget (SEB) framework
 189 that captures the diagnostic processes responsible for the variation in weather conditions. The SEB
 190 expresses the partitioning of net radiation (Q_N , $W m^{-2}$) into sensible (Q_H , $W m^{-2}$) and latent (Q_E , $W m^{-2}$)
 191 heat exchanges with the overlying air and heat exchange with the soil (Q_G , $W m^{-2}$),

$$192 \quad Q_N - Q_G = Q_H + Q_E, \quad (1)$$

193 Q_N accounts for the radiative factors including shortwave radiation received at ($Q_{S\downarrow}$, $W m^{-2}$), and
 194 reflected from ($Q_{S\uparrow}$, $W m^{-2}$) the surface, and longwave radiation received ($Q_{L\downarrow}$, $W m^{-2}$) and emitted
 195 ($Q_{L\uparrow}$, $W m^{-2}$), as follows,

$$196 \quad Q_N = Q_{S\downarrow} - Q_{S\uparrow} + Q_{L\downarrow} - Q_{L\uparrow} \quad (2)$$

197 The land surface scheme (LSS) used here simulates the terms of the SEB using routine weather
 198 observations and the widely used Monin-Obhukov Similarity Theory (MOST); see de Rooy and Holtslag
 199 (1999), Jung et al., (2010), van Heerwaarden et al. (2010) and Lu et al. (2014). MOST uses profile
 200 relationships of wind, near-surface air temperature, and humidity, to describe the vertical exchanges
 201 of momentum, sensible heat (Q_H), and moisture (Q_E), respectively (Paulson, 1970). In addition, the
 202 scheme incorporates simplified parameterizations of radiation components (Q_N) and soil heat flux
 203 (Q_G), following van Ulden and Holtslag (1985); evapotranspiration is obtained using the Penman-
 204 Monteith model (Monteith, 1981). We employ the LSS to simulate hourly surface energy fluxes for
 205 mid-day hours (10-15 hr) from May to August, for the period 2010 to 2019, representing the period
 206 when the hourly forcing meteorological data is available. We focus on the mid-day portion of the day
 207 when the bulk of the surface-air exchanges associated with vegetated surfaces take place. The
 208 application of the LSS approach is fully described in Ishola et al. (2020) and the software
 209 implementation is available from Ishola et al. (2021).

210 During soil water limiting conditions, Q_E becomes constrained by the surface resistance (r_s), which
 211 follows the approach developed by the Jarvis (1976) as implemented by Beljaars and Bosveld (1997),
 212 van de Boer et al. (2014) and Ishola et al. (2020),

$$213 \quad r_s = f_r \frac{r_{s,min}}{LAI} F_{Q_{s\downarrow}}^{-1} F_{\Delta q}^{-1} F_{\theta}^{-1}, \quad (3)$$

214 where f_r is an empirical constant (0.47), $r_{s,min}$ is the minimum stomatal resistance ($110 s m^{-1}$), LAI is
 215 the leaf area index, taken as $2 m^2 m^{-2}$ and F represents dimensionless stress functions (ranging from
 216 0-1) which account for the contributions of incoming shortwave radiation ($Q_{s\downarrow}$), atmospheric moisture
 217 deficit (Δq), and soil moisture content (θ). $F_{Q_{s\downarrow}}$ is taken as

$$218 \quad F_{Q_{s\downarrow}} = \frac{Q_{s\downarrow}(S_{rm} - S_r)}{S_{rm}Q_{s\downarrow} + S_r(S_{rm} - 2Q_{s\downarrow})}, \quad (3a)$$

219 where the empirical coefficients S_{rm} and S_r are $1000 W m^{-2}$ and $230 W m^{-2}$. The moisture deficit
 220 function is,

$$221 \quad F_{\Delta q} = \frac{1}{(1 + h_s \Delta q)}, \quad (3b)$$

222 where the empirical coefficient h_s is $0.16 kg kg^{-1}$. The soil moisture function is

$$223 \quad F_{\theta} = 1 \quad \text{for } \theta > \theta_{FC}, \quad (3c)$$

$$224 \quad F_{\theta} = 1 + c_{soil}(\theta - \theta_{FC}) \quad \text{for } \theta < \theta_{FC}, \quad (3d)$$

225 where θ_{FC} ($0.3 m^3 m^{-3}$) is the assumed volumetric water content at field capacity. The soil moisture
 226 coefficient c_{soil} , is taken as $4.3 m^3 m^{-3}$ at all sites (Ishola et al., 2020).

227 The r_s coefficients used here were previously derived from observations at a number of sites in Ireland
 228 where θ measurements were available. However, as the present study employs gridded θ derived
 229 from ERA5-Land reanalysis data, the LSS may underestimate r_s and consequently, overestimate
 230 Q_E due to potential overestimation of soil water (Dirmeyer et al., 2021) (Figure S1). We employ a
 231 default value for θ_{FC} of $0.3 \text{ m}^3 \text{ m}^{-3}$ as there is little information on field capacity across Ireland and
 232 this value is similar to that employed in the ERA5-Land model (Balsamo et al., 2009). Despite this
 233 simplifying assumption, the general tendency of soil drying and its impact on evapotranspiration
 234 should be captured. This is on the basis that soil moisture-evapotranspiration signals are generally
 235 recognized to occur below the assumed θ_{FC} value, typically between 50 and 80 % of θ_{FC} (e.g.,
 236 Seneviratne et al., 2010). The parameter c_{soil} has been identified as the key physical property
 237 influencing the sensitivity and performance of the LSS (Ishola et al., 2020). We employ the calibrated
 238 value ($4.3 \text{ m}^3 \text{ m}^{-3}$), applied to both wet and seasonally dry soils, and allows us to distinguish soil type
 239 response.

240 Furthermore, we calculated two biophysical metrics, land surface temperature (T_s) (van de Boer et al.,
 241 2014) and evaporative fraction (EF), employing fluxes derived from the LSS as follows

$$242 \quad T_s = T_a + \frac{Q_H r_a}{\rho c_p} + z_a \Gamma_d, \quad (4)$$

$$243 \quad EF = \frac{Q_E}{Q_N - Q_G}, \quad (5)$$

244 where T_a is the near-surface temperature, r_a is the aerodynamic resistance, z_a is the reference height,
 245 Γ_d is the dry adiabatic lapse rate, ρ is the air density and c_p is the specific heat capacity of air. These
 246 biophysical metrics are important for understanding the role of land-atmosphere feedbacks on
 247 extreme weather events such as heatwaves and drought.

248

249 2.6 Data analysis

250 We initially calculated anomalies (Z-score) of monthly precipitation, volumetric water content (θ) and
 251 LAI for the individual months of May to August, relative to the 1999 to 2019 period, to place the 2018
 252 summer drought event in the context of previous such events. For the purposes of presenting the
 253 results from the LSS, we subsequently grouped the individual 14 AWS stations into broadly
 254 representative geographic zones (Figure 1) on the basis of a general definition of agricultural regions
 255 (e.g. Green, 2019) and initial evaluation of precipitation. For example, the northwest (Zone A) tends
 256 to be wetter, due to its proximity to Atlantic storm tracks, experiences cooler temperature in summer
 257 relative to other regions, and has a large proportion of peat soils; the east coast (Zone B) is typically
 258 drier, receives more $Q_{S\downarrow}$ and has a high proportion of moderately and well drained soils. Similar to
 259 the northwest region, the southwest (Zone C) is also wet but experiences higher average
 260 temperatures; soils in this zone are mainly classified as imperfectly or poorly drained. Due to its
 261 favourable climate, this zone is dominated by grassland. The ‘Golden Vale’, a region known for its high-
 262 quality dairy production systems, is located within this zone.

263 Cumulative precipitation and mean deviations of daily θ , vapour pressure deficit (VPD) and LAI were
 264 calculated for each zone for the period May to August, relative to 2010 to 2019. We also applied

265 segmented regression to determine the relationship between daily soil moisture, sensible and latent
266 heat fluxes, employing the evaporative fraction (EF) metric in each zone. The goal here was to identify
267 if critical soil moisture (θ_c) thresholds occurred, and the period during which the θ control of exchange
268 processes became effective. We applied a similar approach using the NIRv data to evaluate and
269 complement the EF based approach; this provides a means of linking θ to vegetation productivity and
270 ecosystem functioning (Buitink et al., 2020).

271 Segmented regression is used to establish the point at which the linear relationship between an
272 independent (X) and independent variable (Y) changes. This is detected as a breakpoint where there
273 is a significant shift in the slope (sensitivity) representing this relationship. Here, soil moisture (θ) is
274 the independent variable and the surface-atmosphere variables (e.g. EF, NIRv) are the dependent
275 variables,

$$276 \quad Y = \alpha X + \omega(X - \psi), \quad (6)$$

277 where, ψ is the breakpoint, which represents the critical soil moisture threshold (θ_c), where the
278 response shifts from a wet to dry regime (segments); the dry/left line ($X \leq \psi$) and wet/right line ($X >$
279 ψ) segments have slopes of α and $\beta = \omega + \alpha$, respectively and ω is the difference-in-slopes. The
280 search for ψ is iterative as the model seeks to find the optimum location for the breakpoint that divides
281 the relationship into two linear segments; the initial value assigned to ψ is 0.25 (based on Seneviratne
282 et al., 2010). Iteration ceases when the model has converged on a solution (Muggeo, 2003). This
283 solution is taken here to be θ_c and distinguishes between the energy-limited and water-limited states
284 of the surface-air exchanges (Seneviratne et al., 2010). The slope magnitude indicates the severity of
285 dry (hereafter α_{EF} and α_{NIRv})/wet (hereafter β_{EF} and β_{NIRv}) segments (Benson and Dirmeyer, 2020;
286 Buitink et al., 2020) and the transition from one state to another occurs at θ_c . We used the CRAN R
287 'segmented' package to estimate these metrics (Muggeo, 2021).

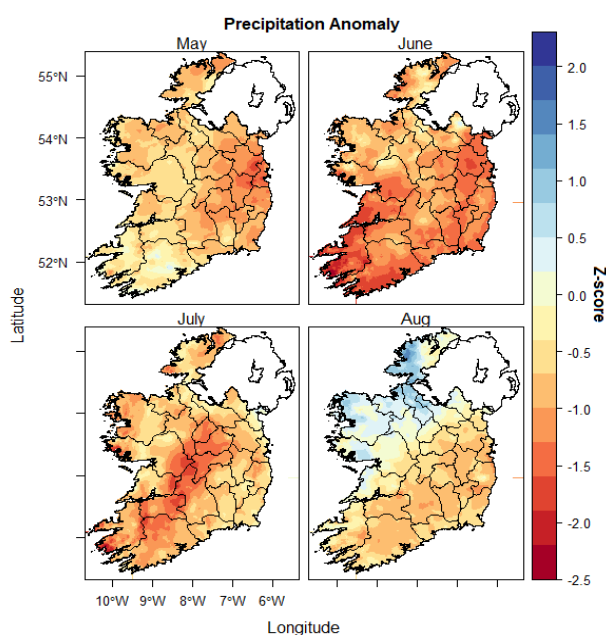
288

289 **3. Results**

290 *3.1 Evolution of 2018 summer drought across Ireland*

291 Figure 2 shows the spatial characteristics of the monthly total precipitation anomalies (Z-score) for
292 the individual summer months of May to August 2018. Applying the drought categories following
293 McKee et al. (1993), the 2018 meteorological drought progressively moved from mild/moderate
294 drought conditions (Z-score of 0 to -1.49) in May to more widespread extreme drought conditions (Z
295 < -2.0) in June, evident across the eastern, southern and southwestern part of the country, while
296 conditions in the northwest remained mild/moderate during these months. Rainfall deficits are
297 shown to gradually improve in subsequent months, with the rainfall anomaly in July characterized as
298 moderate drought conditions, with the exception of the midlands; August was characterized by mild
299 drought conditions in the eastern and southern half of the country, with wet conditions ($Z > 0$) in the
300 north and northwest.

301 To assess the land surface response, the degree of dryness is initially characterized based on anomalies
302 of soil moisture and LAI. The former is based on ERA5-Land which shows reasonable estimates of the
303 available measured soil moisture obtained at three Irish grassland sites, representative of different

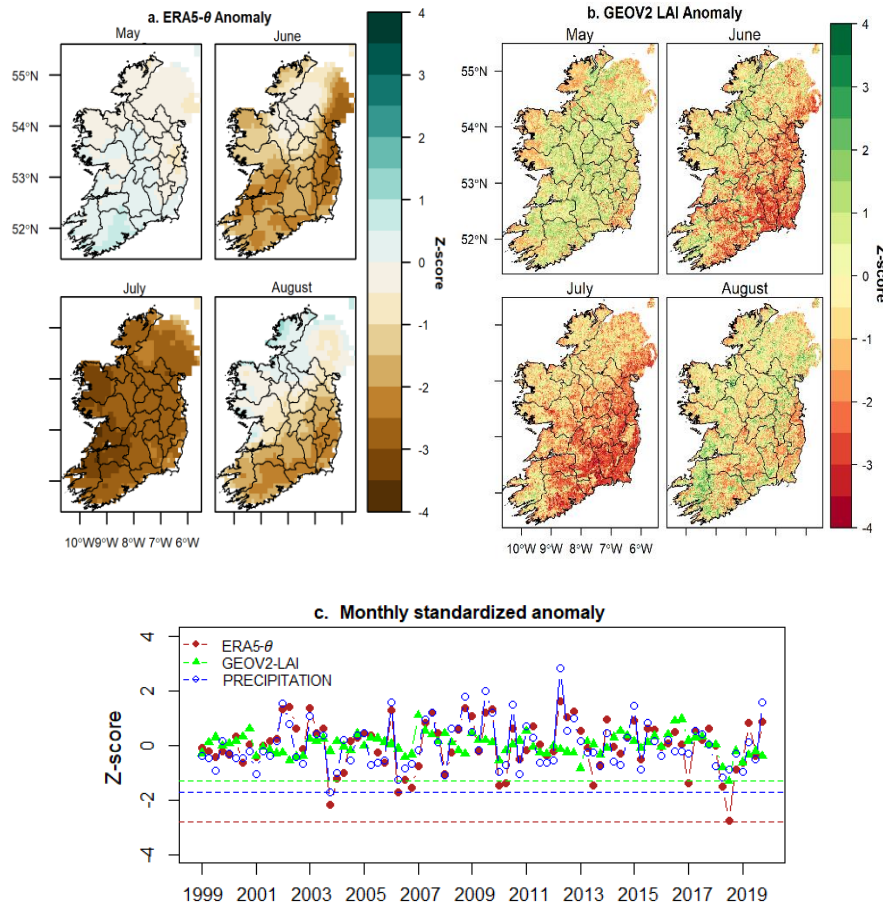


304
 305 **Figure 2. Spatial characteristics of** monthly precipitation anomaly (z-score) for the Republic of Ireland during
 306 summer 2018, relative to 21-year climatology (1999-2019). Thin lines represent county outlines. The anomalies
 307 were calculated from the 1 km gridded precipitation data (Source: Met Éireann)

308
 309 soil textural characteristics (Figure S1). Figure 3a and b show the magnitude and spatial extent of
 310 ERA5-Land θ and GEOV2-LAI anomalies for the individual months of May to August, 2018. In contrast
 311 to the mild/moderate meteorological drought evident in May (Figure 2), soil moisture conditions only
 312 begin to deteriorate in June and become exacerbated into July leading to high negative soil moisture
 313 anomalies ($Z < -2.0$) being experienced across the entire country, with extreme negative anomalies (Z
 314 < -3.0) along the usually wet west coast. While the negative θ anomalies were reduced in the north
 315 and west during August, the remainder of the country continued to experience significant negative θ
 316 anomalies, particularly evident in the south and east of the country (Figure 3a). A strong spatial
 317 coherence is also evident between the observed precipitation (Figure 2), ERA5-Land θ and satellite
 318 derived GEOV2-LAI (Figure 3a and b) as the meteorological and surface drought characteristics evolve
 319 over the study period.

320 To place these conditions in the context of previous summer drought events, Figure 3c displays the
 321 individual monthly (May, June, July and August) anomalies of rainfall, soil moisture (ERA5-Land θ) and
 322 LAI (GEOV2) for the period 1999 to 2019. Although larger rainfall deficits occurred during the 2003
 323 European summer drought, which was one of the driest summers on record (e.g., Casty et al., 2005;
 324 Jaksic et al., 2006), there was no clear impact on vegetation productivity. Thus, the 2003
 325 meteorological drought, while severe, did not develop into agricultural drought across the island, likely
 326 related to the timing of the precipitation deficits which occurred in August of that year. In contrast,
 327 during the summer 2018 event, both water and vegetation stress conditions are evident, as revealed
 328 by the high negative anomalies in precipitation, θ and LAI (Figure 3c). In addition, the largest negative
 329 θ and vegetation anomalies in the 21-year record occurred in July 2018, with a negative peak anomaly
 330 ($Z \approx -2.8$) for θ , concurrent with the peak negative anomaly for LAI ($Z \approx -1.3$).

331 In the next section, we present the results of the land surface scheme, to explore the perturbations in
 332 the surface energy budget associated with the observed surface drying during the summer of 2018.



333

334

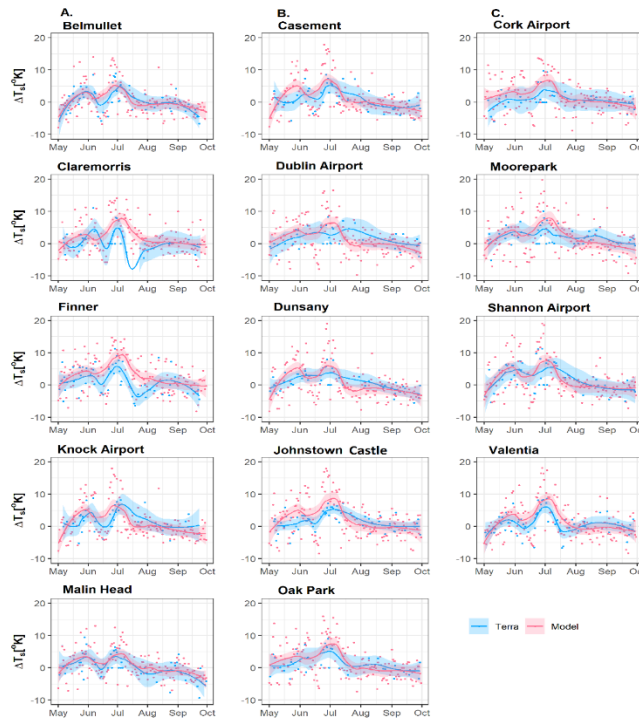
335 **Figure 3.** Monthly anomalies of ERA5-Land surface soil water content (θ) and satellite-derived GEOV2 leaf area
 336 index (LAI) for the individual summer months of 2018, relative to 21-year climatology (1999-2019). (a-b) the
 337 spatial characteristics of both parameters; (c) inter-annual variations of monthly anomalies of θ , LAI and gridded
 338 precipitation, averaged over the entire region (blue, red and green horizontal dotted lines show the lowest
 339 negative scores for precipitation, θ and LAI, respectively).

340

341 3.2 Perturbations of land-atmosphere energy exchanges

342 To evaluate the robustness of the LSS-derived surface energy fluxes, we initially compared the mid-
 343 day observed surface temperature anomaly (relative to 2010-2019), derived from MODIS Terra (for
 344 pixels representing the individual weather stations, Figure 1) and the LSS derived surface temperature
 345 anomaly (ΔT_s) for the respective stations (Figure 4). Results show high positive ΔT_s for both the Terra
 346 and model estimates (peaking at +5 to +10 K and +8 to +15 K, respectively) between late June and
 347 early July across the selected stations. While the temporal profiles of LSS-derived ΔT_s are largely
 348 consistent with the observed Terra ΔT_s , the LSS estimates display a warm bias that can be attributed
 349 to an offset in timing between the LSS model estimated values and time of overpass of the satellite;
 350 the LSS-derived ΔT_s values are based on the average of the values (from 1000 to 1100h), while Terra-
 351 derived ΔT_s values are based on instantaneous satellite observations at 1030h (GMT).

352



353

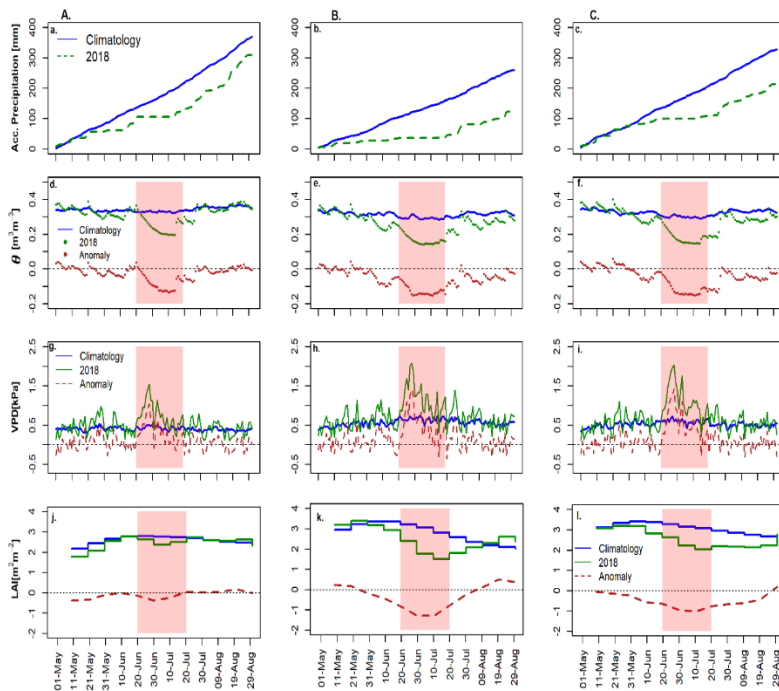
354 **Figure 4.** Temporal evolution of LSS model-derived (Model) mid-day land surface temperature anomaly (ΔT_s),
 355 compared with MODIS Terra (Terra) ΔT_s during 2018 summer, relative to 2010-2019 average across the stations.
 356 The lines are derived from smoothed fits of locally weighted polynomial regression (LOESS). The shaded portions
 357 represent the 5th and 95th percentiles of uncertainty bounds as calculated by LOESS. The columns under A, B and
 358 C indicate stations in each of the previously described zones, as highlighted in Figure 1 and Table 1.

359

360 Figure 5 shows the temporal evolution of the in-situ accumulated rainfall (Figure 5 a-c), ERA5-Land θ
 361 (Figure 5 d-f), in-situ vapour pressure deficit (VPD) (Figure 5 g-i) and satellite-derived LAI (Figure 5 j-l)
 362 for the period May to August 2018, compared with climatology (1999-2019), for the three zones (A,
 363 B, C) previously outlined (Figure 1). The aggregated values are based on the average of the grids
 364 corresponding with the station locations, for the gridded data, and station averages for the observed
 365 data. In each zone, the cumulative rainfall clearly shows a departure from climatology beginning from
 366 just prior to, or around, June 1 (Figure 5 a-c). In the northwest (zone A), the 2018 cumulative rainfall
 367 remains closer to climatology, indicating smaller rainfall deficits experienced during June-August,
 368 relative to east coast (zone B) and southwest (zone C). This is consistent with the gridded precipitation
 369 data in Figure 2. The rainfall deficits also begin later in southwest.

370 In the northwest, θ losses (Figure 5d) due to evapotranspiration during the start of the season are
 371 offset by the normal or above normal rainfall receipts in April and the arrival of Storm Hector in the
 372 zone in mid-June. Decreasing θ becomes evident from mid-June (approx. 2-3 weeks after the onset of
 373 meteorological drought) and reach their lowest negative anomaly (relative to the climatology) of
 374 approximately $-0.13 \text{ m}^3 \text{ m}^{-3}$ (40 % relative change) around the 4th July. Concurrently, VPD increased
 375 from the 21st June and peaks on the 27-28th June with anomalous values (> 200 % relative change) of
 376 +1.0 kPa (Figure 5g), while LAI shows negligible change during this period (Figure 5j).

377

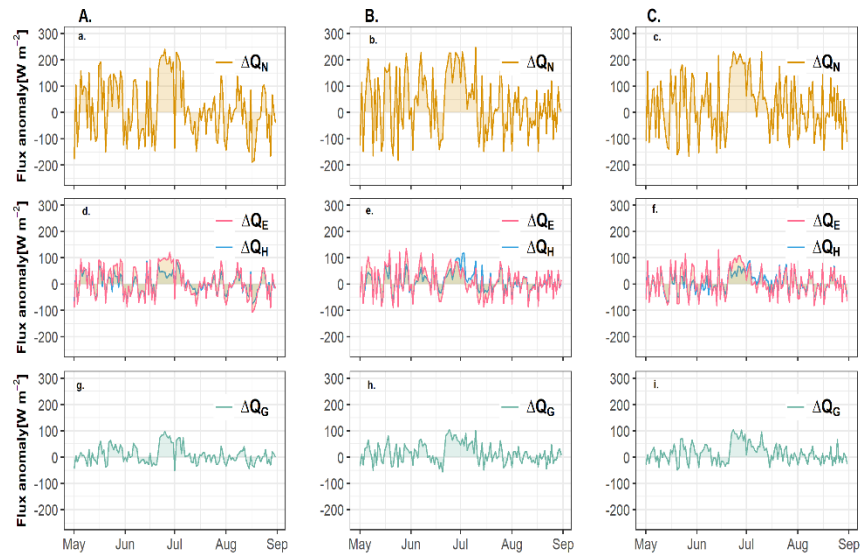


378

379 **Figure 5.** Temporal evolution of AWS observed accumulated precipitation (first row), ERA5-Land volumetric
 380 water content (second row), in situ vapour pressure deficit (third row) and satellite-derived leaf area index
 381 (fourth row); during 2018 summer compared with climatology (1999-2019). Panels A, B and C represent stations
 382 in the respective zones highlighted in Figure 1. Values are based on average of stations (and corresponding grids)
 383 in each zone. The peach shades represent the observed periods of abnormal surface and atmospheric conditions
 384 For the east of the country, the θ anomaly (relative change), which began earlier than in northwest,
 385 is approximately $-0.15 \text{ m}^3 \text{ m}^{-3}$ (50%); this coincides with the highest positive VPD anomaly of $+1.4 \text{ kPa}$
 386 ($> 200\%$) and lowest negative anomaly of LAI of $-1.5 \text{ m}^2 \text{ m}^{-2}$, from 28 June (Figure 5 e, h, k). The timing
 387 of changes in θ , VPD and LAI in the southwest (Figure 5 f, i, l) largely follow those observed in the east,
 388 but slightly lower in magnitude.

389 The highlighted periods of negative surface (e.g., θ , LAI) and atmospheric (e.g., rainfall, VPD)
 390 anomalies (Figure 5) correspond to the LSS-derived periods of higher positive anomalies (relative
 391 change) in both the net radiative and energy fluxes. ΔQ_N anomalies of approximately $+200$ to 250 W
 392 m^{-2} (180-190%) across the three zones (Figure 6a-c) indicate the strong and persistent influence of the
 393 anticyclonic system, which suppressed cloud formation between 22 June and 3 July across all the zones.
 394 Despite the similarity in radiative forcing conditions, anomalies in the mid-day sensible (ΔQ_H) and
 395 latent (ΔQ_E) heat fluxes differ across each of the zones, reflecting differences in the partitioning of
 396 available energy. For instance, in the northwest, the net radiation surplus gives rise to a latent heat
 397 anomaly (ΔQ_E) of $+100$ to 120 W m^{-2} ($\approx 190\%$), largely at the cost of ΔQ_H . This indicates that plants in
 398 this zone were still able to access available soil water, despite the higher ΔQ_N and VPD, between the
 399 22–30 June (Figure 6a; Figure 5g). While the general responses are similar for east and southwest,
 400 with the land surface scheme simulating an enhanced positive ΔQ_E anomaly, of $+60$ to 90 W m^{-2} (140-
 401 190%) and $+50$ to 100 W m^{-2} (130-170%), respectively (Figure 6e-f). However, by the end of June, ΔQ_H
 402 exceeds ΔQ_E in the east and ΔQ_H is equivalent to ΔQ_E in southwest, providing evidence of a land-
 403 atmosphere feedback, evident in the enhanced VPD (Figure 5 h, i), relative to northwest (Figure 5g),
 404 starting from 27 June in the east (Figure 6e) and 1 July in southwest (Figure 6f).

405 Overall, these results show enhanced Q_E , well above normal, caused by high positive anomalies of
 406 ΔQ_N prior to 27th June. The observed changes between late June and early July in the east and
 407 southwest highlight the differentiating role of plant available soil moisture and support the divergent
 408 landscape physiological responses (e.g., LAI - Figure 3b) to atmospheric anomalies relative to the
 409 northwest.



410
 411 **Figure 6.** Temporal evolution of model-derived mid-day anomalous net radiative flux (ΔQ_N) (first row), sensible
 412 heat (ΔQ_H) and latent heat (ΔQ_E) fluxes (second row) and soil heat flux (ΔQ_G) (third row), during 2018 summer,
 413 relative to analysis period (2010-2019). Panels A, B and C are for stations in the respective zones highlighted in
 414 Figure 1. Values represent the day time (10:00-15:00) average.

415

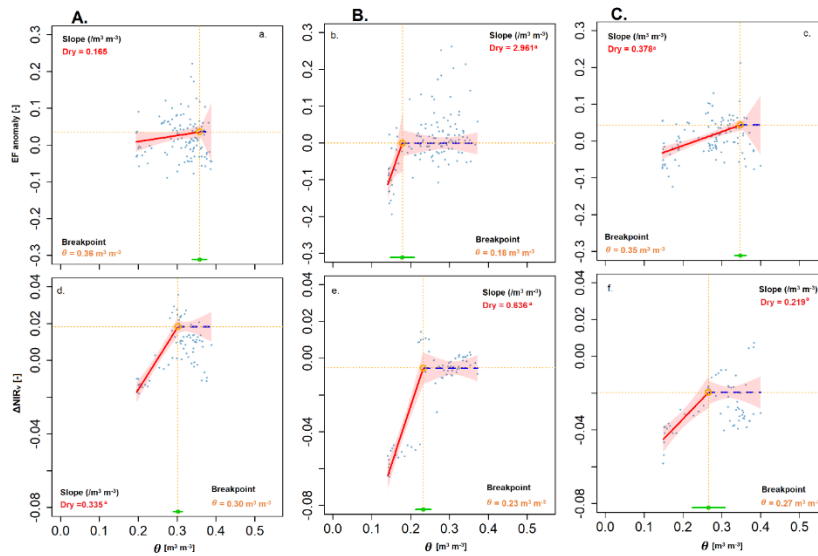
416 3.3 Relationship between soil moisture and surface flux densities

417 To further explore the role of soil moisture availability in drought evolution, we used segmented
 418 regression to examine the relationships between daily ERA5-Land θ and anomalies of EF and NIRv
 419 (Figure 7), and separately for ΔQ_E and ΔQ_H (Figure S2) for each zone. The results for individual stations
 420 are provided in Table S1. It should be noted that the results here are exploratory and based on a LSS
 421 specified θ_{FC} value ($0.3 \text{ m}^3 \text{ m}^{-3}$) (as outlined in Section 2.5).

422 While the models detect a breakpoint (critical θ threshold, $\theta_c \approx 0.36 \text{ m}^3 \text{ m}^{-3}$) separating wet and dry
 423 regime in the northwest zone (Figure 7a), the α_{EF} sensitivity in the dry segment is insignificant and
 424 close to 0. In contrast, the $\theta - \text{NIRv}$ approach identified a critical θ threshold ($\theta_c \approx 0.30 \text{ m}^3 \text{ m}^{-3}$) with
 425 a higher α_{NIRv} sensitivity indicated in the dry segment (adjusted $R^2 = 0.60$ $p\text{-value} = 2.27 \times 10^{-12}$)
 426 (Figure 7d). This indicates that the landscapes in the northwest largely sustain the conditions in which
 427 changes in EF is independent of θ , whereas the NIRv signal is influenced by θ during the summer
 428 season.

429 However, the θ -EF relationship is clearly captured in the east (Figure 7 b, e) where the approach
 430 identified a critical threshold θ_c of $\approx 0.18 \text{ m}^3 \text{ m}^{-3}$, a value that is likely close to the wilting point. The
 431 sensitivity ($\beta_{EF} \approx 0$) is negligible in the wet segment, but a significant and steep α_{EF} slope is observed
 432 in the dry segment (adjusted $R^2 = 0.29$ $p\text{-value} = 0.039$), indicating that EF is constrained and linearly

433 coupled with the surface during the period when θ is below the critical point. Findings are consistent
 434 for the θ -NIRv approach ($\theta_c = 0.23 \text{ m}^3 \text{ m}^{-3}$ and adjusted $R^2 = 0.77$ p -value = 2.44×10^{-12}).



435

436 **Figure 7.** Relationships between soil moisture (θ), evaporative fraction (EF) [first row] and MODIS NIRv [second
 437 row], based on segmented regression analysis during 2018 summer across the zones. The thick red lines are
 438 measures of sensitivity (slope) on the dry segment while dashed blue lines are for wet segment. The dashed
 439 orange lines show the θ -EF and θ -NIRv breakpoints and the horizontal green lines at the bottom show the
 440 confidence interval of θ breakpoints. * significant at p -value < 0.05. Panels A, B and C are for stations in the
 441 respective zones highlighted in Figure 1.
 442

443 The results of this exploratory analysis in the southwest identify a critical θ threshold (θ_c) $\approx 0.35 \text{ m}^3$
 444 m^{-3} , similar to northwest, but with a significantly (p -value = 2.59×10^{-7}) higher α_{EF} sensitivity in the
 445 dry segment (adjusted $R^2 = 0.23$) (Figure 7c). Comparing with the θ -NIRv approach, the α_{NIRv}
 446 sensitivity is similar (adjusted $R^2 = 0.32$) but with a higher estimate ($0.35 \text{ m}^3 \text{ m}^{-3}$ p -value = 0.000125)
 447 of θ_c (Figure 7f).

448 Both the EF and NIRv approaches agree on the coupling for the east and southwest, however, the
 449 differences in estimated θ_c suggest causality in θ -EF framework (e.g., soil type) that may not be
 450 inferred using statistical regression analysis. Independent assessments based on the relations of ERA5-
 451 Land θ with model-derived Q_H and Q_E fluxes (Figure S2) show that Q_H is the major mechanistic factor
 452 driving the θ -EF signals, and likely responsible for the increased atmospheric sensitivity that
 453 contributed to occurrence of the abnormally warm and dry days during summer 2018, as revealed in
 454 the east and southwest.

455 4. Discussion

456 In this study, we evaluated the use of a land surface scheme that employed readily available
 457 meteorological data to assess the impact of the 2018 summer drought on regional land-atmosphere
 458 heat and moisture exchanges. The performance of the scheme was evaluated in comparison with
 459 MODIS-derived surface temperature anomalies (ΔT_s) with results that are consistent with the findings
 460 of Zaitchik et al. (2006) who showed similar timing and distribution of spikes in ΔT_s between MODIS-
 461 derived and model estimates from NCEP/NCAR reanalyses for the summer 2003 drought in France.

462 This supports the argument that Ireland experienced a compound drought event where land-
463 atmosphere feedbacks enhanced its severity. Understanding of the response of the vegetation to
464 these events is limited (e.g., Streck, 2003; Teuling, 2018) however but is important in assessing
465 agricultural productivity, especially.

466 *4.1 Changes in land surface processes during severe drought*

467 During extreme weather events such as drought, perturbations in the surface energy budget will drive
468 changes in near-surface temperature and reductions in available soil water. In soils with limited
469 available soil water, plant water uptake to meet the increasing atmospheric evaporative demand will
470 be restricted (Teuling, 2018), as a result, available Q_N will be converted to Q_H flux. This positive
471 feedback on Q_H can act to amplify drought characteristics. The perturbations of surface exchanges of
472 heat and moisture which impact the patterns of atmospheric temperature are mediated through
473 changes in θ (Seneviratne et al., 2010; Miralles et al., 2014).

474 The analysis of the 2018 event indicates that an increase in net radiative fluxes (ΔQ_N) was evident
475 from May to July and this was associated with decreasing θ and increasing VPD (Figure 5 d-i). LAI
476 response to the changing land surface conditions was evident in the east, southeast and southwest
477 zones (Figure 5 k-l). While the northwest displayed an increase in VPD and decline in θ over this period;
478 the vegetation response was less marked in the LAI response (Figure 3b; Figure 5j), relative to the
479 climatology, for this region. The mild drought conditions experienced in the northwest during June,
480 relative to the rest of the country, were associated with the passage of a rainstorm in mid-June (Met
481 Éireann Report, 2018). In general, the observed magnitude, extent and timing of the 2018
482 meteorological drought are in agreement with those reported by Falzoi et al. (2019). The LSS analysis
483 shows that Q_N was largely partitioned into Q_E rather than Q_H during this period in the northwest,
484 which is typical of grasslands even under extremely warm temperatures (Teuling et al., 2010; Lansu et
485 al., 2020) where soil water remains available to plants. The partitioning of available energy into Q_E is
486 similar for the east and the southwest, but with lower magnitude Q_E anomalies. This enhancement of
487 Q_E even under water limited conditions was likely facilitated by the integrated effects of higher
488 downward shortwave radiation and increased VPD. However, the ratio between Q_E and Q_H in the east
489 and southwest indicates that a greater proportion of Q_N was channelled into Q_H and this is apparent
490 in the negative anomalies of LAI in these zones during the month of June (Figure 3b). The shift from
491 latent to sensible heat and reduction in LAI during June and July indicate decreasing θ , and hence
492 vegetation stress in the region (Figure 5e).

493 The impact on vegetation response, represented by anomalies in GEOV2 LAI, closely tracked the
494 evolving θ conditions (Figure 3b). These findings are consistent with those of Albergel et al. (2019)
495 who found similar perturbations (index > -1.0 and -2.0) in surface θ during the month of July in the
496 UK. Based on our analysis, grassland in the east responded faster to meteorological drought conditions
497 than elsewhere. Several contributing factors are likely to explain this; the southeast is characterised
498 by relatively well drained soils and can experience seasonal θ deficits during 'normal' years. April 2018
499 experienced average, or above average, rainfall at most stations; where soils have storage capacity,
500 such as the imperfectly or poorly drained soils more typical of the southwest and northwest, the
501 additional water offset evaporative losses. Rain in June resulted in θ returning to normal levels in the
502 northwest (Figure 5d) and southwest (Figure 5f). Soil drying was more advanced in the east (Figure
503 5e) and increased due to high Q_E during June (Figure 6b) with a marked response in vegetation,

504 evident in the negative anomalies of LAI, during June. By July, with increased plant stress due to the
505 reduction in θ , the positive Q_N anomaly is expended as Q_H and Q_G , warming the atmosphere,
506 increasing water demand and exacerbating soil moisture and vegetation. A similar reasoning applies
507 to the southwest based on the LSS simulated fluxes (Figure 6c) and is supported by the increasing
508 negative anomalies in LAI in the zone during this month. The response of grasslands then to the
509 drought events depends on the antecedent conditions, geographical area and soil characteristics,
510 findings consistent with Xiao et al. (2009) and Zhang et al. (2012).

511 The positive anomalous ΔQ_H and ΔQ_E are largely correlated with an increase in net radiative flux
512 during early summer but in the east, the negative ΔQ_E values in July can be explained by increasing
513 water-stress conditions in the root zone of grasses. This zone is distinguished by its free-draining soils
514 (Creamer et al., 2014) that makes it especially vulnerable to meteorological drought conditions, if they
515 occur during the growing season (e.g., 2003 versus 2018 – Figure 3c).

516 *4.2 Role of soil moisture in land-atmosphere exchanges during 2018 summer*

517 Soil moisture (θ) can significantly influence terrestrial water, energy, and carbon cycling through its
518 control on Q_E at the land-atmosphere interface. This connection can be explored using a soil moisture-
519 evaporative fraction (θ - EF) framework that distinguishes the transition from wet to dry evaporative
520 regime: (1) a wet regime in which EF is independent of θ ; and, (2) a dry regime where θ and EF are
521 linearly coupled. The critical soil moisture content (widely referred to as critical soil moisture
522 thresholds) that separate these regimes is important as it can help identify the mechanisms
523 responsible for the shift from a normal into a water-stress regime, where the land surface state
524 controls the sensitivity of the atmosphere (Seneviratne et al., 2010).

525 We applied segmented regression analysis on the ERA5-Land θ and estimated EF anomaly to identify
526 the threshold in soil moisture (θ_c) that marks the transition from wet to dry regime; a similar approach
527 was applied to the NIRv data. The estimated θ_c values are identical to those derived using measured
528 θ deeper in the soil layer, from two sites in the Netherlands (Buitink et al., 2020). Hence, these findings
529 suggest that drying soils increase the sensitivity of land-atmosphere coupling, in turn aggravating the
530 surface drying, based on ERA5-Land θ (note that ERA5-Land underestimates very dry soils for a
531 number of Irish sites). In the east, this shift was identified as occurring in late June ($\approx 22^{\text{nd}}$ June),
532 indicating the onset of agricultural drought. The dry regime was sustained for several days (20) during
533 which θ - EF are linearly coupled demonstrating the ‘hypersensitive’ response of this region to
534 meteorological droughts. In a previous study over grassland above saturated soils in the south of
535 Ireland, Jaksic et al. (2006) reported that measured θ status in both dry and wet years are different,
536 but well above wilting point, so that the impact of θ status on net ecosystem functioning is small and
537 identical for both years. This is consistent with our findings over the northwest where the landscape
538 either shows no α_{EF} sensitivity or the θ - EF coupling is too weak to support the theoretical θ - EF
539 framework (Seneviratne et al., 2010). Results of α_{EF} in the southwest also indicated a weak θ - EF
540 coupling, however, the land surface response to reduced θ is evident in the vegetation response
541 (Figure 3b) – further work is necessary to explore this. The differing land responses, as reflected in
542 different estimated θ_c values, also suggest the local effects of predominant soil types across the zones.
543 The zones are characterized by different soil properties (Creamer et al., 2014), in essence, the
544 reinforcement of soil moisture-evaporation signal, which is distinguished by θ_c , partly depends on the
545 nature of the soil and its water holding ability.

546 A further assessment indicates that the signal in EF is largely driven by Q_H during the dry regimes, as
547 revealed in the east (Figure S2). Therefore, Q_H appears to be the mechanistic factor responsible for
548 the unusual shift in land-atmosphere coupling and consequently amplified agricultural drought during
549 summer 2018.

550 ERA5-Land uses monthly climatology of LAI to generate the global reanalyses data (Boussetta et al.,
551 2013), which may contribute to weak θ -EF signals in these zones. There is the possibility that ERA5-
552 Land may have underestimate very dry soils as demonstrated in Figure S1, consequently resulting in
553 the LSS to underestimate the impact of soil moisture anomalies on land-atmosphere feedback
554 mechanisms. The offsets between measured and ERA5-Land θ values are largely represented in values
555 below $0.25 \text{ m}^3 \text{ m}^{-3}$. It should also be noted that the ERA5-Land θ at the surface soil layer was evaluated
556 with measured θ at the deeper soil layer (20 cm) across the sites. The surface θ derived from models
557 or satellites are thought to decouple from θ in the deeper soil profile where plants may take up water
558 depending on root density, and consequently may not explain the dynamics of processes in the root
559 zone (Buitink et al., 2020). However, the choice of ERA5-Land surface θ to diagnose drought processes,
560 as in recent studies (Benson and Dirmeyer, 2020; Dirmeyer et al., 2021), is on the basis that θ
561 anomalies develop progressively down deeper soil layers during a drought event, as plants increase
562 water uptake from near the surface to the subsurface. Thus, θ values may further lead to larger offsets
563 under $0.25 \text{ m}^3 \text{ m}^{-3}$, since the θ at the deeper layers are always higher than at the upper soil layers.
564 This is consistent with Dirmeyer et al. (2021) who noted that ERA5-Land underestimates the impact
565 of very dry soils on extreme temperatures, over Britain in 2018 summer. Finally, the assumed
566 volumetric water content at field capacity (θ_{FC}) of $0.3 \text{ m}^3 \text{ m}^{-3}$, necessary to apply the LSS in the
567 absence of measured θ_{FC} , may also have contributed.

568

569 **5. Conclusion**

570 Here, we evaluated the use of a physically based land surface scheme, in combination with readily
571 available ERA5-land global reanalyses surface soil moisture data, satellite-derived CGLS leaf area index
572 (LAI) and ground-based meteorology, to estimate the surface flux densities and evaporative fraction
573 (EF) to understand the land surface response to the atmospheric forcing during the Summer of 2018.
574 The approach allows us to explore changes in land surface processes and the effect of a soil moisture
575 regime shift on land-atmosphere sensitivities. We demonstrate the application of this framework,
576 utilising data from fourteen weather stations distributed across Ireland, during the 2018 summer
577 record-breaking heat and drought events.

578 The study revealed synoptic timescale variability in anomalous land-atmosphere heat and moisture
579 transfers, across the stations and between dates. Drought-induced perturbations in land surface
580 processes are largely not effective until the period between late June/early July and extend to mid-
581 July in some cases. Prior to this period, the processes were constrained by atmospheric anomalies.
582 That is, in the absence of rainfall, the higher evaporative demand due to warmer temperature
583 enhanced latent heat flux (Q_E) via increase in evapotranspiration rates, leading to the higher soil
584 moisture deficits in July across the country. This is particularly apparent in the east and southeast
585 regions, where drying soils quickly shifted the landscape into a 'dry' regime in which EF is self-limiting,

586 consequently providing a positive land-atmosphere feedback mechanism (increase in land surface
587 temperature and Q_H), beginning from 27th June and further exacerbated agricultural drought in July.

588 Segmented regression analysis of θ -EF interplay has found significant critical soil moisture threshold
589 ($\theta_c \approx 0.18 \text{ m}^3 \text{ m}^{-3}$, and $\theta_c \approx 0.23 \text{ m}^3 \text{ m}^{-3}$ for θ -NIRv analysis) at which land-atmosphere signals
590 potentially become hypersensitive in the east and southeast zone, based on ERA5-Land. These values
591 also represent the point of onset of drought impact on landscapes and ecosystem functioning in this
592 region. Although, the segmented models also identified soil moisture shift across the rest of the
593 country, the linear θ -EF coupling was too weak to conclude that EF was constrained by land surface
594 state in these areas. While spatial variations in precipitation and local effects of soil and vegetation
595 structures may play a critical role in the differing land responses, it should be noted that ERA5-Land
596 underestimates seasonally dry soil moisture regimes for Irish landscapes, which may have broadly
597 informed less and inconsistent impact of soil moisture anomalies on the exchange processes across
598 the region.

599 Nonetheless, the findings of this study are invaluable to speculate the zones and critical soil moisture
600 values under which land-atmosphere exchanges are constrained by the land surface state and further
601 exacerbate surface warming and dryness. This contribution is important, certainly for Ireland, not only
602 because it may help improve the representation of soil moisture factors in Numerical Weather
603 Prediction (NWP) models, but can also help to enhance sub seasonal predictability of drought
604 propagation and early warning systems of summer climate extremes in the future episodes.

605 **Acknowledgments**

606 This study is supported by the Teagasc Irish Agriculture and Food Development Authority under Walsh
607 Fellowship Programme (project: 2016076). The authors are grateful to Met Éireann, the Irish
608 Meteorological Service, for providing routine weather observations and gridded precipitation. The
609 ERA5-Land soil moisture data are obtained from <https://cds.climate.copernicus.eu/>, and MODIS
610 products are available from https://lpdaac.usgs.gov/product_search/ and the satellite-derived
611 GEOV2-LAI data are obtained from <https://land.copernicus.eu/>. We thank the anonymous reviewers
612 for their invaluable comments and suggestions.

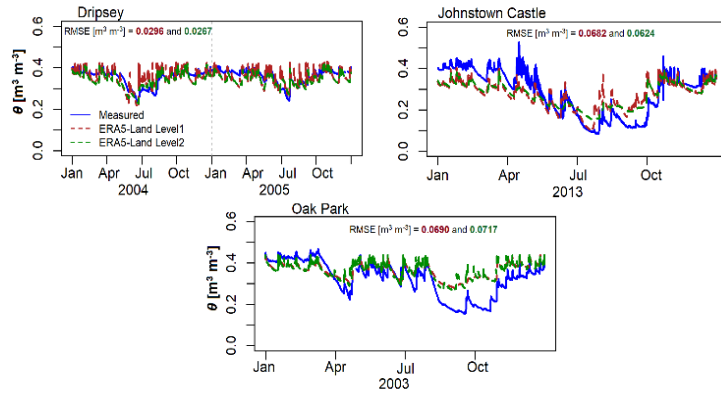
613 **Code availability:** The python code used for flux simulations is available from
614 https://zenodo.org/record/4679843#.YQLf_I5Khpk

615 **Conflict of Interest**

616 The authors declare no competing interests

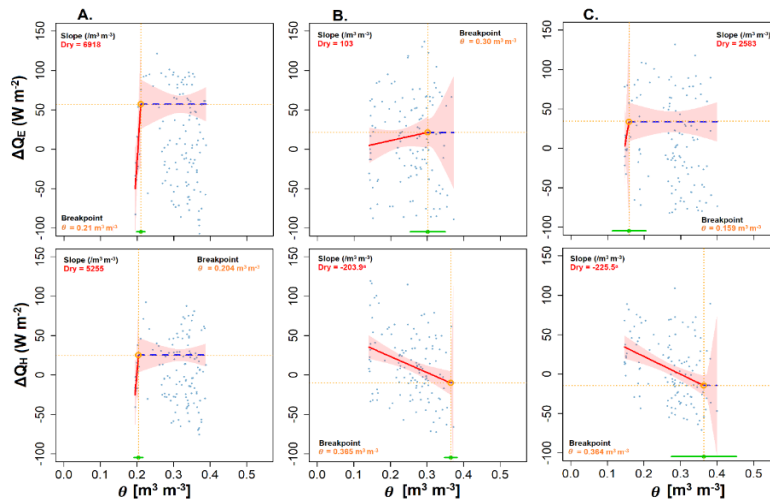
617

618 **Supplementary Information**



619

620 **Figure S1.** Comparisons between hourly measured and ERA5-Land volumetric water content (θ) across three
 621 independent grassland sites. The measured θ values are obtained from eddy covariance flux sites from
 622 previous studies (Ní Choncubhair et al., 2017; Kiely et al., 2018)



623

624 **Figure S2.** Relationships between soil moisture (θ), latent heat flux (ΔQ_E) [first row] and sensible heat flux
 625 (ΔQ_H) [second row], based on segmented regression analysis during 2018 summer across the zones. The thick
 626 red lines are measures of sensitivity (slope) on the dry segment while dashed blue lines are for wet segment.
 627 The dashed orange lines show the θ - ΔQ_E and θ - ΔQ_H breakpoints and the horizontal green lines at the bottom
 628 show the confidence interval of θ breakpoints. ^a significant at p -value < 0.05. Panels A, B and C are for
 629 stations in zones A, B and C, respectively, as highlighted in Figure 1 and Table 1.

630

Station	EF			NIRv		
	θ_c	R^2_{adj}	Start date	θ_c	R^2_{adj}	Start date
Belmullet	0.282	0.04	12 June	0.295	0.37	08 June
Claremorris	0.388	0.09	22 May	0.373	0.18	23 May
Finner	0.244	0.08	09 July	0.328	0.21	26 June
Knock Airport	0.375	0.14	20 June	0.249	0.04	29 June
Malin-Head	0.177	0.28	26 June	0.138	0.46	29 June
Casement	0.203	0.09	26 June	0.389	0.72	22 May
Dublin Airport	0.109	0.48	26 June	0.154	0.31	22 June

Dunsany	0.315	0.04	06 June	0.327	0.26	05 June
Johnstown	0.146	0.44	26 June	0.138	0.59	27 June
Oak Park	0.296	0.10	19 June	0.269	0.56	22 June
Cork Airport	0.336	0.05	28 May	0.177	0.56	29 June
Moorepark	0.358	0.06	27 May	0.218	0.40	25 June
Shannon Airport	0.431	0.10	25 May	0.218	0.04	29 June
Valentia	0.178	0.42	24 June	0.226	-0.002	15 June

631 **Table S1.** Site-specific ERA5-based critical soil moisture content (θ_c , $\text{m}^3 \text{m}^{-3}$) (0-7cm layer) and date of onset of
632 2018 agricultural drought, derived using segmented regression relationships between θ , evaporative fraction
633 (EF), and MODIS NIRv. Stations with relatively stronger θ -EF and θ -NIRv couplings are highlighted in bold.
634 R^2_{adj} is the adjusted R^2 .

635

636 References

637 Akbar, R., Short Gianotti, D. J., McColl, K. A., Haghghi, E., Salvucci, G. D., & Entekhabi, D.,
638 2018. Estimation of landscape soil water losses from satellite observations of soil
639 moisture. *Journal of Hydrometeorology*, 19, 871–889

640 Albergel, C., Dutra, E., Bonan, B., Zheng, Y., Munier, S., Balsamo G., de Rosnay, P., Muñoz-Sabater,
641 J., and Calvet J-C., 2019. Monitoring and Forecasting the impact of the 2018 summer heatwave
642 on vegetation, *Remote Sensing*, 11, 520, doi:10.3390/rs11050520

643 Alexander, L., 2011. Climate science: extreme heat rooted in dry soils, *Nat. Geosci.* 4, 12–13.
644 doi:10.1038/ngeo1045

645 Allen, R. G., Pereira, L. S., Raes, D. and Smith, M., 1998. Crop evapotranspiration. Guidelines for
646 computing crop water requirements. *Irrigation and Drainage Paper No. 56*. Rome: FAO.

647 Badgley, G., Field, C. B., and Berry, J. A., 2017. Canopy near-infrared reflectance and terrestrial
648 photosynthesis, *Sci. Adv.*, 3, e1602244, <https://doi.org/10.1126/sciadv.1602244>

649 Badgley, G., Anderegg, L. D. L., Berry, J. A., and Field, C. B., 2019. Terrestrial gross primary production:
650 Using NIRV to scale from site to globe, *Global Change Biol.*, 25, 3731–
651 3740, <https://doi.org/10.1111/gcb.147299>

652 Baldocchi, D. D., Ryu, Y., Dechant, B., Eichelmann, E., Hemes, K., Ma, S., Sanchez, C. R., Shortt, R., Szutu,
653 D., Valach, A., Verfaillie, J., Badgley, G., Zeng, Y., and Berry, J. A., 2020 Outgoing Near Infrared
654 Radiation from Vegetation Scales with Canopy Photosynthesis Across a Spectrum of Function,
655 Structure, Physiological Capacity and Weather, *J. Geophys. Res.-Biogeo.*, 125,
656 e2019JG005534, <https://doi.org/10.1029/2019JG0055344>

657 Balsamo, G., Viterbo, P., Beljaars, A., van den Hurk, B., Hirschi, M., Betts, A. K., Scipal, K., 2009. A
658 Revised Hydrology for the ECMWF model: Verification from Field Site to Terrestrial Water
659 Storage and Impact in the Integrated Forecast System, *Journal of Hydrometeorology*, 10, 623–
660 643.

661 Baret, F., Weiss, M., Lacaze, R., Camacho, F., Makhmarad, H., Pacholczyk, P., Smetse, B., 2013. GEOV1:
662 LAI, FAPAR essential climate variables and FCOVER global time series capitalizing over existing
663 products, Part 1: Principles of development and production, *Remote Sens. Environ.*, 137, 299–
664 309.

665 Beljaars, A. C. M. and Bosveld, F. C., 1997. Cabauw Data for the Validation of Land Surface
666 Parameterization Schemes *J. Climate* 10, 1172 – 1193. Benson, D. O. and Dirmeyer, P. A., 2020.
667 Characterizing the relationship between temperature and soilmoisture extremes and their
668 role in the exacerbation of heatwaves over the Contiguous United States. *J. Clim*, 34 (6), 2175-
669 2187

670 Benson, D. O. and Dirmeyer, P. A., 2020. Characterizing the relationship between temperature and
671 soilmoisture extremes and their role in the exacerbation of heatwaves over the Contiguous
672 United States. *J. Clim*, 34 (6), 2175-2187

673 Boussetta, S., Balsamo, G., Beljaars, A., Kral, T., and Jarlan, L. 2013. Impact of a satellite-derived leaf
674 area index monthly climatology in a global numerical weather prediction model. *International*
675 *Journal of Remote Sensing*, 34(9–10), 3520–3542.
676 <https://doi.org/10.1080/01431161.2012.716543>

677 Buitink, J., Swank, A. M., van der Ploeg, M., Smith, N. E., Benninga, H.-J. F., van der Bolt, F., Carranza,
678 C. D. U., Koren, G., van der Velde, R., and Teuling, A. J., 2020. Anatomy of the 2018 agricultural
679 drought in the Netherlands using in situ soil moisture and satellite vegetation indices, *Hydrol.*
680 *Earth Syst. Sci.*, 24, 6021–6031, <https://doi.org/10.5194/hess-24-6021-2020>

681 Buras, A., Rammig, A., Zang, C. S., 2019. Quantifying impacts of the drought 2018 on European
682 ecosystems in comparison to 2003. *Biogeosciences*, 17, 1655–1672.

683 Casty C, Wanner H, Luterbacher J, Esper J, Böhm R. 2005. Temperature and precipitation variability in
684 the European Alps since 1500. *Int. J. Climatol.* 25: 1855–1880, doi: 10.1002/joc.1216.

685 Conti, S., Meli, P., Minelli, G., Solimini, R., Toccaceli, V., Vichi, M., Beltrano, C., Perini L., 2005.
686 Epidemiologic study of mortality during the Summer 2003 heat wave in Italy. *Environ. Res.*,98,
687 390–399.

688 Creamer, R.E., Simo, I., Reidy, Carvalho, J., Fealy, R., Hallett, S., Jones, R., Holden, 829 A., Holden, N.,
689 Hannam, J., Massey, P., Mayr, T., McDonald, E., O'Rourke, S., Sills, P., Truckell, I., Zawadzka, J.
690 and Schulte, R.P.O. 2014. Irish Soil Information System. Synthesis Report (2007-S-CD-1-S1). EPA
691 STRIVE Programme, Wexford.

692 Denissen, J. M., Teuling, A. J., Reichstein, M. & Orth, R., 2020. Critical soil moisture derived from
693 satellite observations over Europe. *J. Geophys. Res. Atmos.*, 125, e2019

694 Denissen, J. M. C., Orth, R., Wouters, H., Miralles, D. G., van Heerwaarden, C. C., de Arellano, J. V.-G.,
695 Teuling, A. J., 2021. Soil moisture signature in global weather balloon soundings, *npj Climate and*
696 *Atmospheric Science*, 4, 13.

697 de Rooy, W. C. and Holtslag, A. A. M., 1999. Estimation of surface radiation and energy flux densities
698 from single-level weather data. *J. Appl. Meteor.*, 38, 526– 540.

699 Dillon E., Moran B., Lennon J., Donnellan T. 2018. Teagasc National Farm Survey 2018 Results.
700 Available online at [https://www.teagasc.ie/publications/2019/National-Farm-Survey-](https://www.teagasc.ie/publications/2019/National-Farm-Survey-Preliminary-Results-2018.php)
701 [Preliminary-Results-2018.php](https://www.teagasc.ie/publications/2019/National-Farm-Survey-Preliminary-Results-2018.php) Last accessed November, 2019.

702 Dirmeyer, P. A., Balsamo, G., Blyth, E. M., Morrison, R., and Cooper, H. M., 2021. Land-atmosphere
703 interactions exacerbated the drought and heatwave over northern Europe during summer
704 2018. *AGU Advances*, 2, e2020AV000283. <https://doi.org/10.1029/2020AV000283>

705 Dole, R., Hoerling, M., Perlwitz, J., Eischeid, J., Pegion, P., Zhang, T., Quan, X-W., Xu, T., Murray D.,
706 2011. Was there a basis for anticipating the 2010 Russian heat wave? *Geophys. Res. Lett.* 3,
707 L06702. doi: 10.1029/2010GL046582

- 708 Falzoi, S., Gleeson, E., Lambkin, K., Zimmermann, J., Marwaha, R., O'Hara, R., Green, S., Fratianni S.,
709 2019. Analysis of the severe drought in Ireland in 2018. *Weather*, 99 (99), 1- 6.
710 doi:10.1002/wea.3587
- 711 Feldman, A. F., Short Gianotti, D. J., Trigo, I. F., Salvucci, G. D. & Entekhabi, D., 2019. Satellite-based
712 assessment of land surface energy partitioning-soil moisture relationships and effect of
713 confounding variables. *Water Resour. Res.*, 55, 10657–10677
- 714 Fennessy, M. J and Kinter, J. L., 2011. Climatic feedbacks during the 2003 European heatwave. *J. Clim.*,
715 24, 5953–67.
- 716 Fink, A. H, Brücher, T, Krüger, A, Leckebusch, G. C, Pinto, J. G. and Ulbrich, U., 2004. The 2003 European
717 summer heatwaves and drought – synoptic diagnosis and impacts. *Weather*, 59, 209–16
- 718 García-Herrera, R, Díaz, J, Trigo, R. M, Luterbacher, J. and Fischer, E. M., 2010. A review of the
719 European summer heatwave of 2003. *Crit. Rev. Environ. Sci. Technol.*, 40, 267–306
- 720 Green, S., 2019. Investigation into the bio-physical constraints on farmer turn-out-date decisions using
721 remote sensing and meteorological data. PhD Thesis, University College Cork.
722 <http://hdl.handle.net/10468/7795>.
- 723 Haghighi, E., Short Gianotti, D. J., Akbar, R., Salvucci, G. D. and Entekhabi, D., 2018 Soil and
724 atmospheric controls on the land surface energy balance: a generalized framework for
725 distinguishing moisture-limited and energy-limited evaporation regimes. *Water Resour. Res.* 54,
726 1831–1851
- 727 Hersbach, H., Dee, D., 2016. ERA-5 reanalysis is in production, ECMWF newsletter, number 147, Spring
728 2016, p. 7
- 729 Ishola, K. A., Fealy, R., Mills, G., Fealy, R., Green, S., Jimenez-Casteneda A. and Adeyeri, O. E., 2018.
730 Developing regional calibration coefficients for estimation of hourly global solar radiation in
731 Ireland. *International Journal of Sustainable Energy*, 38 (3), 297 – 311.
732 <https://doi.org/10.1080/14786451.2018.1499645>.
- 733 Ishola, K. A., Mills, G., Fealy R. M., Ní Choncubhair Ó., Fealy R., 2020. Improving a land surface Scheme
734 for estimating sensible and latent heat fluxes above grassland with contrasting soil moisture
735 zones. *Agric. Fores. Meteor.*, 294, <https://doi.org/10.1016/j.agrformet.2020.108151>
- 736 Ishola, K. A., Fealy, R., and Mills, G., 2021. SURFLEX: (Version v1.1.0). Zenodo.
737 <http://doi.org/10.5281/zenodo.4679843>
- 738 Jaksic, V., Kiely, G., Albertson, J., Oren, R., Katul, G., Leahy, P., Byrne, K.A., 2006. Net ecosystem
739 exchange of grassland in contrasting wet and dry years. *Agri. For. Meteorol.* 139, 323–334.
- 740 Jarvis, P., 1976. The interpretation of leaf water potential and stomatal conductance found in canopies
741 in the field. *Philos. Trans. Roy. Soc. London B*, 273, 593–610.
- 742 Jung, M., Reichstein, M., Ciais, P., Seneviratne, S. I., Sheffield, J., Goulden, M. L., Bonan, G., Cescatti,
743 A., Chen, J., de Jeu, R., Dolman, A. J., Eugster, W., Gerten, D., Gianelle, D., Gobron, N., Heinke,
744 J., Kimball, J., Law, B. E., Montagnani, L., Mu, Q., Mueller, B., Oleson, K., Papale, D., Richardson,
745 A. D., Roupsard, O., Running, S., Tomelleri, E., Viovy, N., Weber, U., Williams, C., Wood, E.,
746 Zaehle, S., and Zhang, K., 2010. Recent decline in the global land evapotranspiration trend due
747 to limited moisture supply, *Nature*, 467, 951–954.
- 748 Keane, T. and Collins, J.F. (Eds.), 2004. Climate, Weather and Irish Agriculture, AGMET, UCD, Belfield,
749 Dublin 4.
- 750 Kiely, G., Leahy, P., Lewis, C., Sottocornola, M., Laine, A., Koehler, A.-K., 2018. GHG fluxes from
751 Terrestrial Ecosystems in Ireland. Research report No. 227.EPA Research Programme,

752 Wexford. Available online at
753 https://www.epa.ie/pubs/reports/research/climate/Research_Report_227.pdf

754 Knist, S., Goergen, K., Buonomo, E., Christensen, O.B., Colette, A., Cardoso, R.M., Fealy, R.,
755 Fernandez, J., Garcia-Diez, M., Jacob, D., Kartsios, S., Katragkou, E., Mayer, S., van Meijgaard,
756 E., Nikulin, G., Soares, P.M.M., Sobolowski, S., Szepszo, G., Teichmann, C., Vautard, R.,
757 Warrach-Sagi, K., Wulfmeyer, V. and Simmer, C., 2017. Land atmosphere coupling in EURO-
758 CORDEX evaluation experiments. *Journal of Geophysical Research Atmospheres*, 122, 79–103.

759 Kornhuber, K., Osprey, S., Coumou, D., Petri, S., Petoukhov, V., Rahmstorf, S., and Gray, L., 2019.
760 Extreme weather events in early summer 2018 connected by a recurrent hemispheric
761 wave-7 pattern. *Environmental Research Letters*, 14(5), 054002. <https://doi.org/10.1088/1748-9326/ab13bf>
762 <https://doi.org/10.1088/1748-9326/ab13bf>

763 Lansu, E. M., van Heerwaarden, C. C., Stegehuis, A. I., Teuling, A. J., 2020. Atmospheric aridity and
764 apparent soil moisture drought in European forest during heatwaves. *Geophysical Research*
765 *Letters*, 47, e2020GL087091. <https://doi.org/10.1029/2020GL087091>

766 Li, M., Wu, P., Ma, Z., 2020. A comprehensive evaluation of soil moisture and soil temperature from
767 third generation atmospheric and land reanalysis data sets. *International Journal of*
768 *Climatology*, 1 – 23, DOI: 10.1002/joc.6549

769 Lu, J., R. Tang, H. Tang, and Z.-L. Li, 2014. A new parameterization scheme for estimating surface
770 energy fluxes with continuous surface temperature, air temperature, and surface net radiation
771 measurements, *Water Resour. Res.*, 50, 1245–1259

772 Magnusson, L., Ferranti, L., Vamborg, F., 2018. Forecasting the 2018 European heatwave. *ECMWF*
773 *Newsletter*, 157, 4.

774 McDonnell, J., Lambkin, K., Fealy, R., Hennessy, D., Shalloo, L. and Brophy, C., 2018. Verification and
775 bias correction of ECMWF forecasts for Irish weather stations to evaluate their potential
776 usefulness in grass growth modelling. *Met. Apps*, 25, 292-301.

777 McEniry, J., Crosson, P., Finneran, E., McGee, M., Keady, T.W.J. and O’Kiely, P., 2013. How much
778 grassland biomass is available in Ireland in excess of livestock requirements?. *Irish Journal of*
779 *Agricultural and Food Research*, 52, 67–80

780 McKee, T.B., N.J. Doesken and J. Kleist., 1993. The relationship of drought frequency and duration to
781 time scale. In: Proceedings of the Eighth Conference on Applied Climatology, Anaheim,
782 California, 17–22 January 1993. Boston, American Meteorological Society, 179–184.

783 Met Eireann Report, 2018. A summer of heatwaves and droughts. Available online at
784 <https://www.met.ie/cms/assets/uploads/2018/09/summerfinal3.pdf> , last accessed
785 November, 2019.

786 Miralles D. G., Gentine, P., Seneviratne S. I., Teuling A. J., 2019. Land-atmosphere feedbacks during
787 droughts and heatwaves: state of the science and current challenges. *Ann. N. Y. Acad. Sci.* 1436,
788 19 – 35. doi: 10.1111/nyas.13912

789 Miralles, D. G., Teuling, A. J., van Heerwaarden, C. C., & de Arellano, J.-G., 2014. Mega-heatwave
790 temperatures due to combined soil desiccation and atmospheric heat accumulation. *Nature*
791 *Geoscience*, 7(5), 345.

792 Monteith, J., 1981. Evaporation and surface temperature. *Q. J. R. Meteorol. Soc.*, 107, 1–27.

793 Moore, P., 2020. Summer 2018. Available online at
794 <https://www.met.ie/cms/assets/uploads/2020/06/Summer2018.pdf>, last accessed February,
795 2021

- 796 Muggeo, V. M. R., 2003. Estimating regression models with unknown break-points. *Statistics in*
797 *Medicine*, 22(19), 3055–3071. <https://doi.org/10.1002/sim.1545>
- 798 Muggeo, V. M. R., 2021. Regression models with break-points/change-points estimation. An R
799 'segmented' package version 1.3-3. Accessed on 10 March, 2021.
- 800 Murphy, C., Wilby, R.L., Matthews, T.K., Horvath, C., Crampsie, A., Ludlow, F., Noone, S., Brannigan, J.,
801 Hannaford, J., McLeman, R., Jobbova, E., 2020. The forgotten drought of 1765 – 1768:
802 Reconstructing and re-evaluating historical droughts in the British and Irish isles. *International*
803 *Journal of Climatology*, 1 – 23, DOI: 10.1002/joc.6521
- 804 Ní Choncubhair, Ó., B. Osborne, J. Finnan, G. Lanigan, 2017. Comparative assessment of ecosystem C
805 exchange in *Miscanthus* and reed canary grass during early establishment, *GCB Bioenergy*, 9,
806 280 – 298, doi: 10.1111/gcbb.12343.
- 807 Noone S, Broderick C, Duffy C., Matthews, T., Wilby, R. L., Murphy, C., 2017. A 250-year drought
808 catalogue for the Island of Ireland (1765-2015). *Int. J. Climatol.* 37(S1): 239–254.
- 809 Paulson, C. A., 1970. The Mathematical Representation of Wind Speed and Temperature Profiles in
810 the Unstable Atmospheric Surface Layer, *J Appl. Meteor.*, 9, 857–861.
- 811 Peel, M. C., Finlayson, B. L., and McMahon, T. A., 2007. Updated world map of the Köppen-Geiger
812 climate classification, *Hydrol, Earth Syst. Sci.*, 11, 1633–1644. Peichl, M., Carton, O. and Kiely, G.,
813 2012. Management and climate effects on carbon dioxide and energy exchanges in a maritime
814 grassland, *Agric. Ecosys. Environ.*, 158, 132 – 146.
- 815 Rösner, B., Benedict, I., van Heerwaarden, C., Weerts, A., Hazeleger, W., Bissolli, P., and Trachte, K.,
816 2019. The long heat wave and drought in Europe in 2018. *Bulletin of the American*
817 *Meteorological Society*, 100(9), S222–S223.
- 818 Schaaf, C. and Wang, Z., 2015. MCD43A4 MODIS/Terra+ Aqua BRDF/Albedo Nadir BRDF Adjusted Ref
819 Daily L3 Global-500 m V006 [Data set], NASA EOSDIS Land Processes
820 DAAC, <https://doi.org/10.5067/MODIS/MCD43A4.006>
- 821 Schuldt, B., Buras, A., Arend, M., Vitasse, Y., Beierkuhnlein, C., Damm, A., Gharun, M., Grams, T.E.E.,
822 Hauck, M., Hajek, P., Hartmann, H., Hiltbrunner, E., Hoch, G., Holloway-Phillips, M., Korner, C.,
823 Larysch, E., Lubbe, T., Nelson, D. B., Rammig, A., Rigling, A., Rose, L., Ruehr, N. K., Schumann, K.,
824 Weiser, F., Werner, C., Wohlgemuth, T., Zang, C. S., Kahmen, A., 2020. A first assessment of the
825 impact of the extreme 2018 summer drought on Central European forests. *Basic and Applied*
826 *Ecology*, 45, 86–103.
- 827 Seneviratne, S.I., Corti, T., Davin, E. L., Hirschi, M., Jaeger, E. B., Lehner, I., Orlowsky B., Teuling, A. J.,
828 2010. Investigating soil moisture–climate interactions in a changing climate: a review. *Earth Sci.*
829 *Rev.*, 99, 125–161.
- 830 Stap L. B., van den Hurk B. J. J. M., van Heerwaarden C. C., Neggers R. A. J., 2014. Modeled Contrast in
831 the response of the surface energy balance to heatwaves for forest and grassland. *J. Hydromet.*,
832 15, 973 – 989.
- 833 Streck, N. A. (2003). Stomatal response to water vapor pressure deficit: An unsolved issue. *Current*
834 *Agricultural Science and Technology*, 9(4), 317–322.
- 835 Teuling, A. J., 2018. A hot future for European droughts. *Nature Climate Change*, 8, 364 – 365.
- 836 Teuling, A. J., Seneviratne, S. I., Stöckli, R., Reichstein, M., Moors, E., Ciais, P., Luysaert S., van den
837 Hurk B., Ammann C., Bernhofer C., Dellwik E., Gianelle D., Gielen B., Grunwald T., Klumpp K.,
838 Montagnani L., Moureaux C., Sottocornola M., Wohlfahrt G., 2010. Contrasting response of
839 European forest and grassland energy exchange to heatwaves. *Nature Geoscience*, 3(10), 722–
840 727.

- 841 van de Boer, A., Moene, A. F. , Graf, A., Simmer, C. and Holtslag, A. A. M., 2014. Estimation of the
842 refractive index structure parameter from single-level daytime routine weather data. *Applied*
843 *Optics*, 53 (26), 5944 – 5960.
- 844 van Hateren, T. C., Chini, M., Matgen, P., Teuling, A., 2021. Ambiguous Agricultural Drought:
845 Characterising Soil Moisture and Vegetation Droughts in Europe from Earth Observation.
846 *Remote Sensing*, 13 (10), 1990. <https://doi.org/10.3390/rs13101990>
- 847 van Heerwaarden, C. C. and Teuling, A. J., 2014 Disentangling the response of forest and grassland
848 energy exchange to heatwaves under idealized land–atmosphere coupling, *Biogeosciences*, 11,
849 6159–6171.
- 850 van Heerwaarden, C. C., Vila-Guerau de Arellano, J., Gounou, A., Guichard, F., & Couvreur, F.,
851 2010. Understanding the daily cycle of evapotranspiration: A method to quantify the influence
852 of forcings and feedbacks. *Journal of Hydrometeorology*, 11(6), 1405– 1422.
- 853 van Loon, A.F., 2015. Hydrological drought explained. *WIREs Water*, 2, 359–392
- 854 van Ulden, A. P., and A. A. M. Holtslag, 1985. Estimation of atmospheric boundary layer parameters
855 for diffusion applications. *J. Climate Appl. Meteor.*, 24, 1196–1207.
- 856 Verger, A., Baret, F., Weiss, M., 2014. Near real time vegetation monitoring at global scale. *IEEE J. Sel.*
857 *Top. Appl. Earth Obs. Remote Sens.*, 7, 3473–3481.
- 858 Vicente-Serrano, S. M., Domínguez-Castro, F., Murphy, C., Hannaford, J., Reig, F., Peña-Angulo, D.,
859 Trambly, Y., Trigo, R. M., Mac Donald, N., Luna, M. Y., Mc Carthy, M., Van der
860 Schrier, G., Turco, M., Camuffo, D., Noguera, I., García-Herrera, R., Becherini, F., Della Valle, A.,
861 Tomas-Burguera, M., El Kenawy, A., 2020. Long-term variability and trends in meteorological
862 droughts in Western Europe (1851–2018), *International Journal of Climatology*, 1 – 28, DOI:
863 10.1002/joc.6719
- 864 Viterbo, P., 1996: The representation of surface processes in general circulation models. Ph.D. thesis,
865 University of Lisbon, 201 pp. [Available from P. Viterbo, ECMWF, Shinfield Park, Reading RG2
866 9AX, United Kingdom.]
- 867 Walsh S., 2012. A summary of climate averages for Ireland, 1981 – 2010. MET Eireann
868 CLIMATOLOGICAL NOTE No. 14, Dublin. Available online at [https://www.met.ie/climate-](https://www.met.ie/climate-ireland/SummaryClimAvgs.pdf)
869 [ireland/SummaryClimAvgs.pdf](https://www.met.ie/climate-ireland/SummaryClimAvgs.pdf)
- 870 Wan, Z., Hook, S., Hulley, G. (2015). *MOD11A1 MODIS/Terra Land Surface Temperature/Emissivity*
871 *Daily L3 Global 1km SIN Grid V006* [Data set]. NASA EOSDIS Land Processes DAAC. Accessed
872 2021-01-29 from <https://doi.org/10.5067/MODIS/MOD11A1.006>
- 873 Wang, W., Ertsen, M. W., Svoboda, M. D., Hafeez, M., 2016. Propagation of Drought: From
874 Meteorological Drought to Agricultural and Hydrological Drought. *Adv. Meteor.*, 6547209,
875 <https://doi.org/10.1155/2016/6547209>
- 876 Xiao, J., Zhuang, Q., Liang, E., Shao, X., McGuire, A. D., Moody, A., Kicklighter, D. W., Melillo, J. M.,
877 2009. Twentieth-century droughts and their impacts on terrestrial carbon cycling in China. *Earth*
878 *Interact.* 13, 1–31.
- 879 Zaitchik, B. F., Macalady, A. K., Bonneau, L. R. and Smith, R. B., 2006. Europe’s 2003 heat wave: A
880 satellite view of impacts and land–atmosphere feedbacks. *Int. J. Climatol.* 26, 743–769.
- 881 Zhang, L., Xiao, J., Li, J., Wang, K., Lei, L. and Guo, H., 2012. The 2010 spring drought reduced primary
882 productivity in southwestern China. *Environmental research Letters*, 7(4), 1748-9326.
- 883 Zscheischler, J., Westra, S., Hurk, B. J. J. M. van den, Seneviratne, S. I., Ward, P. J., Pitman, A., Agha
884 Kouchak, A., Bresch, D. N., Leonard, M., Wahl, T., and Zhang, X., 2018. Future climate risk from
885 compound events. *Nature Climate Change*, 8(6), 469–477.